Universidad de Oviedo

Department of Electrical, Electronics, Communications and Systems Engineering

PhD Thesis

Stability Analysis and Control Methods to Mitigate Low-Frequency Oscillation in High-Speed Trains

by

Paul Alejandro Frutos Galarza

PhD Program in Energy and Process Control
Electrical Energy Conversion and Power Systems Research Line

December 2023

Universidad de Oviedo

Department of Electrical, Electronics, Communications and Systems Engineering

PhD Thesis

Stability Analysis and Control Methods to Mitigate Low-Frequency Oscillation in High-Speed Trains

by

Paul Alejandro Frutos Galarza

Dissertation submitted in fulfillment of the requirements for the degree of Doctor of Philosophy in the Energy and Process Control PhD program at the University of Oviedo

Supervisor: PhD. Prof. Fernando Briz.
Supervisor: PhD. Prof. Juan Manuel Guerrero.

December 2023

Universidad de Oviedo

Departamento de Ingeniería Eléctrica, Electrónica, de Comunicaciones y de Sistemas

Tesis Doctoral

Análisis de Estabilidad y Métodos de Control para Mitigar la Oscilación de Baja Frecuencia en Trenes de Alta Velocidad

Paúl Alejandro Frutos Galarza

Tesis presentada en cumplimiento de los requisitos para la obtención del grado de Doctor en el programa de Doctorado en Energía y Control de Procesos de la Universidad de Oviedo

Supervisor: PhD. Prof. Fernando Briz.
Supervisor: PhD. Prof. Juan Manuel Guerrero.

December 2023

To my mother Mirian-Judith, my family and friends.

Acknowledgements

First, I would like to express my sincere gratitude and recognition to my thesis advisors, Prof. Fernando Briz and Prof. Juan Manuel Guerrero. I appreciate their dedication, time, patience, and unwavering assistance throughout this thesis process.

Second, I would also like to thank the members of the Ingeteam R&D Department: Igor Larrazabal, David Ortega, Iker Muniategui, and Aitor Endemaño, for their collaboration, valuable comments, and support. Furthermore, I extend special thanks to Iban Vicente for his guidance and technical support over the years.

Third, my sincerest gratitude goes to Prof. Philippe Ladoux and Dr. Nicolas Roux from the Laplace Laboratory in Toulouse, France. I am grateful for the opportunity to collaborate with them and learn from their expertise.

I would also like to express my special gratitude to my laboratory colleagues during these years: Mariam Saeed Hazkial, Ahmed Fathy Youssef Moham Abouzeid, Edson de Souza Lima Junior, Nihal Vantagodi, Tadele Lijalem Yirisaw and Sara Roos.

Finally, I want to acknowledge my family members with profound appreciation for their unwavering dedication and support.

Resumen

La electrificación se ha convertido hoy en día en un tema destacado dentro del sector del transporte, cuyo objetivo principal es reducir las emisiones de gases de efecto invernadero y mitigar el impacto del cambio climático en nuestro planeta. La electrificación del transporte implica la sustitución gradual de vehículos propulsados por combustibles fósiles por homólogos eléctricos, abarcando diversos modos de transporte, como vehículos de carretera, sistemas ferroviarios, aviones y barcos. Los ferrocarriles eléctricos, en particular, ofrecen varias ventajas relevantes sobre otros medios de transporte, incluida una eficiencia energética muy alta y, en consecuencia, menores emisiones, así como menores costos operativos. Además, los ferrocarriles eléctricos pueden incorporar fácilmente sistemas de frenado regenerativo que convierten la energía cinética del tren nuevamente en electricidad, devolviéndola a la red eléctrica para que la utilicen otros trenes o la red pública. A diferencia de las locomotoras a diésel, los ferrocarriles eléctricos tienen la flexibilidad de funcionar con una variedad de fuentes de energía, incluida la energía renovable.

Los convertidores electrónicos de potencia son los elementos fundamentales para la integración de múltiples fuentes de energía, elementos de tracción y equipos auxiliares. Si bien la presencia de una gran cantidad de convertidores electrónicos de potencia puede resultar beneficiosa en términos de eficiencia y controlabilidad, pueden ocurrir fenómenos inesperados debido a sus interacciones. Entre estos está el fenómeno de oscilación de baja frecuencia, que puede provocar un corte de energía en la subestación del sistema ferroviario y, en consecuencia, la interrupción del tráfico.

Esta tesis está dirigida al modelado, análisis y comprensión del fenómeno de oscilación de baja frecuencia (LFO) en sistemas ferroviarios alimentados por catenaria. Las herramientas desarrolladas y utilizadas en este trabajo incluyen: análisis en el dominio de la frecuencia, identificación de valores propios, modelos de pequeña señal y simulaciones en el dominio del tiempo.

Se estudiará la influencia de los elementos constructivos y los parámetros de control en la aparición de LFO. Estos incluyen la longitud y las características de la línea de contacto, elementos pasivos de la unidad de tracción como la inductancia de fuga del transformador y la capacitancia del enlace DC, el diseño y anchos de banda del control, y los sistemas de sincronización. Se explorará la sintonización adecuada de los

controladores de trenes para evitar este tipo de inestabilidad.

Además, se ha desarrollado un nuevo modelo analítico de pequeña señal de la admitancia de entrada del tren. Para ello se obtiene el modelo de pequeña señal de cada elemento dinámico de los lazos de control, incluido el cálculo y modelado del integrador generalizado de segundo orden (SOGI) en el marco de referencia síncrono. Se utilizan métodos numéricos para la validación de los modelos. El concepto de la transformación en pequeña señal de vectores desde el marco de referencia dq al marco de referencia estimado $\widehat{dq}$ se presenta para modelar la dinámica debida a errores en la rotación de coordenadas. Las debidas herramientas matemáticas fueron desarrolladas para esta tarea. A partir de este modelo, se realiza un análisis de estabilidad del sistema ferroviario en diferentes condiciones de operación, confirmando la capacidad del modelo para predecir la inestabilidad de baja frecuencia.

Adicionalmente, se considerarán y compararán dos estrategias de control destinadas a mitigar el fenómeno LFO. El principio de dichos métodos se basa en el control de la oscilación del enlace de DC y la utilización de una impedancia virtual, respectivamente.

Finalmente, se realiza la réplica experimental del fenómeno LFO. Realizar experimentos en la red ferroviaria no es fácil, ni siquiera viable. Alternativamente, la red ferroviaria puede ser emulada utilizando un convertidor electrónico de potencia, que alimentaría el convertidor de potencia del tren sometido a prueba. Para este fin, se requiere un emulador de tipo Power-Hardware-in-the-loop (PHIL). En esta tesis, se realiza el diseño y construcción de un PHIL reducido a escala capaz de reproducir el comportamiento dinámico de la red real a bajas frecuencias. Se demostrará que el diseño y ajuste del control PHIL no es trivial. El diseño y la verificación del control PHIL se explican en detalle.

Abstract

Electrification has become a prominent topic within the transportation sector today, primarily aimed at reducing greenhouse gas emissions and mitigating the impact of climate change on our planet. Transportation electrification involves the gradual replacement of fossil fuel-powered vehicles with electric counterparts, encompassing various modes of transportation such as on-road and off-road vehicles, rail systems, airplanes, and ships. Electric railways, in particular, offer several relevant advantages over other means of transportation, including very high energy efficiency and consequently reduced emissions, as well as lower operational costs. Moreover, electric railways can easily incorporate regenerative braking systems that convert the train's kinetic energy back into electricity, returning it to the power grid for use by other trains or the utility grid. Additionally, electric railways have the flexibility to be powered by a variety of energy sources, including renewable energy, as opposed to diesel locomotives.

Electronic power converters are the pivotal elements for the integration of multiple energy sources, traction drives, and auxiliary equipment. While the presence of a large number of power electronic converters can be beneficial in terms of efficiency and controllability, unexpected phenomena can occur due to their interactions. Specifically, low-frequency oscillation of the contact-line voltage can lead to a power outage of the traction substation and, consequently, to the shutdown of train traffic.

The thesis is aimed towards the modeling, analysis, and understanding of low-frequency oscillation (LFO) in catenary-fed railway systems. Tools developed and used in this work include frequency-domain analysis, eigenvalue identification, small-signal models, and time-domain simulations.

The influence of constructive elements and control parameters in the appearance of LFO will be studied. These include contact-line length and characteristics, traction unit passive elements such as transformer leakage inductance, DC-link capacitance, control design and bandwidths, and synchronization systems. Proper tuning of train controllers will be explored in order to avoid low-frequency instability.

Furthermore, a new analytical small-signal model of the train input admittance has been developed. For this purpose, small-signal models of each dynamic element in the control loops are obtained, including the calculation of the second-order generalized integrator (SOGI) model in the synchronous frame. Numerical methods are used for

the validation of the models. The concept of the small-signal vector transformation from the actual dq-frame to the estimated $\widehat{dq}$-frame is presented to model the dynamics due to errors in the coordinate rotation; the mathematical tool was developed for this task. Based on this model, a stability analysis of the railway system is performed in different operating conditions, confirming the ability of the model to predict low-frequency instability.

Additionally, two control strategies aimed to mitigate LFO will be considered and compared. Their principle of operation is based on DC-link oscillation control and by means of a virtual impedance, respectively.

Experimental replication of the LFO phenomenon is finally addressed. Running experiments in the actual railway network is not easy, or even viable. Alternatively, the railway network can be emulated using a power electronic converter, which would feed the train power converter under test. A power-hardware-in-the-loop (PHIL) emulator is required for this purpose. The design of a down-scaled PHIL able to reproduce the dynamic behavior of the actual network at low frequencies was addressed in this thesis. It will be shown that PHIL control design and tuning are not trivial. PHIL control design and verification are explained in detail.

Nomenclature

Variable names

v_s	Substation voltage
i_s	Catenary-line current
v_c	Catenary-line voltage at PCC
v_n	4QC input voltage
$\widehat{v}_n$	Estimated 4QC input voltage
i_n	Leakage inductance current
$\widehat{i}_n$	Estimated leakage inductance current
v_t	4QC terminal voltage
v_{dc}	DC-link voltage
i_{dc}	DC-link current
i_L	Load current
θ	Catenary-line voltage phase angle
$\widehat{\theta}$	Estimated Catenary-line voltage phase angle
$\tilde{\theta}$	Angle estimation error
P_{ac}	Instantaneous power at PCC
P_{dc}	Instantaneous power at DC-side
P_L	Load power
f_0	Fundamental frequency (Hz)
ω_0	Fundamental frequency (rad/s)
f_{sw}	Switching frequency (Hz)
f_s	Sample frequency (Hz)

Domain transformations

v	Generic variable in the time domain
V	Variable in the Laplace domain
$V(j\omega)$	Variable in the frequency domain
$\mathbf{v} = [v_d, v_q]^T$	Real space vector in the time domain in the synchronous dq-frame
$\mathbf{V} = [V_d, V_q]^T$	Real space vector in the Laplace domain in the synchronous dq-frame

Reference frame transformations

v^e	Superscript indicating matrices, transfer functions, vectors, and vector components in the synchronous true reference frame
$v^{\hat{e}}$	Superscript indicating matrices, transfer functions, vectors and vector components in the estimated synchronous reference frame
v^s	Superscript indicating matrices and vectors in the stationary reference frame
$\mathbf{v^x} = [v_d^x, v_q^x]^T$	Real space vector in the time domain in a generic reference frame $x \, \epsilon \, \{e, \widehat{e}\}$
$\boldsymbol{v_{dq}^x} = v_d^x + jv_q^x$	Complex space vector in the time domain in a generic reference frame $x \, \epsilon \, \{e, \widehat{e}\}$
$\mathbf{V^x} = [V_d^x, V_q^x]^T$	Real space vector in the Laplace domain in a generic reference frame $x \, \epsilon \, \{e, \widehat{e}\}$
$\boldsymbol{V_{dq}^x} = V_d^x + jV_q^x$	Complex space vector in the Laplace domain in a generic reference frame $x \, \epsilon \, \{e, \widehat{e}\}$
$\mathbf{v^s} = [v_\alpha, v_\beta]^T$	Real space vector in the time domain in the stationary reference frame
$\boldsymbol{v_{\alpha\beta}^s} = v_\alpha + jv_\beta$	Complex space vector in the time in the stationary reference frame
$\mathbf{V^s} = [V_\alpha, V_\beta]^T$	Real space vector in the Laplace in the stationary reference frame
$\boldsymbol{V_{\alpha\beta}^s} = V_\alpha + jV_\beta$	Complex space vector in the Laplace in the stationary reference frame

Systems

$g(t)$	Impulse response in the time domain
$G(s)$	Transfer function in the Laplace domain

Acronyms

LFO	Low-Frequency Oscillation.
PCC	Point of Common Coupling.
SOGI	Second-Order Generalized Integrator.
PLL	Phase-Locked Loop.
VSC	Voltage Source Converter.
4QC	Four Quadrature Converter.
QSG	Quadrature Signal Generator.
PWM	Pulse-Width Modulation.
FLL	Frequency Locked Loop.
AC	Alternating Current.
DC	Direct Current.
PI	Proportional Integral (controller).
PD	Proportional Derivative (controller).
PID	Proportional Integral Derivative (controller).
RES	Resonant (controller).
LPF	Low-Pass Filter.
IEEE	Institute of Electrical and Electronics Engineers.
ESC	Electrical System Compatibility.
SLC	Stability Limit Curve.
SIL	Software-In-The-Loop.
HIL	Hardware-In-The-Loop.
PHIL	Power-Hardware-In-The-Loop.
SRF	Synchronous Reference Frame.
IGBT	Insulated-Gate Bipolar Transistor.
DG	Distributed Generation.
PLC	Power Line Communications.
ESR	Equivalent Series Resistance.
UUT	Unit Under Test.
POD	Power Oscillation Damping.
SISO	Single-Input Single-Output.
MIMO	Multiple-Input Multiple-Output.

Contents

List of Figures

List of Tables

Chapter 1

Introduction

1.1 Background

Electric rail vehicles, such as trains and trams, have a distinctive characteristic of being constantly connected to a power supply system while in operation. This is different from other modes of transportation like electric cars, buses, aircraft, and ships, which carry the necessary energy onboard.

The constant connection to the power supply system allows rail vehicles to receive a continuous and reliable source of electric power, which is crucial for their operation over long distances. However, it also means that rail vehicles are more dependent on the railway infrastructure for their power supply.

Modern rail vehicles that operate in the railway system include a large number of power electronic converters aimed to improve performance and efficiency. Despite the benefits, complex dynamic interactions between the power supply network and the controlled power converters can produce undesired phenomena, which might result in power system instability.

Achieving harmonious operation of all active and passive electric elements to ensure stable operation of railway system can be challenging. This is often referred to as *electrical system compatibility* (ESC), which encompasses the smooth interaction of electric components within the railway system such as electric rail vehicles, power supply infrastructure, electrical telecommunication, interlocking, signaling infrastructure and others [3].

Phenomenon affecting the regular operation of railway system due to the interaction between off-board and on-board elements is often classified into three different groups: Harmonic resonance [4,5], Electrical resonance instability [6] and low-frequency oscillations (LFOs). [2, 7–13].

Harmonic resonance is due to switching voltages and associated high-frequency currents of line-side converters in the traction machine, which may be amplified by electrical resonances in the power supply system (i.e. resonances of LC elements of the catenary-line). Usually, the range of these frequencies is three times the fundamental frequency and above [5]. This phenomenon leads to the degradation of catenary-line voltage and current. Possible consequences include interference in communication lines and the rail signaling system, overheating, and malfunction in the electric protection systems [14].

Electrical resonance instability is due to resonances in the railway system caused by feedback loop effects between the line-side converter controllers and the power supply system. The range of frequency is a few hundred Hz up to a few thousand Hz [15]. The main difference between resonant stability and harmonic resonance is that the second involves dynamic effects due to the interaction with the control of the power converters. Electrical resonance can result in over-voltages and associated over-currents at the train location but also at other locations along the power supply network; electromagnetic interference issues have also been reported [16].

The LFO phenomenon occurs due to dynamic interaction at low frequencies between the power supply system and electric vehicles. It has been reported worldwide for different types of railway networks under different operating conditions, including the 15 kV/16.7 Hz power system supplied from rotary converters [2], the 12 kV/25 Hz system with static frequency converters [9], and 25 kV/50 Hz power systems supplied from the public grid such as the case observed in the sector of Thionville in France [1], shown in Figure 1.1. Table 1.1 shows a summary of the reported events. LFO phenomenon can cause a number of serious issues, such as the malfunction of the protection system, over-voltage, and over-current, which could damage the electrical/electronic equipment and cause transportation delays [12].

In the 15 kV/16.7 Hz railway system, LFOs have been produced mainly due to a lack of damping in rotary converters [17]. In the 25 kV/50 Hz infrastructure, there are two specific scenarios in which the LFO phenomenon has been identified:

1. Multiple trains in the depot (i.e. all the vehicles located at the same place) [10]
2. A train operating at a very long distance from a substation [7]

From the point of view of the stability analysis, these two scenarios are equivalent, as is explained in [1, 11, 18]. This thesis will focus on the study of LFO in the AC 25 kV/50 Hz infrastructure.

When LFO occurs, an amplitude modulation of contact-line (i.e. catenary-line) voltage and current is produced. An example of this is shown in Figure 1.1, with f_{osc} being the oscillation frequency of the voltage and current envelopes. This is seen in the frequency spectra of catenary voltage and current as a fundamental frequency component at f_0 along with two side-band components at $(f_0 \pm f_{osc})$ as explained in [21]. It is observed from the events reported in Table 1.1 that the oscillation frequencies reached values up to 7 Hz.

Table 1.1: Reported LFO cases.

N º	Case	f_0 (Hz)	f_{osc} (Hz)	Year
1	Zürich, Switzerland [11]	16.7	5	1995
2	Norway [2, 8]	16.7	1.6	2007
3	Washington, USA [19, 20]	25	3	2006
4	Siemens test, Germany [7]	50	7	2006
5	Thionville, France [1]	50	5	2008
6	Hudong Depot, China [12]	50	2-4	2008
7	Shanhaiguan Hub, China [12]	50	6-7	2011

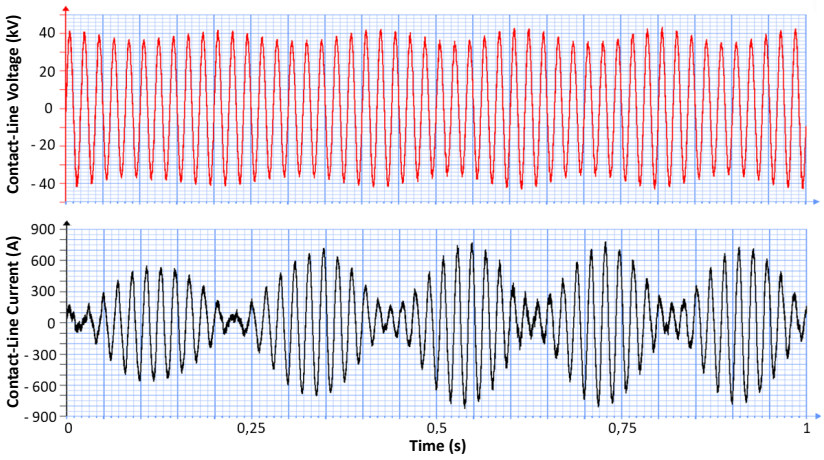

Figure 1.1: Contact-line voltage and current supplied by the substation. AC 25 kV/50 Hz electric power supply. Measured in Thionville, France [1].

1.2 Electric railway system

In this thesis, *Electric railway system* refers to all the components used for the generation, conversion, transmission, and consumption of energy for electric railway transport, including the control elements. It can be divided into two main blocks: the power supply network (from generation to transmission) and the traction vehicle. Both are described next.

1.2.1 Power supply network

The appearance of the AC 16.7 Hz electrification system is linked to the fact that at the beginning of the 20^{th} century, the technology did not allow the construction of traction motors using 50 Hz power. Therefore, the supply frequency was reduced to avoid switching problems [22]. As the electricity supply is specific, the railway network has its own production or frequency conversion plants. The supply of the railway system is carried out from the three-phase public network by means of synchronous-synchronous rotating groups. It therefore implies a rigid coupling between the frequency of the industrial network and the frequency of the railway network. The frequency of the railway network is then equal to one-third of the industrial frequency $50/3 = 16.7$ Hz. Such is the case of electrification in Sweden and Norway [23].

Further technological developments in power electronics and electric motor drives in electric vehicles made it possible to change the network frequency to supply the energy directly from the public network at grid-frequency $f_0 = 50$ Hz. In this case, the high-voltage network is connected through a substation to provide a catenary voltage of 25 kV. The substations in the 25 kV/50 Hz power system are very simple in comparison with rotary converters in the 15 kV/16.7 Hz system because they don't need a mechanical transformation of the energy, power transformers feed directly the contact-line (i.e. catenary-line), as shown in Figure 1.2.

Each substation feeds the catenaries on both sides of a sectioning station. In other words, halfway between the two substations, there is a sectioning station that electrically separates two adjacent sectors. The network is thus divided into sectors whose power supply is independent of the adjacent sectors, a train passing from one to another during its journey, as shown in Figure 1.2.

Depending on the power involved and the location, the substation can be fed between 63 kV and 400 kV (e.g., 250 kV). The spacing between substations can vary from 30 km to 90 km depending on the traffic and the profile of the line. This system is deployed in France, Denmark, Spain, Luxembourg, and Italy as well as worldwide in the main railway networks such as Russia, China and India [23].

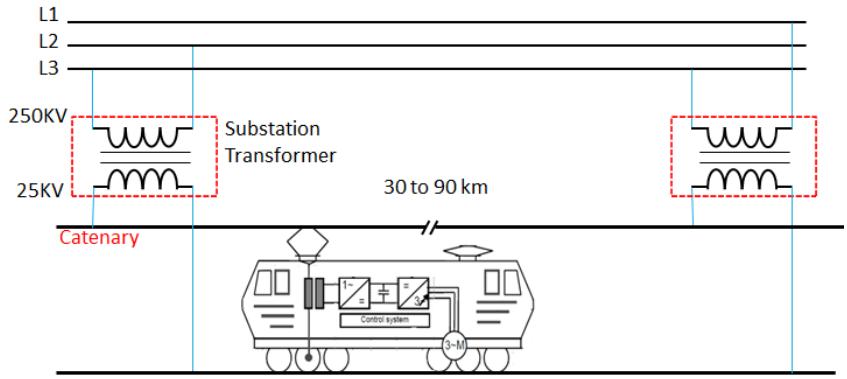

Figure 1.2: Contact-line voltage and current supplied by the substation. AC 25 kV/50 Hz electric power supply.

1.2.2 Electric vehicle (Train)

Figure 1.3 shows a typical layout of a modern electric train. The DC-link connects the line-side and motor-side converters. The line-side converter connects the vehicle with the power system through a step-down transformer. The line-side converter is a single-phase voltage source converter (VSC), also called a four-quadrant converter (4QC). Its task is to supply the DC-link capacitor from the overhead contact-line and includes the required control loops to keep the DC-link voltage constant. The three-phase voltage source inverter (VSI) feeding the traction motors are connected to the DC-link. Induction motors are the preferred solution for traction drives.

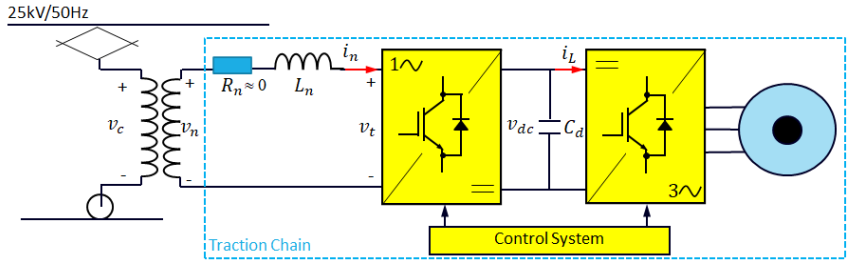

Figure 1.3: Electric vehicle (Train) with one traction chain

The line-side converter can operate in all four quadrants, independently controlling active and reactive power. This enables regenerative braking as well as controllability of the reactive power in the AC catenary [23].

Figure 1.3 shows a train with only one traction chain. However, a train could have connected in parallel several traction chains. In this thesis, the number of traction chains in a train will be specified for each case study.

1.2.3 Railway system model for LFO study

Due to the nature of LFO phenomenon subject of this thesis, it is possible to introduce some simplifications in the power supply system shown in Figure 1.2 and in the train model shown in Figure 1.3.

The power supply network will be modeled as an ideal voltage source at a fixed frequency, the upstream grid impedance Z_{ug}, the substation impedance Z_{sst}, and the contact-line (i.e. transmission-line) impedance. For the study of LFO, an equivalent circuit of the transmission-line based only on resistance and inductance is widely used [7, 11, 12, 21], as line capacitive effects can be safely neglected at low frequency. Therefore, the transmission-line impedance can be expressed as $Z_{cl} = d \times Z'_{cl}$, which depends on the distance (d) between the traction unit and the substation (i.e. contact-line length). Then, the total power supply network impedance (Z_s) is given by (1.1), where R_s is the total network resistance and L_s is the total network inductance.

$$Z_s = L_s s + R_s = 2 \times Z_{ug} + Z_{sst} + d \times Z'_{cl} \tag{1.1}$$

This simplified RL model is also supported by the experience reported in [11], and also is considered in the European standard document for the compatibility of rolling stock and infrastructure EN-50388-2.

On the other hand, switching harmonics of the machine-side inverter will not affect the low-frequency dynamics involved in the LFO phenomenon [17, 24]. Therefore, It is safe to replace the traction drives with an equivalent linear load, enormously simplifying analysis and simulations.

Two different train designs will be considered in the thesis, namely Train-A and Train-B. Both are described in the following.

1.2.3.1 Railway system model - Train-A

Figure 1.4 shows the main elements of the simplified railway traction system model using Train-A for LFO study, where v_s is the substation voltage, v_c is the catenary-line voltage at the point of common coupling (PCC), and i_s is the catenary-line current. Here the voltage at the secondary of the transformer is defined as the input voltage v_n; i_n is the AC-side current and the 4QC terminal voltage is v_t.

A cascaded control structure consisting of an outer voltage control loop and an inner current control loop is seen in Figure 1.4, the details are shown in Figure 1.5. In this control system, the DC-link voltage v_{dc} is regulated through the AC-side current i_n. The 4QC control shown in Figure 1.4 operates in dq coordinates, aligning the d-axis with the catenary voltage v_c. Current controller was tuned using zero-pole cancellation [25], the gains being obtained as shown by (1.2)-(1.3), with $\omega_{bcc} = 2\pi \cdot BWcc$, and $BWcc$ being the desired bandwidth in Hz. Typically, the current control bandwidth is in a range of 50 to 120 Hz.

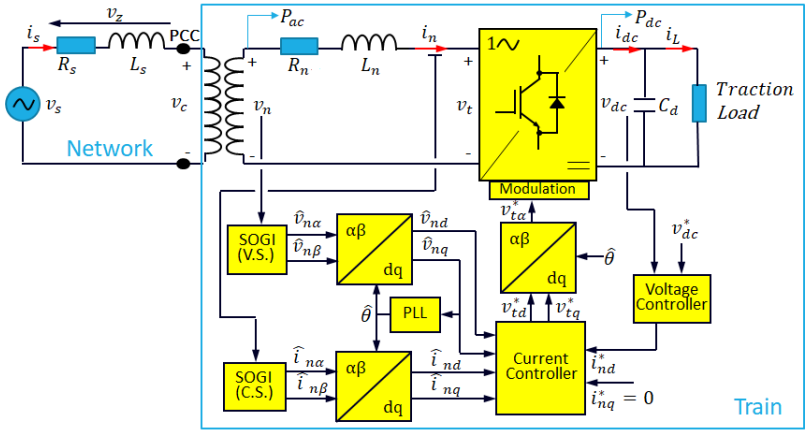

Figure 1.4: Railway control system model. Train-A.

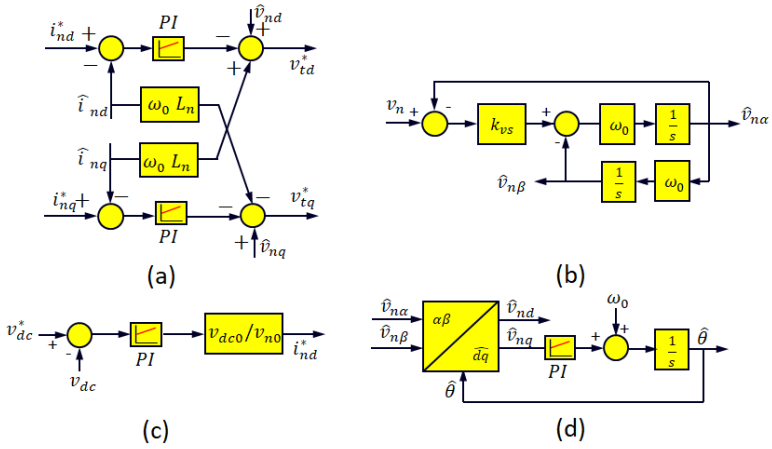

Figure 1.5: Control system elements. (a) Current controller (b) Voltage SOGI (c) DC-link Voltage Controller (d) Phase-locked loop

$$k_{pCC} = L_n \cdot \omega_{bcc} \tag{1.2}$$
$$k_{iCC} = R_n \cdot \omega_{bcc} \tag{1.3}$$

The DC-link voltage controller was tuned with a bandwidth $BWvc$ according to [25] (1.4)-(1.5), being $\omega_{bvc} = 2\pi \cdot BWvc$ and C_d the DC link capacitor. Typically, the voltage control bandwidth is in a range of 5 to 12 Hz.

$$k_{pVC} = C_d \cdot \omega_{bvc} \tag{1.4}$$
$$k_{iVC} = C_d \cdot \frac{\omega_{bvc}^2}{4} \tag{1.5}$$

A phase-lock loop (PLL) is used to estimate the grid voltage phase angle $\hat{\theta}$, which is required for the coordinate transformations into the synchronous reference frame [13]. The PLL was designed and tuned as described in [26], where the selection of the proportional gain k_{PLL} involves a trade-off between PLL filtering capability and dynamic response, and the integral gain is chosen as $k_{iPLL} = k_{PLL}^2/2$. A second-order generalized integrator (SOGI) is used as a filter and as a quadrature signal generator (QSG). The gain k_{vs} of the second order generalized integrator (SOGI) was chosen as described in [7].

1.2.3.2 Railway system model - Train-B

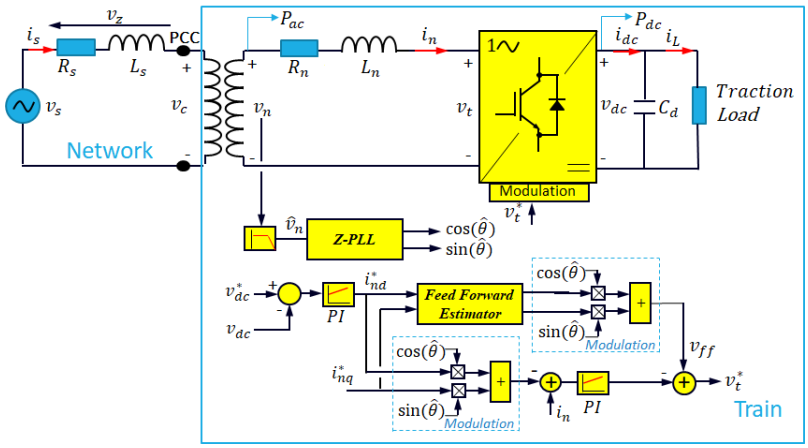

Figure 1.6: Railway control system model. Train-B.

Figure 1.6 shows the railway traction system model using Train-B. Two cascaded

loops regulate the voltage of the DC-link (slow dynamics) and the 4QC current (fast dynamics) using proportional-integral (PI) regulators. The inner current control loop is an instantaneous waveform control involving a sinusoidal reference obtained, after modulation, from the current set-points in the d- and q- axes [27]. This inner loop is improved with a feedforward estimator that anticipates the voltage drop across the input transformer impedance [27]. To achieve unit power factor, system synchronization is performed using the estimated contact-line voltage phase angle ($\hat{\theta}$), which is calculated using a PLL based on zero crossing detection [27], called in this document Z-PLL. The estimated angle is used for coordinate transformation between the stationary reference frame and the synchronous reference frame (i.e. dq frame). In order to obtain the desired current control bandwidth $BWcc$, controllers were tuned using (1.6) and (1.7) with $\omega_{bcc} = 2\pi \cdot BWcc$, as described in [27].

$$k_{pCC} = L_n \cdot \omega_{bcc} \tag{1.6}$$

$$k_{iCC} = \frac{L_n \cdot \omega_{bcc}^2}{\pi} \tag{1.7}$$

To obtain the desired voltage control bandwidth $BWvc$, voltage controller gains were tuned using (1.8) and (1.9) [27], with $\omega_{bvc} = 2\pi \cdot BWvc$.

$$k_{pVC} = C_d \cdot \omega_{bvc} \tag{1.8}$$

$$k_{iVC} = \frac{C_d \cdot \omega_{bvc}^2}{\pi} \tag{1.9}$$

1.3 General and specific objectives

The main objective of this thesis is to support Ingeteam R&D department in the understanding and knowledge acquisition of the LFO phenomenon in the AC 25 kV/50 Hz electrical railway power supply network. This comprises comprehension of the mechanism affecting the LFO phenomenon, the development of tools to analyze the influence of train electrical and control elements, and the development of tuning methodologies and other possible remedial actions to guarantee the system's resilience against LFO.

The specific objectives of this thesis are:

- Understanding of the different types of instability phenomena reported in the railway systems.
- Replication of the LFO phenomenon by simulations using MATLAB/Simulink in the scenarios and conditions where they have occurred. This implies an adequate modeling of the power supply system and the train, considering all the dynamic elements that contribute to the LFO.

- Selection, development, and implementation of the methods and techniques to perform the stability analysis of the railway system.
- Analysis of the influence of system constructive and operational parameters to the low-frequency instability, including contact-line impedance, consumed power on the DC-link that supplies the three-phase motor drives, the bandwidth of current and voltage controllers, transformer leakage inductance, DC-link capacitance, synchronization system, quadrature signal generation system, and feedforward signals.
- Development of a detailed analytical small-signal model of the four-quadrant converter control system, which allows to analyze the dynamic behavior of the interconnection between the power supply network and the train. It is required that this model can find the stability limits (i.e. maximum number of traction units or maximum distance from the substation) to predict the appearance of LFO.
- Implementation of the different control options of the four-quadrant AC/DC converter that is the main element on the train which interacts with the catenary-line dynamics.
- Implementation of control strategies specifically for the mitigation of LFO and imbalances caused by connecting several trains in the catenary interacting with each other.
- Designing and building a scaled test bench that emulates the catenary-line dynamics using a power electronic converter, which would feed a scaled version of the train four-quadrant converter in order to reproduce the LFO phenomenon.

1.4 Outline of the document

The outline of the document is as follows:

- **Chapter 1** introduces the research line of this dissertation. Background of low-frequency stability phenomenon is provided. The electric railway system is introduced as well as the system models used for the study of LFO. The objectives of this thesis are established. Finally, an outline of the report is presented.
- **Chapter 2** describes the study of LFO phenomenon using frequency-domain analysis. This chapter uses the output impedance of the power supply combined with the estimation of the train input admittance in the dq-frame to predict the stability limit. Validation of the model implies time domain simulation. Furthermore, this chapter presents an extended stability analysis for multiple trains in multiple locations of the catenary-line.

- **Chapter 3** presents the use of small-signal analytical models to study the LFO. Calculation of the small-signal model of the train input admittance is described. For this purpose, models of current control, DC-link control, PLL, and SOGI are developed. The main contributions in this chapter are the development of QSG-SOGI in the actual dq-frame as well as the dynamics due to errors in the coordinate rotations.
- **Chapter 4** presents the eigenvalue identification method to characterize the system dynamic behavior when LFO occurs. This method allows to understand the impact of the system parameters (e.g., current and voltage controller bandwidths) which can influence the appearance of LFO. Eigenvalue migration will be shown to be a powerful tool to assess the risk of instability.
- **Chapter 5** describes and compares two control strategies aimed to mitigate LFO applied to the 4QC, namely power oscillation damping (POD) and the virtual-impedance-based suppression method.
- **Chapter 6** presents the design of a catenary emulator aimed to reproduce the power supply network dynamics at low frequencies. A test bench implementation is described. Experimental results are provided in this chapter.
- **Chapter 7** summarizes the main conclusions and the results achieved during the development of this dissertation. Furthermore, ideas for future research are presented.
- **Appendix A** shows a detailed calculation of dynamics elements that influence the LFO. 1.- QSG-SOGI transfer function in synchronous *dq*-frame. 2.- Frame transformation of single-phase AC-side filter.
- **Appendix B** shows the journals and conference publications derived from this dissertation.

Chapter 2

Analysis in frequency domain

This chapter presents a stability analysis of the LFO phenomenon in the frequency domain. Stability criteria are applied over the impedance-based small-signal model of the railway traction system [2, 6, 11, 28]. The case of multiple trains located at a specific place in the power supply network (e.g. trains at the depot) and the case of a train operating at a very long distance from a substation will be considered. It will be shown that for stability analysis, both scenarios are equivalent. Stability study can be reduced therefore to an equivalent case that only takes into account the interaction between the power supply impedance and a single traction chain.

Train-B described in Section 1.2.3 will be used in this chapter. Constructive and operational parameters that contribute to low-frequency instability analyzed in this chapter include: contact-line length (i.e. distance from the substation); power consumed by traction drives; bandwidth of current and voltage controllers; transformer leakage inductance; DC-link capacitance; synchronization method; and feedforward signals. Since the trains have independent control of active and reactive power, it is advantageous to perform the stability study in the frequency domain using a dq synchronous reference frame [18, 27]. The train input admittance in the dq-frame required for the stability analysis is obtained using a frequency response test as described in [10]. Nyquist and Bode diagrams are used to determine the system stability limit, which corresponds to either the maximum distance from a substation at which a traction unit can operate safely, or the maximum number of traction chains connected in parallel on a specific contact-line sector. This ability to predict the stability limit allows for obtaining the Stability Limit Curve (SLC) in the complex impedance plane (R_s, X_s) [18]. This curve is a characteristic of each traction chain, and it is useful to find the stability limit of the traction chain in any network. The methods for stability analysis discussed in this chapter are validated by means of time-domain simulations.

2.1 Stability theory for LFO

Finding the limits for stability of a railway system (distance from the train to the substation or number of trains located in a section operating simultaneously) can be performed using tools for linear systems if models compatible with these methods (i.e. transfer functions or frequency response) are available.

The train-network connection can be represented using the model in (2.1), where V_s is the supply voltage at the substation, V_c is the contact-line voltage where the train is connected, and I_s is the contact-line current.

$$V_s = Z_s(j\omega)I_s + V_c \tag{2.1}$$

However, a number of non-linear elements can be seen in Figures 1.4 and 1.6, which will affect to V_c. The analysis of LFO can be performed by using linearized models at a given operating point (V_{s0}, I_{s0}, V_{c0}) as described by (2.2), where the delta symbol (δ) refers to the small variations of the voltages and currents around the specific operating point at which the analysis will be performed.

$$V_{s0} + \delta V_s = Z_s(j\omega)\big(I_{s0} + \delta I_s\big) + \big(V_{c0} + \delta V_c\big) \tag{2.2}$$

The network impedance, $Z_s(j\omega)$, is an RL circuit, which is linear and does not depend therefore on the operating point. The train behaves as a current source with a corresponding parallel input admittance, which determines the catenary current [2], see Figure 2.1. Train admittance defined by (2.3) depends on the operating point. Line impedance and train admittance are considered time-invariant in the analysis.

$$Y_T(j\omega) = \frac{\delta I_s}{\delta V_c} \tag{2.3}$$

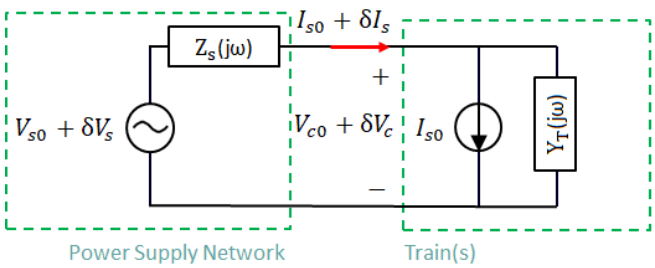

Figure 2.1: Railway system modelling for stability studies [2]

The train input admittance could be obtained by modeling analytically the electric drives and controls. However, this is not trivial. Alternatively, the input admittance

can be obtained using a frequency sweep as will be explained in Section 2.1.3. The train in such case is considered as a black box. This second approach is especially appealing as the train manufacturers do not often share specific information about the control design.

The railway system model from (2.2) can be separated into a steady circuit at the operating point (2.4) and the small signal model in (2.5), that is further explained in Section 2.1.1.

$$V_{s0} = Z_s(j\omega)I_{s0} + V_{c0} \tag{2.4}$$

$$\delta V_s = Z_s(j\omega)\delta I_s + \delta V_c \tag{2.5}$$

The stability analysis only remains valid near the operating point, and the results must be analyzed with caution when it is extended to more general operating conditions.

2.1.1 Impedance-based small-signal model

The small-signal model of the traction railway system in the frequency domain, developed and presented in [2, 6, 11, 28], is shown in Figure 2.2(a), where $Z_b(j\omega)$ is the base network impedance and n is a scaling factor of base impedance, its meaning will be defined for each case being analyzed. For instance, it could be the impedance of an electric sector, the impedance at the stability limit, or the impedance per distance (if the substation impedance can be neglected). The total network impedance is (2.6).

$$Z_s(j\omega) = n \cdot Z_b(j\omega) \tag{2.6}$$

The input admittance of a single traction chain is $Y_t(j\omega)$. The total input admittance is given by (2.7), m being the number of traction chains.

$$Y_T(j\omega) = m \cdot Y_t(j\omega) \tag{2.7}$$

Figure 2.2 shows that the railway traction small-signal model can be represented as a closed-loop system, whose transfer function is given by (2.8). Equation (2.9) defines the open loop transfer function.

$$\frac{\delta I_s}{\delta V_s} = \frac{m\,Y_t(j\omega)}{1 + n\,m\,Y_t(j\omega)Z_b(j\omega)} = \frac{Y_T(j\omega)}{1 + Y_T(j\omega)Z_s(j\omega)} \tag{2.8}$$

$$D(j\omega) = Y_T(j\omega)Z_s(j\omega) \tag{2.9}$$

The denominator of (2.8) is the characteristic equation [29,30]. To guarantee system stability, it must not be equal to zero for any frequency [29,30]. From the point of view of the stability analysis, the factor n multiplying the base impedance and the number

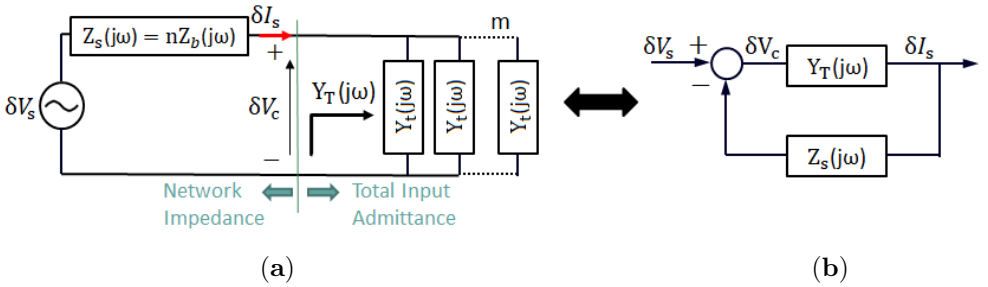

Figure 2.2: Closed loop system equivalence of small-signal model for n network impedance units and m traction chains. (**a**) Railway traction system small-signal model, (**b**) Equivalent closed loop system.

of traction chains m are interchangeable, meaning that $m \cdot n$ will be a critical coefficient of the characteristic equation. Therefore, a system composed of a number of identical traction chains can be equivalent to a system with a single traction chain fed through a multiple of the power base impedance.

2.1.2 Network impedance in dq reference frame

As explained in Section 1.2.3, the control of the train is implemented in a dq reference frame with the d-axis aligned to the contact-line voltage. This allows independent control of active and reactive power using the currents i_{nd} and i_{nq} respectively. Therefore, the power supply and the train form a multiple-input and multiple-output (MIMO) system in the dq reference frame.

The network impedance matrix in the dq reference frame is given by (2.10) [28,31], where, $\omega_0 = 2\pi f_0$ is the fundamental angular frequency.

$$\mathbf{Z_s}(j\omega) = \begin{bmatrix} Z_{s-dd}(j\omega) & Z_{s-dq}(j\omega) \\ Z_{s-qd}(j\omega) & Z_{s-qq}(j\omega) \end{bmatrix} = \begin{bmatrix} R_s + j\omega L_s & -\omega_0 L_s \\ \omega_0 L_s & R_s + j\omega L_s \end{bmatrix} \tag{2.10}$$

2.1.3 Train admittance in the dq-frame and frequency scanning algorithm

A method to obtain the train input admittance in the dq-frame is described in this subsection. This method is valid for any vehicle since it considers the train as a black box, presenting the advantage that it is not necessary to know the details of electric and control system parameters.

To measure the train input admittance, superimposition of a low-frequency small signal to the train's input voltage is required; see Figure 2.3. This method, commonly

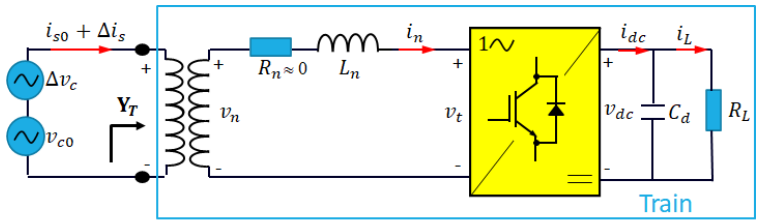

Figure 2.3: Test to measure the train input admittance by imposing perturbations in the train input voltage at different frequencies.

used in perturbation theory [10], involves setting the machine's operating point to its nominal voltage and subsequently adding small fluctuations in the amplitude of the contact-line voltage at a low frequency. By measuring the frequency response of the train's current and calculating the amplitude and phase shift of both the current and voltage signals, the Bode diagram of the train admittance can be obtained.

The input admittance matrix of the train in the synchronous frame is defined as (2.11), where small-signal variations in the $d \rightarrow \cos(\omega_0 t)$ and $q \rightarrow \sin(\omega_0 t)$ components of the contact-line voltage, ΔV_{cd} and ΔV_{cq}, are applied to the train at a certain perturbation angular frequency, ω, see (2.12). The terms with sub-index "$_0$" stand for the steady state voltage. As mentioned in Section 1.1, LFOs have been reported to reach values up to 7 Hz. Therefore, for this study, the perturbation frequencies are in a range up to 20 Hz.

$$\begin{aligned}\mathbf{Y_T}(j\omega) &= \begin{bmatrix} Y_{T-dd}(j\omega) & Y_{T-dq}(j\omega) \\ Y_{T-qd}(j\omega) & Y_{T-qq}(j\omega) \end{bmatrix} \\ &= \begin{bmatrix} \left.\frac{\Delta I_{sd}\angle\phi_d}{\Delta V_{cd}}\right|_{\Delta V_{cq}=0} & \left.\frac{\Delta I_{sd}\angle\phi_d}{\Delta V_{cq}}\right|_{\Delta V_{cd}=0} \\ \left.\frac{\Delta I_{sq}\angle\phi_q}{\Delta V_{cd}}\right|_{\Delta V_{cq}=0} & \left.\frac{\Delta I_{sq}\angle\phi_q}{\Delta V_{cq}}\right|_{\Delta V_{cd}=0} \end{bmatrix}\end{aligned} \tag{2.11}$$

$$\begin{aligned}v_{c0} + \Delta v_c =& \big(V_{cd0} + \Delta V_{cd}\sin(\omega t)\big)\cos(\omega_0 t) \\ &+ \big(V_{cq0} + \Delta V_{cq}\sin(\omega t)\big)\sin(\omega_0 t)\end{aligned} \tag{2.12}$$

$$\begin{aligned}i_{s0} + \Delta i_s =& \big(I_{sd0} + \Delta I_{sd}\sin(\omega t + \phi_d)\big)\cos(\omega_0 t) \\ &+ \big(I_{sq0} + \Delta I_{sq}\sin(\omega t + \phi_q)\big)\sin(\omega_0 t)\end{aligned} \tag{2.13}$$

The current components from (2.13), $(\Delta I_d, \angle\phi_d)$ and $(\Delta I_q, \angle\phi_q)$, related to each perturbation frequency, can be extracted from the measured current [10, 28] using any

optimization method that minimize the error between the measured current and the theoretical one [10,28]. In this work, `lsqnonlin` function from MATLAB, which applies least squares identification [32], was used.

Examples of measured dq admittance matrices for specific traction chains are shown in Sections 2.2.1 and 2.2.6.

2.1.4 Stability criteria in frequency domain

A train connected to an ideal voltage source (i.e. $Z_s(j\omega) = 0$) is a stable system [33]. The impedance of the railway power supply network is a passive element (i.e. RL element), which implies it is also stable. Therefore, these two elements are stable in open loop. Stability criteria for the interconnection of these two elements in a closed-loop system are presented in this section for the study of the LFO phenomenon.

A factorization of the system open loop transfer function $\mathbf{D}(j\omega)$ is given by (2.14), where $\mathbf{\Lambda}(j\omega)$ (2.15) is the eigenvalue matrix and $\mathbf{P}$ is the eigenvector matrix [28, 34].

$$\mathbf{D}(j\omega) = \mathbf{Y_T}(j\omega)\mathbf{Z_s}(j\omega) = \mathbf{P}\mathbf{\Lambda}(j\omega)\mathbf{P}^{-1} \tag{2.14}$$

$$\mathbf{\Lambda}(j\omega) = \begin{bmatrix} \lambda_1(j\omega) & 0 \\ 0 & \lambda_2(j\omega) \end{bmatrix} \tag{2.15}$$

Representing $\mathbf{\Lambda}(j\omega)$ as a diagonal matrix allows to study the stability of the eigenvalues $\lambda_1(j\omega)$ and $\lambda_2(j\omega)$ as two decoupled single-input single-output (SISO) systems.

Rever criterion applied in a Bode diagram [18] and Nyquist criterion [29] are widely used to analyze the stability of SISO systems in the frequency domain. Both criteria are equivalent, and either one is used at convenience in this thesis. These criteria have been selected since they are trusted and verified, and have been employed in previous studies of low-frequency stability; e.g. Rever criterion was selected for the study performed in [28, 34], while the Nyquist criterion was used in [11, 31, 35].

The stability criterion in the Bode diagram specifies that the closed-loop system is stable if, at the phase crossover frequency f_c (i.e., where the phase of eigenvalues $\lambda_{1,2}$ reaches $-180°$), the magnitude of the open loop transfer function is less than 1 in absolute units (i.e. less than 0 decibels) [18]. Similarly, the Nyquist criterion establishes that the closed loop system is stable if the eigenvalues do not encircle $(1, -180°)$ in the complex plane [29].

The gain margin is defined as $GM = 1/\left|\lambda_{1,2}(j2\pi f_c)\right|$. Therefore, stability is ensured for a gain margin larger than 1 using a linear scale (i.e. positive values in dB). At point $|\lambda_{1,2}| = 1$, the phase margin is defined as $PM = \angle\lambda_{1,2} - (-180°)$ [29].

2.2 Influence of infrastructure and traction chain parameters

This section illustrates how to use stability criteria developed in Section 2.1 in a particular scenario. The railway system with train-B shown in Figure 1.6 was chosen for this analysis. Section 2.2.1 presents the traction chain used in this study. Section 2.2.2 studies the influence of contact-line length; three different cases are studied. Validation of the analysis is performed by means of time simulations. Section 2.2.3 deals with the impact of the power consumption on the DC link, stability and its limits are calculated for a specific contact-line. Section 2.2.4 addresses the combined effect of transformer leakage inductance and current controller parameters. Section 2.2.5 deals with the influence of the DC-link capacitor and the voltage controller bandwidth. Section 2.2.6 studies the characteristics of the phase-locked loop (PLL) and the impact of the feedforward signal, and four combined cases are considered. Finally, conclusions are drawn in Section 2.4.

2.2.1 Traction chain input admittance

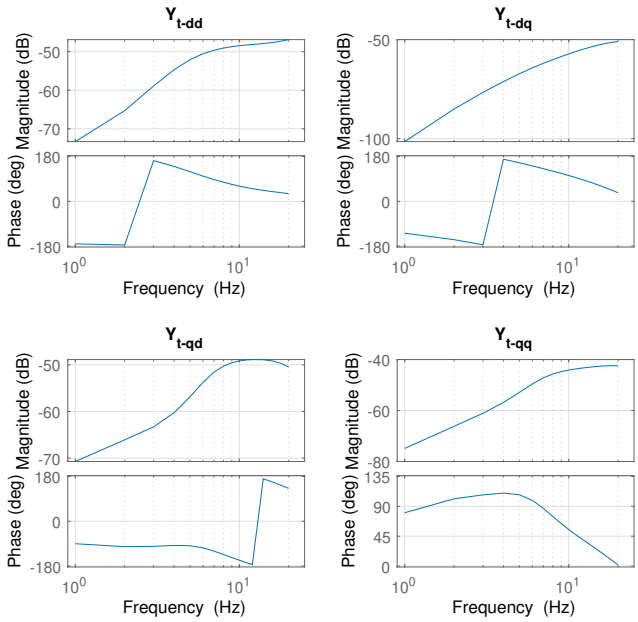

Figure 2.4: Traction-chain input admittance. Frequency range: 1 - 20 Hz

The dq input admittance of the traction chain is presented in Figure 2.4. It was

obtained using the frequency scanning algorithm presented in Section 2.1.3. The electrical and control parameters of the traction chain are found in Table 2.1. Note that the real part of the admittance components Y_{t-dd} and Y_{t-dq} at low frequency are negative. This is important to keep in mind since a negative admittance may cause instability.

Table 2.1: Traction chain parameters

Symbol	Description	Value
V_c	RMS Contact-Line Voltage	25 kV
f_0	Fundamental frequency	50 Hz
L_n	Leakage inductance	1 mH
C_d	DC-link Capacitor	16 mF
BW_{VC}	Voltage control bandwidth	8 Hz
BW_{CC}	Current control bandwidth	100 Hz
P_{DC}	Power at DC-link	100 kW

2.2.2 Influence of contact-line length

In this section, a train connected to a contact-line with different lengths (i.e. different network impedance) is analyzed. Only one traction chain per train is considered (i.e. $m = 1$). The study presents three different cases: a stable system, a system at its stability limit, and an unstable system. Time-domain simulations will be used to verify the stability analysis performed in the frequency domain.

2.2.2.1 Network impedance

The components of the network impedance Z_s are the upstream grid impedance Z_{ug}, the substation impedance Z_{sst}, and the contact-line impedance $Z_{cl} = d \times Z'_{cl}$, which depends on the distance (d) between the traction unit and the substation (i.e. contact-line length) [28]. See (1.1).

The parameters used in this study are the following [27]:

- $Z_{ug} = (0.5\ \Omega;\ 80°)$
- $Z_{sst} = (5.5\ \Omega;\ 80°)$
- $Z'_{cl} = (0.5\ \Omega/\text{km};\ 80°)$

The total network line impedance $Z_s = nZ_b$ is used for each case of study, where the base impedance corresponds to the impedance at the stability limit, $Z_b = (448.1\ \Omega;\ 80°)$, which occurs at a distance of 883.3 km. A value $n = 1$ corresponds to the stability limit case; $n = 0.5$ and $n = 1.5$ will be used as examples for the

stable and unstable cases. Notice that the distance to reach the stability limit is theoretical [28], and it is much higher than the typical length of a sector (around 50 km). Theoretical distances are used to facilitate the stability study (i.e. to find the stability limit) if only one traction chain is being considered [34], so, for a unit equipped with more than one traction chain, the distance limit is reduced according to the equivalence between n and m, as explained in Section 2.1.1. For example, considering 50 km as the maximum length of a sector in a 25 kV/50 Hz power supply system and vehicles equipped with four traction chains, the stability limit equivalence occurs when 3.55 vehicles are operating at the end of the sector line.

2.2.2.2 Stability analysis

Using the traction chain input admittance matrix and the network impedance matrix, the system eigenvalues of the open-loop transfer function for the three study cases are calculated from (2.14); they are shown in Figure 2.5, Bode diagrams and Nyquist plots are provided. The marked dots in the Bode diagram indicate the gain and phase margins.

It is seen from Figure 2.5 that increasing the contact-line length increases the magnitude of the total network impedance, but the phase remains unaffected. Therefore, the variation of contact-line length modifies only the magnitude of the eigenvalues λ_1 and λ_2 as shown in Figure 2.5(a). Furthermore, it is seen that the phase of eigenvalue λ_2 never intersects -180° at any frequency, which means that this eigenvalue is not causing instability. This applies to the three study cases. The same conclusion is reached using the Nyquist stability criterion in Figure 2.5(b) since λ_2 never encloses -1.

From Figure 2.5(a), it is seen that for the stable case (red curve), the eigenvalue λ_1 at phase crossover frequency $f_c = 4.75$ Hz (i.e. crossing phase at -180°) has a magnitude lower than 1, which fulfills the stability criterion explained in Section 2.1.4. Increasing the power supply impedance by a factor of two (i.e. from $n = 0.5$ to $n = 1$) will move the eigenvalue from $\lambda_1(j2\pi f_c) = (0.5, -180^\circ)$ to $\lambda_1(j2\pi f_c) = (1, -180^\circ)$, causing the system to reach the stability limit (blue curve). Similarly, when the network impedance is increased by a factor $n = 1.5$, the eigenvalue will go to $\lambda_1(j2\pi f_c) = (1.5, -180^\circ)$, see the yellow curve in Figure 2.5(a); thus, the system is not fulfilling the stability criterion anymore and it becomes unstable. It is essential to observe that the crossover frequency for $n = 1$ corresponds to the oscillation frequency at the stability limit.

The same analysis can be done using the Nyquist plot from Figure 2.5(b). For the stable case, the eigenvalue λ_1 does not enclose -1, which fulfills the Nyquist stability criterion; however, the eigenvalue λ_1 intersects the negative real axis; which means, a risk of instability is present when the gain is increased (i.e. increasing the power supply impedance or the number of traction chains, see the equivalence of n and m explained in Section 2.1.1). For $n = 1$, the eigenvalue curve λ_1 intersects the -1 (limit case); for $n = 1.5$, the curve λ_1 encircle -1, and the system becomes unstable.

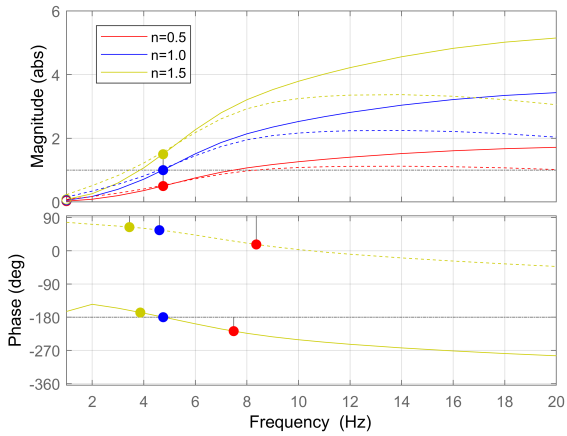

(a)

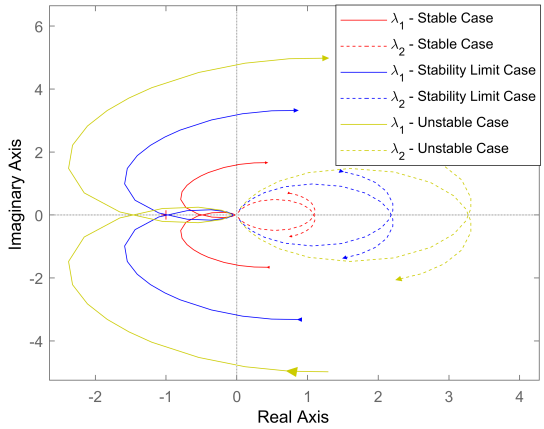

(b)

Figure 2.5: System eigenvalues (λ_1, λ_2) of the three study cases. Stable case (red): gain margin = 2 at 4.75 Hz; stability limit case (blue): gain margin = 1 at 4.75 Hz; unstable case (yellow): gain margin = 0.667 at 4.75 Hz. (**a**) Bode Diagram, (**b**) Nyquist Diagram.

The gain margin indicates the number of network impedance units or traction chains that are needed for the system to reach the stability limit. As already explained for the network impedance, the base impedance was chosen such that $n = 1$ corresponds to the limit case. Under this assumption, the gain margin is $1/n$. For the cases of $n = 1.5$ and $n = 0.5$ being considered, the gain margin will be $2/3$ when the system is unstable and 2 for the stable case, see Figure 2.5.

Finally, notice that in the Bode diagram, a negative phase margin is associated with a stable system. This fact arises from the negative component of the traction chain admittance (see Figure 2.4). When the traction chain is integrated into the power supply network, this negative component leads to positive feedback in the closed-loop system.

2.2.2.3 Simulation results

Time-domain simulations were performed to verify the stability analysis developed in the previous section. Figure 2.6 shows the simulation for the operating point of each study case. DC-link voltage, contact-line voltage, and traction chain current are presented. Initially, the system is operating at a stable state close to the substation;

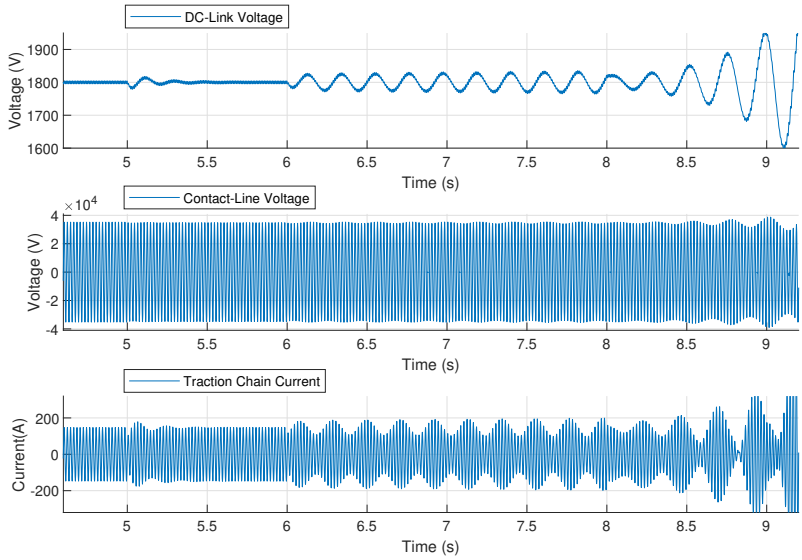

Figure 2.6: Time-domain simulations. From top to bottom: DC-link voltage, contact-line voltage, and train current. Step changes of power supply impedance are consecutively applied during the simulation time. The stable case, stability limit case, and unstable case are found at times $t = 5$ s, $t = 6$ s and $t = 8$ s, respectively.

then, the power supply impedance is increased in three steps. The first step change of $0.5 \cdot Z_b$ occurs at $t = 5$ s; here, the system experiences a small oscillation that is damped quickly, and the system returns to the steady state (i.e. stable case). A second step change of $0.5 \cdot Z_b$ in the power supply impedance occurs at $t = 6$ s, where the time response is oscillatory and no damping is present, but the system is still stable; the oscillation frequencies of the DC-link voltage, the envelope of the contact-line voltage and the current correspond to the oscillation frequency predicted by the impedance-based stability analysis; a frequency around 4.75 Hz can be seen in Figure 2.6. Finally, following a further increase of the power supply impedance at $t = 8$ s, the system becomes unstable.

2.2.2.4 Stability limit curve in the network reactance (X_s) and resistance (R_s) complex plane

As shown in Section 2.2.2.2, the stability limit of the system can be predicted using the network impedance and the traction chain admittance. Thus, for a specific train with an associated total input admittance $\mathbf{Y_T}$, a set of values of network reactance X_s and network resistance R_s can be tested to find a curve $X_s = X_s(R_s)$ in the complex impedance plane that takes the system to the stability limit [28]. This curve can be obtained based on an iterative process using three nested repetitive loops (e.g. 'for'-loop). The first loop is used to modify the value of R_s, the next loop modifies the inductance L_s, and the third loop checks fulfillment of the critical condition of stability by the eigenvalues. This iterative process is performed using discrete steps, the following thresholds are defined for the eigenvalues that reach the stability limit:

- $-180° < \angle\lambda_{1,2} < -178°$
- $0.98 < |\lambda_{1,2}| < 1$

Figure 2.7 shows the stability limit curve of the traction chain in the network reactance (X_s) and resistance (R_s) complex plane with an additional dimension to show the oscillation frequency. The stability limit curve separates the stable region and the unstable region.

From this figure, it can be seen that to go from the unstable region to the stable region, the network resistance must be increased, which suggests that this resistance works as a damping mechanism. On the other hand, for larger values of the reactance, the railway traction power system becomes unstable.

Two different types of contact-lines with different ratios of reactance and resistance (i.e. different phase) are considered in the figure to locate the stability limit. The contact-line impedance grows linearly with the distance (as a parametric variable) until reaching the stability limit, which is the crossing point between the SLC and the impedance linear curve. Figure 2.7 shows the operating point of the three study cases when the traction chain is located at a different distance from the substation.

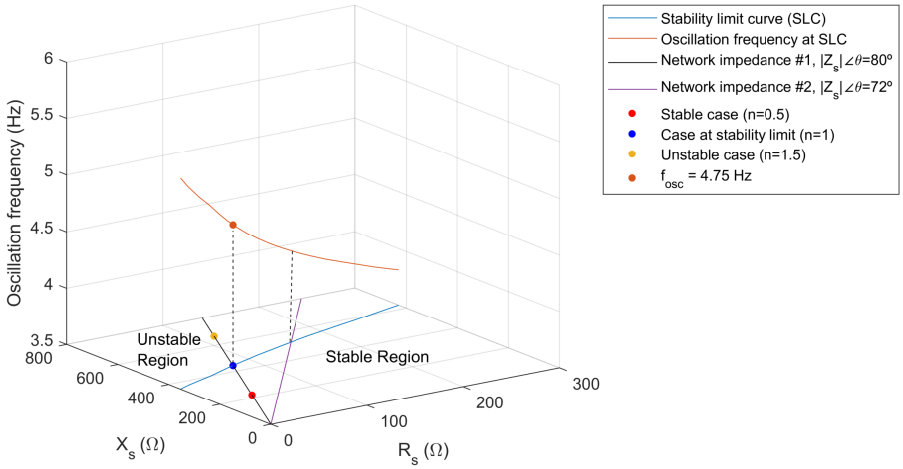

Figure 2.7: Stability limit curve of the traction chain in the network reactance (X_s) and resistance (R_s) complex plane with the corresponding oscillation frequencies. At P_{DC} = 100 kW. Power supply system: 25 kV/50 Hz.

2.2.3 Influence of power absorbed at the DC-link

For this study, the case at stability limit from Section 2.2.2 is considered as a reference (i.e. base case). System stability is studied for variations in power consumption at the DC link. For this purpose, the traction chain input admittance matrix is calculated for different power levels and stability is checked using the network base impedance ($Z_s = Z_b$) from the last section.

Since the eigenvalue λ_2 has no risk of instability, it is neither considered nor plotted. The Bode diagram of the eigenvalue λ_1 is shown in Figure 2.8, where the evolution of the gain margin and the phase margin are determined as a function of power consumption from 100 kW to 1.2 MW. Increasing the power from 100 to 500 kW increases the gain margin while it reduces the oscillation frequency; thus, the system stability is improved, and the limit distance increases as well. This is also seen in Figure 2.9, which shows the stability limit curve plotted for different levels of power. The intersection point of each stability limit curve with the network impedance gives the distance limit and the maximum network impedance that ensures stability for each power level. It is noted that for power levels greater than 500 kW, the phase of the eigenvalue λ_1 is always below the limit $-180°$ (cf. Figure 2.8), so the gain margin becomes infinite and there is no risk of instability at any distance for this specific contact-line. This also can be appreciated from Figure 2.9, where the stability limit curves for power levels of 600 kW and 700 kW never cross the network impedance curve.

Figure 2.9 shows that the slope of SLC increases with power, which means that for

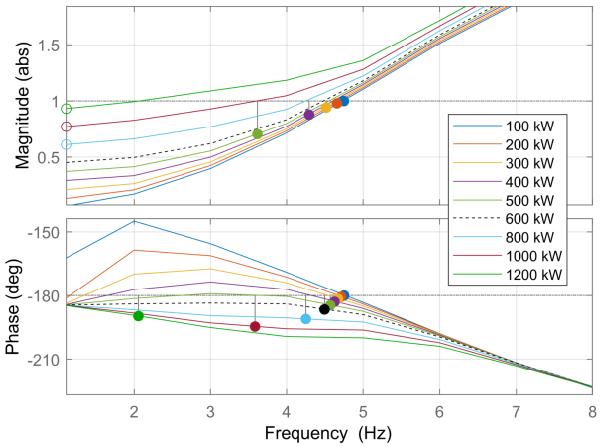

Figure 2.8: Bode diagram of system eigenvalue λ_1 for different levels of power consumption. Network Impedance: $Z_s = Z_b$.

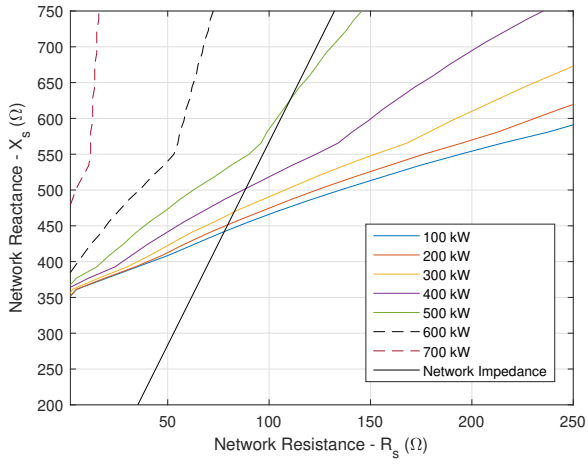

Figure 2.9: Stability limit curve of traction chain in the network reactance (X_s) and resistance (R_s) complex plane. Different levels of power consumption.

higher power consumption, less damping (i.e. network resistance) is needed to maintain system stability.

As mentioned in Section 2.2.2.2, a negative phase margin is associated with a stable system since the negative component of the input admittance leads to positive feedback in the train-network closed-loop system. Interestingly, it is seen from Figure 2.8 that starting from low power levels, the phase margin decreases (i.e. system stability improves) as the power increases up to a certain value. However, for very high powers the phase margin starts to increase getting closer to zero; in other words, the phase at crossover frequency starts to increase getting closer to $-180°$ at very low frequencies. Therefore, the risk of instability due to LFO needs to be checked both at very high powers as well as for low power.

2.2.4 Influence of 4QC current controller bandwidth and transformer leakage inductance

This section discusses the impact that the inner current controller can have on LFO formation, as well as the influence of leakage inductance of the traction chain transformer. Stability analysis is performed using the network impedance at the stability limit ($Z_s = Z_b$) discussed in Section 2.2.2. The power consumed at the DC link is set to $P_{DC} = 100$ kW.

2.2.4.1 Influence of 4QC current controller bandwidth with fixed transformer leakage inductance

The input admittance of a traction chain was calculated for different values of the current controller bandwidth ($\omega_{bcc} = 2\pi \cdot BWcc$), so k_{pCC} and k_{iCC} were modified and tuned using (1.6) and (1.7), the rest of electrical and control parameter remaining constant.

According to Figure 2.10, increasing the current controller bandwidth leads to a rise in the gain margin, which improves system stability and increases the distance limit. Moreover, it is noticed that the oscillation frequency at the stability limit (i.e. phase crossover frequency) increases as well.

It is seen in Figure 2.11 that the stability limit curve shifts parallel to the base case at $BWcc = 100$ Hz and proportionally to the increase of the bandwidth. This characteristic suggests a linear relationship among the current control bandwidth, the gain margin, and the maximum distance from the substation that a traction chain can reach (or the maximum number of traction units in the line, see Section 2.1.1).

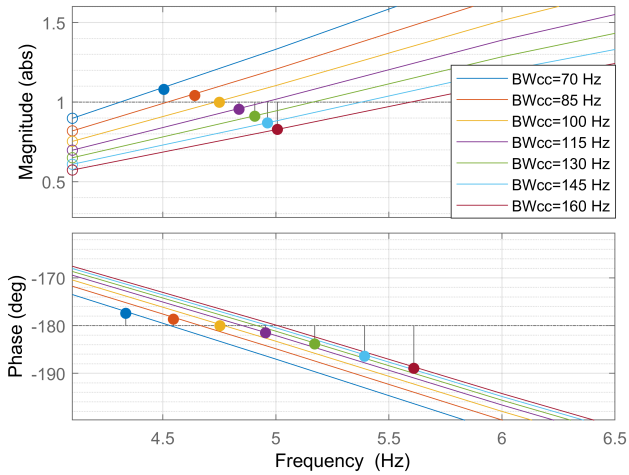

Figure 2.10: Bode diagram of the system eigenvalue λ_1. Variation of current controller bandwidth with fixed transformer leakage inductance.

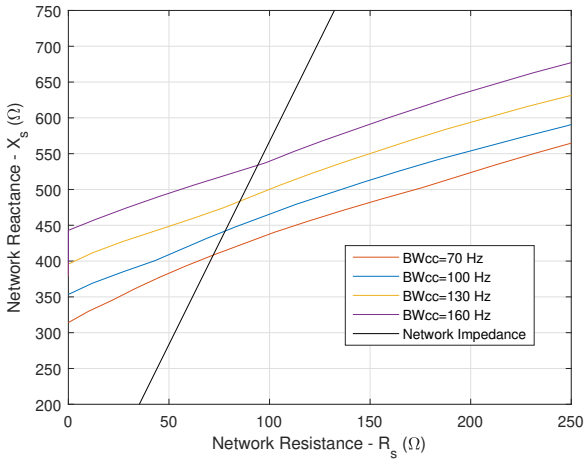

Figure 2.11: Stability limit curve of a traction chain in the network reactance (X_s) and resistant (R_s) complex plane. Variation of current controller bandwidth with fixed transformer leakage inductance.

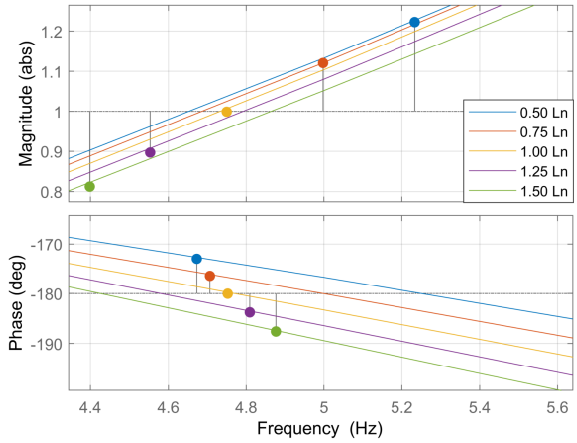

Figure 2.12: Bode diagram of the system eigenvalue λ_1. Variation of leakage inductance with fixed current controller parameters.

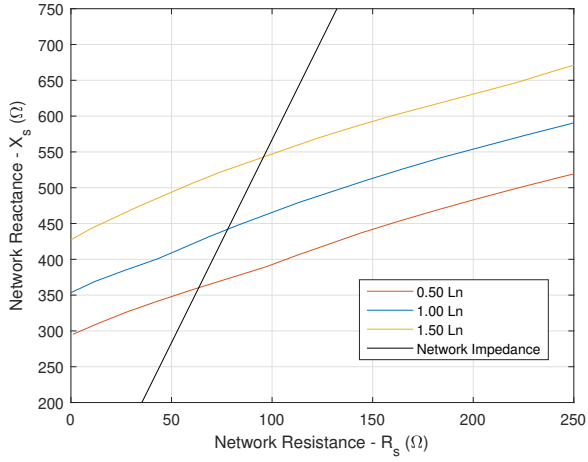

Figure 2.13: Stability limit curve of a traction chain in the network reactance (X_s) and resistance (R_s) complex plane. Variation of leakage inductance with fixed current controller parameters.

2.2.4.2 Influence of the transformer leakage inductance with fixed current controller gains

Figure 2.12 shows the Bode diagram of eigenvalue λ_1 when the transformer leakage inductance L_n varies from 50% to 150% of its base value (1 mH). The rest of the electrical and control parameters are kept constant, including current controller gains (i.e. k_{pCC},k_{iCC}). From Figure 2.12, it is seen that larger values of the leakage inductance are seen to improve LFO stability, while the phase crossover frequency is reduced. Furthermore, Figure 2.13 shows that for larger values of leakage inductance, the stability limit curve shifts up parallel to the reference curve. From these figures, a linear relation seems to exist among the transformer leakage inductance, the gain margin, and the distance limit.

It is important to notice that increasing the leakage inductance, while current controller gains (i.e. k_{pCC}, k_{iCC}) remain constant, provokes current control mistuning. It results in a decrease of the current control bandwidth ($BWcc$), which should decrease the stability limit according to results found in Section 2.2.4.1. Therefore, two effects are happening at the same time in this analysis, and they are opposite. The next section deals with this issue to determine the real effect of leakage inductance variations.

2.2.4.3 Influence of the transformer leakage inductance variation with fixed current controller bandwidth

In this section, variations in the leakage inductance are made while the control parameters k_{pCC} and k_{iCC} are adjusted to maintain the current regulator bandwidth constant at 100 Hz.

Figure 2.14 shows the eigenvalue λ_1 and the gain margin for different values of the inductance, from 50% to 150% of the base value (1 mH). It can be seen that increasing L_n increases the gain margin; thus, the stability is improved. This is also confirmed by the results shown in Figure 2.15, where stability limit curves resulting from inductance variations are parallel to the reference case. From this figure, a linear relation between the inductance variation and the limit distance is also suggested.

2.2.4.4 Summary and Discussion

Table 2.2 summarizes the results from the analysis performed in this section. A linear relationship among leakage inductance, current controller bandwidth, and the gain margin was found in this study.

The variation of the current controller bandwidth as described in Section 2.2.4.1 results in a proportional variation of the gain margin. According to Section 2.2.4.3, when the controllers are adjusted to keep the bandwidth constant, the independent effect of the leakage inductance variation provokes proportional variations in the gain

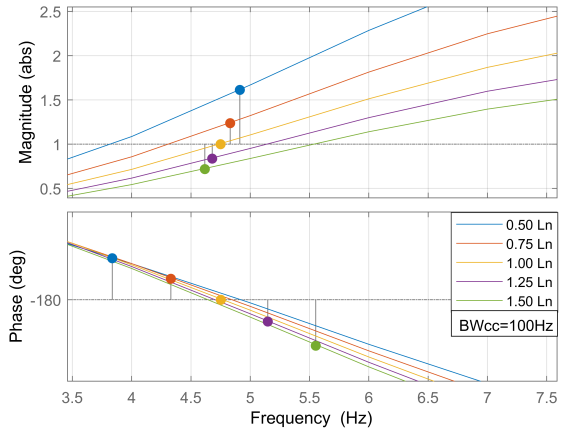

Figure 2.14: Bode diagram of the system eigenvalue λ_1. Variation of leakage inductance while keeping the current controller bandwidth at 100 Hz.

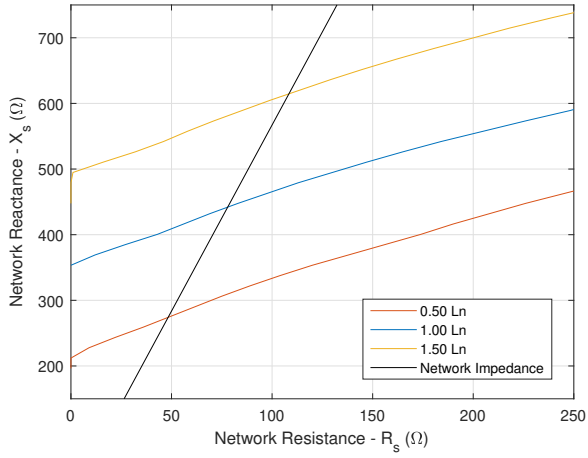

Figure 2.15: Stability limit curve of a traction chain in the network reactance (X_s) and resistant (R_s) complex plane. Variation of leakage inductance while keeping the current controller bandwidth at 100 Hz.

margin as well. On the other hand, from Section 2.2.4.2, it is known that the variation of only the leakage inductance implies the opposite effect on the bandwidth; therefore, a coupled effect that cancels the action of the inductance variation is presented; thus, the gain margin variation results in the superposition of the first two independent effects as shown in the table.

Comparing Figures 2.13 and 2.15, it is clear that the effect of leakage inductance variations while keeping constant the current control bandwidth has a larger impact compared to the case where only leakage inductance is modified.

Table 2.2: Impact of current controller and transformer leakage inductance in LFO stability. Arrows ↑ stands for increments and ↓ stands for decrements.

L_n	k_{pCC} & k_{iCC} Adjusted	$BWcc$	Stability margins
-	YES	↑	↑ ↑
↑	YES	-	↑ ↑ ↑
↑	NO	↓	↑ ↑ ↑+ ↓↓= ↑

2.2.5 Influence of voltage controller bandwidth and DC-link capacitance

This section discusses the impact that the voltage controller can have on LFO stability, as well as the influence of the DC-link capacitance. Stability analysis is performed using the network impedance at the stability limit of the reference case ($Z_s = Z_b$) presented in Section 2.2.2. The power consumed at the DC link is $P_{DC} =$ 100 kW.

2.2.5.1 Influence of voltage controller bandwidth with fixed DC link capacitor

The input admittance of the traction chain was calculated for different values of the voltage controller bandwidth ($\omega_{bvc} = 2\pi \cdot BWvc$), with k_{pVC} and k_{iVC} being tuned using (1.8) and (1.9). The remaining electrical and control parameters have been kept constant.

According to Figures 2.16 and 2.17, decreasing the voltage controller bandwidth increases the gain margin, which improves system stability and increases the distance limit. Furthermore, it is observed that this action provokes the oscillation frequency decreases. From Figure 2.17, smaller values of voltage controller bandwidth have stability limit curves with larger slopes, which means that less damping (i.e. network resistance) is needed to maintain system stability when the network inductance increases.

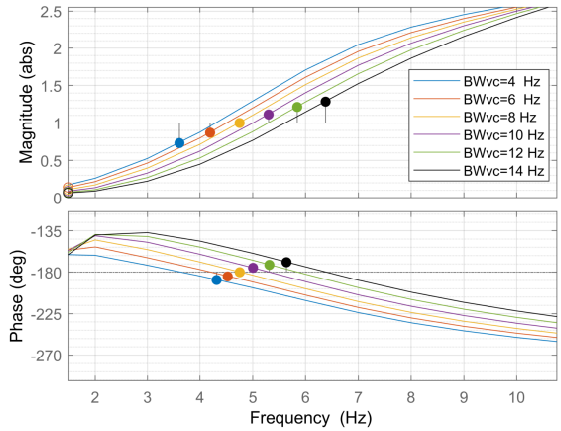

Figure 2.16: Bode diagram of the system eigenvalue λ_1 for different values of voltage controller bandwidth with fixed DC link capacitor.

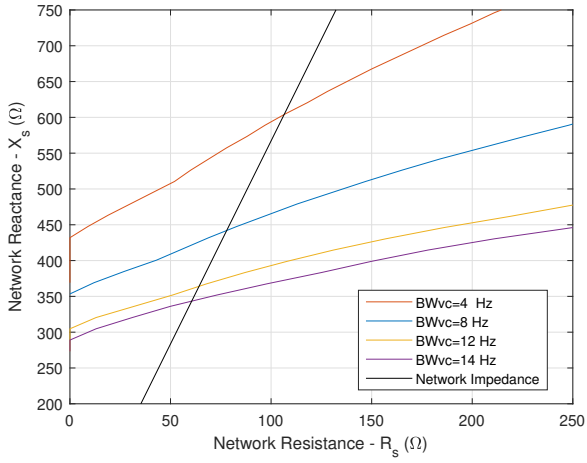

Figure 2.17: Stability limit curve of a traction chain in the network reactance (X_s) and resistant (R_s) complex plane. Variation of voltage controller bandwidth with fixed DC link capacitor.

2.2.5.2 Influence of DC-link capacitor with fixed voltage controller gains

Figure 2.18 shows the Bode diagram of the critical eigenvalue λ_1 for different values of the DC-link capacitance, from 50% to 200% of its base value (16 mF). The rest of the electrical and control parameters are kept constant.

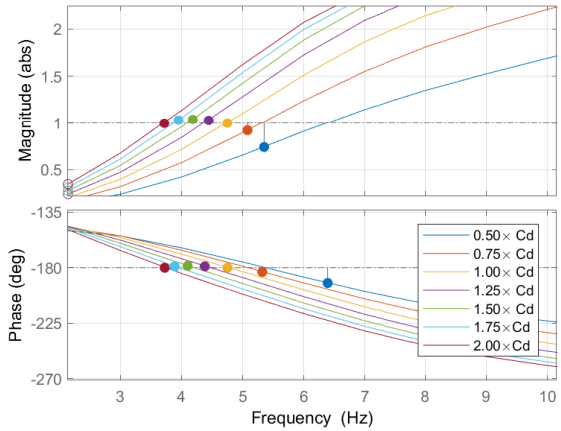

Figure 2.18: Bode diagram of the system eigenvalue λ_1. Variation of DC-link capacitance with fixed voltage controller gains.

In this study, the variation of DC-link capacitance has a non-linear impact on LFO stability. Figure 2.18 shows the gain margin decreases for values of C_d from 50% to 150% its base value (16 mF). However, for values greater than 150% of the base value, the gain margin increases. Therefore, increasing C_d leads to an unstable system, but at some point, this action is reversed. This means the existence of a capacitance that minimized the gain margin, which should be avoided.

Similar behavior is also observed in Figure 2.19, which shows that decreasing capacitance by half has a considerable improvement in the stability limit curve. Increasing capacitance slightly decreases the stability limit, but when the capacitance reaches 200% of its base value, the limit is the same as the reference case.

Increasing C_d always provokes decrements in the phase crossover frequency (i.e. oscillation frequency).

This section considers the scenario in which capacitors age over time, losing the ability to store electric charges. Figure 2.18 shows the degradation of the capacitance benefits the traction chain low-frequency stability.

It is important to note that the variation in DC-link capacitance, while voltage controller gains (i.e. k_{pVC}, k_{iVC}) remain constant, will affect the voltage controller bandwidth. The next section deals with this issue.

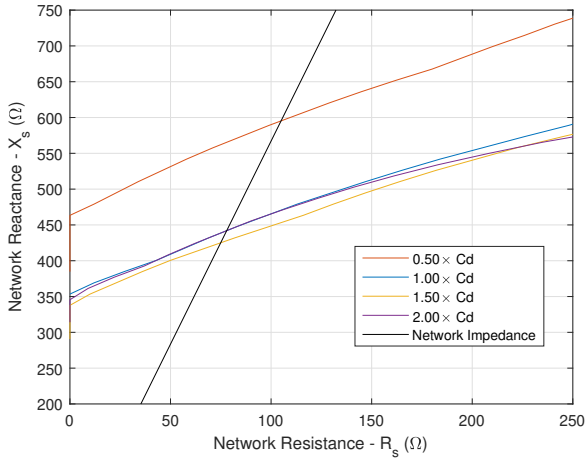

Figure 2.19: Stability limit curve of a traction chain in the network reactance (X_s) and resistant (R_s) complex plane. Variation of DC-link capacitance with fixed voltage controller gains.

2.2.5.3 Influence of DC-link capacitor with fixed voltage controller bandwidth

In this section, variations in the DC-link capacitance are made while the control parameters k_{pVC} and k_{iVC} are adjusted in order to maintain a constant bandwidth of 8 Hz according to (1.8) and (1.9).

Figure 2.20 shows the eigenvalue λ_1 and the gain margin evolution for different values of the capacitance, from 50% to 200% of its nominal value (16 mF).

Decreasing C_d raises monotonously (i.e. non-linear increments) the gain margin; thus, stability is improved. Notice that the gain margin seems to improve faster at lower values of C_d. In other words, the system is more sensitive at lower values of C_d. Variations at high values of C_d produce very small changes in the gain margin/stability limit.

Decreasing the value of the capacitance is an advantage since bigger capacitors are bulky and expensive; however, it will imply losing filter capabilities (i.e. increment of voltage ripple) and system controllability. Therefore, trade-off analysis is required to obtain the best design.

2.2.5.4 Discussion

Although the study for the variation of voltage controller bandwidth and DC-link capacitance shows a non-linear relationship among these parameters and the stability

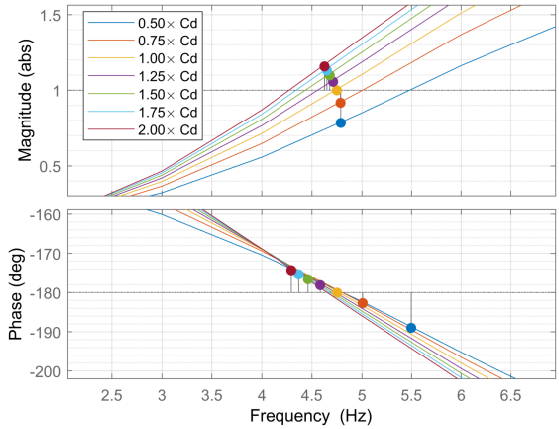

Figure 2.20: Bode diagram of the system eigenvalue λ_1. Variation of DC-link capacitance while keeping the voltage controller bandwidth at 8 Hz.

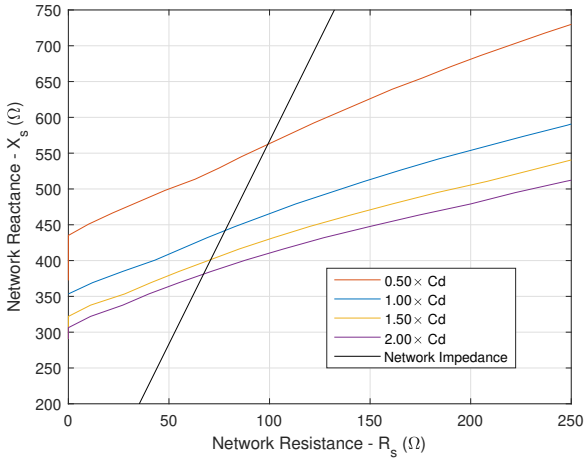

Figure 2.21: Stability limit curve of a traction chain in the network reactance (X_s) and resistant (R_s) complex plane. Variation of DC-link capacitance while keeping the voltage controller bandwidth at 8 Hz.

margins, lower voltage control loop bandwidths and lower values of DC-link capacitance always improve the LFO stability in the range of values considered in this study.

A linear behavior was found only in a very small variation range (around 10% of nominal values). Table 2.3 summarizes the relationships between the variation of the parameters and the stability margins for this small variation range. Three events are identified. First, decreasing the voltage controller bandwidth increases the stability margins. Second, the variation of DC-link capacitance, while the voltage controller bandwidth is kept constant, is inversely proportional to the variation of the stability margins. Finally, decreasing only the DC-link capacitance implies the superposition of the first two events.

Table 2.3: Impact of very small variations of voltage controller and DC-link capacitance on LFO stability. Arrows ↑ stands for increments and ↓ stands for decrements.

C_d	k_{pVC} & k_{iVC} Adjusted	BWvc	Stability margins
-	YES	↓	↑↑
↓	YES	-	↑↑↑
↓	NO	↑	↑↑↑+ ↓↓= ↑

2.2.6 Impact of synchronization system and feedforward signal

In this section, the influence of the synchronization system and the feedforward signal v_{ff} are studied.

Two PLL options are considered: PLL #1 is the synchronization method described in [27], called Z-PLL, which achieves the synchronization by determining the zero-crossing of contact-line voltage, see Figure 1.6. PLL #1 is the synchronization system used in the stability studies already performed in Subsections 2.2.2 to 2.2.5. PLL #2 is described in [26, 36] and it consists of a phase detector in a feedback loop; this option uses a second-order generalized integrator to generate the quadrature signal, see Figure 1.5(d).

Figure 2.22 shows the estimated frequency time response for both PLLs when a step occurs in the frequency of the contact-line voltage. Both PLLs provide zero steady state error, being PLL #2 faster than PLL #1.

The feedforward signal v_{ff} is shown in the control diagram of Figure 1.6, it is used to improve the response of the current control to disturbances. Two different configurations are considered for the generation of the feedforward signal. First, using the feedforward estimator block, as shown in the control diagram in Figure 1.6; second, the signal v_{ff} can also be generated directly from the output of the contact-line voltage filter, being $v_{ff} = \hat{v}_n$.

Four different cases are therefore studied and compared when PLL and feedforward signal are considered together, as summarized in Table 2.4. Figure 2.23 shows the

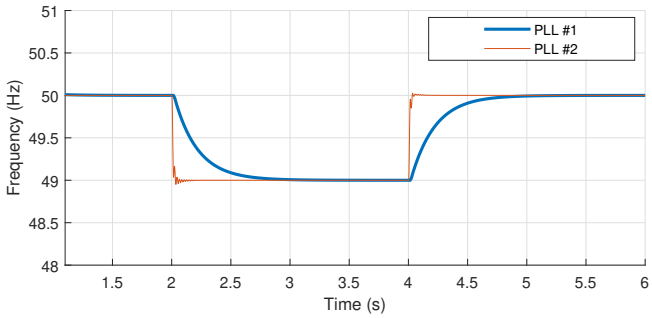

Figure 2.22: Estimated frequency step response of two different phase-locked loops. At $t = 2$ s, contact-line voltage frequency changes from $f = 50$ Hz to $f = 49$ Hz; at $t = 4$ s, the frequency goes back to $f = 50$ Hz.

traction chain input admittance, and Figure 2.24 shows the critical system eigenvalue λ_1 using Bode and Nyquist plots for the four study cases.

Table 2.4: Study Cases: influence of the PLL and the feedforward (FF)

	PLL #1	PLL #2	Estimated FF	Direct FF	Stability Ranking
Case 1	X		X		LOW
Case 2		X	X		HIGH
Case 3	X			X	HIGH
Case 4		X		X	HIGH

Case 1, using the PLL #1 and the feedforward estimator, is the reference case at the stability limit ($GM = 1$), see Figure 2.24. The replacement of only the PLL (i.e. case 2) improves the stability margin by a factor larger than 2. With case 3, only the generation of the feedforward signal is modified, and the stability is improved by at least a factor of 2. In summary, replacing only the PLL or only the feedforward estimator improves stability. In case 4, both the PLL and feedforward are modified; as expected, system stability improves, but the improvement is not the addition of each individual effect of cases 2 and 3, see Figure 2.24.

The stability analysis of cases 1 and 2 might suggest that PLL #1 is the main source of instabilities. However, the stability margin of case 3, that is using PLL #1, would not support this assumption. For cases 3 and 4, the feedforward signal is taken directly from the contact-line voltage filter, which means that no dynamic influence of the synchronization system (i.e. PLL) exists in the generation of the feedforward signal. Thus, the impact of the PLL can really be noticed when the estimator block is used to generate the feedforward signal such as in cases 1 and 2. Since the main difference between PLL #1 and PLL #2 is the system delay in the transient state as shown in Figure 2.22, this suggests that the delay in the feedforward signal has an

important influence on LFO stability.

In summary, large stability margins are presented in cases 3 and 4 since only a small delay of the contact-line voltage filter influences the feedforward signal dynamics. In case 2, the feedforward signal delay comes from the voltage filter and PLL #2, which is a fast synchronization system, resulting in a small signal delay. In case 1, the feedforward signal delay comes from the voltage filter and PLL #1, which presents slow dynamics, resulting in a large feedforward signal delay.

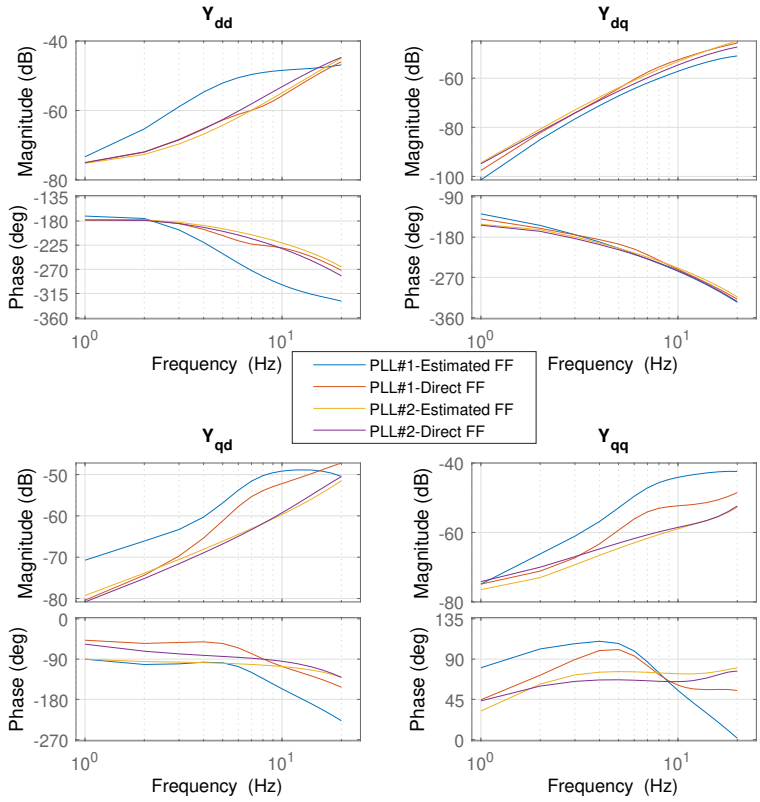

Figure 2.23: Traction chain input admittance. Frequency range: 1–20 Hz. Influence of the PLL and the feedforward.

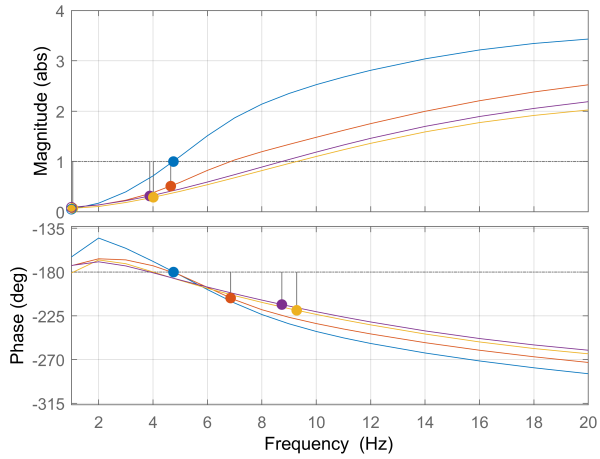

(a)

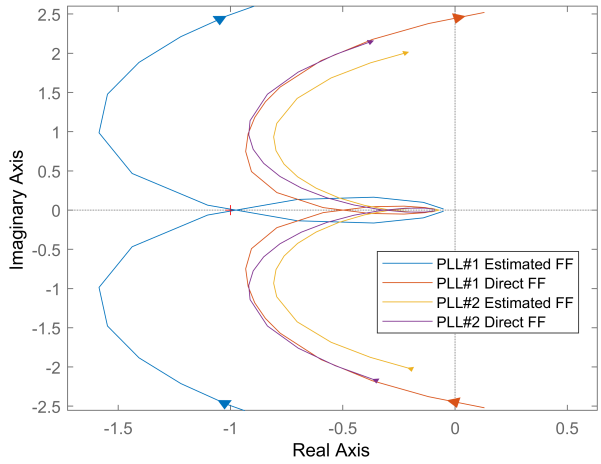

(b)

Figure 2.24: System eigenvalue λ_1. Influence of the PLL and the feedforward. (**a**) Bode diagram, (**b**) Nyquist diagram.

2.2.6.1 Influence of the contact-line voltage filter in the feedforward signal

For this study, the feedforward signal is the output of the contact-line voltage filter (i.e. direct feedforward), being $v_{ff} = \hat{v}_n$. Three different contact-line voltage filters will be tested. The PLL #2 is being used.

The Filter #1 is the contact-line voltage filter used in the stability studies already performed in Subsections 2.2.2 to 2.2.5. Filter #2 is a band-pass filter with a slower response, and Filter #3 is a first-order high bandwidth low-pass filter with a very fast response. The contact-line voltage filter is in charge of filtering the third and fifth voltage harmonics; however, the goal of this study was not the rejection of harmonics, but rather a sinusoidal contact-line voltage waveform with no harmonics is considered; therefore, the criterion for choosing the voltage filter was based on the speed of the dynamic response that minimizes delays. Figure 2.25 shows the step response of the d-axis component of the estimated contact-line voltage to test the filter dynamics and to check the feedforward signal delay. Filter #3 is closer to the case of having no filter since almost no delays are present.

Figure 2.26 shows the traction chain input admittance, and Figure 2.27 shows the critical system eigenvalue λ_1 using Bode and Nyquist plots for the three different filters, the reference case at stability limit (with PLL #1, estimated feedforward, and Filter #1) is also plotted. As expected, the stability margin is proportional to the filter delay. From Figure 2.27, it is clear that the system with the fastest filter (i.e. Filter #3) has the largest gain margin.

Figure 2.26 shows that for the cases with better stability margins, the phase of the input admittance Y_{qq} gets closer to 0° at very low frequencies (i.e. the gain margin is

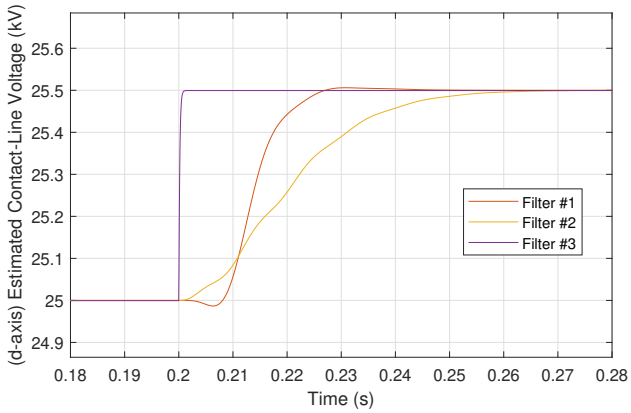

Figure 2.25: Contact-line voltage filters test. Time response of the estimated contact-line voltage (d-axis component). The contact-line voltage is measured at the secondary of transformer, which means that $\hat{v}_c = k \cdot \hat{v}_n$, being $k = 25.5$ the transformer turn ratio.

proportional to the phase of the input admittance Y_{qq} at very low frequencies).

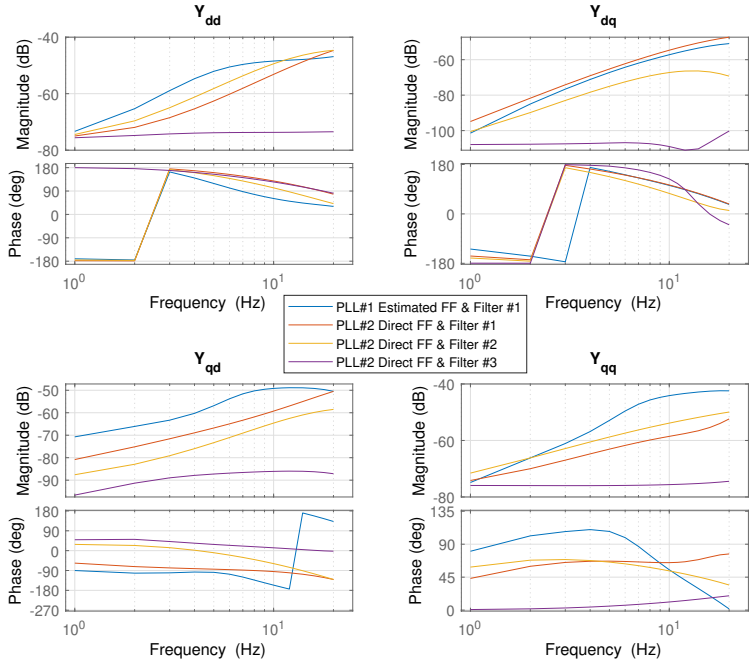

Figure 2.26: Traction chain input admittance. Frequency range: 1–20 Hz. Contact-line voltage filter influence.

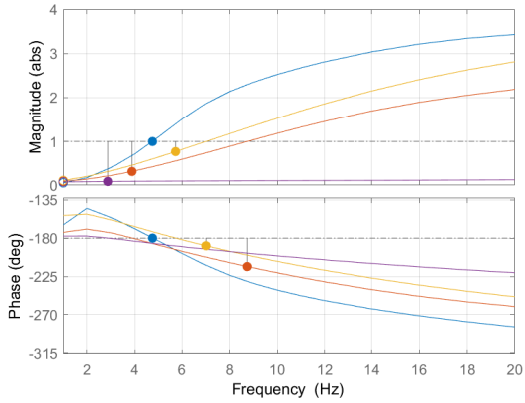

(a)

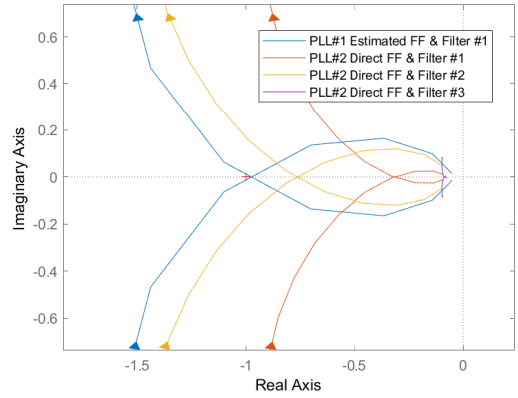

(b)

Figure 2.27: System eigenvalue λ_1. Influence of contact-line voltage filter. (**a**) Bode diagram, (**b**) Nyquist diagram.

2.3 Stability Analysis for Multiple Trains at Different Locations

In this section, the LFO stability analysis of the railway system is study when multiple trains are operating at different locations in the catenary network. Figure 2.28 shows the linearized railway system model. The catenary network is seen to be divided in n sections.

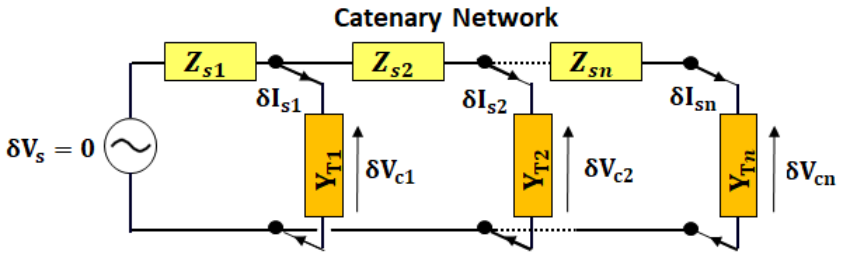

Figure 2.28: Linearized railway system: Multiples trains at multiples locations

The new admittance matrix $\mathbf{Y_T}$ in the dq-frame can be obtained from (2.16). It is seen to be a diagonal matrix consisting of the input admittance of each train. The network impedance matrix $\mathbf{Z_s}$ in the dq-frame, which is obtained from (2.17), is seen to be a full-filled matrix. The dimension of both matrices is $2n \times 2n$. The stability analysis is performed in the same way as explained in Section 2.1. Therefore; the eigenvalues of the open-loop transfer function, $\mathbf{Y_T Z_s}$, which is a MIMO system, are calculated according to (2.14). Bode and Nyquist diagrams are used to predict the system stability limit. Time-domain simulations are used for verification.

$$
\begin{aligned}
\delta\mathbf{I_s} &= \mathbf{Y_T}\delta\mathbf{V_c} \\
\begin{bmatrix} \delta\mathbf{I_{s1}} \\ \dots \\ \delta\mathbf{I_{sn}} \end{bmatrix} &= \begin{bmatrix} \mathbf{Y_{T1}} & \mathbf{0} & \mathbf{0} \\ \mathbf{0} & \dots & \mathbf{0} \\ \mathbf{0} & \mathbf{0} & \mathbf{Y_{Tn}} \end{bmatrix} \begin{bmatrix} \delta\mathbf{V_{c1}} \\ \dots \\ \delta\mathbf{V_{cn}} \end{bmatrix} \\
\begin{bmatrix} \delta I_{s1d} \\ \delta I_{s1q} \\ \dots \\ \dots \\ \delta I_{snd} \\ \delta I_{snq} \end{bmatrix} &= \begin{bmatrix} Y_{T1-dd} & Y_{T1-dq} & 0 & 0 & 0 & 0 \\ Y_{T1-qd} & Y_{T1-qq} & 0 & 0 & 0 & 0 \\ 0 & 0 & \dots & \dots & 0 & 0 \\ 0 & 0 & \dots & \dots & 0 & 0 \\ 0 & 0 & 0 & 0 & Y_{Tn-dd} & Y_{Tn-dq} \\ 0 & 0 & 0 & 0 & Y_{Tn-qd} & Y_{Tn-qq} \end{bmatrix} \begin{bmatrix} \delta V_{c1d} \\ \delta V_{c1q} \\ \dots \\ \dots \\ \delta V_{cnd} \\ \delta V_{cnq} \end{bmatrix}
\end{aligned}
\tag{2.16}
$$

$$
\begin{array}{rcl}
\delta\mathbf{V_c} & = & -\mathbf{Z_s}\delta\mathbf{I_s} \\
\begin{bmatrix} \delta\mathbf{V_{c1}} \\ \dots \\ \delta\mathbf{V_{cn}} \end{bmatrix} & = & -\begin{bmatrix} \mathbf{Z_{s1}} & \dots & \mathbf{Z_{s1}} \\ \dots & \dots & \dots \\ \mathbf{Z_{s1}} & \dots & \sum_{i=1}^{n}\mathbf{Z_{si}} \end{bmatrix}\begin{bmatrix} \delta\mathbf{I_{s1}} \\ \dots \\ \delta\mathbf{I_{sn}} \end{bmatrix} \\
\begin{bmatrix} \delta V_{c1d} \\ \delta V_{c1q} \\ \dots \\ \dots \\ \delta V_{cnd} \\ \delta V_{cnq} \end{bmatrix} & = & -\begin{bmatrix} Z_{s1-dd} & Z_{s1-dq} & \dots & \dots & Z_{s1-dd} & Z_{s1-dq} \\ Z_{s1-qd} & Z_{s1-qq} & \dots & \dots & Z_{s1-qd} & Z_{s1-qq} \\ \dots & \dots & \dots & \dots & \dots & \dots \\ \dots & \dots & \dots & \dots & \dots & \dots \\ Z_{s1-dd} & Z_{s1-dq} & \dots & \dots & \sum_{i=1}^{n} Z_{si-dd} & \sum_{i=1}^{n} Z_{si-dq} \\ Z_{s1-qd} & Z_{s1-qq} & \dots & \dots & \sum_{i=1}^{n} Z_{si-qd} & \sum_{i=1}^{n} Z_{si-qq} \end{bmatrix}\begin{bmatrix} \delta I_{s1d} \\ \delta I_{s1q} \\ \dots \\ \dots \\ \delta I_{snd} \\ \delta I_{snq} \end{bmatrix}
\end{array}
\tag{2.17}
$$

2.3.1 Catenary network with two sections

In this subsection, stability of railway system is analyzed for trains located in two different locations. In this case, the total input admittance $\mathbf{Y_T}$, and the network impedance $\mathbf{Z_s}$ are described by (2.18) and (2.19), respectively.

$$
\mathbf{Y_T} = \begin{bmatrix} Y_{T1-dd} & Y_{T1-dq} & 0 & 0 \\ Y_{T1-qd} & Y_{T1-qq} & 0 & 0 \\ 0 & 0 & Y_{T2-dd} & Y_{T2-dq} \\ 0 & 0 & Y_{T2-qd} & Y_{T2-qq} \end{bmatrix}\begin{bmatrix} \delta V_{c1d} \\ \delta V_{c1q} \\ \delta V_{c2d} \\ \delta V_{c2q} \end{bmatrix} \tag{2.18}
$$

$$
\mathbf{Z_s} = \begin{bmatrix} Z_{s1-dd} & Z_{s1-dq} & Z_{s1-dd} & Z_{s1-dq} \\ Z_{s1-qd} & Z_{s1-qq} & Z_{s1-qd} & Z_{s1-qq} \\ Z_{s1-dd} & Z_{s1-dq} & Z_{s1-dd} + Z_{s2-dd} & Z_{s1-dq} + Z_{s2-dq} \\ Z_{s1-qd} & Z_{s1-qq} & Z_{s1-qd} + Z_{s2-qd} & Z_{s1-qq} + Z_{s2-qq} \end{bmatrix} \tag{2.19}
$$

The single-phase impedance of both network sections, Z_{s1} and Z_{s2}, are defined by (2.20) and (2.21). The distance from substation to location #1 is d_1, and $d_T = d_1 + d_2$ is distance from substation to location #2, being d_2 the distance between location #1 and location #2.

$$
Z_{s1} = 2 \times Z_{ug} + Z_{sst} + d_1 \times Z'_{cl} \tag{2.20}
$$

$$
Z_{s2} = d_2 \times Z'_{cl} \tag{2.21}
$$

Impedance of the first section Z_{s1} in seen to include the upstream grid impedance Z_{ug}, the substation impedance Z_{sst}, and the contact-line impedance per km Z'_{cl}. Impedance of the second section Z_{s2} only considers the contact-line impedance per km. The same values used in Section 2.2.2.1 will be used in the analysis following.

Two different scenarios are analyzed. The first one, considers a railway system that have trains in the depot and a single train running far from substation, only one train model is employed for this analysis. The second scenario considers different train models running far from the substation.

2.3.1.1 Multiple trains at depot and single train running

In this study case, the stability of the railway system is tested when 10 trains are connected to the network in the depot near to the substation (distance $d_1 = 2$ km) and a train is operating far from the substation at low-power consumption. Distance d_2 at which this train is operating is increased until the system reaches the stability limit.

The train model used for this test is the train-B described by Figure 1.6, with four traction chains connected in parallel. The train input admittance is $\mathbf{Y_{TB}} = 4\mathbf{Y_t}$, being $\mathbf{Y_t}$ the traction chain admittance. The traction chain control and electrical parameters are the same used in Section 2.2.1, they are described in Table 2.1. This admittance is shown in Figure 2.4. Since only one train model is used, the total input admittance matrix is described by (2.22). Power consumption at the DC-link of each traction chain is 100 kW.

$$\mathbf{Y_T} = \begin{bmatrix} \mathbf{10Y_{TB}} & 0 \\ 0 & \mathbf{Y_{TB}} \end{bmatrix} \tag{2.22}$$

Figure 2.29(a) and (b) shows the Bode and Nyquist diagrams of the eigenvalues when the system operates at its stability limit, which occurs for distance $d_2 = 71$ km. From Bode diagram, the gain and phase margins of the critical eigenvalue λ_1 are seen to be zero, the crossover frequency (i.e. oscillation frequency) is 4.75 Hz. Since only one train model is employed eigenvalues λ_1 and λ_3 share the same phase, this also occurs for eigenvalues λ_2 and λ_4. Nyquist plot shows that eigenvalue λ_1 intersects -1.

Figure 2.30 shows the time domain simulation with signals measured in the train running far from substation. Initially, the train is operating in the steady state at distance $d_2 = 31$ km. At $t = 6$ s, step change in the distance is applied, reaching $d_2 = 51$ km, at this point some oscillations are seen but the system is stable. At $t = 7$ s, distance increases to $d_2 = 71$ km (i.e. $d_T = 73$ km) reaching the stability limit, the oscillation frequency is f_{osc}=4.75 Hz, which agrees with the value obtained from the frequency-domain analysis in Figure 2.29. Finally, at $t = 9$ s distance increases to $d_2 = 91$ km making the system unstable.

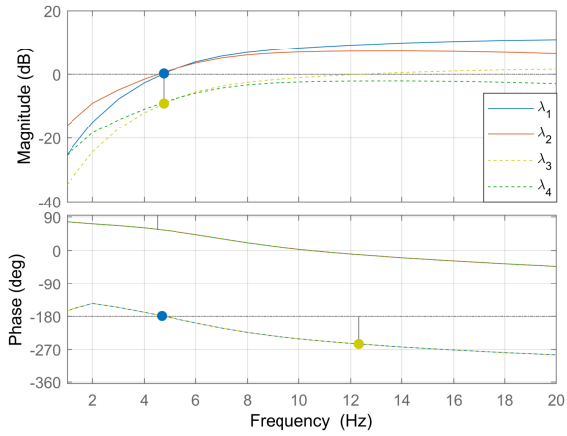

(a)

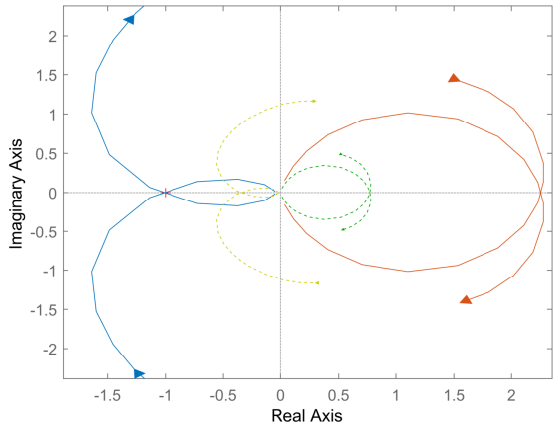

(b)

Figure 2.29: System eigenvalues (λ_1, λ_2, λ_3, λ_4) for the stability limit case. Oscillation frequency at 4.75 Hz. (**a**) Bode Diagram, (**b**) Nyquist Diagram.

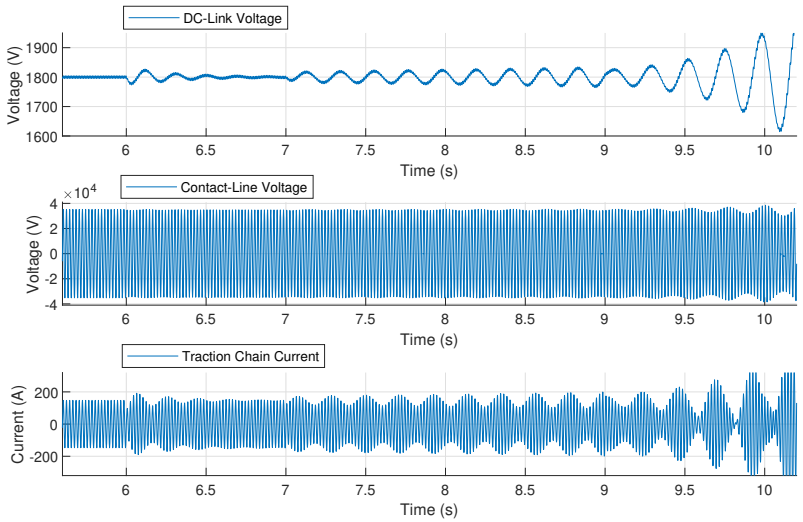

Figure 2.30: Time-domain simulations. From top to bottom: DC-link voltage, contact-line voltage, and traction chain current. Step changes of distance d_2 are consecutively applied during the simulation time. The stable system, stability limit, and unstable case are found at times $t = 6$ s, $t = 7$ s and $t = 9$ s, respectively.

2.3.1.2 Different trains in the contact-line

This scenario considers two trains with different input admittance operating in different locations. Both trains used train-B control configuration shown in Figure 1.6, and have four traction chains connected in parallel. Traction chain parameters from Table 2.1 are used; however, the current and voltage control bandwidths are different for each model, as well as the synchronization system, as shown in Table 2.5 (for description of synchronization systems see Section 1.2.3). Figure 2.31 shows the traction chain input admittance of models B1 and B2. The power consumption at the DC-link of each traction chain is 100 kW.

Description	Model-B1	Model-B2
Voltage Control Bandwidth	8 Hz	7 Hz
Current Control Bandwidth	100 Hz	70 Hz
Synchronization system	Z-PLL	PLL

Table 2.5: Traction chain parameters (Comparison)

For this study case, train-B1 is operating at distance $d_1 = 45$ km from the substation, the distance d_2 for train-B2 being increased until the stability limit is reached.

Figure 2.32(a) and (b) shows the Bode and Nyquist diagram of the eigenvalues when the system reaches its stability limit. This occurs when the train-B2 is at distance $d_2 = 64$ km. For that reason, the gain margin and phase margin of the eigenvalue λ_1 are GM=0 db and PM=0°, respectively. The crossover frequency is 4.5 Hz. Nyquist plot shows that eigenvalue λ_1 intersects -1.

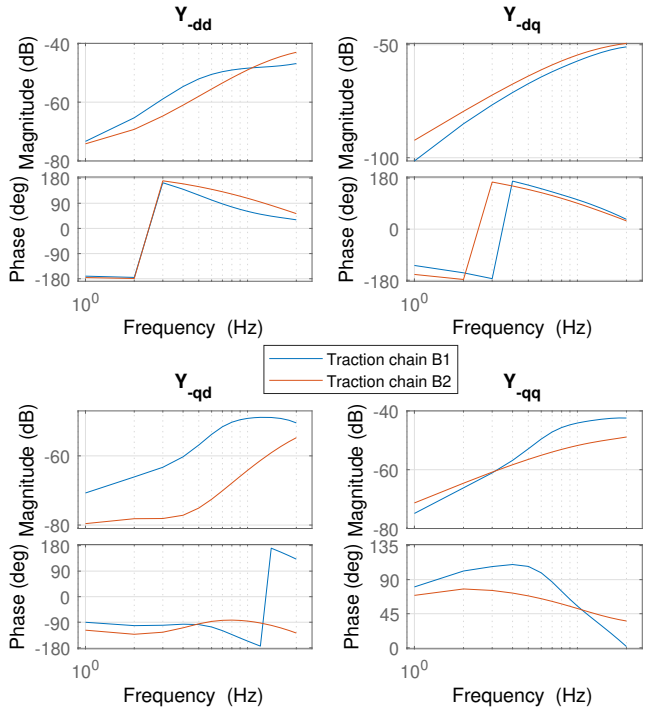

Figure 2.31: Traction-chain input admittance of models B1 and B2. Frequency range: 1 - 20 Hz

Figure 2.33 shows the results obtained by means of time domain simulation, the signals were measured in a traction chain of train model-B2. Initially, train-B2 is operating at distance $d_2 = 24$ km. At $t = 6$ s, step change in the distance is applied, reaching $d_2 = 44$ km, at this point some oscillations are seen but the railway system remains stable. At $t = 7$ s, the distance increases to $d_2 = 64$ km (i.e. $d_T = 109$ km) reaching the stability limit. The oscillating frequency is f_{osc}=4.5 Hz. Finally, at $t = 9$ s the distance increases to $d_2 = 84$ km, what makes the system unstable.

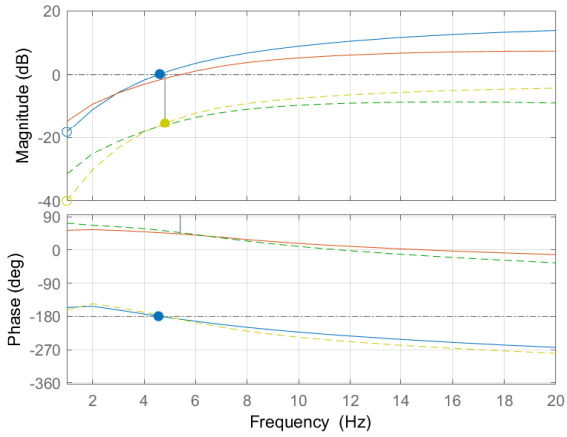

(a)

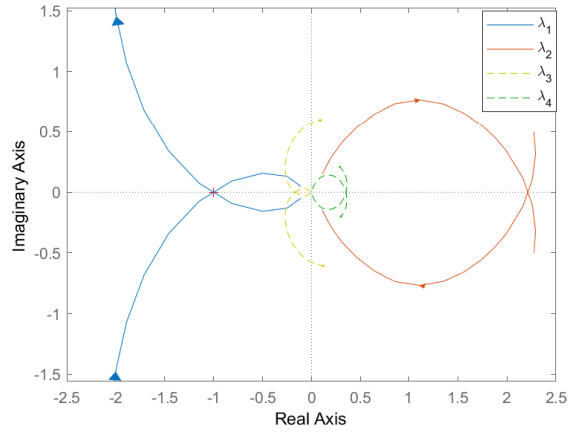

(b)

Figure 2.32: System eigenvalues (λ_1, λ_2, λ_3, λ_4) of the stability limit case. Oscillation frequency at 4.5 Hz. (**a**) Bode Diagram, (**b**) Nyquist Diagram.

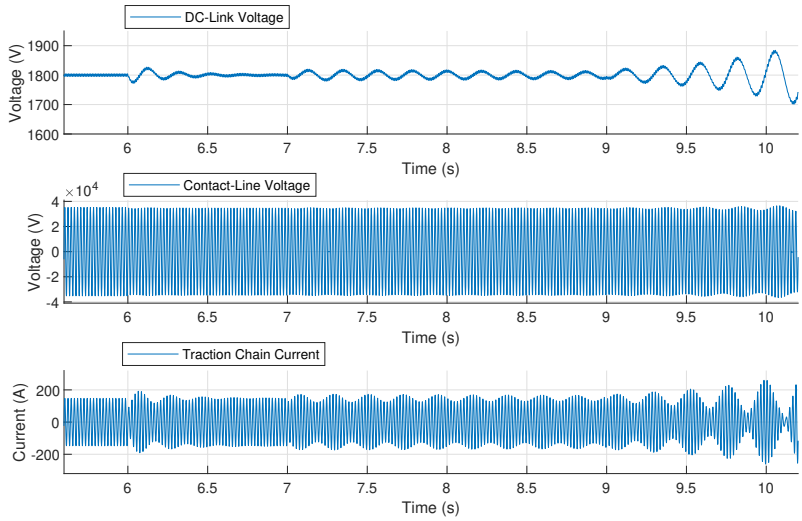

Figure 2.33: Time-domain simulations. From top to bottom: DC-link voltage, contact-line voltage, and traction chain current (Train-B2). Step changes of distance d_2 are consecutively applied during the simulation time. The stable system, stability limit, and unstable case are found at times $t = 6$ s, $t = 7$ s and $t = 9$ s, respectively.

2.4 Conclusions

In this chapter, impedance-based stability analysis techniques in the frequency domain have been used to study the impact of electrical and control parameters in the appearance of LFO, including contact-line length (i.e. distance from the substation), consumed power, the bandwidth of current and voltage controllers, leakage inductance of the transformer, DC-link capacitor, synchronization system, and feedforward signal. Time-domain simulations were further used to validate the results of the analysis.

The influence of the contact-line length and number of traction chains on LFO has been widely reported. The study of the impact of power consumption shows that the worst case for instability is operation at low power. The stability limit curve for different power consumption levels was presented showing similar results.

Increments of current control bandwidth with fixed leakage inductance lineally increase the stability limit. Similar linear behavior applies for the case of the increments of leakage inductance with or without adjusting the control bandwidth. The increment of the current control bandwidth is limited due to sample/switching frequency. Although increasing the value of the transformer inductance is advantageous for LFO phenomenon and for filtering the AC-side current, it limits the power transfer capability. Therefore, trade-off analysis is required to obtain the optimal value of inductance.

Decreasing voltage controller bandwidth with fixed DC-link capacitor always increases the gain margin. However, this action compromises controllability.

On the other hand, the variation of DC-link capacitance with fixed voltage controller gains showed a non-linear relationship with the stability margins. Increasing C_d leads to an unstable system, but at some point, this action is reversed. This means the existence of a capacitance that minimized the gain margin, which should be avoided.

Decreasing C_d with fixed voltage controller bandwidth increases monotonously stability margins, which seem to improve faster at lower values of C_d. However, decreasing the value of the capacitor will imply losing filter capabilities (i.e. increment of voltage ripple) and system controllability. Therefore, trade-off analysis is required to obtain the best design.

Delays of the feedforward signal were observed to increase the risks of LFO. If the feedforward signal depends on PLL dynamics, a faster PLL dynamics improves the low-frequency stability.

The stability study of the railway system was performed for multiple trains operating at different locations using Nyquist and Bode criteria. This method haven been proven with time domain simulations showing that it is accurate enough to predict the stability limit.

Chapter 3

Analysis using small-signal models

The system resulting from the connection of two or more dynamic systems (e.g. grid and power converters) will be stable if all the elements are passive [37]. The passivity of a system is ensured when the differential input admittance, also referred to as input admittance [38], has a non-negative real part (i.e. non-negative conductance). Usually, the grid (i.e. power supply network) is considered a passive system, since it consists of R, L, and C elements; however, controlled power electronics converters are not.

The differential input admittance of power converters can be calculated using small-signal models, or it can be obtained using frequency sweep methods as the one described in Section 2.1.3. Different small-signal models to calculate the input admittance in both single-phase and three-phase voltage source converters (VSCs) have been presented in the literature [17, 37, 39]. However, most of these works focus on specific elements (e.g. current control) but do not include all the dynamic elements affecting to LFO. Another relevant aspect to consider is that AC catenaries are single-phase systems. Therefore, extrapolation of analysis and results developed for three-phase systems might not be straightforward. On one hand, contrary to a three-phase system, single-phase systems cannot transfer continuous power. Furthermore, one or more quadrature signal generator (QSG) systems [40] are often needed for the control of single-phase systems. Finally, the design of the PLL is also different. QSGs and PLL will be shown to have a significant influence on the appearance of LFO.

In [13] and [6] a small-signal model of 4QC input admittance was developed to study railway system instability phenomena, including resonant instability and LFO; however, the model fails to accurately calculate the train admittance in the low-frequency range.

In [38], the input admittance of a three-phase VSC was calculated including all

the dynamic elements (i.e. synchronization system, feedforward filter, etc). However, that work focused on a three-phase balanced system (i.e. symmetric dynamic transfer function), and does not include elements which can be relevant for single-phase systems with asymmetrical transfer functions as the QSG.

It often happens that there are elements in the system which are insensitive to errors in the coordinate rotations, while other elements will be affected. Modeling this phenomenon will require the use of multiple reference frames. Three different reference frames are used for the study presented in this Chapter: stationary reference frame; true synchronous reference frame, which is aligned with the fundamental component of the catenary voltage; and estimated synchronous reference frame, which is the one used by the control, but which will be subjected to errors. Small-signal vector transformation from the actual synchronous frame to the estimated synchronous frame will be shown to be key for the development of accurate analytical models of the train-network interactions.

This chapter presents the calculation of the analytical small-signal model of train-A input admittance. Only one traction chain (single 4QC converter) is considered without loss of generality in the conclusions. Dynamic elements considered for the analysis include:

- DC-link voltage controller.
- Inner current controller.
- Phase-locked loop (PLL) used for synchronization.
- Second-order generalized integrator (SOGI) used for filtering and quadrature signal generation.
- Delays due to discrete implementation of the control and to the PWM.

Verification of the analytical model is performed by means of full system simulation model of the catenary and 4QC converter.

The chapter is organized as follows: Notation and reference frames used in this chapter are first defined in Section 3.1. Section 3.2 deals with modeling the small-signal 4QC input admittance; Section 3.3 presents stability analysis of the railway system for several trains operating at the depot under different operating points; sensitivity analysis of train electrical and control parameter is developed in Section 3.4; finally, conclusions are drawn in Section 3.5.

3.1 Notation and reference frames

This section is aimed to complement the Nomenclature at the beginning of this document, especially regarding the reference frames that will be used throughout the chapter. Both complex vector [41] and matrix notation [42] will be used.

3.1.1 Equivalence between complex vector and matrix notation

The use of complex vector notation is convenient for dynamic analysis of symmetric three-phase systems (e.g. balanced impedance) [43, 44]. However, for asymmetrical systems, it is necessary to use matrix notation with the corresponding real space vectors. Using matrix notation, models in the time domain will be of the form shown in (3.1), where g^e and $\mathbf{g^e}$ are time transfer functions.

$$\begin{gathered}\mathbf{v^e} = \mathbf{g^e i^e} \\ \begin{bmatrix} v_d^e \\ v_q^e \end{bmatrix} = \begin{bmatrix} g_{dd}^e & g_{dq}^e \\ g_{qd}^e & g_{qq}^e \end{bmatrix} \begin{bmatrix} i_d^e \\ i_q^e \end{bmatrix}\end{gathered} \tag{3.1}$$

An example of the equivalence between matrix notation and complex numbers for symmetric systems (i.e. $g_{dd}^e = g_{qq}^e$ and $g_{dq}^e = -g_{qd}^e$) is shown in equations (3.2)-(3.4).

$$\mathbf{v^e} = \begin{bmatrix} v_d^e \\ v_q^e \end{bmatrix} \quad \longleftrightarrow \quad \boldsymbol{v_{dq}^e} = v_d^e + j v_q^e \tag{3.2}$$

$$\mathbf{i^e} = \begin{bmatrix} i_d^e \\ i_q^e \end{bmatrix} \quad \longleftrightarrow \quad \boldsymbol{i_{dq}^e} = v_d^e + j v_q^e \tag{3.3}$$

$$\mathbf{v^e} = \begin{bmatrix} g_{dd}^e & g_{dq}^e \\ g_{qd}^e & g_{qq}^e \end{bmatrix} \mathbf{i^e} \quad \longleftrightarrow \quad \boldsymbol{v_{dq}^e} = (g_{dd}^e - j g_{dq}^e) \boldsymbol{i_{dq}^e} \tag{3.4}$$

Transforming (3.4) to Laplace domain, (3.5) is obtained. Transfer functions in the Laplace domain are represented using uppercase letters.

$$\mathbf{V^e} = \begin{bmatrix} G_{dd}^e(s) & G_{dq}^e(s) \\ G_{qd}^e(s) & G_{qq}^e(s) \end{bmatrix} \mathbf{I^e} \quad \longleftrightarrow \quad \boldsymbol{V_{dq}^e} = \Big(G_{dd}^e(s) - j G_{dq}^e(s) \Big) \boldsymbol{I_{dq}^e} \tag{3.5}$$

3.1.2 Reference Frames

In the analysis presented in this chapter three different reference frames are considered:

- Actual synchronous dq-frame
- Estimated synchronous $\widehat{dq}$-frame
- Stationary $\alpha\beta$-frame

Matrices, vectors, and vector components are denoted with the superscript '^{e}' to make reference to the actual dq-frame; on the other hand, the superscript '$^{\widehat{e}}$' is used to refer to the estimated $\widehat{dq}$-frame. Therefore, the variables of the railway system model from Figure 1.4 are renamed according to this special notation as shown in Figure 3.1.

Variables (i.e. vector components) in the stationary $\alpha\beta$-frame are insensitive to errors in the coordinate rotations, not requiring therefore a superscript. However, matrices and vectors in the stationary reference frame are identified by the superscript '^{s}'.

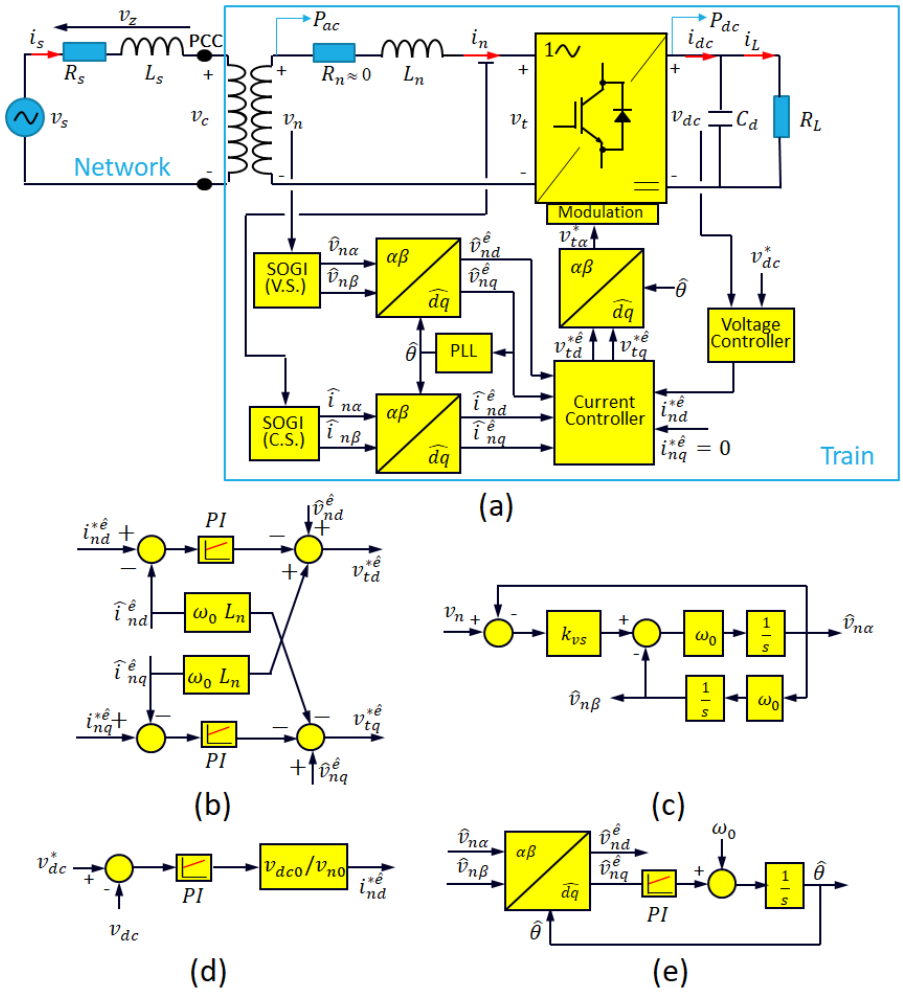

Figure 3.1: Railway control system model. Superscript '^{e}' refers to variables in the actual grid dq-frame. Superscript '$^{\hat{e}}$' refers to variables in the estimated grid dq-frame.

The AC voltages and currents in the single-phase railway system shown in Figure 3.1 are treated as vectors in the stationary reference frame by considering a virtual quadrature component [45]. These quantities are transformed to the actual dq-frame aligned with the fundamental component of the catenary voltage v_c. The angle of rotation θ is defined by (3.6), where ω_0 is the power supply fundamental frequency

imposed by the substation.

$$d\theta/dt = \omega_0 \tag{3.6}$$

In order to implement the current controller in the estimated synchronous reference frame, the PLL estimates the catenary voltage phase angle $\widehat{\theta}$. This angle defines the estimated $\widehat{dq}$-frame, which ideally coincides with the actual dq-frame.

Vector transformations from the actual $dq-$ and estimated $\widehat{dq}$-frames to the stationary reference frame are given by (3.7) and (3.8), respectively. Therefore, the relation between vectors in the actual and estimated $\widehat{dq}$-frames is given by (3.9), where $\tilde{\theta}$ is the angle estimation error (3.10) (see Figure 3.2).

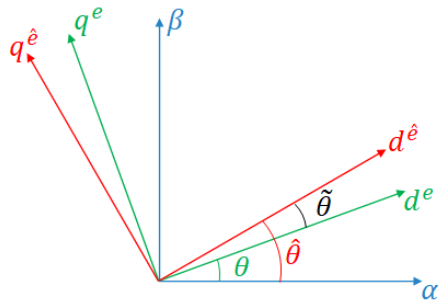

Figure 3.2: Stationary reference frame and dq-frames

$$\boldsymbol{v}^{\boldsymbol{s}}_{\boldsymbol{\alpha\beta}} = e^{j\theta}\boldsymbol{v}^{\boldsymbol{e}}_{\boldsymbol{dq}} \tag{3.7}$$

$$\boldsymbol{v}^{\boldsymbol{s}}_{\boldsymbol{\alpha\beta}} = e^{j\widehat{\theta}}\boldsymbol{v}^{\widehat{\boldsymbol{e}}}_{\boldsymbol{dq}} \tag{3.8}$$

$$\boldsymbol{v}^{\widehat{\boldsymbol{e}}}_{\boldsymbol{dq}} = e^{-j\tilde{\theta}}\boldsymbol{v}^{\boldsymbol{e}}_{\boldsymbol{dq}} \tag{3.9}$$

$$\tilde{\theta} = \widehat{\theta} - \theta \tag{3.10}$$

Due to the integral action of the PLL, the error angle $\tilde{\theta}$ is zero in the steady state. However, PLL dynamics will result in transient errors which must be included in the model as they can contribute to the LFO phenomenon.

In the Laplace domain, and using matrix notation, the vector transformation in (3.9) can be expressed by (3.11) using the $dq/\widehat{dq}$ transformation matrix $\mathbf{T}_{\tilde{\theta}}$. In the steady state, transformation matrix $\mathbf{T}_{\tilde{\theta}}$ is equivalent to the identity matrix.

$$\mathbf{V}^{\widehat{\mathbf{e}}} = \mathbf{T}_{\tilde{\theta}}\mathbf{V}^{\mathbf{e}} \tag{3.11}$$

3.2 Train input admittance small-signal model in the dq-frame

The train admittance in the actual dq-frame is defined as the ratio between the differential catenary current vector $\delta\mathbf{I_s^e}$ and the differential catenary voltage vector $\delta\mathbf{V_s^e}$. However, for ease of modeling and calculations, it can be expressed in terms of the differential 4QC input voltage vector $\delta\mathbf{V_n^e}$, and the differential 4QC input current vector $\delta\mathbf{I_n^e}$, as shown in (3.12), where k is the transformer turns ratio.

$$\mathbf{Y_t} = \frac{\delta\mathbf{I_s^e}}{\delta\mathbf{V_c^e}} = \frac{1}{k^2}\frac{\delta\mathbf{I_n^e}}{\delta\mathbf{V_n^e}} \tag{3.12}$$

Small-signal models of the elements relevant to LFO analysis are presented in this section. These include errors in coordinate rotations, QSG-SOGI, PLL, current controller, and DC-link voltage controller.

3.2.1 Error angle $\tilde{\theta}$ influence on the small-signal $dq/\widehat{dq}$ vector transformation

As explained in Section 3.1.2, the error angle $\tilde{\theta}$ only appears during transients and can be assumed to be small. A linear approximation of vector transformation (3.9) is obtained by taking partial derivatives (3.13), where $\tilde{\theta}_0$ and $\boldsymbol{v_{dq0}^e}$ are steady state quantities.

$$\begin{aligned}\delta\boldsymbol{v}_{\boldsymbol{dq}}^{\widehat{\boldsymbol{e}}} &= \left.\frac{\partial\left(e^{-j\tilde{\theta}}\boldsymbol{v_{dq}^e}\right)}{\partial\boldsymbol{v_{dq}^e}}\right|_0 \delta\boldsymbol{v_{dq}^e} + \left.\frac{\partial\left(e^{-j\tilde{\theta}}\boldsymbol{v_{dq}^e}\right)}{\partial\tilde{\theta}}\right|_0 \delta\tilde{\theta} \\ &= e^{-j\tilde{\theta}_0}\delta\boldsymbol{v_{dq}^e} - je^{-j\tilde{\theta}_0}\boldsymbol{v_{dq0}^e}\delta\tilde{\theta}\end{aligned} \tag{3.13}$$

In steady state, actual and estimated $\widehat{dq}$-frames are aligned; therefore, $\tilde{\theta}_0 = 0$. Consequently vectors in actual and estimated dq frames are equal (i.e. $\boldsymbol{v_{dq0}} \equiv \boldsymbol{v_{dq0}^e} = \boldsymbol{v_{dq0}^{\widehat{e}}} = v_{d0} + jv_{q0}$), which yields (3.14).

$$\delta\boldsymbol{v}_{\boldsymbol{dq}}^{\widehat{\boldsymbol{e}}} = \delta\boldsymbol{v_{dq}^e} - j\boldsymbol{v_{dq0}}\delta\tilde{\theta} \tag{3.14}$$

Applying the Laplace transform to (3.14), (3.15) is obtained.

$$\delta\boldsymbol{V}_{\boldsymbol{dq}}^{\widehat{\boldsymbol{e}}} = \delta\boldsymbol{V_{dq}^e} - j\boldsymbol{v_{dq0}}\delta\tilde{\Theta} \tag{3.15}$$

Using matrix notation (3.15) can be rewritten as (3.16). Notice that the steady state complex vector $\boldsymbol{v_{dq0}}$ is now written as the real space vector $\mathbf{V_0}$.

$$\begin{gathered}\delta\mathbf{V}^{\widehat{\mathbf{e}}} = \delta\mathbf{V}^{\mathbf{e}} - \begin{bmatrix} 0 & -1 \\ 1 & 0 \end{bmatrix}\mathbf{V_0}\delta\tilde{\Theta} \\ \begin{bmatrix} \delta V_d^{\widehat{e}} \\ \delta V_q^{\widehat{e}} \end{bmatrix} = \begin{bmatrix} \delta V_d^{e} \\ \delta V_q^{e} \end{bmatrix} - \begin{bmatrix} 0 & -1 \\ 1 & 0 \end{bmatrix}\begin{bmatrix} v_{d0} \\ v_{q0} \end{bmatrix}\delta\tilde{\Theta}(s)\end{gathered} \tag{3.16}$$

Equation (3.16) provides the small-signal vector transformation $dq/\widehat{dq}$ in the Laplace domain. It is observed from these derivations that the small-signal behavior of any vector in the estimated dq reference frame is a function of the small-signal behavior of the vector in the actual dq reference frame as well as of the small-signal behavior of the angle estimation error $\tilde{\theta}$.

3.2.2 QSG-SOGI and PLL influence on the small-signal $dq/\widehat{dq}$ vector transformation

The small-signal model of the single-phase four quadrature converter depends on PLL and QSG-SOGI dynamics. In this section, first both elements are independently modeled and later merged to produce a combined small-signal model.

3.2.2.1 QSG-SOGI

The QSG-SOGI structure is commonly used in single-phase systems, such as AC catenaries, due to its simple implementation, filtering properties, and capability to provide the quadrature signal [36, 46]. The structure of the QSG-SOGI is presented in Figure 3.1(c). The input voltage V_n is applied to the QSG-SOGI system, generating the estimated input voltage signal $\widehat{V}_{n\alpha}$ and creating the estimated virtual quadrature component $\widehat{V}_{n\beta}$. These filtered signals are used for synchronization and as feedforward to the current control loop.

Defining $V_{n\alpha} = V_n$, and considering that $V_{n\beta}$ is an ideal virtual quadrature component of the input voltage, using matrix notation the QSG-SOGI transfer function can be expressed as (3.17). The transfer functions of the second-order band-pass filter and QSG are given by (3.18) and (3.19) respectively. The corresponding frequency response is shown in Figure 3.3.

$$\begin{gathered}\widehat{\mathbf{V}}^{\mathbf{s}}_{\mathbf{n}} = \mathbf{H}^{\mathbf{s}}_{\mathbf{vs}}\mathbf{V}^{\mathbf{s}}_{\mathbf{n}} \\ \begin{bmatrix} \widehat{V}_{n\alpha} \\ \widehat{V}_{n\beta} \end{bmatrix} = \begin{bmatrix} H_{v\alpha}(s) & 0 \\ H_{v\beta}(s) & 0 \end{bmatrix}\begin{bmatrix} V_{n\alpha} \\ V_{n\beta} \end{bmatrix}\end{gathered} \tag{3.17}$$

$$H_{v\alpha}(s) = \frac{\widehat{V}_{n\alpha}}{V_n} = \frac{k_{vs}\omega_0 s}{s^2 + k_{vs}\omega_0 s + \omega_0^2} \tag{3.18}$$

$$H_{v\beta}(s) = \frac{\widehat{V}_{n\beta}}{V_n} = \frac{k_{vs}\omega_0^2}{s^2 + k_{vs}\omega_0 s + \omega_0^2} \tag{3.19}$$

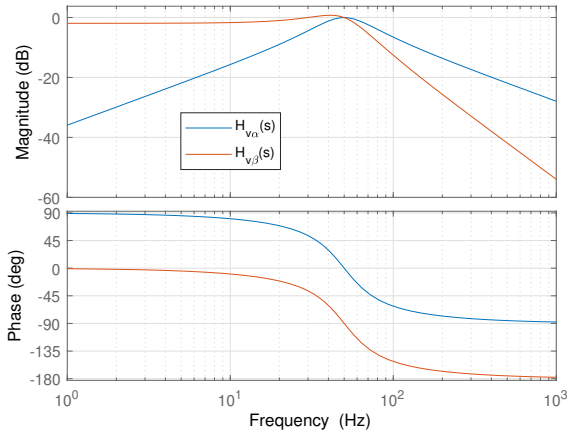

Figure 3.3: Frequency response in the stationary reference frame of $H_{v\alpha}(s)$ (SOGI-Filter) & $H_{v\beta}(s)$ (quadrature signal generator)

The Laplace-domain equation in the $\alpha\beta$ reference frame (3.17) becomes a convolution in the time domain as shown in (3.20), with $h_{v\alpha}(t)$ and $h_{v\beta}(t)$ being the impulse response of (3.18) and (3.19) respectively.

$$\begin{bmatrix} \widehat{v}_{n\alpha} \\ \widehat{v}_{n\beta} \end{bmatrix} = \begin{bmatrix} h_{v\alpha}(t) & 0 \\ h_{v\beta}(t) & 0 \end{bmatrix} * \begin{bmatrix} v_{n\alpha} \\ v_{n\beta} \end{bmatrix} \tag{3.20}$$

Transformation to the actual dq reference frame is given by (3.21).

$$\begin{aligned} \begin{bmatrix} \widehat{v}^e_{nd} \\ \widehat{v}^e_{nq} \end{bmatrix} =& \mathbf{t}_\theta \left(\begin{bmatrix} h_{v\alpha}(t) & 0 \\ h_{v\beta}(t) & 0 \end{bmatrix} * \mathbf{t}_\theta^{-1} \begin{bmatrix} v^e_{nd} \\ v^e_{nq} \end{bmatrix} \right) \\ \mathbf{t}_\theta =& \begin{bmatrix} \cos\omega_0 t & \sin\omega_0 t \\ -\sin\omega_0 t & \cos\omega_0 t \end{bmatrix} \end{aligned} \tag{3.21}$$

Solving the convolution and taking the Laplace transform of (3.21) (see Ap-

pendix A.1), (3.22)-(3.26) are obtained.

$$\begin{aligned} \widehat{\mathbf{V}}^{\mathbf{e}}_{\mathbf{n}} &\approx \mathbf{H}^{\mathbf{e}}_{\mathbf{vs}}\mathbf{V}^{\mathbf{e}}_{\mathbf{n}} \\ \begin{bmatrix} \widehat{V}^{e}_{nd} \\ \widehat{V}^{e}_{nq} \end{bmatrix} &\approx \begin{bmatrix} H^{e}_{vs-dd}(s) & H^{e}_{vs-dq}(s) \\ H^{e}_{vs-qd}(s) & H^{e}_{vs-qq}(s) \end{bmatrix} \begin{bmatrix} V^{e}_{nd} \\ V^{e}_{nq} \end{bmatrix} \end{aligned} \tag{3.22}$$

$$H^{e}_{vs-dd}(s) = H^{e}_{vs-qq}(s) \tag{3.23}$$

$$H^{e}_{vs-qd}(s) = -H^{e}_{vs-dq}(s) \tag{3.24}$$

$$\begin{aligned} H^{e}_{vs-dd}(s) =& \frac{1}{4}\big(H_{v\alpha}(s+j\omega_0) + H_{v\alpha}(s-j\omega_0)\big) \\ &+ \frac{j}{4}\big(H_{v\beta}(s+j\omega_0) - H_{v\beta}(s-j\omega_0)\big) \end{aligned} \tag{3.25}$$

$$\begin{aligned} H^{e}_{vs-qd}(s) =& \frac{1}{4}\big(H_{v\beta}(s+j\omega_0) + H_{v\beta}(s-j\omega_0)\big) \\ &- \frac{j}{4}\big(H_{v\alpha}(s+j\omega_0) - H_{v\alpha}(s-j\omega_0)\big) \end{aligned} \tag{3.26}$$

It is noted that since (3.17) is not a symmetric system, frequency components around $2\omega_0$ can appear in the synchronous reference frame [42]. This is discussed in Appendix A.1. Since this study is focused on LFO, frequency components around $2\omega_0$ are not expected to affect, and will not be further discussed. Consequently, $\mathbf{H}^{\mathbf{e}}_{\mathbf{vs}}$ is the approximated QSG-SOGI transfer function that relates the actual input voltage $\mathbf{V}^{\mathbf{e}}_{\mathbf{n}}$ and the estimated input voltage $\widehat{\mathbf{V}}^{\mathbf{e}}_{\mathbf{n}}$, both in the actual dq-frame.

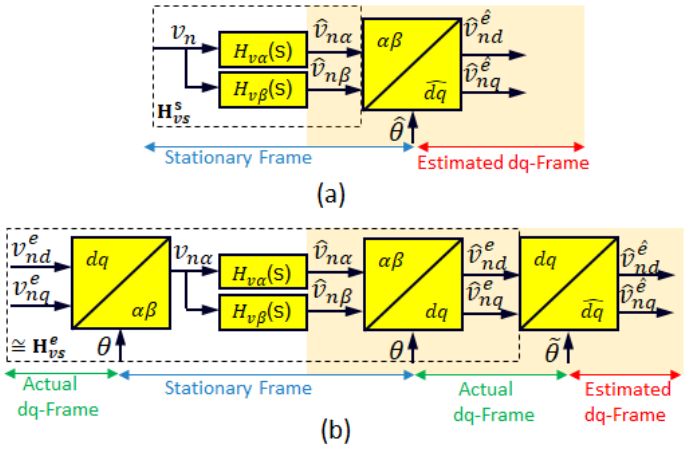

Figure 3.4: (a) QSG-SOGI in $\alpha\beta$-frame and the park transformation to the estimated $\widehat{dq}$-frame. (b) $\alpha\beta - dq - \widehat{dq}$ decomposition & QSG-SOGI in actual dq-frame

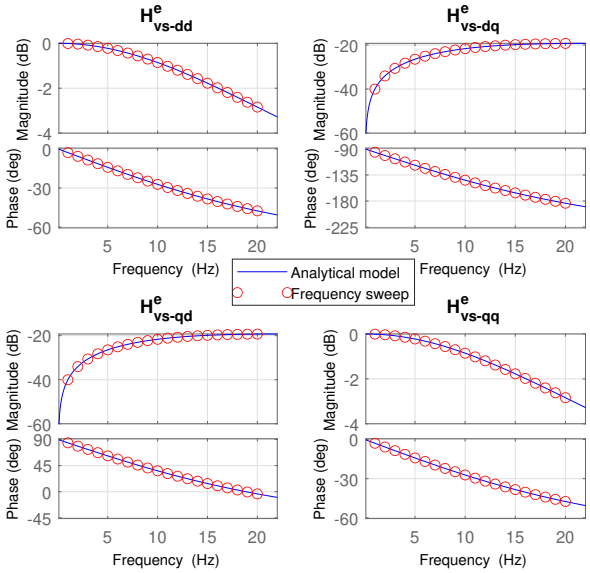

Figure 3.5: Frequency response: SOGI transfer function ($\mathbf{H^e_{vs}}$) in the actual dq-frame. Analytical low-frequency model vs. frequency sweep of simulation model.

Figure 3.4(a) shows the voltage QSG-SOGI block diagram and the park transformation into the estimated $\widehat{dq}$-frame. Figure 3.4(b) shows; first, $\alpha\beta - dq - \widehat{dq}$ decomposition (i.e. rotation action, performed by the estimated angle $\widehat{\theta}$, is decomposed in cascade rotations performed by θ and $\tilde{\theta}$) in to order to obtain the estimated input voltage in the actual dq-frame $\widehat{\mathbf{V}}^{\mathbf{e}}_{\mathbf{n}}$; second, the QSG-SOGI transformation from stationary frame to the actual dq-frame. Finally, the QSG-SOGI frequency response can be obtained from the relationship between the input voltage and the estimated input voltage, both in the actual dq-frame.

Figure 3.5 shows the frequency response obtained from both, using the analytical model of the SOGI (3.22), and from simulation using the dynamic model shown in Figure 3.4(b), the agreement being remarkable. Notice that SOGI diagonal transfer functions $H^e_{vs-dd}(s)$ and $H^e_{vs-dd}(s)$ work as first order low-pass filters.

The current QSG-SOGI has the same structure as the voltage QSG-SOGI shown in Figure 3.1(c), but the gain now is k_{cs}. Consequently, the preceding methodology and discussion to obtain the current QSG-SOGI transfer function in the actual dq-frame $\mathbf{H^e_{cs}}$ also apply in this case.

3.2.2.2 Phase-Locked Loop

The PLL structure in dq-frame is shown in Figure 3.6. The controller transfer function is (3.27). Selection of the proportional gain k_{PLL} involves a trade-off between filtering capability and dynamic response, and the integral gain was chosen as k_{iPLL}=$k_{PLL}^2/2$ [26].

$$F_{PLL}(s) = k_{PLL} + \frac{k_{iPLL}}{s} \tag{3.27}$$

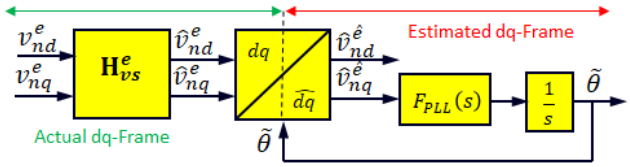

Figure 3.6: Phase locked loop in dq-frame

The linear relationship between the error angle $\tilde{\theta}$ and the estimated input q-axis voltage in the estimated frame $\hat{v}_{nq}^{\hat{e}}$ is readily observed from the figure. It is therefore straightforward to obtain the small-signal transfer function (3.28).

$$\delta\tilde{\Theta} = \frac{F_{PLL}(s)}{s}\delta\hat{V}_{nq}^{\hat{e}} \tag{3.28}$$

By applying the small-signal transformation (3.15) to the estimated input voltage complex vector $\widehat{\boldsymbol{V}}_{\boldsymbol{ndq}}^{\hat{\boldsymbol{e}}}$, (3.29) is derived.

$$\begin{aligned} \delta\widehat{\boldsymbol{V}}_{\boldsymbol{ndq}}^{\hat{\boldsymbol{e}}} &= \delta\widehat{\boldsymbol{V}}_{\boldsymbol{ndq}}^{\boldsymbol{e}} - j\boldsymbol{v}_{\boldsymbol{ndq0}}\delta\tilde{\Theta} \\ \delta\widehat{V}_{nd}^{\hat{e}} + j\delta\widehat{V}_{nq}^{\hat{e}} &= \left(\delta\widehat{V}_{nd}^{e} + j\delta\widehat{V}_{nq}^{e}\right) - j\left(v_{nd0} + jv_{nq0}\right)\delta\tilde{\Theta} \end{aligned} \tag{3.29}$$

Where $\boldsymbol{v}_{\boldsymbol{ndq0}}$ is defined by (3.30) because in the steady state, estimated and real values of input voltage in both dq-frames are equal.

$$\boldsymbol{v}_{\boldsymbol{ndq0}} \equiv \widehat{\boldsymbol{v}}_{\boldsymbol{ndq0}}^{\hat{\boldsymbol{e}}} = \widehat{\boldsymbol{v}}_{\boldsymbol{ndq0}}^{\boldsymbol{e}} = \boldsymbol{v}_{\boldsymbol{ndq0}}^{\hat{\boldsymbol{e}}} = \boldsymbol{v}_{\boldsymbol{ndq0}}^{\boldsymbol{e}}. \tag{3.30}$$

Equation (3.31) is obtained by taking only the imaginary part of (3.29). Notice that in steady state $v_{nq0} = 0$ since the d-axis is aligned with the fundamental component of the input voltage.

$$\delta\widehat{V}_{nq}^{\widehat{e}} = \delta\widehat{V}_{nq}^{e} - v_{nd0}\delta\tilde{\Theta} \tag{3.31}$$

Replacing (3.31) in (3.28), the small-signal model of the error angle is given by (3.32).

$$\delta\tilde{\Theta} = \underbrace{\frac{F_{PLL}(s)}{s + v_{nd0}F_{PLL}(s)}}_{G_{pll}(s)}\delta\widehat{V}_{nq}^{e} \tag{3.32}$$

Equation (3.32) shows that small variations of the error angle $\tilde{\theta}$ depend on the small variations of the q-axis component of the estimated input voltage $\widehat{v}_{nq}^{e}$, which means it depends implicitly on the SOGI dynamics. This is further analyzed in the following section.

3.2.2.3 Combined effect of QSG-SOGI and PLL in the small-signal $dq/\widehat{dq}$ vector transformation

So far PLL and SOGI have been analyzed independently. However, the small-signal vector transformation depends on both elements.

To include the PLL influence, (3.32) is used to replace the differential error angle in (3.16), obtaining (3.33).

$$\delta\mathbf{V}^{\widehat{\mathbf{e}}} = \delta\mathbf{V}^{\mathbf{e}} - \begin{bmatrix} 0 & -1 \\ 1 & 0 \end{bmatrix}\mathbf{V_0}G_{pll}(s)\delta\widehat{V}_{nq}^{e} \tag{3.33}$$

Equation (3.33) can be written as a function of the differential estimated input voltage vector $\delta\widehat{\mathbf{V}}_{\mathbf{n}}^{\mathbf{e}}$ instead of using only its q-axis component $\delta\widehat{V}_{nq}^{e}$. This is shown by (3.34).

$$\delta\mathbf{V}^{\widehat{\mathbf{e}}} = \delta\mathbf{V}^{\mathbf{e}} - \begin{bmatrix} 0 & -1 \\ 1 & 0 \end{bmatrix}\mathbf{V_0}\begin{bmatrix} 0 & G_{pll}(s) \end{bmatrix}\begin{bmatrix} \delta\widehat{V}_{nd}^{e} \\ \delta\widehat{V}_{nq}^{e} \end{bmatrix} \tag{3.34}$$

Defining the matrix $\mathbf{G_{PLL}(V_0)}$ (3.35), which is a function of the operating point voltage vector $\mathbf{V_0}$, and using it in (3.34), yields (3.36).

$$\mathbf{G_{PLL}(V_0)} = \begin{bmatrix} 0 & -1 \\ 1 & 0 \end{bmatrix}\mathbf{V_0}\begin{bmatrix} 0 & G_{pll}(s) \end{bmatrix} \tag{3.35}$$

$$\delta\mathbf{V}^{\widehat{\mathbf{e}}} = \delta\mathbf{V}^{\mathbf{e}} - \mathbf{G_{PLL}(V_0)}\delta\widehat{\mathbf{V}}_{\mathbf{n}}^{\mathbf{e}} \tag{3.36}$$

Finally, using (3.22) in (3.36) to add explicitly the SOGI dynamics, the small-signal $dq/\widehat{dq}$ vector transformation (3.37) is obtained. Notice that this transformation is a function of the differential input voltage vector in the actual dq-frame $\delta\mathbf{V_n^e}$, same as the input admittance (3.12).

$$\delta\mathbf{V}^{\widehat{\mathbf{e}}} = \delta\mathbf{V^e} - \mathbf{G_{PLL}}(\mathbf{V_0})\mathbf{H_{vs}^e}\delta\mathbf{V_n^e} \tag{3.37}$$

A similar expression to (3.37) using a different derivation method was presented in [38]. However, that solution didn't include SOGI dynamics and it was presented for the particular case of the input voltage and input current vectors. The derivation presented in this thesis is more general, as for any vector (e.g. input voltage, estimated input voltage, input current, estimated input current, reference input current, 4QC terminal voltage, and so on).

Equation (3.37) will be used to obtain the small-signal current control model in Section 3.2.3 and the DC-link control in Section 3.2.4.

3.2.3 Current Control

The AC-side 4QC model in Figure 3.1(a) is defined by the LR system in (3.38), being v_t the voltage in the 4QC terminals.

$$v_n = L_n\frac{di_n}{dt} + R_n i_n + v_t \tag{3.38}$$

Assuming that ideal orthogonal components for voltage and current signals in (3.38) are available, and transforming the equivalent $\alpha\beta$ system to the actual dq-frame, the model (3.39)-(3.40) in Laplace domain is obtained. See Appendix A.2 for a detailed calculation of the transformation.

$$\mathbf{V_n^e} = \mathbf{Z_n^e}\mathbf{I_n^e} + \mathbf{V_t^e} \tag{3.39}$$

$$\mathbf{Z_n^e} = \begin{bmatrix} L_n s + R_n & -\omega_0 L_n \\ \omega_0 L_n & L_n s + R_n \end{bmatrix} \tag{3.40}$$

Figure 3.7 shows the current control system in the estimated $\widehat{dq}$-frame, as well as the subsequent transformation to the actual reference frame, when there are errors in the angle estimation.

The current controller transfer function matrix $\mathbf{G_{cc}^{\widehat{e}}}$ in the estimated $\widehat{dq}$-frame is shown in (3.41), where the PI current controller transfer function is given by (3.42).

$$\mathbf{G_{cc}^{\widehat{e}}} = \begin{bmatrix} G_{cc}^{\widehat{e}}(s) & 0 \\ 0 & G_{cc}^{\widehat{e}}(s) \end{bmatrix} \tag{3.41}$$

$$G_{\mathrm{cc}}^{\hat{e}}(s) = k_{pCC} + \frac{k_{iCC}}{s} \tag{3.42}$$

Cross-coupling decoupling is achieved using (3.43).

$$\mathbf{G}_{\omega_0 \mathbf{L_n}}^{\hat{\mathbf{e}}} = \begin{bmatrix} 0 & -\omega_0 L_n \\ \omega_0 L_n & 0 \end{bmatrix} \tag{3.43}$$

The voltage command $\mathbf{V_t^{*\hat{e}}}$ generated by the controller is obtained using (3.44), where $\widehat{\mathbf{V}}_{\mathbf{n}}^{\hat{\mathbf{e}}}$ is the estimated input voltage in the estimated $\widehat{dq}$-frame (3.45), $\widehat{\mathbf{I}}_{\mathbf{n}}^{\hat{\mathbf{e}}}$ is the estimated inductance current in the estimated $\widehat{dq}$-frame (3.46), and $\mathbf{I_n^{*\hat{e}}}$ is the current reference in the estimated $\widehat{dq}$-frame. The $dq/\widehat{dq}$ transformation matrix $\mathbf{T}_{\tilde{\theta}}$ was already defined in Section 3.1.2.

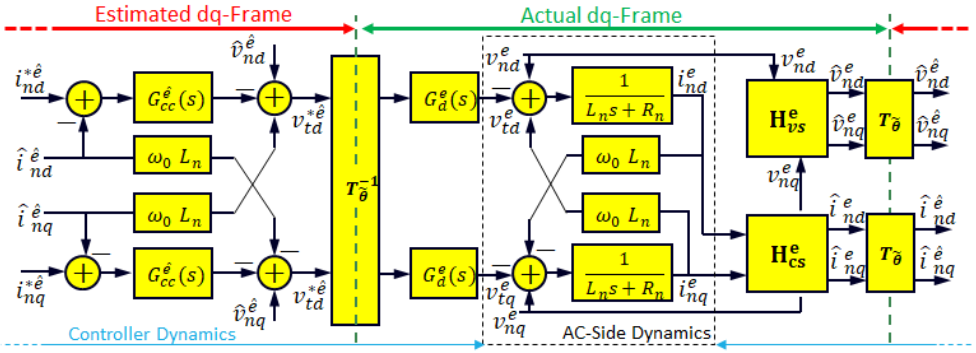

Figure 3.7: Current control system in actual and estimated dq frames. AC-side dynamics and controller dynamics

$$\mathbf{V_t^{*\hat{e}}} = \widehat{\mathbf{V}}_{\mathbf{n}}^{\hat{\mathbf{e}}} - \mathbf{G}_{\mathbf{cc}}^{\hat{\mathbf{e}}} \left(\mathbf{I_n^{*\hat{e}}} - \widehat{\mathbf{I}}_{\mathbf{n}}^{\hat{\mathbf{e}}} \right) - \mathbf{G}_{\omega_0 \mathbf{L_n}}^{\hat{\mathbf{e}}} \widehat{\mathbf{I}}_{\mathbf{n}}^{\hat{\mathbf{e}}} \tag{3.44}$$

$$\widehat{\mathbf{V}}_{\mathbf{n}}^{\hat{\mathbf{e}}} = \mathbf{T}_{\tilde{\theta}} \mathbf{H}_{\mathbf{vs}}^{\mathbf{e}} \mathbf{V}_{\mathbf{n}}^{\mathbf{e}} \tag{3.45}$$

$$\widehat{\mathbf{I}}_{\mathbf{n}}^{\hat{\mathbf{e}}} = \mathbf{T}_{\tilde{\theta}} \mathbf{H}_{\mathbf{cs}}^{\mathbf{e}} \mathbf{I}_{\mathbf{n}}^{\mathbf{e}} \tag{3.46}$$

Control delays can affect significantly the performance of the current regulator. The delay is modeled as (3.47). The total time delay $T_d = 1.5T_s$ accounts for computation time (i.e. T_s) and zero-order hold (i.e. $0.5T_s$) [47], where $T_s = 1/f_s$ is the control sampling time, which is the inverse of the sampling frequency f_s.

$$G_d^e(s) = e^{-T_d s} \tag{3.47}$$

Finally, the terminal voltage vector $\mathbf{V_t^e}$ in the actual *dq*-frame is defined by (3.48)-(3.49), where $\mathbf{I}$ is the identity matrix.

$$\mathbf{G_d^e} = G_d^e(s)\mathbf{I} \tag{3.48}$$

$$\mathbf{V_t^e} = \mathbf{G_d^e T_{\widetilde{\theta}}^{-1} V_t^{*\widehat{e}}} \tag{3.49}$$

Using (3.39)-(3.49) the closed-loop current control system that corresponds to the block diagram in Figure 3.7 is defined by (3.50)-(3.51).

$$\mathbf{I_n^e} = \mathbf{Z_f^{-1}}(\mathbf{I} - \mathbf{G_d^e H_{vs}^e})\mathbf{V_n^e} + \mathbf{Z_f^{-1} G_d^e T_{\widetilde{\theta}}^{-1} G_{cc}^{\widehat{e}} I_n^{*\widehat{e}}} \tag{3.50}$$

$$\mathbf{Z_f} = \mathbf{Z_n^e} + \mathbf{G_d^e T_{\widetilde{\theta}}^{-1} G_{cc}^{\widehat{e}} T_{\widetilde{\theta}} H_{cs}^e} - \mathbf{G_d^e T_{\widetilde{\theta}}^{-1} G_{\omega_0 L_n}^{\widehat{e}} T_{\widetilde{\theta}} H_{cs}^e} \tag{3.51}$$

One inconvenience of (3.50)-(3.51) is that it includes vectors and transfer functions in two different reference frames. By transforming all terms to the actual synchronous reference frame using (3.52)-(3.54), (3.55)-(3.56) are obtained.

$$\mathbf{I_n^{*\widehat{e}}} = \mathbf{T_{\widetilde{\theta}} I_n^{*e}} \tag{3.52}$$

$$\mathbf{G_{cc}^e} = \mathbf{T_{\widetilde{\theta}}^{-1} G_{cc}^{\widehat{e}} T_{\widetilde{\theta}}} \tag{3.53}$$

$$\mathbf{G_{\omega_0 L_n}^e} = \mathbf{T_{\widetilde{\theta}}^{-1} G_{\omega_0 L_n}^{\widehat{e}} T_{\widetilde{\theta}}} \tag{3.54}$$

$$\mathbf{I_n^e} = \mathbf{Z_f^{-1}}(\mathbf{I} - \mathbf{G_d^e H_{vs}^e})\mathbf{V_n^e} + \mathbf{Z_f^{-1} G_d^e G_{cc}^e I_n^{*e}} \tag{3.55}$$

$$\mathbf{Z_f} = \mathbf{Z_n^e} + \mathbf{G_d^e G_{cc}^e H_{cs}^e} - \mathbf{G_d^e G_{\omega_0 L_n}^e H_{cs}^e} \tag{3.56}$$

It is important to mention that the reference frame transformation of a system produces a frequency displacement in the corresponding transfer function. The effect of an error between estimated and actual frequencies therefore implies a change in the Laplace operator $s \longrightarrow s + j\widetilde{\omega}$, where $\widetilde{\omega} = d\widetilde{\theta}/dt$ is the frequency error. In the steady state, actual and estimated *dq* frames are aligned (i.e. $\widetilde{\omega} = 0$ and $\widetilde{\theta} = 0$). On the other hand, during transients, these frames are not aligned anymore (i.e. $\widetilde{\theta} \neq 0$); however, the frequency error $\widetilde{\omega}$ is always very small compared to ω_0 [38], and can be safely neglected. Therefore, although the angles of both synchronous frames could be different, it is considered that both *dq*-frames are rotating at the same frequency, and (3.57) can be assumed.

$$\mathbf{G^e} = \mathbf{T_{\widetilde{\theta}}^{-1} G^{\widehat{e}} T_{\widetilde{\theta}}} \approxeq \mathbf{G^{\widehat{e}}} \tag{3.57}$$

Using (3.57), the transfer functions $\mathbf{G_{cc}^e}$ and $\mathbf{G_{\omega_0 L_n}^e}$ can be approximated by (3.58)

and (3.59), respectively.

$$\mathbf{G^e_{cc}} \approxeq \mathbf{G^{\hat{e}}_{cc}} \tag{3.58}$$

$$\mathbf{G^e_{\omega_0 L_n}} \approxeq \mathbf{G^{\hat{e}}_{\omega_0 L_n}} \tag{3.59}$$

The small-signal model of (3.55) is given by (3.60)

$$\delta\mathbf{I^e_n} = \mathbf{Z_f^{-1}}(\mathbf{I} - \mathbf{G^e_d H^e_{vs}})\delta\mathbf{V^e_n} + \mathbf{Z_f^{-1}G^e_d G^e_{cc}}\delta\mathbf{I^{*e}_n} \tag{3.60}$$

Using the small-signal vector transformation (3.37), and considering that in the steady state the reference current and the 4QC current are equal in both dq-frames (i.e. $\mathbf{I_{n0}} \equiv \mathbf{I^{*\hat{e}}_{n0}} = \mathbf{I^{*e}_{n0}} = \mathbf{I^{\hat{e}}_{n0}} = \mathbf{I^e_{n0}}$), the differential reference current vector $\delta\mathbf{I^{*e}_n}$ is given by (3.61).

$$\delta\mathbf{I^{*e}_n} = \delta\mathbf{I^{*\hat{e}}_n} + \mathbf{G_{PLL}}(\mathbf{I_{n0}})\mathbf{H^e_{vs}}\delta\mathbf{V^e_n} \tag{3.61}$$

where $\mathbf{G_{pll}}(\mathbf{I_{n0}}) = \begin{bmatrix} 0 & -i_{nq0}G_{pll}(s) \\ 0 & -i_{nd0}G_{pll}(s) \end{bmatrix}$

Replacing (3.61) in (3.60), the small-signal closed-loop current control system model (3.62) is obtained, the corresponding block diagram is represented in Figure 3.8.

$$\delta\mathbf{I^e_n} = \mathbf{Z_f^{-1}}(\mathbf{I} - \mathbf{G^e_d H^e_{vs}})\delta\mathbf{V^e_n} + \mathbf{Z_f^{-1}G^e_d G^e_{cc}}(\delta\mathbf{I^{*\hat{e}}_n} + \mathbf{G_{pll}}(\mathbf{I_{n0}})\mathbf{H^e_{vs}}\delta\mathbf{V^e_n}) \tag{3.62}$$

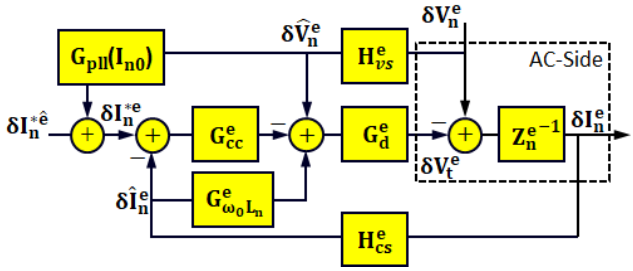

Figure 3.8: Small-signal model of current control in dq-frame. AC-side dynamics and controller dynamics

Rearranging (3.62), the small-signal closed-loop current control system model is expressed by (3.63).

$$\delta\mathbf{I^e_n} = \mathbf{G_{ci}}\delta\mathbf{I^{*\hat{e}}_n} + \mathbf{Y_{ci}}\delta\mathbf{V^e_n} \tag{3.63}$$

where $\mathbf{G_{ci}} = \mathbf{Z_f^{-1}G^e_d G^e_{cc}}$

and $\mathbf{Y_{ci}} = \mathbf{Z_f^{-1}}\left(\mathbf{I} - \mathbf{G^e_d H^e_{vs}} + \mathbf{G^e_d G^e_{cc} G_{pll}}(\mathbf{I_{n0}})\mathbf{H^e_{vs}}\right)$

3.2.4 DC-Link Voltage Control

3.2.4.1 DC-Link Voltage Dynamics

Since the impedance of the 4QC is mainly inductive ($R_n \approx 0$), associated Joule losses can be safely neglected. Commutation losses in the converter are neglected as well due to LFO occurring at low power consumption [24]. Under these assumptions, power conservation between the converter AC-side and DC-side can be assumed (3.64).

$$\underbrace{v_{dc}i_{dc}}_{P_{dc}} \approxeq \underbrace{v_{nd}^e i_{nd}^e + v_{nq}^e i_{nq}^e}_{P_{ac}} \tag{3.64}$$

Taking partial derivatives in (3.64), the small-signal variation in the DC-side current is obtained (3.65), with subscript "$_0$" indicating operating point values.

$$\begin{aligned}\delta i_{dc} =& \frac{v_{nd0}}{v_{dc0}}\delta i_{nd}^e + \frac{i_{nd0}}{v_{dc0}}\delta v_{nd}^e + \frac{v_{nq0}}{v_{dc0}}\delta i_{nq}^e \\ &+ \frac{i_{nq0}}{v_{dc0}}\delta v_{nq}^e - \frac{v_{nd0}i_{nd0} + v_{nq0}i_{nq0}}{v_{dc0}^2}\delta v_{dc}\end{aligned} \tag{3.65}$$

Performing the Laplace transform and considering that in the steady state, the train operates with unity power factor (i.e. $i_{nq0} = 0$), the input voltage vector is aligned with the synchronous frame (i.e. $v_{nq0} = 0$), and $P_{dc0} \approxeq P_{ac0} = v_{nd0}i_{nd0}$, (3.66) is obtained.

$$\delta I_{dc} = \frac{v_{nd0}}{v_{dc0}}\delta I_{nd}^e + \frac{i_{nd0}}{v_{dc0}}\delta V_{nd}^e - \frac{v_{nd0}i_{nd0}}{v_{dc0}^2}\delta V_{dc} \tag{3.66}$$

Loads connected to the DC-link include traction converters and auxiliary loads. For LFO analysis they can be modeled as an equivalent resistor [11,17] as explained in Section 1.2.3. The small-signal model of the 4QC DC-side coincides in this case with the transfer function of the RC circuit (3.67), as seen in Figure 3.1(a).

$$\delta V_{dc} = \left(\frac{R_L}{R_L C_d s + 1}\right)\delta I_{dc} \tag{3.67}$$

Finally, combining (3.67) and (3.66), (3.68) is obtained, where (3.69) and (3.70) relate small variation of DC-link voltage with the d-axis component of input voltage and 4QC inductance current.

$$\delta V_{dc} = G_{iv}(s)\delta I_{nd}^e + G_{vv}(s)\delta V_{nd}^e \tag{3.68}$$

$$G_{iv}(s) = \frac{v_{nd0}}{v_{dc0}} \frac{1}{C_d s + 2/R_L} \tag{3.69}$$

$$G_{vv}(s) = \frac{i_{nd0}}{v_{dc0}} \frac{1}{C_d s + 2/R_L} \tag{3.70}$$

3.2.4.2 Voltage Controller

The voltage controller is shown in Figure 3.1(d). It is modeled as (3.71), with k_d (3.72) being the gain relating AC and DC quantities. The PI controller transfer function is given by (3.73).

$$I_{nd}^{*\widehat{e}} = k_d G_{vc}(s) \left(V_{dc}^* - V_{dc}\right) \tag{3.71}$$

$$k_d = \frac{i_{nd0}}{i_{dc0}} = \frac{v_{dc0}}{v_{nd0}} \tag{3.72}$$

$$G_{vc}(s) = k_{pVC} + \frac{k_{iVC}}{s} \tag{3.73}$$

Considering that the DC-link voltage command V_{dc}^* in (3.71) is constant, the small-signal model in (3.74) is obtained.

$$\delta I_{nd}^{*\widehat{e}} = -k_d G_{vc}(s) \delta V_{dc} \tag{3.74}$$

Replacing the differential DC-link voltage in (3.74) by the expression in (3.68) yields:

$$\delta I_{nd}^{*\widehat{e}} = -k_d G_{vc}(s) G_{iv}(s) \delta I_{nd}^{e}(s) - k_d G_{vc}(s) G_{vv}(s) \delta V_{nd}^{e} \tag{3.75}$$

Transforming (3.75) to use matrix notation, the relationship between the input voltage, the train current, and the reference current is obtained (3.76), where $\mathbf{G_{vc}}$, $\mathbf{G_{iv}}$ and $\mathbf{G_{vv}}$ are defined by (3.77), (3.78) and (3.79) respectively.

$$\delta \mathbf{I_n^{*\widehat{e}}} = -k_d \mathbf{G_{vc}} \mathbf{G_{iv}} \delta \mathbf{I_n^e} + k_d \mathbf{G_{vc}} \mathbf{G_{vv}} \delta \mathbf{V_n^e} \tag{3.76}$$

$$\mathbf{G_{vc}^e} = G_{vc}^e(s) \mathbf{I} \tag{3.77}$$

$$\mathbf{G_{iv}} = \begin{bmatrix} G_{iv}(s) & 0 \\ 0 & 0 \end{bmatrix} \tag{3.78}$$

$$\mathbf{G_{vv}} = \begin{bmatrix} G_{vv}(s) & 0 \\ 0 & 0 \end{bmatrix} \tag{3.79}$$

3.2.5 Train input admittance

Combining the DC-link voltage small-signal dynamics given by (3.76) and the closed-loop current control dynamics given by (3.63), the small-signal input admittance of the train seen by the secondary of the traction transformer (i.e. ratio between differential input voltage vector and differential 4QC current vector) is obtained as (3.80). The corresponding block diagram is shown in Figure 3.9.

$$\mathbf{Y_{tn}} = \frac{\delta \mathbf{I_n^e}}{\delta \mathbf{V_n^e}} = \frac{\mathbf{I} - \mathbf{G_d^e H_{vs}^e} - k_d \mathbf{G_d^e G_{cc}^e G_{vc} G_{vv}} + \mathbf{G_d^e G_{cc}^e G_{pll}(I_{n0}) H_{vs}^e}}{\mathbf{Z_n^e} + \mathbf{G_d^e G_{cc}^e H_{cs}^e} - \mathbf{G_d^e G_{\omega_0 L_n}^e H_{cs}^e} + k_d \mathbf{G_d^e G_{cc}^e G_{vc} G_{iv}}} \tag{3.80}$$

For the sake of clarity, the process followed to obtain matrices and parameters involved in the calculation of the input admittance $\mathbf{Y_{tn}}$ is listed below.

1. Obtain matrix $\mathbf{Z_n^e}$ (3.40)
2. Obtain matrix $\mathbf{H_{cs}^e}$ and $\mathbf{H_{vs}^e}$ (3.22)
3. Gains of current controller, obtain matrix $\mathbf{G_{cc}^e} \approxeq \mathbf{G_{cc}^{\widehat{e}}}$ (3.41)
4. Cross-coupling decoupling, obtain matrix $\mathbf{G_{\omega_0 L_n}^e} \approxeq \mathbf{G_{\omega_0 L_n}^{\widehat{e}}}$ (3.43)
5. Gains of voltage controller, obtain matrix $\mathbf{G_d^e} = G_d^e(s)\mathbf{I}$ (3.47)
6. Obtain matrix $\mathbf{G_{pll}(I_{n0})}$ (3.61)
7. Gains of voltage controller, obtain matrix $\mathbf{G_{vc}^e} = G_{vc}^e(s)\mathbf{I}$ (3.73)
8. Obtain matrix $\mathbf{G_{iv}}$ and $\mathbf{G_{vv}}$ from (3.78) and (3.79)

Finally, the train admittance seen from the catenary line is given by (3.81).

$$\mathbf{Y_t} = \frac{1}{k^2}\mathbf{Y_{tn}} \tag{3.81}$$

Correctness of (3.81) was confirmed by means of simulation using the frequency sweep method described in 2.1.3. Train and control parameters used in the calculation and simulation are shown in Table 3.1. The results are presented in Figure 3.10, the level of agreement being remarkable.

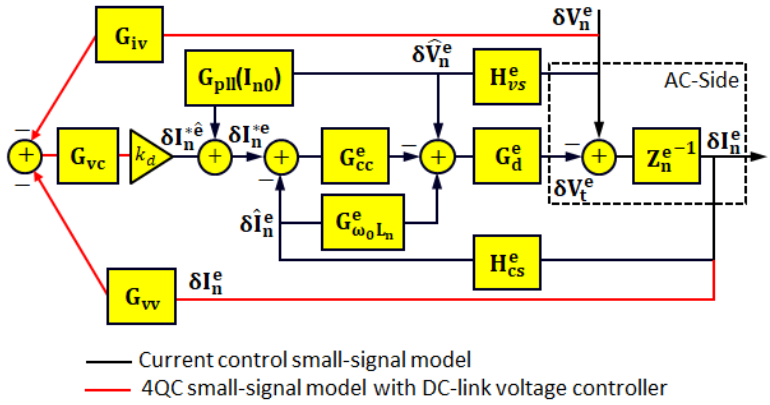

Figure 3.9: Block diagram of the 4QC (train) input admittance in the actual dq-frame $\mathbf{Y_{tn}}$

Symbol	Description	Value
V_c	RMS Catenary Voltage	25 kV
f_0	Catenary frequency	50 Hz
V_{dc}	Nominal DC-link Voltage	3600 V
k	Transformer Ratio	14.12
L_n	4QC Inductance	3 mH
R_n	4QC Resistance	10 mΩ
C_d	DC-link Capacitance	10 mF
$BWvc$	Voltage Control Bandwidth	5 Hz
$BWcc$	Current Control Bandwidth	50 Hz
k_{vs}	Voltage SOGI Gain	0.80
k_{cs}	Current SOGI Gain	1
k_{pll}	Phase-Locked Loop Gain	6
f_{sw}	Switching Frequency	700 Hz
f_s	Sampling Frequency	1400 Hz
P_{dc}	DC link Load	50 kW

Table 3.1: Train parameters

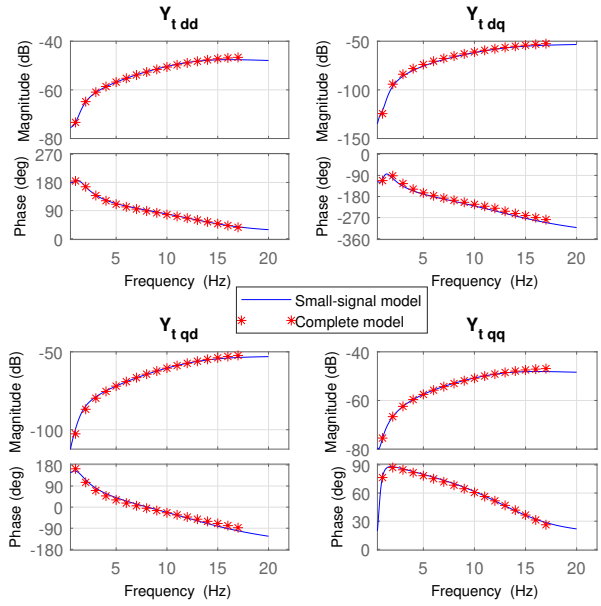

Figure 3.10: Train input admittance in the actual *dq*-frame obtained from the analytical small-signal model vs frequency swept of complete simulation model

3.3 Stability Analysis

In this section, the stability criteria described in Section 2.1 are applied to analyze the case of multiple trains in depot. The effect of increasing the power consumption in the DC-link is also studied.

3.3.1 Stability analysis for the case of multiple trains on depot

For the sake of simplicity, in this analysis it is considered that all the trains in the depot are identical (i.e. they have the same electrical and control parameters) and operating at the same base power of 50 kW; therefore, they have the same input admittance. The analysis for the case of different input admittance would follow the same methodology, the equivalent admittance would be the sum of the individual admittances [1].

Being m the number of identical trains, three different cases are presented: stable system ($m = 17$), system at its stability limit ($m = 27$), and unstable system ($m = 37$). Time-domain simulations are used to verify the analysis.

The specific train admittance used for the analysis is shown in Figure 3.10, which

corresponds to the train parameters in Table 3.1. The components of the network impedance Z_s are the upstream grid impedance Z_{ug}, and the substation impedance Z_{sst} as seen in (3.82). This equation does not consider the transmission line impedance per km since it is assumed that the trains are parked very close to the substation.

$$Z_s = 2 \times Z_{ug} + Z_{sst} \tag{3.82}$$

The following impedance parameters at fundamental frequency ω_0 are used in this study [28]:

$$|Z_{ug}| = 0.5\Omega, \angle Z_{ug} = 80^\circ \; ; \; |Z_{sst}| = 5.5\Omega, \angle Z_{sst} = 80^\circ$$

Once the train admittance matrix, network impedance matrix, and number of trains are defined, the eigenvalues of the system in the range of frequencies of interest are calculated using (2.14).

Nyquist plots and the Bode diagrams for the three cases are shown in Figure 3.11(a) and Figure 3.11(b) respectively. The gain margin is marked with filled circles in the Bode plots. The frequency response obtained using the simulation model is also shown to assess the accuracy of the analytical small-signal model. From Figure 3.11(b) it is seen that increasing the number of trains at the depot, only increases the magnitude of eigenvalues λ_1 and λ_2, the phase remaining constant. As noticed in Figure 3.11(b), the phase of the eigenvalue λ_2 never intersects 180°, therefore it is not causing any instability. This applies to the three examined cases. Nyquist stability criterion confirms the same result since λ_2 never encloses -1.

It is observed from the Nyquist plot in Figure 3.11(a) that for $m = 17$, the eigenvalue λ_1 (green curve) does not enclose -1, which fulfills the Nyquist stability criterion. For $m = 27$, the eigenvalue λ_1 (blue curve) almost crosses -1, meaning that the system is at the stability limit. For $m = 37$ trains, the red curve encloses -1; thus, the system is not fulfilling the stability criterion anymore and the system becomes unstable.

Similarly, it is observed from Bode plots in Figure 3.11(b) that for $m = 17$ (stable case), $|\lambda_1|$ at phase crossover frequency f_c is less than 0 dB (i.e. positive gain margin), which fulfills the stability criterion. At the system stability limit for $m = 27$, $|\lambda_1|$ at the crossover frequency is 0 dB, in this case, the crossover frequency f_c will define the oscillation frequency, that is 4.5 Hz. If there are more than 27 trains connected to the power supply network, $|\lambda_1|$ at the crossover frequency will take positive values (i.e. negative gain margin) and the system will become unstable.

Time domain simulations of the three cases are shown in Figure 3.12. Catenary voltage, DC-link voltage, and inductor current per train are shown. Initially, the system is operating with $m = 7$ trains at the depot; here the system is in steady state; at $t = 5$ s, ten more trains are connected to the network as a step change (i.e. $m = 17$); here, the system experiences small oscillations that are damped quickly, and the system remains stable. A second step change in the number of trains (i.e. $m = 27$) occurs at $t = 6$ s. Time response in this case is pure oscillatory. The negligible damping indicates that the system is at the stability limit. The frequency of the oscillations observed in

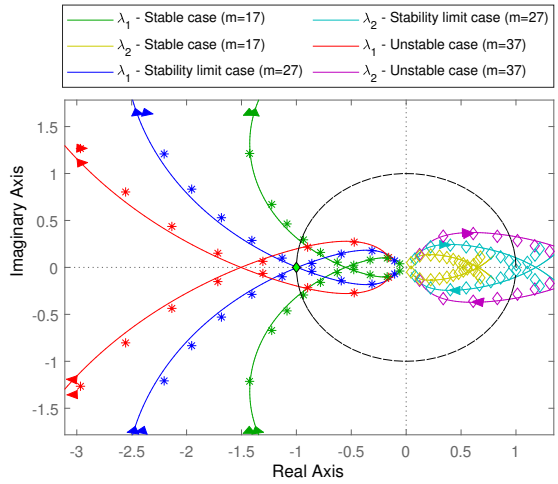

(a) Nyquist plot

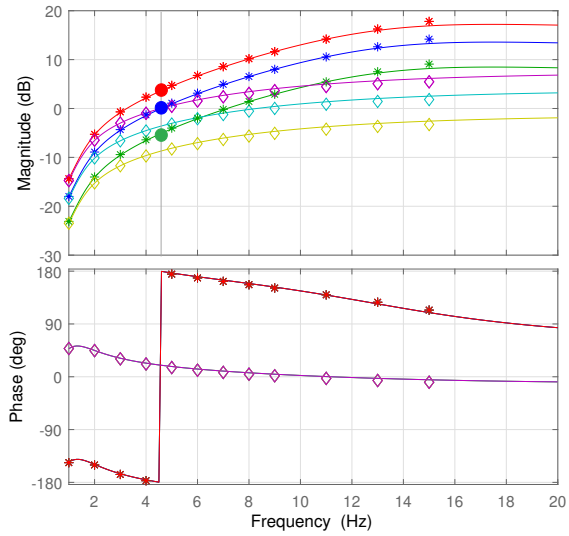

(b) Bode Diagram

Figure 3.11: System eigenvalues using the small-signal analytical model (continuous line), for different number of trains m in the depot (DC-link power consumption 50 kW). $m = 17$ (stable), $m = 27$ (limit of stability) and $m = 37$ (unstable). System eigenvalues obtained from frequency swept using complete simulation model are indicate with marks ($\lambda_1 \rightarrow *$, $\lambda_2 \rightarrow \Diamond$).

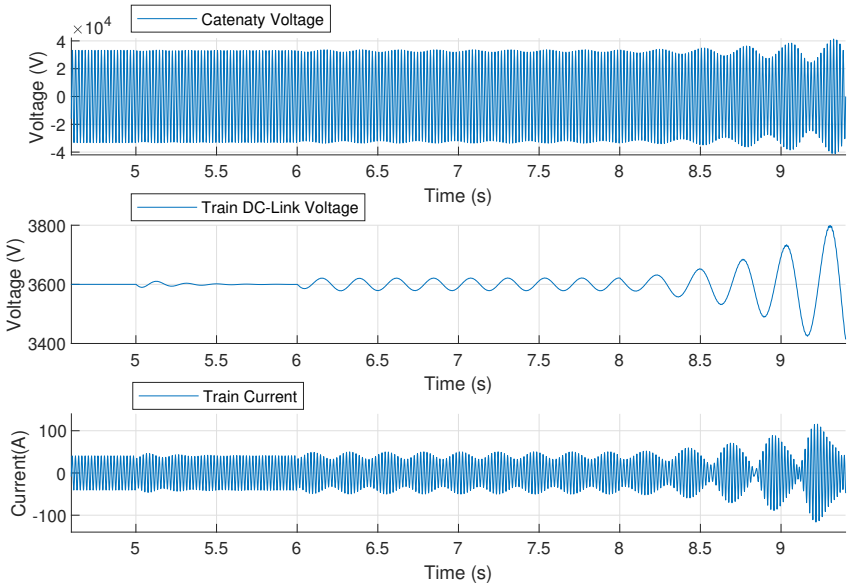

Figure 3.12: Time-domain simulations when the number of trains in depot change as follows: $m = 7$ for $t < 5$ s (initial steady state); $m = 17$ at $t = 5$ s (stable case), $m = 27$ at $t = 6$ s (limit case), $m = 37$ at $t = 8$ s (unstable case).

all the signals ≈ 4.5 Hz, which is seen to be in good agreement with the frequency predicted from the small-signal-based analysis. Finally, following a third step change in the number of trains (i.e. $m = 37$) at $t = 8$ s, the system becomes unstable.

3.3.2 Influence of power consumption at the DC-link

This subsection analyzes the influence of the power consumption. The number of trains and the rest of the electrical and control parameters remain the same as in the previous subsection. The base point for this study is the limit of stability (i.e. GM=0 dB) reached with $m = 27$ identical trains on depot operating at 50 kW each.

As discussed in Section 3.3.1, the eigenvalue λ_2 doesn't pose any risk of instability; therefore, it is not shown. Nyquist plot and Bode diagram of system eigenvalue λ_1 are shown in Figure 3.13 for four different levels of power consumption at the DC-link.

Since the trains are operating at the depot, only auxiliary systems are drawing power. Consequently, the increments of power are relatively small. Figure 3.13(a) shows that increasing the dc-link power consumption improves the system stability. Similarly, Figure 3.13(b) shows that going from 50 kW to 100 kW increases the gain margin, which means the system moves away from the stability limit becoming more

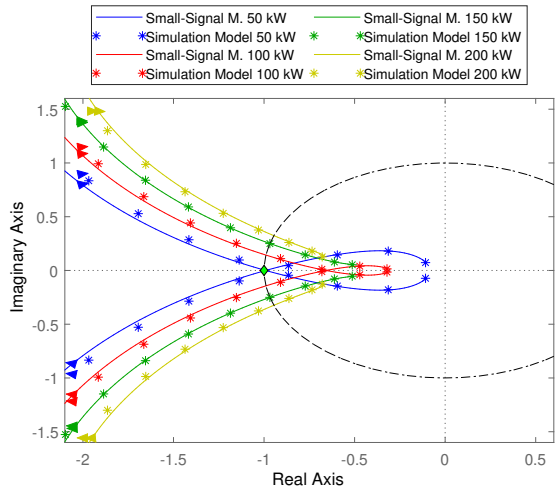

(a) Nyquist Plot

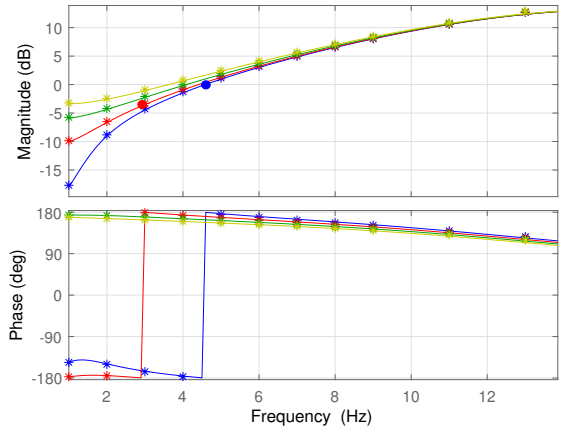

(b) Bode Diagram

Figure 3.13: Critical system eigenvalue λ_1 for different levels of DC-link power consumption. $m = 27$ trains at depot. Analytical small-signal model and frequency swept of the complete simulation model.

stable while it reduces the oscillation frequency. At 150 kW and 200 kW the phase of the eigenvalue λ_1 is below 180°, which means that it never intersects the 180° line at any low frequency, having no risk of LFO instability. The fact that increasing the power increases system stability is in agreement with the results reported in [11, 13, 17, 28].

3.4 Sensitivity Analysis

In this section, the sensitivity analysis of the system stability to train electrical and control parameters using the small-signal model is performed. As in the previous sections, identical trains connected at the depot are considered.

The reference operating point for this analysis is the stability limit case presented in Section 3.3.1 with $m = 27$ trains connected at the depot, operating at a power of 50 kW each. For the sensitivity analysis, variation of the critical eigenvalue λ_1 with incremental variation of a given parameter is obtained, with the rest of the system parameters remaining constant. The range of variation of the parameters being considered is 0.8 to 1.2 from its base value.

Figure 3.14(a) and (b) show the gain margin and oscillation frequency (i.e. phase crossover frequency) as a function of the per unit value of different electrical or control parameter of the train, respectively. At the stability limit operating with nominal values, the gain margin is GM = 1 (i.e. 0 dB), and the oscillation frequency is 4.5 Hz. The slope of each curve gives the sensitivity of the gain margin and oscillation frequency. Positive slopes in Figure 3.14(a) indicate that the system becomes more stable as the parameter being considered increases, the contrary occurs for negative slopes. According to the magnitude of slopes in Figure 3.14(a) LFO shows high sensitivity to L_n, current and voltage control bandwidths, medium sensitivity to current and voltage SOGI, while sensitivity to C_d is low, practically no sensitivity to PLL tuning is observed. Table. 3.2 summarizes the results shown in Figure 3.14.

It is observed that increasing the voltage-control bandwidth ($BWvc$) decreases the gain margin of the system while increasing the current-control bandwidth ($BWcc$) increases the gain margin. This strongly suggests that the spectral separation between current and voltage controller bandwidths improves LFO stability and it will play a critical role in the occurrence of LFO.

Figure 3.14 shows that increasing voltage-SOGI gain increases the gain margin. This result agrees with the analysis presented in Section 2.2.6.1. The voltage-SOGI generates the feedforward signal; therefore, increasing voltage-SOGI gain implies an increase in the voltage filter bandwidth, which decreases feedforward signal delays, improving the system stability. On the hand, increasing the current-SOGI gain increases the gain margin and improves stability because it decreases delays in the current control loop.

Larger values of transformer inductance significantly improve stability, while larger values of capacitance bring the system closer to the stability limit by a small step.

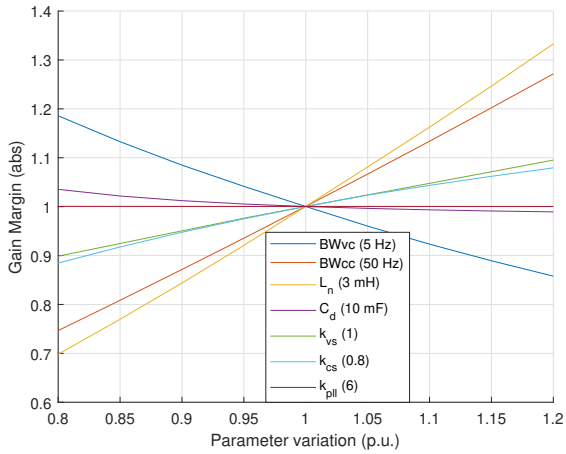

(a) Gain Margin

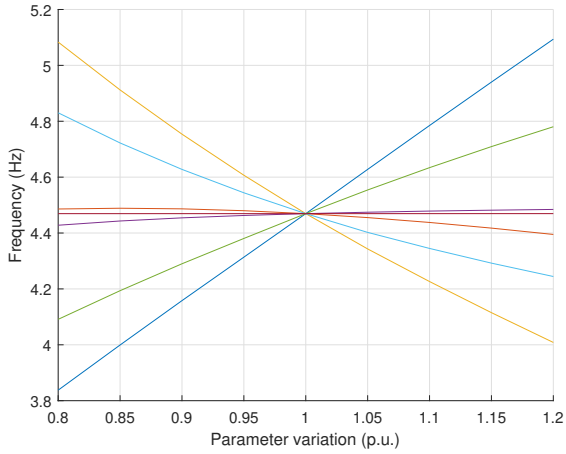

(b) Oscillation Frequency

Figure 3.14: a) Gain Margin of critical system eigenvalue λ_1 and b) oscillation frequency, as a function of p.u. parameter variation

	Gain Margin (GM)	Oscillation Frequency
$BWvc$	$\downarrow\downarrow\downarrow$	$\uparrow\uparrow\uparrow$
$BWcc$	$\uparrow\uparrow\uparrow\uparrow$	$\downarrow$
L_n	$\uparrow\uparrow\uparrow\uparrow\uparrow$	$\downarrow\downarrow\downarrow$
C_d	$\downarrow$	$\uparrow$
k_{vs}	$\uparrow\uparrow$	$\uparrow\uparrow$
k_{cs}	$\uparrow\uparrow$	$\downarrow\downarrow$
k_{pll}	-	-

Table 3.2: Sensitivity of low-frequency stability to train parameters. $\uparrow$ and $\downarrow$ stands for positive sensitivity and negative sensitivity. Number of arrows show the degree of sensitivity.

Finally, it is noted that the trajectories shown in Figure 3.14 are not necessarily straight lines. This is due to the non-linear nature of the system. This suggests that parameter sensitivity when more than one parameter changes might not agree with the results obtained from simple superposition of the effects of changing parameters individually.

3.5 Conclusions

An accurate train small-signal input admittance model was developed and presented in this chapter. The small-signal model was developed in the synchronous frame, and its frequency response matched with the frequency sweep of the simulation of the complete (non-linear) model of the train. Consequently, the small-signal model enables the analysis of the impact of key design and operation parameters on LFO by means of analytical functions. An approximated small-signal model of the QSG-SOGI in the synchronous frame valid in the low-frequency range was calculated and included in the system along with the PLL to model the dynamics due to errors in the coordinate rotation. Models of current and DC-link voltage control systems were also developed.

A stability analysis of the railway system was performed and checked with numerical methods. The different cases were analyzed for different numbers of trains operating at the depot, showing that increasing the number of trains increases the risk of instability.

The train small-signal input admittance model combined with power network impedance was able to predict the appearance of low-frequency oscillation when trains are operating at low power consumption with only auxiliary systems energized.

Finally, using the small-signal model, the sensitivity analysis of the system stability to train electrical and control parameters was presented, showing high sensitivity to the leakage inductance and control bandwidths, medium sensitivity to SOGI, low sensitivity to DC-link capacitance, and practically no sensitivity to PLL.

Chapter 4

Analysis using eigenvalues identification

In this chapter, eigenmodes are used to characterize the system dynamic behavior when the LFO phenomenon occurs. Time-domain simulations of the train-network system are performed to obtain the system dynamics in different scenarios. Then, associated eigenvalues are calculated by means of numerical estimation techniques. System parameters considered for the analysis presented in this chapter include: catenary length; power consumption; characteristics of on-board catenary side converter: current and dc voltage control bandwidths, SOGI, PLL; leakage inductance of the transformer; and DC-link capacitor. The sensitivity of LFO stability to the variation of these parameters is discussed.

The railway system model with train-A from Figure 1.4 is used to perform this analysis. A vehicle with six traction chains is considered. The system parameters are shown in Table 4.1. The power consumed by the vehicle was only 300 kW (low power condition).

Symbol	Description	Value
V_c	RMS Catenary Voltage	25 kV
f_0	Catenary frequency	50 Hz
V_{dc}	Nominal DC-link Voltage	3600 V
k	Transformer Ratio	14.12
L_n	4QC Inductance	6 mH
R_n	4QC Resistance	10 mΩ
C_d	DC-link Capacitance	10 mF
$BWvc$	Voltage Control Bandwidth	10 Hz
$BWcc$	Current Control Bandwidth	100 Hz
k_{vs}	Voltage SOGI Gain	0.80
k_{cs}	Current SOGI Gain	1
k_{pll}	Phase-Locked Loop Gain	6
f_{sw}	Switching Frequency	1000 Hz
f_s	Sampling Frequency	2000 Hz
P_T	Total Power Consumption	300 kW

Table 4.1: Railway system parameters.

4.1 Eigenvalue migration due to catenary-line length

Using time-domain simulations of the train-network system Figure 4.1 is obtained. It shows the transient response to a disturbance of the DC-link voltage, for different lengths of catenary-line. Degradation of DC-link voltage control as the distance increases is readily observed, eventually leading to instability. Transient responses shown in Figure 4.1 can be modeled as a set of complex conjugated eigenvalues as shown in Figure 4.2. The following terms are defined from Figure 4.2: ω_n is the natural frequency, σ is the attenuation constant, and θ is the eigenvalue angle. Using these last two terms, the damping ratio ζ, is defined by (4.1) [48], and the settling time T_s, is defined by (4.2) as the time required by the response to reach and steady within a specified range of 2% of the final value [48]. Notice that the damping ratio is zero when $\theta = \pi/2$, which is the stability limit.

The trajectory followed by the eigenvalues as the catenary length increases shows a decreasing damping coefficient and slowing dynamics, which results in a degradation of the system behavior, eventually becoming unstable.

$$\zeta = \frac{\sigma}{\omega_n} = \cos(\theta) \tag{4.1}$$

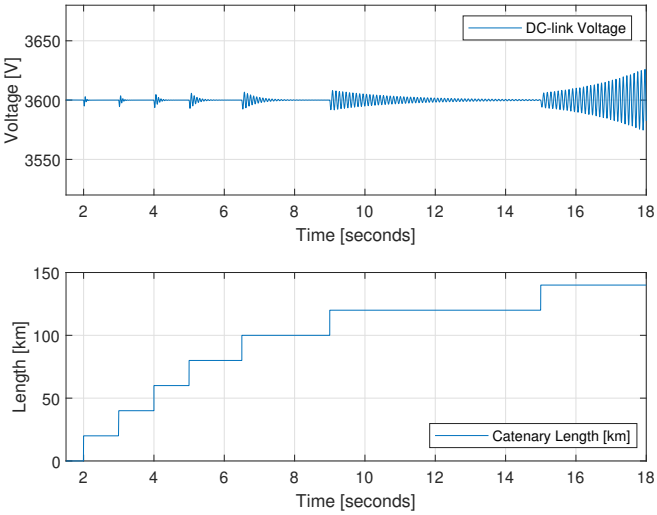

Figure 4.1: DC-link time response for variations in catenary-line length

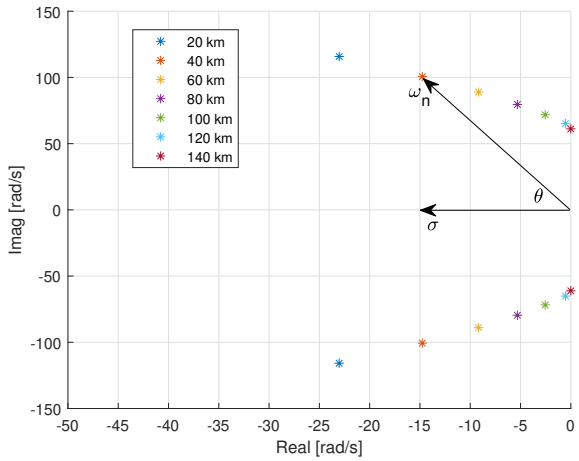

Figure 4.2: Eigenvalue migration as a function of catenary-line length.

$$T_s = \frac{\ln(0.02)}{\sigma} \tag{4.2}$$

4.2 Eigenvalue migration with catenary length and consumed power

Eigenvalue migration with load power is shown in Figure 4.3 for three different catenary lengths, short line (20 km), medium line (60 km), and long line (120 km). It is interesting to note that the overall shape of the eigenvalue trajectory is similar for all three cases. Lower power consumption results in lower damping, i.e. higher instability risk. A closer analysis also reveals that long catenaries combined with low power consumption, lead to the highest risk of instability, which is consistent with the behavior reported in Chapters 2 and 3.

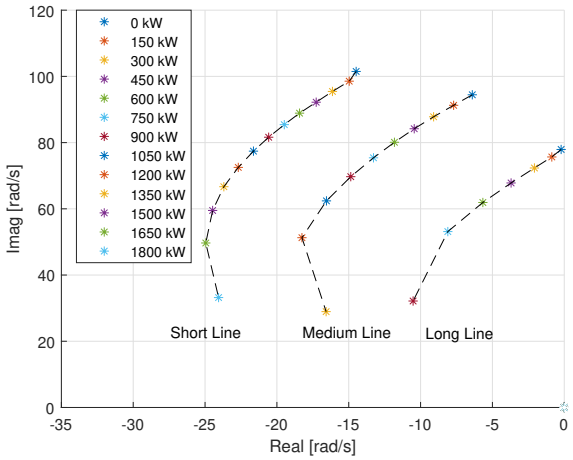

Figure 4.3: Eigenvalue migration for variations in load power. Cases: short line (20 km), medium line (60 km) and long line (120 km).

4.3 Eigenvalue migration with DC-link voltage and current control bandwidths

The influence of the 4QC voltage and current control closed-loop bandwidths is discussed in this section. For the sake of simplicity, four scenarios are considered for

catenary length and power consumption: 1) low distance - low power; 2) low distance - high power; 3) high distance - low power; 4) high distance - high power.

Figure 4.4 shows the eigenvalues for different current-control and voltage-control bandwidths for the long-distance catenary - low power consumption case. The general trend is that for a given current control bandwidth, higher voltage-control bandwidths result in eigenvalue angle θ (as defined in Figure 4.2) closer to $\pi/2$ which means shorter damping ratio and larger settling times (σ decreases) and larger natural frequency. On the other hand, it is observed that for a given voltage control bandwidth, larger current-control bandwidths result in a larger damping ratio, shorter settling times (σ increases), and larger natural frequencies.

From Figure 4.4 it can also be noticed that eigenvalue migration due to simultaneous variation in voltage-control bandwidths and voltage-control bandwidth in this region are close to being orthogonal. It is concluded from Figure 4.4 that rather than the bandwidth of the current and voltage control loops, the ratio BWcc/BWvc will be critical for system stability.

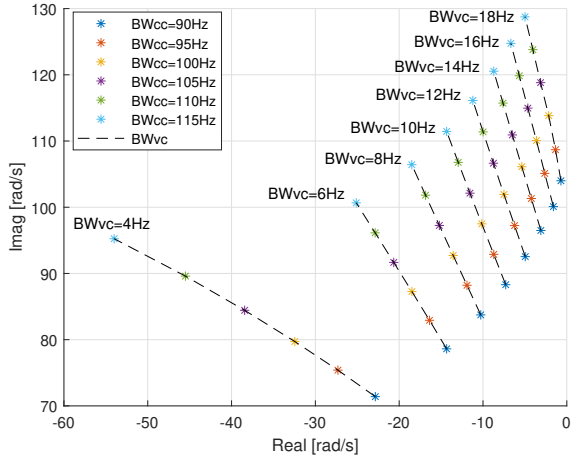

Figure 4.4: Eigenvalue migration as a function of DC-link voltage and current control bandwidths, for the case of a long catenary and low power consumption. BWcc and BWvc stand for current and voltage control bandwidths.

Figure 4.5 to 4.7 shows the damping ratio, settling time, and natural frequency, as a function of BWcc and BWvc, for two different values of the current control bandwidth and the four scenarios discussed at the beginning of this section are considered: 1) low distance - low power; 2) low distance - high power; 3) high distance - low power; 4) high distance - high power. The following conclusions are reached:

- It is observed from Figure 4.5 that the damping ratio (i.e. system stability) always increases as the BWcc/BWvc ratio increases. Low values of the BWcc/BWvc

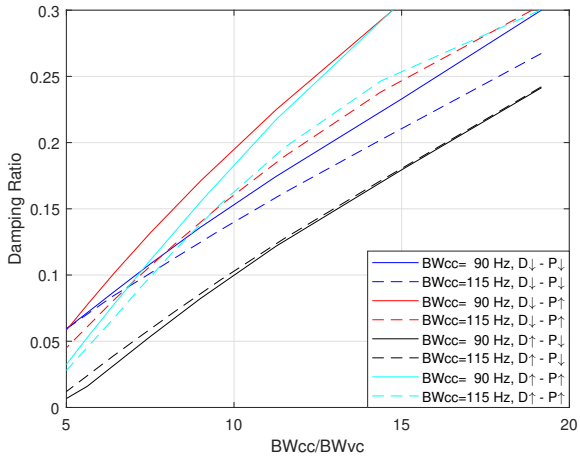

Figure 4.5: Damping ratio as a function of BWcc/BWvc ratio for different current control bandwidths (90 Hz and 115 Hz). D↓ and D↑ stand for low (20 km) and high distance (120 km), P↓ and P↑ stand for low and high power respectively.

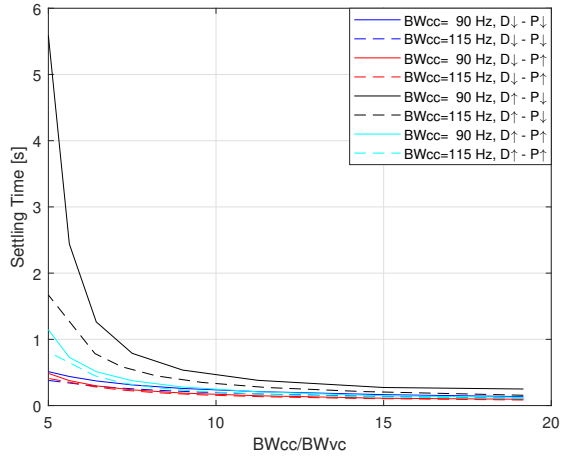

Figure 4.6: Settling Time as a function of BWcc/BWvc ratio for different current control bandwidths (90 Hz and 115 Hz). D↓ and D↑ stand for low (20 km) and high distance (120 km), P↓ and P↑ stand for low and high power respectively.

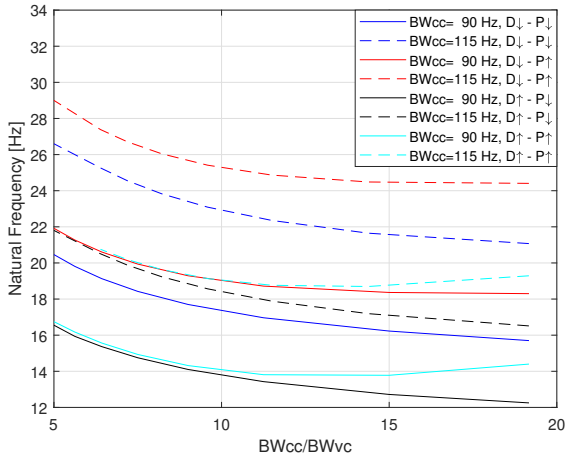

Figure 4.7: Natural Frequency as a function of BWcc/BWvc ratio for different current control bandwidths (90 Hz and 115 Hz). D↓ and D↑ stand for low (20 km) and high distance (120 km), P↓ and P↑ stand for low and high power respectively.

ratio will jeopardize system stability for any operation mode. This trend is independent of the catenary distance and load power.

- From Figure 4.5, it is observed that high distance - low power scenario shows the highest risk of instability (lower damping ratio). The damping ratio is seen to change linearly with BWcc/BWvc, independent of BWcc.

- The damping ratio increases when the load power level increases and decreases when the catenary-line increases. This behavior is consistent with previous studies [13].

- It is observed from Figure 4.6 that the settling time of the oscillations decreases as BWcc/BWvc increases. Low BWcc/BWvc ratios in the high distance - low power scenario values result in significant settling times, i.e. DC-link voltage oscillation can persist for seconds.

- The natural frequency shown in Figure 4.7 decreases as the BWcc/BWvc ratio increases in most cases, but differences by a factor of 2 can be observed depending on the scenario.

4.4 Eigenvalue migration due to the leakage inductance of transformer and DC-link capacitor

In this section, variations in the leakage inductance are introduced while the control gains k_{pCC} and k_{iCC} are re-tuned according to (1.2) and (1.3) to maintain the current regulator bandwidth constant at a value of 100 Hz. Similarly, variations in the DC-link capacitance are introduced while the voltage control gains k_{pVC} and k_{iVC} are re-tuned to maintain a constant bandwidth of 10 Hz according to (1.4) and (1.5).

The analysis is performed for the case of a catenary length of 120 km and a power consumption of 300 kW. In this operating conditions the system is close to the stability limit.

Figure 4.8 shows the eigenvalue migration as a function of the transformer leakage inductance and the DC-link capacitance. Range of variation of the leakage inductance and capacitance are indicated in the caption.

It is observed that larger values of inductance improve stability against LFO, while larger values of the capacitance move the system towards to the stability limit. The eigenvalue migration due to inductance changes is seen to be highly linear. On the other hand, eigenvalue migration due to capacitance changes is monotonic (the variations of eigenvalues decreases as the capacitance increases). Furthermore, it is seen that variations of inductance and capacitance do not interfere with each other when control bandwidths are maintained constant.

Figure 4.9 shows a zoomed view of eigenvalue migration due to the DC-link capacitance variations at $L_n = 6$ mH. Here, the capacitance range of variation is wider than before (from 0.4 to 1.6 its nominal value). The figure is showing how the sensitivity of eigenvalues decreases as the capacitance increases, for instance, it is very difficult to note changes in the system dynamics for capacitance values over 150% its nominal value. Similar behavior was reported in Section 2.2.5.3. In conclusion, Figure 4.9 shows the sensitivity of the system for small capacitance is high, around the operational point (O.P.) is low, and it is very low for larger capacitances. Details of sensitivity analysis is performed in Section 4.7.

Although greater values of inductance improve stability, designing a transformer to get a larger value of leakage inductance could limit the power transfer capability. Smaller values of capacitance improve the low-frequency stability, which is an advantage since bigger capacitors are bulky and expensive; however, the DC-link capacitance has to be big enough to ensure the correct operation of the 4QC (i.e. system controllability) and to filter the voltage ripple.

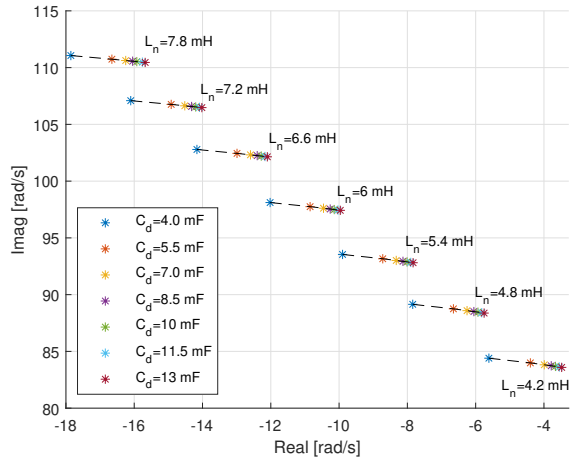

Figure 4.8: Eigenvalue migration as a function of leakage inductance and DC-link capacitance. The inductance is increased in steps of $\Delta L_n = 0.6$ mH, from $L_n = 4.2$ mH to $L_n = 7.8$ mH. The DC-link capacitance is increased in steps of $\Delta C_d = 1.5$ mF, from $C_d = 4$ mF to $C_d = 13$ mF.

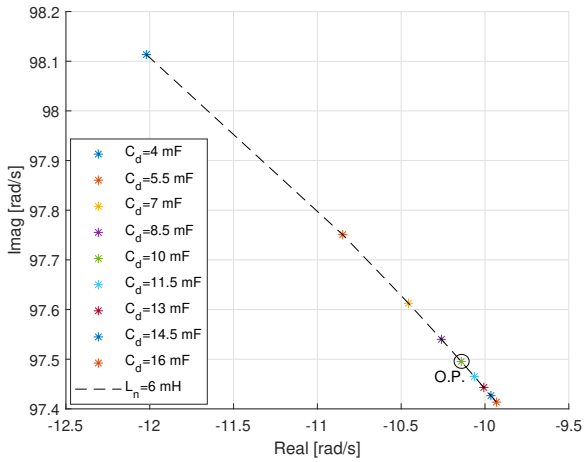

Figure 4.9: Eigenvalue migration as a function of DC-link capacitance. The leakage inductance is constant $L_n = 6$ mH. The DC-link capacitance is increased in steps of $\Delta C_d = 1.5$ mF, from $C_d = 4$ mF to $C_d = 16$ mF.

4.5 Eigenvalue migration with SOGI tuning

In addition to the control bandwidths discussed previously, other elements involved in the control are the voltage and current SOGI. The transfer function of the SOGI acting as a filter is given by (3.18), and its transfer function acting as a quadrature signal generator is given by (3.19).

Figure 4.10 shows the eigenvalue migration for variations in gains k_{vs} and k_{cs} of voltage and current SOGI. Increasing either voltage or current SOGI gain migrates the eigenvalues away from the stability limit (i.e., larger damping ratio). However, increasing SOGI gain implies an increase in the bandwidth, which could compromise the SOGI low-pass filter characteristic. It is concluded that a trade-off is required.

These results agree with the analysis presented in Section 2.2.6.1. The voltage-SOGI generates the feedforward signal; therefore, increasing SOGI gain decreases feedforward signal delays, which improves stability. On the other hand, increasing the current-SOGI gain decreases delays in the current control loop, which is better for the system stability.

Sensitivity analysis of SOGI is performed in Section 4.7.

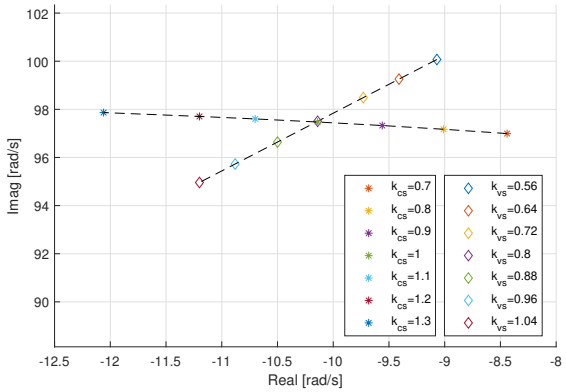

Figure 4.10: Eigenvalue migration for variations in gains k_{vs} and k_{cs} correspond to voltage and current SOGI. The gains are varied within a range of 0.7 to 1.3 of their nominal values, k_{vs}=0.8 and k_{cs}=1.

4.6 Eigenvalue migration with PLL tuning

Figure 4.11 shows eigenvalue migration for variations in the proportional gain k_{PLL}. As mentioned in Section 1.2.3.1, the integral gain was chosen as k_{iPLL}=$k_{PLL}^2/2$.

Increasing k_{PLL} by a factor as large as ten is seen to have a marginal effect on the migration of eigenvalues. A sensitivity of PLL is performed in Section 4.7.

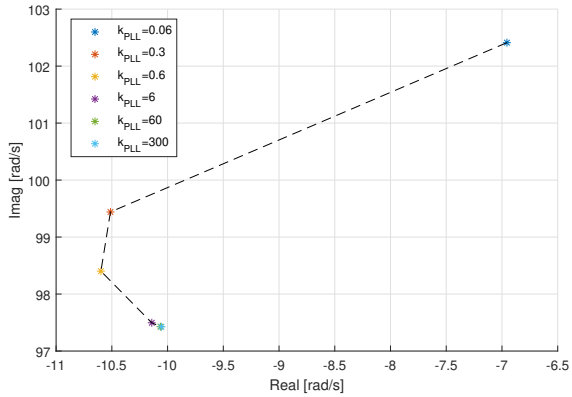

Figure 4.11: Eigenvalue migration for variations in gain k_{PLL}

4.7 Sensitivity analysis

An approach to analyze the sensitivity to system parameters discussed in the previous subsections is to obtain the variation of the eigenvalues to an incremental variation of a given parameter, with the rest of system parameters remain constant.

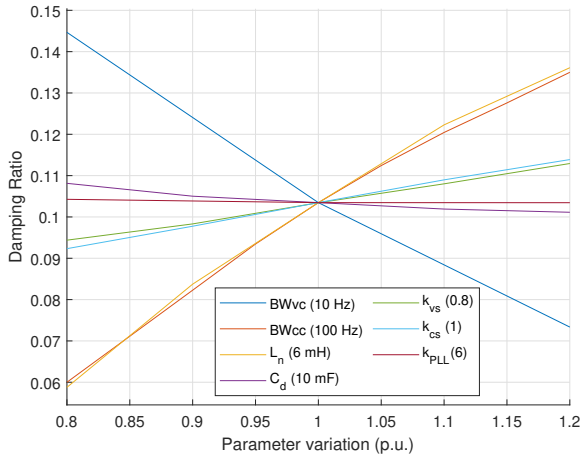

Figure 4.12: Damping ratio as a function of p.u. parameter variation

Figure 4.12 to 4.14 show the variation of damping ratio, settling time, and natural frequency, which results from this analysis. The analysis is performed for the case of a catenary length of 120 km and a power consumption of 300 kW. The system is in

this case close to the stability limit. System parameters being considered are changed within a range of 0.8 to 1.2 from their base value.

From Figures 4.12 to 4.14 the magnitude of the slope of each curve at the operational point (O.P) gives the sensitivity of the damping ratio, settling time, and natural frequency to per-unit (p.u.) variation of each parameter being considered with respect to its base value. For the damping ratio, positive slopes indicate that the system becomes more stable as the parameter being considered increases, the contrary occurs for negative slopes. Natural frequency is related to oscillation frequency at the stability limit, positive slopes indicate faster oscillations.

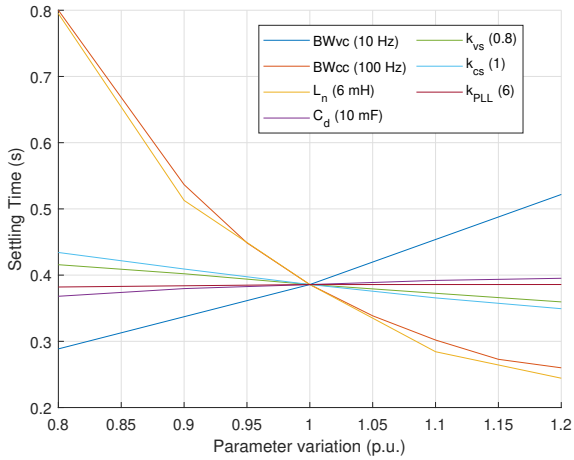

Figure 4.13: Settling time as a function of p.u. parameter variation

Table 4.2 summarizes the results shown in Figure 4.12 to 4.14. It is observed that for the operating point being considered, LFOs show high sensitivity to L_n and control bandwidths, while sensitivity to SOGI parameters and C_d is low, practically no sensitivity to PLL tuning is observed.

Increasing the voltage-control bandwidth decreases the damping of the system, while increasing the current-control bandwidth, increases the damping of the system. Rather than the absolute values of the current and voltage control bandwidths, the system response is primarily given by the ratio BWcc/BWvc. This is in accordance with the analysis presented in Section 4.3. It is concluded that lower values of BWcc/BWvc significantly increase the risk of LFO.

Finally, it is noted that the trajectories shown in Figure 4.12 to 4.14 are not necessarily straight lines. This is due to the non-linear nature of the system. This suggests that parameter sensitivity will depend on the operating point. Same conclusion was achieved in Chapter 3 from the study using small-signal models.

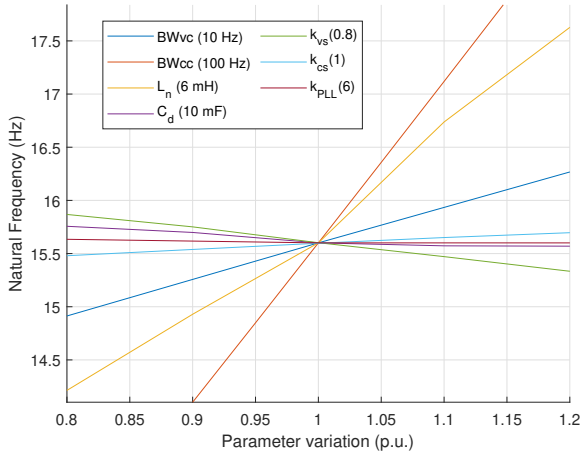

Figure 4.14: Natural Frequency as a function of p.u. parameter variation

Table 4.2: Sensitivity of dynamic system characteristics at O.P. Arrows ↑ and ↓ stands for positive sensitivity and negative sensitivity. The number of arrows indicates the degree of sensitivity.

	Damping R.(ζ)	Settling T.(T_s)	Natural Freq. (ω_n)
BWvc	↓↓↓	↑↑↑	↑↑↑
BWcc	↑↑↑	↓↓↓	↑↑↑↑
L_n	↑↑↑	↓↓↓	↑↑↑↑
C_d	↓	↑	↓
k_{vs}	↑↑	↓↓	↓↓
k_{cs}	↑↑	↓↓	↑
k_{PLL}	-	-	-

4.8 Conclusions

Time-domain simulation combined with eigenvalue migration analysis is proposed in this chapter for the analysis of LFO phenomenon in AC railway systems. The proposed method allows an insightful visualization of the sensitivity of LFO to catenary and train parameters, and consequently identifying critical modes of operation, as well as to propose remedial actions.

It is concluded from the analysis performed in this chapter that the worst scenario for LFO stability occurs for the case of trains operating far from substation and with low-power consumption. Catenary inductance (i.e. infrastructure parameter) and BWcc/BWvc ratio (i.e. AFE control parameters) are the main two factors affecting to system stability.

Larger values of transformer inductance improve stability against LFO, while larger values of the the capacitance take the system closer to the stability limit. The eigenvalue migration due to inductance increments is linear. On the other hand, migration due to capacitance is monotonic (the variations of eigenvalues decreases as the capacitance increases). Finally, variations of inductance and capacitance do not interfere with each other when control gains are adapted to keep the bandwidths constant.

Increasing SOGI gain, increases the filter bandwidth, which decreases system delays (i.e. faster dynamics). This action improves LFO stability.

Chapter 5

4QC control strategies for LFO mitigation

LFO mitigation can be addressed by either improving the power supply systems or the onboard systems. Among the first, [49] and [50] proposed either the installation of voltage stabilizers in the substations or the capacity upgrade of the traction transformer. However, a replacement or modification of substations of which the vast majority still have many years of useful lifetime places obvious cost concerns [51]. Improving the onboard systems is therefore a more appealing option. Two approaches can be followed.

- Improve 4QC converter control tuning in order to increase the stability limit (i.e. maximum number of trains or distance). This action can be performed according to the results obtained in parameter variation studies from Chapters 2 and 4.
- Adding supplementary controllers to the actual 4QC control system.

This chapter addresses the second option. More specifically, it describes the implementation of two controllers in the train aimed specifically to mitigate the LFO phenomenon: Power oscillation damping (POD), which is presented in Section 5.1, and the Virtual-impedance-based control method presented in Section 5.2. For this study, train-A with the parameters presented in Table 3.1 from Section 3.2.5 is employed.

5.1 Power oscillation damping (POD)

The power oscillation damping method is a technique used in electrical power systems to stabilize the system and mitigate the effects of power oscillations [52–56].

The POD control continuously monitors the electrical parameters of the power grid, such as voltage and current. It detects the presence of power oscillations. These oscillations are often characterized by fluctuations in voltage or power flow, and they can occur due to various factors, including sudden changes in load or the integration of renewable energy sources. Upon detecting oscillations, the control system activates specialized devices within the grid. These devices are capable of injecting or absorbing active and/or reactive power [52, 56].

This method is particularly valuable in power grids with a high penetration of renewable energy sources (such as wind or solar). These sources can introduce variability and uncertainty, leading to power oscillations that need to be controlled [52]. Furthermore, POD control has been employed in large and interconnected power grids where the oscillations can propagate over long distances and affect the entire network [52, 54].

In [8] and [53] POD was implemented in a controlled rectifier connected to a weak grid. In this case, the POD control system consists of an external loop connected to the converter DC-link control system. The RMS value of the PCC voltage is used as the input signal of the control structure to detect the oscillations. In this chapter, a similar POD structure is implemented; however, the d-axis of the PCC voltage will be used instead of its RMS value, improving computational time and taking advantage of having the converter controllers in the *dq*-frame. Before describing the control method, the concepts of constant power operation and power conservation in the 4QC are described below.

5.1.1 Constant input power operation

From the Train-A system, see Figure 1.4, the train input power is defined in the RMS domain and in the *dq*-frame by (5.1) and (5.2), respectively.

$$P_{ac} = v_{nRMS}\, i_{nRMS} \cos\varphi \tag{5.1}$$

$$P_{ac} = v_{nd} i_{nd} + v_{nq} i_{nq} \tag{5.2}$$

Since the controller will force the input voltage vector to be aligned with the d-axis of the synchronous frame, then $v_{nq} = 0$; furthermore, it is assumed that in the steady state, the train operates with unity power factor (i.e. $\cos\varphi = 1$ and $i_{nq0} = 0$). Therefore, the input active power can be expressed by (5.3).

$$P_{ac} = v_{nRMS} i_{nRMS} = v_{nd} i_{nd} \tag{5.3}$$

The input active power can be obtained using the RMS value of AC quantities, or using *dq* quantities (5.3), the last option was chosen in this chapter.

In order to study the small-signal dynamics of the input power P_{ac}, (5.4) is obtained using partial derivation.

$$\delta P_{ac} = i_{nd0} \delta v_{nd} + v_{nd0} \delta i_{nd} \tag{5.4}$$

An important factor that influence instability of railway systems is constant power operation. Considering the train controllers are in charge of maintaining the input power P_{ac} constant, consequently $\delta P_{ac} = 0$. Solving (5.4) under this condition, the input admittance is shown to be negative (5.5), which means that under constant power operation, the railway system may be unstable [17, 38].

$$Y_t = \frac{\delta i_n}{\delta v_n} = -\frac{i_{nd0}}{v_{nd0}} \tag{5.5}$$

Equation (5.5) shows that input admittance at specific power depends on input voltage and input current operating point (v_{nd0}, i_{nd0}). Notice that the value of v_{nd0} is positive by definition, while i_{nd0} is positive if the train is demanding power and negative if it is returning energy to the supply network (i.e. regenerative braking). Therefore, negative admittance (risk of instability) appears only when the vehicle demands energy.

5.1.2 Power conservation

As explained in Section 3.2.4.1, the AC-side filter impedance of the 4QC is mainly inductive ($R_n \approx 0$); furthermore, commutation loses in the converter are neglected. Then, power conservation between the converter AC-side and DC-side can be assumed according to (5.6).

$$P_{dc} \cong P_{ac} \tag{5.6}$$

Considering the active power in the DC-link capacitor is zero due to its voltage being controlled; then, the traction load power $P_L \cong P_{dc}$, and (5.7) can be assumed.

$$P_L \cong P_{ac} = v_{nd} i_{nd} \tag{5.7}$$

If the traction motor at DC-link operates as a constant power element, the input power P_{ac} will try to be a constant value due to power conservation.

Equation (5.7) can be expressed in terms of DC-link voltage and load current as shown by (5.8). For a constant current demand (i.e. load is a constant current source), and taking into account the voltage controller forces the DC-link voltage to be constant, the input power will try to be constant as well.

$$v_{dc} i_L \cong P_{ac} = v_{nd} i_{nd} \tag{5.8}$$

Finally, considering the traction load as a resistance, (5.9) can be used. In this case, for a constant load R_L, and considering the DC-link voltage will try to be constant due to the control action, the input power will also become constant.

$$\frac{v_{dc}^2}{R_L} \cong P_{ac} = v_{nd} i_{nd} \tag{5.9}$$

In conclusion, independent that the traction load is modeled as a constant power element, constant current source, or resistive element, the controllers will force DC-link voltage v_{dc} to reach the voltage reference $v_{dc}^{*} = cte$, which provokes constant power operation. For the study of LFO, the dynamic of traction load is not really an influencing factor in comparison with dynamics of 4QC inner current controller and outer voltage controller [6,13]. In this study, the traction load is modeled as a resistive element.

5.1.3 POD control system action

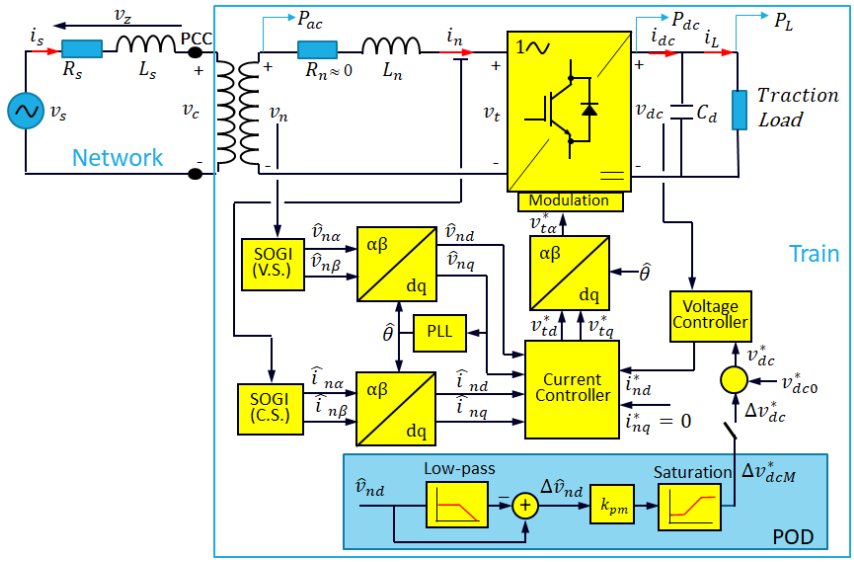

Figure 5.1: Power oscillation damping control system by modulation of the DC-link voltage

Figure 5.1 shows a train using the power oscillation damping control system based on modulation of the DC-link voltage. This control structure uses the estimated value of the d-axis input voltage $\widehat{v}_{nd}$ that oscillates in phase with the RMS catenary-line voltage. As shown in Figure 5.1, the DC-part of the estimated input voltage is removed, keeping only the oscillations (i.e. $\Delta\widehat{v}_{nd}$), which are scaled by the gain k_{pm} to finally being added to the DC-link voltage reference v_{dc}^{*}.

The working principle of POD can be explained in terms of constant power operation. When the LFO phenomenon occurs, input voltage oscillation and input current oscillation are opposite, which means that if the input voltage v_n increases, the input current i_n decreases. Conversely, if the input voltage decreases, the input current increases. This is equivalent to say that the train has a negative input admittance as already explained in Section 5.1.1. The POD control system modifies the constant

power dynamics: if now the input voltage increases, the DC-link reference voltage will increase as well, and hence the input current reference will also increase, and vice versa. Therefore, the system is trying to compensate the constant power characteristic, leading to the real part of train admittance being zero or positive.

5.1.4 POD simulation results

Simulation results using POD control are shown in Figure 5.2. This test is performed when the train is operating far from the substation during coasting (i.e. moving under its own momentum, with the motor demanding very low-power or not at all).

Initially, the system is in a steady state when the train is located at 130 km away from the substation. Train power consumption is 300 kW (i.e. low power condition). At $t = 4$ s, a step change in the distance is applied in order to reach the stability limit at 150 km. At this point, low-frequency oscillations around 6 Hz appear in the railway system. Note that oscillations in the input voltage v_{nd} and the input current i_{nd} are out of phase nearly 180° (i.e. when the input voltage increases, the input current decreases, and vice versa), which means that at this point of operation (v_{nd1}, i_{nd1}) the train presents a negative input admittance as already explained.

Until now, the voltage controller is trying to keep a constant DC-link voltage. When POD control is turned on at $t = 6$ s, modulation of DC-link voltage reference by POD starts. The DC-link voltage reference is seen to follow the input voltage oscillations, which stops train controllers from forcing constant power operation as explained in Section 5.1.3.

The POD control takes less than 0.5 s to stabilize the system, reaching a new steady state. Notice that although the input power is the same, the train is operating at a different input voltage and input current operating point (v_{nd2}, i_{nd2}) due to a change in catenary-length impedance. The operating point in DC-link voltage and load current is still the same.

At $t = 9$ s, POD control is turned off, and the train-network system becomes unstable again.

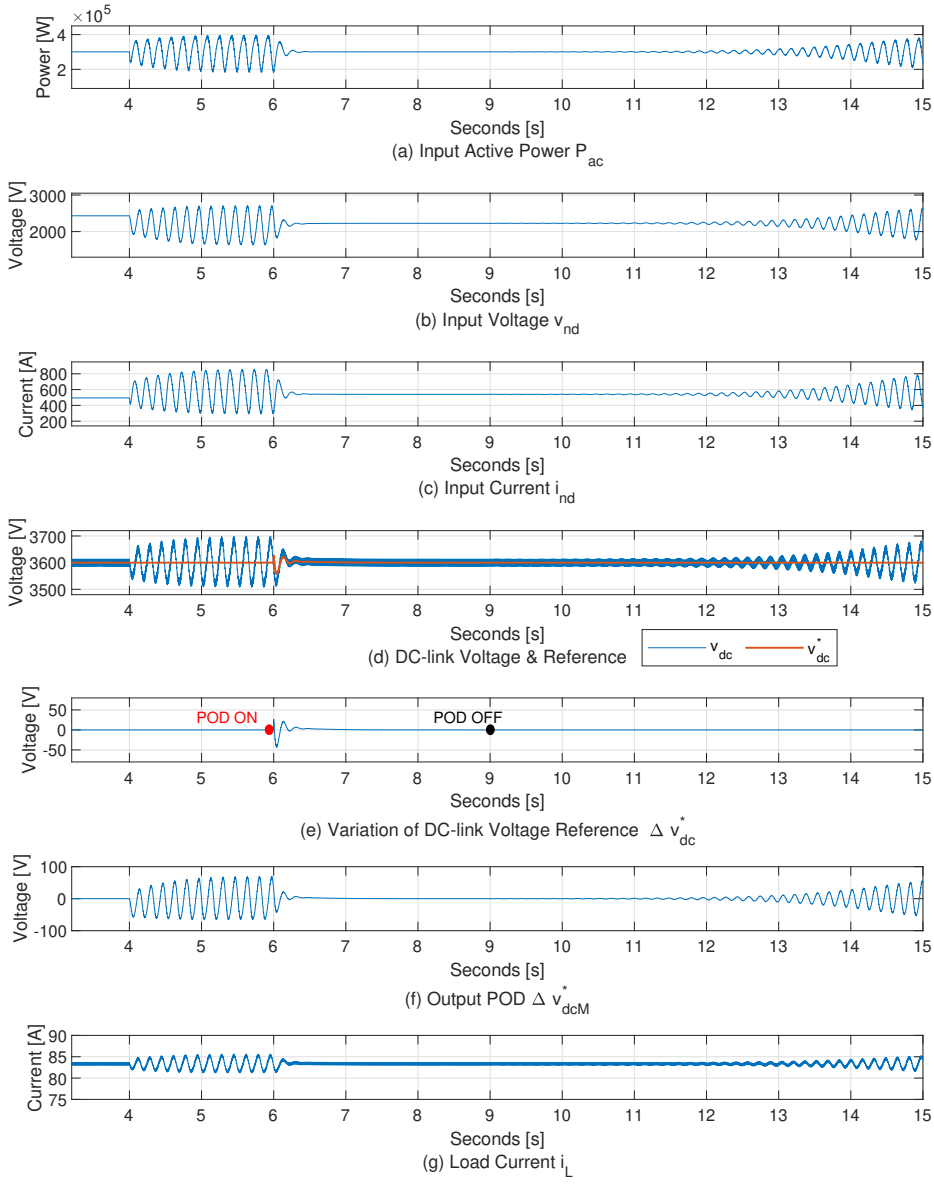

Figure 5.2: Power oscillation damping control test. Power consumption 300 kW. Distance increases (step change) from 130 km to 150 km at $t = 4$ s. POD control is turned on at $t = 6$ s and turned off at $t = 9$ s.

5.2 Virtual-impedance-based control method

Virtual-impedance-based control is a strategy used in power systems and electronics to manage the interactions between various components, such as inverters, converters, and loads. This technique is used to regulate power flow [57, 58], improve stability [59–61], and enhance the overall performance of these systems [62–64]. In this section, this control method consists of creating by software a virtual impedance, which is connected in series with the train input port as shown by Figure 5.3(a) to increase the system damping. The series virtual impedance is implemented based on the feedback of the current as explained below.

5.2.1 Virtual impedance calculation

Initially, the AC-side 4QC dynamics of the converter corresponds to an RL system, shown by (5.10)

$$\mathbf{V_n} = \mathbf{Z_n}\mathbf{I_n} + \mathbf{V_t} \tag{5.10}$$

The 4QC terminal voltage vector $\mathbf{V_t}$ is given by (5.11), where $\mathbf{G_d} = G_d(s)\mathbf{I}$ is the delay transfer function matrix (i.e. computation time and zero-order hold delays) already defined by (3.47) and (3.48) in Section 3.2, and $\mathbf{V_t^*}$ is the voltage command generated by the controllers.

$$\begin{aligned} \mathbf{V_t} &= \mathbf{G_d}\mathbf{V_t^*} \\ &= \mathbf{G_d}(\mathbf{V_{t1}^*} + \mathbf{V_{t2}^*}) \end{aligned} \tag{5.11}$$

$$\mathbf{V_{t1}^*} = \mathbf{G}_{\omega_0 \mathbf{L_n}}\mathbf{I_n} - \mathbf{G_{cc}}(\mathbf{I_n^*} - \mathbf{I_n}) + \widehat{\mathbf{V}}_\mathbf{n} \tag{5.12}$$

$$\mathbf{V_{t2}^*} = \mathbf{G_{vir}}\mathbf{I_n} \tag{5.13}$$

The voltage command $\mathbf{V_t^*}$ comes from two controllers. The first one, $\mathbf{V_{t1}^*}$ (5.12), comes from the current controller and feedforward voltage $\widehat{\mathbf{V}}_\mathbf{n}$. The second command $\mathbf{V_{t2}^*}$ (5.13), is generated by the controller $\mathbf{G_{vir}}$, which emulates the dynamics of the virtual admittance $\mathbf{Z_{vir}}$ defined by (5.14).

$$\mathbf{Z_{vir}} = \mathbf{G_d}\mathbf{G_{vir}} \tag{5.14}$$

Using (5.11) to (5.14) in (5.10), results in the dynamic equation (5.15) that models the 4QC AC-side LR circuit in series with the virtual impedance as shown in Figure 5.3(a).

$$\mathbf{V_n} = \mathbf{Z_n}\mathbf{I_n} + \mathbf{Z_{vir}}\mathbf{I_n} + \mathbf{G_d}\mathbf{V_{t1}^*} \tag{5.15}$$

Figure 5.3(b) shows the schematics of the current control system including the virtual-admittance-based control. The current controller transfer function matrix $\mathbf{G_{cc}}$

using PI controllers, was already defined in (3.41) in Section 3.2, as well as the cross-coupling decoupling matrix $\mathbf{G}_{\omega_0 \mathbf{L_n}}$ (3.43).

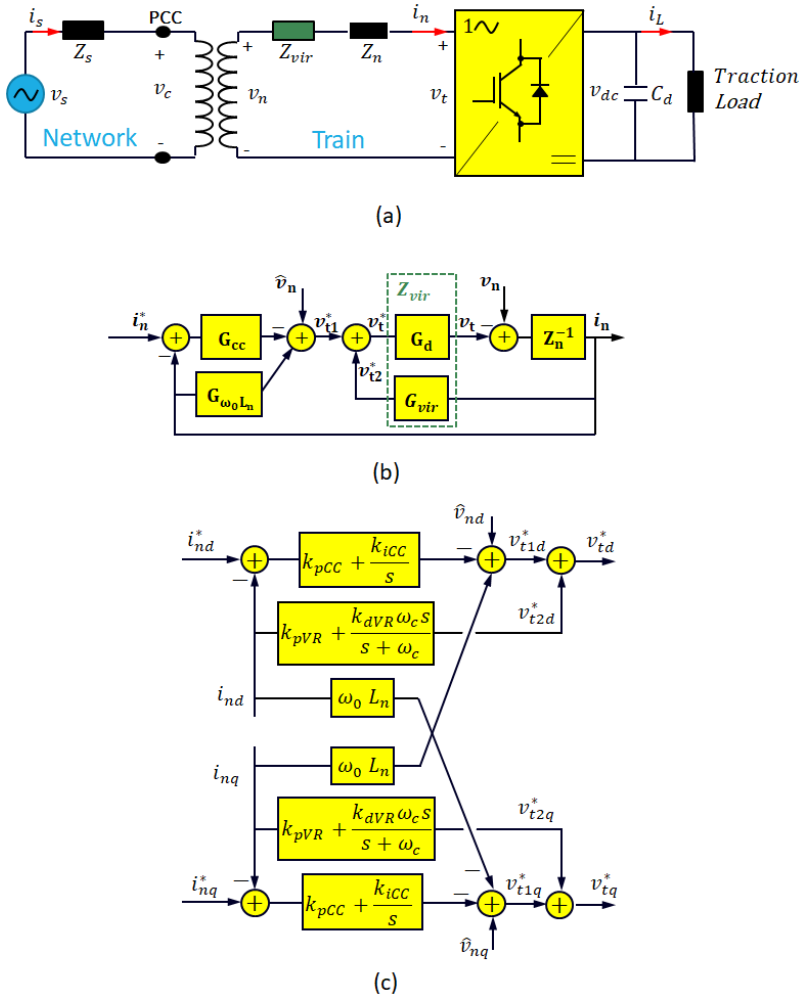

Figure 5.3: Diagrams of virtual-impedance-based control method. (a) Railway system with a series virtual impedance in the AC-side of the 4QC (b) Schematics of the closed-loop control system with input admittance control (c) Detailed PI current controller with PD+filter controller to generate virtual impedance dynamics.

The transfer function matrix $\mathbf{G_{vir}}$ was chosen to be a proportional derivative controller (5.16), the reason will be explained later, being k_{pVR} the proportional gain, and k_{dVR} the derivative gain.

$$\mathbf{G_{vir}} = \begin{bmatrix} k_{pVR} + k_{dVR} s \frac{\omega_c}{s+\omega_c} & 0 \\ 0 & k_{pVR} + k_{dVR} s \frac{\omega_c}{s+\omega_c} \end{bmatrix} \tag{5.16}$$

To avoid the sensitivity to noise of the PD controller due to the increase of the gain with frequency, a low-pass filter is added, where ω_c is the cut-off frequency. As characteristic harmonics of the 4QC are around $2f_0$, the cut-off frequency of the low pass filter should be set below this frequency, in this case, 80 Hz was chosen. In the low-frequency range, the low-pass filter does not influence the compensation effect, and the delay transfer function is considered $G_d(s) \approxeq 1$. Therefore, at low frequencies, the virtual impedance can be approximated by (5.17).

$$Z_{vir}(s) = G_d(s) G_{vir}(s) = R_{vir} + L_{vir} s \quad \approxeq \quad k_{pVR} + k_{dVR} s \tag{5.17}$$

The last equation shows that the proportional gain of the controller simulates a virtual resistance meanwhile the derivative gain simulates a virtual inductance.

Figure 5.3(c) shows in detail the PI current controller with the PD controller and its filter in the *dq* reference frame.

5.2.2 Simulation results of virtual-impedance-based control

Adding resistance to a series impedance implies adding damping to the system. Parameter variation and sensitivity analysis performed in Sections 2.2.4 and 3.4, respectively, showed that increasing the 4QC inductance improves system instability. Therefore, the virtual-impedance-based control test is considering the following cases:

a) $k_{pVR} = 0.150$ & $k_{dVR} = 0.012$ - Virtual resistance and inductance

b) $k_{pVR} = 0.150$ & $k_{dVR} = 0.000$ - Only virtual resistance

c) $k_{pVR} = 0.000$ & $k_{dVR} = 0.012$ - Only virtual inductance

Case a) considers virtual admittance with resistance and inductive parts, in case b) only virtual resistance is used and in case c) only virtual inductance is applied.

This test is shown in Figure 5.4, it is performed when the train is operating far from the substation during coasting, demanding only 300 kW, which are the same conditions in the POD test shown in Subsection 5.1.4. Same as in the POD test, the system is in the steady state when the train is located at 130 km away from the substation. At $t = 4$ s, a step change in the distance is applied in order to reach the stability limit at 150 km. At this point, low-frequency oscillations around 6 Hz appear in the railway system.

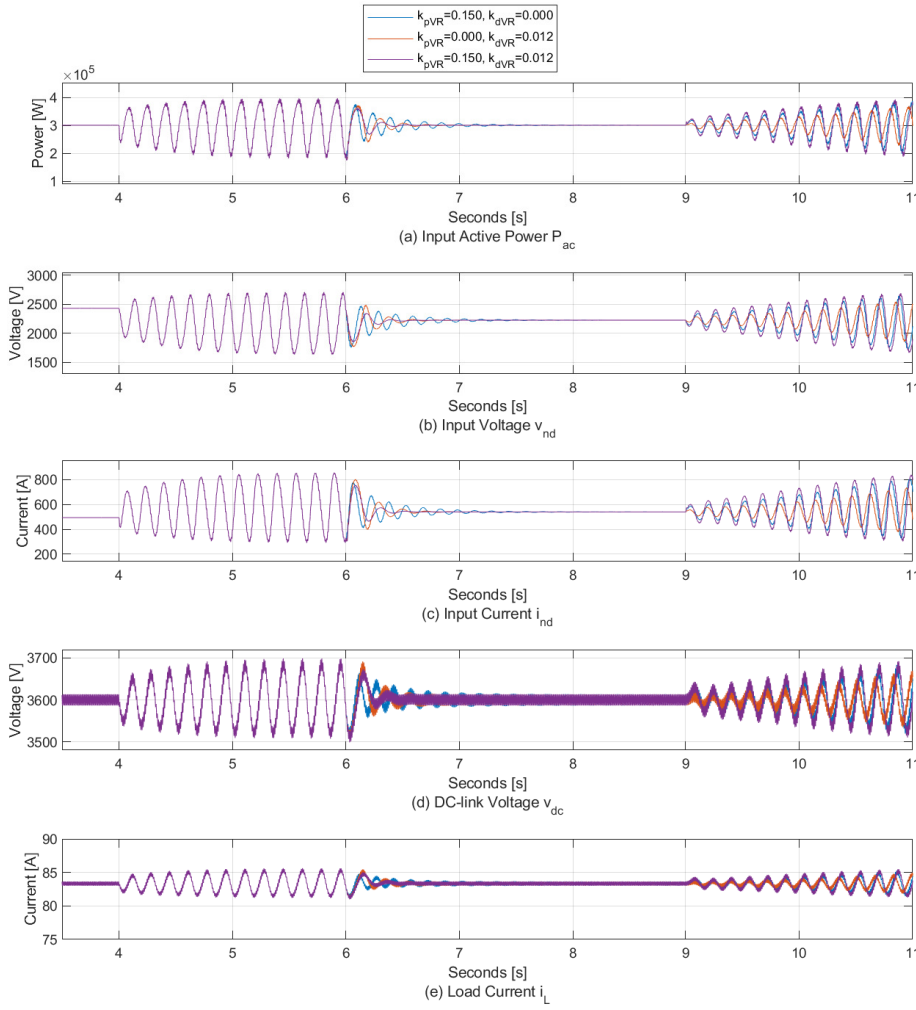

Figure 5.4: Virtual-impedance-based control test. Power oscillation damping control test. Power consumption 300 kW. Distance increases (step change) from 130 km to 150 km at $t = 4$ s. POD control is turned on at $t = 6$ s and off at $t = 9$ s.

The virtual-impedance-based control is turned on at $t = 6$ s, introducing additional damping to the system and making the system stable again. In Case (a) the control action takes less than 0.5 s to stabilize the system, case (b) takes around 0.6 s and case (c) takes more than 1 s. Therefore, a virtual impedance with restive and inductive elements seems to be the best option. Different values of virtual resistance and inductance could be considered for testing; however, this could be a matter of future work.

After the system reaches a new steady state, the operating point of input voltage and input current is different than before due to catenary-line change.

At $t = 9$ s, the control action is turned off, and the train-network system becomes unstable again.

Figure 5.5 shows the controller output signals v^*_{t2d} and v^*_{t2q} of the simulation test to obtain the operational point at steady state. An additional case considering half of the proportional gain was added. As noticed, when the controller is activated (between $t = 8$ s and $t = 9$ s), the operational point depends on the proportional gain. The influence of the derivative gain can be seen on transients.

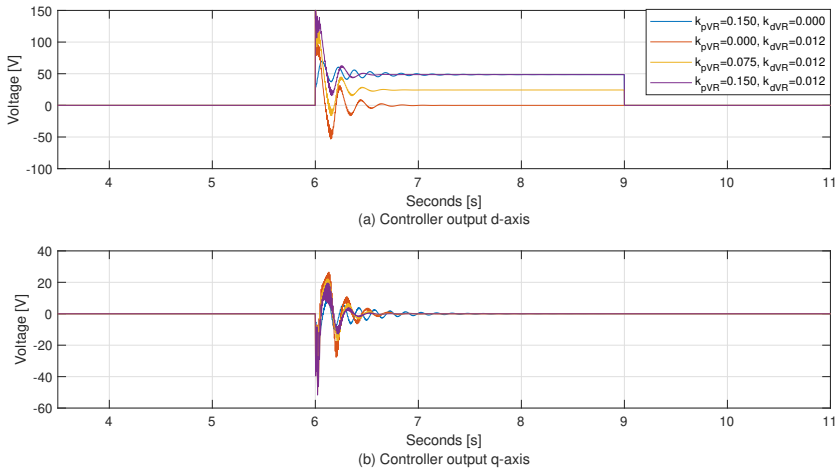

Figure 5.5: Virtual-impedance-based control test. Controller output signals v^*_{t2d} and v^*_{t2q}

5.3 POD vs Virtual-impedance-based control

Figure 5.6 shows the comparison of the tests performed for the POD and virtual-impedance-based control systems already presented in Section 5.1.4 and Section 5.2.2, respectively. Only the case with virtual resistance and inductance was considered for the comparison.

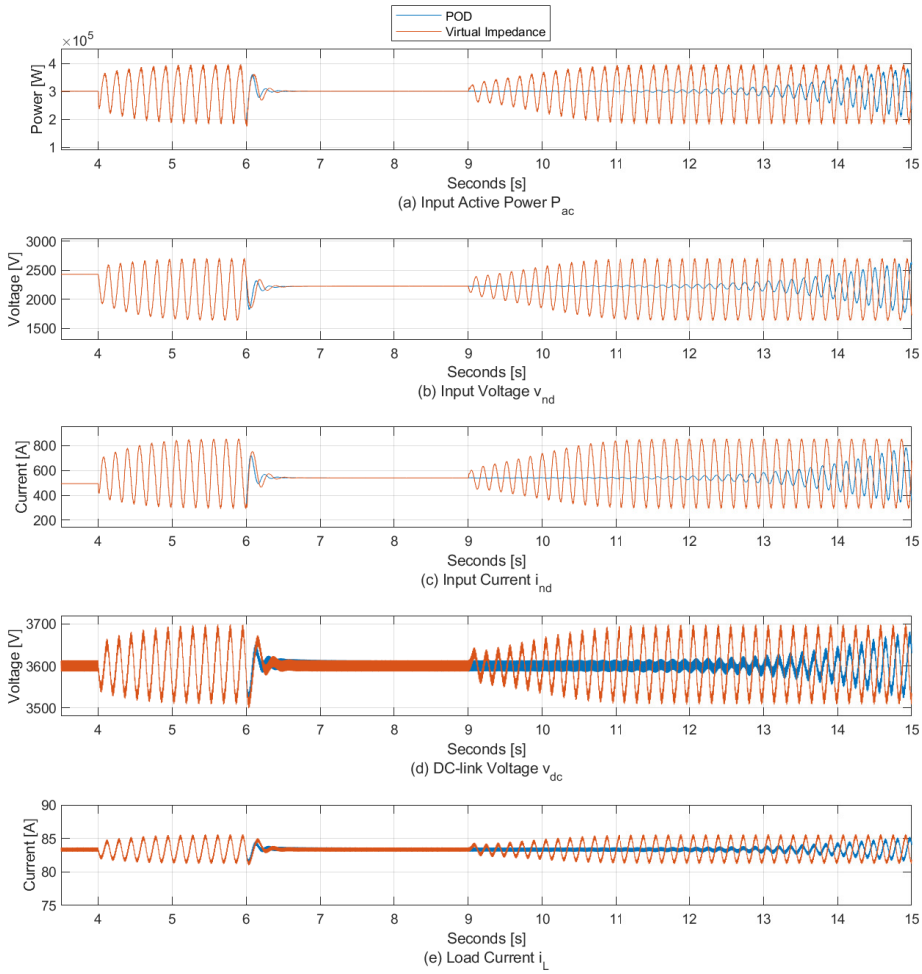

Figure 5.6: POD vs virtual-impedance-based control ($k_{pVR} = 0.150$, $k_{dVR} = 0.012$). Power consumption 300 kW. Distance increases (step change) from 130 km to 150 km at $t = 4$ s. POD control is turned on at $t = 6$ s and off at $t = 9$ s.

Although both controllers are able to mitigate the LFO phenomenon the POD control seems to be faster and its transient is smooth in comparison with the virtual-impedance-based control.

When the controllers are turned off, the system that was using POD control takes longer to show visible instability than the virtual-impedance-based control. The reason is POD is an external controller that provides DC-link voltage reference variation Δv_{dc}^* around $v_{dc}^* = 3600$; therefore, controller output at the steady state produce very small values around zero that do not represent a sudden change at the moment of turning off the controller.

On the other hand, a virtual-impedance-based controller provides control action in an internal loop, which manages part of the generation of the voltage command v_t^*. When this controller is turned off, the other internal controllers try to compensate for the output of the controller action creating a sudden disturbance that takes the system faster to instability.

5.4 Conclusions

The two control methods presented in this chapter showed a good performance to mitigate low-frequency oscillations when a single train is operating far from the substation during coasting (i.e. operating at low power conditions).

Meanwhile, the POD control action modifies the external voltage control loop to avoid constant power operation, the virtual-impedance-based control is acting in the internal current control loop adding damping to the system in the form of virtual resistance and inductance.

Chapter 6

LFO Emulation Using Power Hardware in the Loop

Testing the LFO phenomenon in a railway traction network is not easy, as the results would only be valid for that specific network, also it could affect other users operating in the catenary-line [11]. Alternatively, train-network interactions can be studied by means of simulations. Available approaches for this purpose would include offline simulations, real-time simulation platforms such as software-in-the-loop (SIL), hardware-in-the-loop (HIL), and power-hardware-in-the-loop (PHIL), each having advantages and disadvantages. Off-line simulations are commonly used during the initial analysis. However, real-time simulations are required at further development stages to properly evaluate the performance of the control.

SIL simulation integrates the compiled source control code into a time-domain simulation. In HIL solutions, the source code is implemented on the actual control platform; different options exist in this case, mainly related to time resolution, e.g., depending on whether switching events are reproduced or only the average behavior over a switching period is considered [65–67]. Independently of the implementation being used, no physical power flow occurs.

Finally, PHIL usually is made up of two parts: the emulator, and the unit under test (UUT). The emulator consists of an electronic power converter and associated real-time control, which interacts with the UUT, involving power exchange [68–70]. This allows testing of UUT parts such as power semiconductor devices, transformers, capacitors, and inductors under close-to-real-world operating conditions before their integration into the real system.

The aim of this chapter is to design, model, and build an emulator prototype of the railway traction network, able to reproduce the low-frequency oscillation phenomenon. In this study, the UUT consists of a four-quadrant power converter, which is responsible

for generating the DC-link feeding all onboard systems. The interactions between the emulator and the 4QC should reliably reproduce the LFO phenomenon occurring in the real railway traction system. The emulator will be used to validate the response of the 4QC in adverse scenarios regarding LFO, and redesign train voltage and current controllers if needed.

The chapter is organized as follows: Section 6.1 discusses different design options for the emulator; Section 6.2 presents the filter design for the train-emulator connection; simulation results are presented in Section 6.3; Section 6.4 deals with the test bench construction and experimental results; finally, conclusions are drawn in Section 6.5.

It is finally noted that the prototype shown in this chapter is intended as a proof of concept and was designed for downscale power and voltage values (10 kW AC 200 V/50 Hz), which are significantly smaller than the actual full-rated system values (n-hundred kW AC 25 kV/50 Hz). Still, the experience acquired during the development of this prototype is considered useful for the future design of a full-rated emulator.

6.1 Traction Network Emulator Design

This section discusses different approaches for the design of the railway traction network emulator aimed to reproduce the LFO phenomenon. In order to perform this task, the emulator should be able to simulate the railway system dynamics. This implies changing the network resistance R_s and inductance L_s with the desired distance from the train to the substation.

6.1.1 System description

As discussed in Section 1.2, the two main elements of the railway system model are the power supply network (i.e. ideal voltage source and distance depending impedance) and the train, see Figure 6.1(a). The emulator replaces the power supply network feeding the train as shown in Figures 6.1(b), 6.1(c) and 6.1(d).

The emulator consists of two main structures:

- Real-time simulator. It reproduces the dynamic behavior of the power supply network in real time, its output being the catenary voltage reference, v_c^*. Its design is discussed in Subsection 6.1.2.
- Single-phase voltage source inverter (VSI) operating in a grid-forming mode. It supplies the desired catenary voltage v_c to the train, it is described in Subsection 6.1.3.

It is noted that in the railway system model from Figure 1.4 in Section 1.2.3.1, the power supply network current i_s and the train current i_n are different due to the

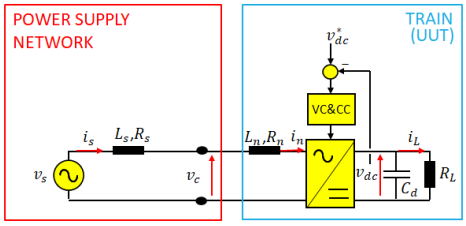

(a) Railway system model

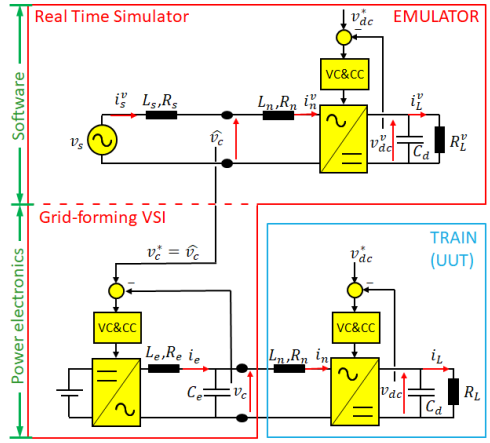

(b) Emulator model option 1 (Open loop) - Resistive load R^v_L

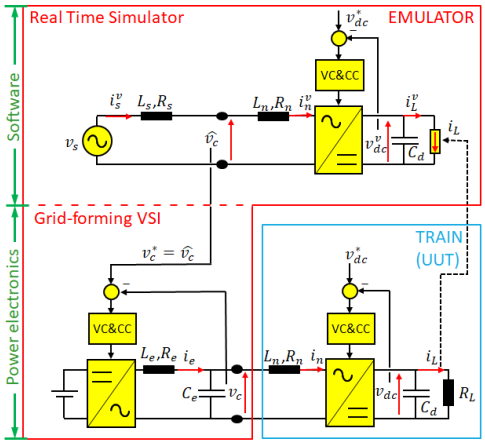

(c) Emulator model option 2 (Closed loop) - Controlled current source

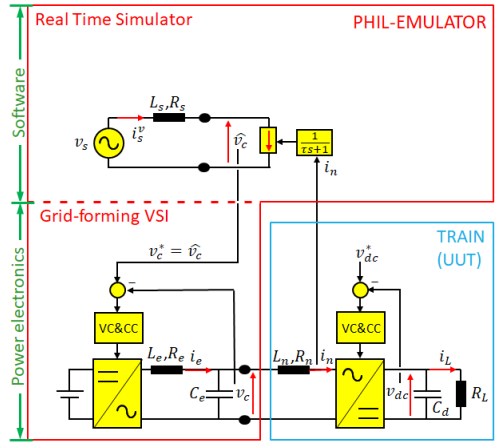

(d) Emulator model option 3 (PHIL)

Figure 6.1: Railway system model and emulator models. Superscript "^{v}" indicates virtual variables.

step-down transformer present in the traction unit. For the analysis in this chapter, the transformer will not be considered, therefore $i_s = i_n$ as shown in Figure 6.1(a). However, it was preferred to keep both current in the schematics to visualize the actual physics of the system.

6.1.2 Real-Time Simulator

The design of the real-time simulator is not trivial. Three different options will be discussed, which correspond to different stages of this research, i.e. later options improve the limitations found in the preceding ones. The reason to include earlier designs is to highlight those aspects which will play a relevant role in the accurate emulation of the LFO phenomenon occurring in the railway system.

For the discussion following, variables that exist only in the simulator, i.e. virtual variables, will be indicated by a superscript "v". There are variables that coincide both in the virtual domain and in the physical domain. Such variables do not include the "v" superscript.

6.1.2.1 Option 1: Open-Loop

In this option, the simulator generates the catenary voltage reference, v_c^*, simulating the complete railway system. The configuration is shown in Figure 6.1(b). The simulator includes a virtual power supply network and a virtual train. The load connected to the virtual DC-link is a constant resistance R_L^v. A concern for this option is that it requires previous knowledge of train parameters as it runs in parallel with the physical train (i.e., real train). Furthermore, there is no feedback from the physical train to the emulator. Consequently, this option works properly only for constant values of train load R_L, since in this case, $R_L^v = R_L$. However, if a change in load R_L is desired, the change should occur simultaneously with the change of R_L^v in the virtual domain. This can be problematic due to the lack of communication between the emulator and the physical train. Option 2 overcomes this drawback, as will be discussed following.

6.1.2.2 Option 2: Closed-Loop

This option is shown in Figure 6.1(c), and it is conceived to overcome the limitations observed in Option 1. R_L^v is now replaced by a controlled current source as a virtual load. By doing this, the load current in the simulator will track the measured load current i_L which circulates through the real load R_L. Therefore, this option allows emulation with varying loads.

Regardless of this improvement, a drawback of both options 1 and 2 is that they require precise knowledge of control design and tuning of the UUT to emulate catenary voltage dynamics. This knowledge is not often available. The approach discussed next is aimed at overcoming this drawback.

6.1.2.3 Option 3: PHIL

This option is shown in Figure 6.1(d). A virtual RL circuit is used to obtain the estimated catenary voltage $\widehat{V}_c(s)$. From the railway system model in Figure 6.1(a), the equation defining the catenary voltage $V_c(s)$ is given by (6.1).

$$V_c(s) = V_s(s) - (L_s s + R_s)\, I_s(s) \tag{6.1}$$

Since this equation is a non-causal system, it cannot be used for estimation purposes. A low-pass filter is added for real-time implementation, see (6.2) and Figure 6.2. A time constant of $\tau = 31.8$ μs was selected, corresponding to a cut-off frequency of 5 kHz. This is the maximum frequency complying with the Nyquist-Shannon criteria considering 10 kHz as the sampling frequency of the grid-forming VSI [29].

$$\widehat{V}_c(s) = V_s(s) - \frac{(L_s s + R_s)}{\tau s + 1} I_n(s) \tag{6.2}$$

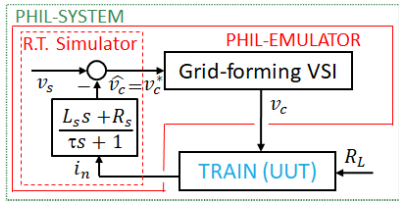

Figure 6.2: Real-time simulator block diagram in the PHIL system.

A simplified representation of a PHIL system is shown in Figure 6.2. Here, the closed-loop configuration that the real-time simulator creates between the grid-forming VSI and the train is easily seen. An appealing characteristic of this option is that it does not require previous knowledge of train characteristics. The train can be considered a black box, the emulator behaving as a power supply network whose properties are independent of the load (i.e. train). This option also allows the implementation and testing of control strategies aimed to mitigate LFO such as Power-Oscillation-Damping [8] and Virtual-Impedance-Based Suppression Method [71].

6.1.3 Grid-forming VSI

The block diagram of the single-phase VSI is shown in Figure 6.3. It consists of a two-level single-phase converter (H-bridge), which is fed from a voltage source on the DC-side, and has an LC filter connected to its AC side. Unipolar modulation is used in this study.

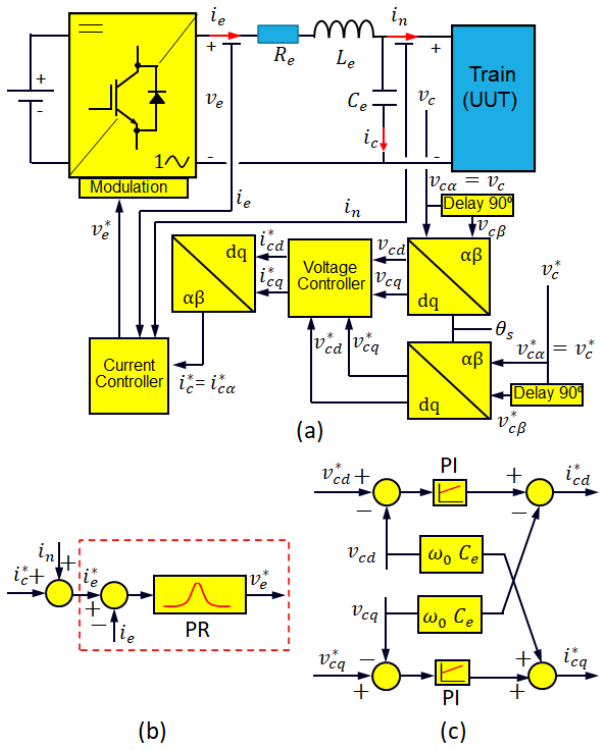

Figure 6.3: Grid-forming single-phase VSI. (a) Overall block diagram, (b) Current controller, (c) Voltage controller.

The cascaded control shown in Figure 6.3 is used. The inner loop controls the inductor current i_e, while the outer loop controls the capacitor voltage v_c (i.e. catenary voltage), to which the traction unit is connected.

Current control is performed in a stationary reference frame using a proportional-resonant (PR) controller as shown in Figure 6.3(b). The corresponding transfer function is given by (6.3), where k_{pCC-e} and k_{rCC-e} are the gains to be tuned to obtain the desired closed loop current control bandwidth $BWcc_{-e}$ [72], see (6.4) and (6.5). The basic concept of the PR controller is to provide an infinite gain at a selected resonant frequency, as this will guarantee zero steady-state error at that frequency [73]. The resonant controller can be seen therefore as a generalization of the PI controller, in which the infinite gain occurs not at DC, but at the desired frequency. In this case, the resonance frequency is the fundamental frequency f_0. The coefficient K_f in (6.5) adjusts the bandpass of the transfer function (6.3), it takes values from 0.25 to 1 [72]. Furthermore, in Figure 6.3(b), the measured train current i_n is added to the current command as a feedforward term to improve the dynamic response of the voltage control loop [25].

$$PR(s) = 2k_{pCC-e}\frac{s^2 + s\left(k_{rCC-e}/k_{pCC-e}\right) + \left(2\pi f_0\right)^2}{s^2 + \left(2\pi f_0\right)^2} \tag{6.3}$$

$$k_{pCC-e} = \sqrt{2}\left(2\pi BWcc_{-e}\right)L_e \tag{6.4}$$
$$k_{rCC-e} = K_f\left(2\pi BWcc_{-e}\right)^2 L_e \tag{6.5}$$

The catenary voltage control is performed in a synchronous reference frame using a PI controller as shown in Figure 6.3(c), where the proportional gain and the integral gain are given by (6.6) and (6.7) as function of the desired voltage control bandwidth $BWvc_{-e}$.

$$k_{pVC-e} = \sqrt{2}\left(2\pi BWvc_{-e}\right)C_e \tag{6.6}$$
$$k_{iVC-e} = \left(2\pi BWvc_{-e}\right)^2 C_e \tag{6.7}$$

A virtual quadrature component of the catenary voltage is obtained by delaying 90° the alpha component. The filter in (6.8) is used for this purpose. Feedforward terms are used in the voltage controller to eliminate cross-coupling between $d-$ and $q-$axes, see Figure 6.3(c).

$$G_{Delay-90}(s) = \frac{2\pi f_0 - s}{s + 2\pi f_0} \tag{6.8}$$

6.1.4 Extension to Multiple Trains Case

From Subsections 6.1.3 to 6.1.1, it is noted that the emulator is aimed to replace the traction network. In the case when multiple trains are in the depot (i.e. located at the same place), it does not modify the network topology since all the trains are connected in parallel. Therefore, only one train with an equivalent input admittance can be used.

On the other hand, for the case of multiple trains operating in the same power supply section at different locations, the network topology must be modified to include additional connection nodes, therefore, the virtual network in the real-time simulator must be modified, but the proposed methodology would still apply. Also, additional virtual trains can be added.

These analyses are not included in this thesis, but it is worth it to mention them for future work.

6.2 Inverters and Filter Design

The design of inverters and passive elements of the downscale prototype is addressed in this section. As observed in Figures 6.1(b), 6.1(c) and 6.1(d), grid-forming VSI and 4QC are connected through LC+L filters. The inductance L_n corresponds to the 4QC inductance. It should be large enough to filter the current harmonics, but realizing that excessively large values will limit power transfer capability. Therefore, a trade-off is required. For simulations and test bench, a DC-link voltage $V_{dc} = 300$ V has been selected for the inverters, with a catenary peak voltage of $V_c = 200$ V. These voltages were chosen to provide a large safety margin with respect to power devices and DC-link capacitor voltage limits, as some of the experiments reproducing LFO might produce large excursions of the voltages. Nominal power of 10 kW, with a current ripple $< 4\%$ of the train nominal current have been defined as design targets.

The maximum transfer power with a unity power factor between train and network is given by (6.9) [51]. From this equation, a value of $L_n = 7.1$ mH is obtained to transfer the targeted power $P_n = 10$ kW. Due to availability issues, a value of $L_n = 6$ mH was selected.

$$P_n = \frac{\sqrt{V_c^2 V_{dc}^2 - V_c^4}}{2X_n} \tag{6.9}$$

Current ripple can be approached using (6.10), where load angle ψ is the phase difference between catenary voltage v_c and the 4QC terminal voltage v_t [51].

$$\Delta i(\%) = \frac{\pi\sqrt{2}V_c\,(1 - (V_t/V_{dc})\cos(\psi))}{(f_{sw}/f_0)X_n I_n}100 \tag{6.10}$$

For the targeted current ripple limit of 4 % and the selected value of L_n, the switching frequency provided by (6.10) is $f_{sw} = 7.5$ kHz. A slightly larger value, $f_{sw} = 10$ kHz, was finally chosen.

Once L_n is selected, there would be two degrees of freedom for the design of the catenary emulator LC filter [74]. An option in this case is to analyze the LC+L filters as an equivalent LCL filter. It is advantageous for the design of LCL filters to have the same values for both inductances, as this minimizes the size of the filter components [75].

Assumed that the inductances have been selected such that $L_e = L_n = L$, and neglecting the resistive terms of inductances and capacitors, the transfer function between the capacitor voltage at the point of coupling (i.e. v_c) and the voltage is applied by any of the two inverters (i.e. v_t, v_e) is given by (6.11). The filter behaves as a second-order system, a resonance occurring at the cut-off frequency ω_c which is given by (6.12).

$$\frac{V_c(s)}{V(s)} = \frac{1}{s^2 LC_e + 2} \tag{6.11}$$

$$\omega_c = \sqrt{\frac{2}{LC_e}} \tag{6.12}$$

Capacitor C_e was chosen to get a cut-off frequency around 600 Hz, which is much higher than the fundamental frequency but far enough from the switching frequency. The parameters of 4QC and VSI filters are presented in Tables 6.1 and 6.2 respectively. Figure 6.4 shows the resulting Bode diagram from (6.11). It is observed that the attenuation at the switching frequency is larger than -50 dB.

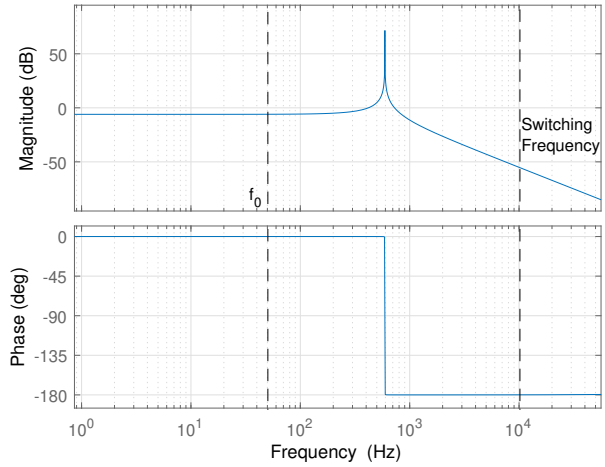

Figure 6.4: Bode diagram of capacitor vs. inverter voltage. $V_c(j\omega)/V(j\omega)$.

Any topology able to produce a single-phase AC voltage with a fundamental frequency of 50 Hz would be suitable for the grid-forming VSI. Two issues should be considered. First, since the LFO will occur when the active power is flowing from the emulator to 4QC, the grid-forming converter will not be required to absorb power. Second, to reduce the effects of switching harmonics produced by the grid-forming inverter and ease the design of the LC filter at the output of the emulator, high switching frequencies and/or multilevel topologies (e.g., NPC) are preferable. However, cost and control complexity must be also considered. A two-level full bridge has been used for the downscaled prototype developed in this chapter. The same topology has been considered for the 4QC.

Symbol	Description	Value
Power supply network		
L_s	Line Inductance (Limit)	10 mH
R_s	Line Resistance (Limit)	150 mΩ
V_s	Supply Voltage Amplitude	200 V
f_0	Fundamental Frequency	50 Hz
Train (4QC)		
L_n	4QC Inductance	6 mH
R_n	4QC Resistance	10 mΩ
f_{sw}	Switching Frequency	10 kHz
$BWvc$	Voltage Control Bandwidth	10 Hz
$BWcc$	Current Control Bandwidth	100 Hz
R_L	Resistive Load	200 Ω
V_{dc}	DC-link Voltage	300 V

Table 6.1: Train-Network parameters.

Symbol	Description	Value
L_e	Emulator Inductance	6 mH
R_e	Emulator Resistance	10 mΩ
C_e	Emulator Capacitance	24 mF
f_{sw}	Switching Frequency	10 kHz
$BWvc_{-e}$	Voltage Control Bandwidth	50 Hz / 100 Hz
$BWcc_{-e}$	Current Control Bandwidth	500 Hz / 1000 Hz

Table 6.2: Network emulator parameters.

6.3 Simulation Results

In this section, time-domain simulations of the emulation methods proposed in Section 6.1 (see Figure 6.1) are carried out to test their performance.

The behavior of the railway system model in Figure 6.1(a) will be first simulated in Subsection 6.3.1 to be later used as a reference to assess the performance of the different methods. Power supply network parameters and train control parameters are shown in Table 6.1.

Regarding the catenary emulator, it has been observed during this work that the bandwidths of the voltage and current controllers of the grid-forming VSI will strongly affect the emulator capability to accurately reproduce LFO. To illustrate this, the behavior of the different emulator designs was tested for two different sets of control bandwidths; set #1 is ($BWvc_{-e}$ = 50 Hz, $BWcc_{-e}$ = 500 Hz), and set #2 is ($BWvc_{-e}$ = 100 Hz, $BWcc_{-e}$ = 1000 Hz). Emulator parameters are shown in Table 6.2. On the other hand, train voltage and current control bandwidths, $BWvc$ and $BWcc$, were kept constants for all the cases.

6.3.1 LFO using railway system model

Figure 6.5 shows the DC-link voltage, catenary voltage, and train current using the railway system model shown in Figure 6.1(a), when step-like changes occur in the network impedance. Such changes would reproduce the effect of increasing the transmission line length from the substation transformer to the traction unit. It is noted that while step-like changes will not occur in the real system, still they are a useful excitation to obtain relevant parameters of the system as the damping ratio, settling time, oscillation frequency, and eigenvalues. Indeed, step-like changes have been frequently used for LFO and stability studies [7, 11, 17]. As shown in Figure 6.5, LFOs progressively develop when the impedance increases, the stability limit occurring at $L_s = 10$ mH and $R_s = 150$ mΩ. ,

Since increasing the network impedance decreases system damping and increases the settling time, it is inferred that critical system eigenvalues move from the negative real side of the complex plane (i.e. stable region) to the right (i.e. unstable region). At the stability limit, the real component of critical eigenvalues is zero, and the imaginary component can be identified from the oscillation frequency, which is $f_{osc} \approx$ 9 Hz.

6.3.2 LFO using open-loop emulator (Option 1)

Figure 6.6 shows LFO when network inductance and resistance increase using option 1 of the emulator in Figure 6.1(b). Only the results for set #1 of voltage and current control bandwidths are presented, as no significant differences were found for this particular case using set #2.

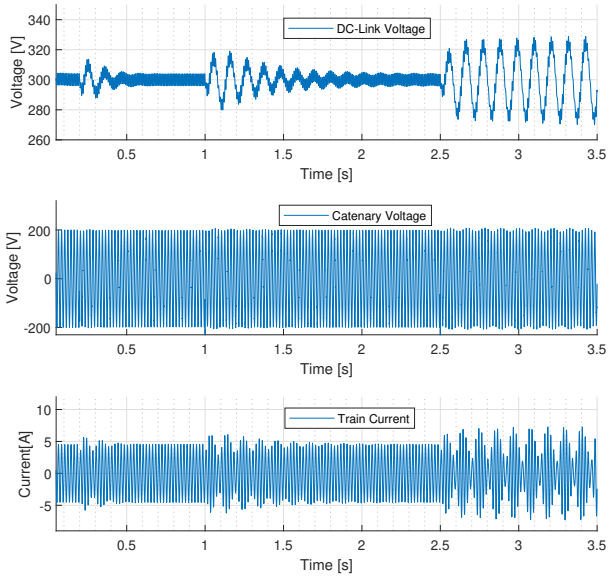

Figure 6.5: Simulation results. LFO when line inductance and resistance increase from L_s = 4 mH - R_s = 60 mΩ to L_s = 10 mH - R_s = 150 mΩ in steps of ΔL_s = 2 mH and ΔR_s = 30 mΩ at t=0.2 s, t=1 s, and t=2.5 s.

The DC-link voltage response of the real railway system model is also shown in Figure 6.6 for comparison purposes. A good agreement is observed between real and emulated systems. However, simulations using this option are only possible if the load R_L is constant, and the precise knowledge of train control design is available as discussed in Subsection 6.3.6, which might not be always possible.

6.3.3 LFO using closed-loop emulator (Option 2)

Time-domain simulation results using the emulator model option 2 are shown in Figure 6.7 for the two different sets of controller bandwidths. As shown in Figure 6.7(a), the system becomes unstable when the change in line impedance is applied. Increasing VSI control bandwidth slightly reduces the rate of increase of the oscillations, but still, the system is unstable as shown in Figure 6.7(b). These results suggest that this option is not advisable as it fails to reproduce the LFO phenomenon of interest.

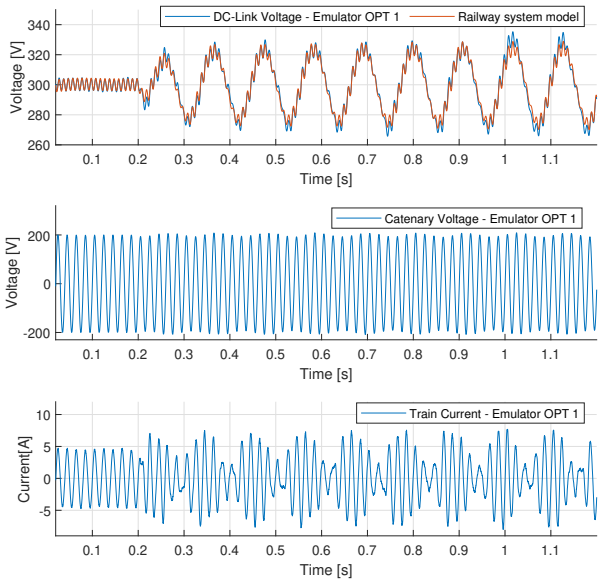

Figure 6.6: Simulation results. Response to line impedance changes using option 1 for the emulator. Line impedance increases from $L_s = 8$ mH, $R_s = 120$ mΩ to $L_s = 10$ mH, $R_s = 150$ mΩ at $t = 0.2$ s. From top to bottom: DC-link Voltage, catenary voltage, and train current. $BWcc_{-e} = 500$ Hz, $BWvc_{-e} = 50$ Hz.

6.3.4 LFO using PHIL emulator (Option 3)

Time-domain simulations using the PHIL-Emulator are shown in Figure 6.8. The case for bandwidths set #1 is shown in Figure 6.8(a). The response is seen to be more damped compared to the actual power system response, LFO also occurring at lower frequencies (8 Hz for the emulator vs. 9 Hz for the actual railway system model). The improvement when VSI controllers bandwidths are increased can be observed in Figure 6.8(b), but oscillations are seen still to be slightly damped and occur at a slightly lower frequency compared to the actual railway system case.

6.3.5 Response to load changes

Time-domain simulations showing the response to a step change in the load using the emulator model options 1 and 3 are shown in Figure 6.9. Option 2 was not considered for this test since its performance has already been found to be inferior in Subsection 6.3.3.

From Figure 6.9 it is observed that in steady-state the emulated system and the

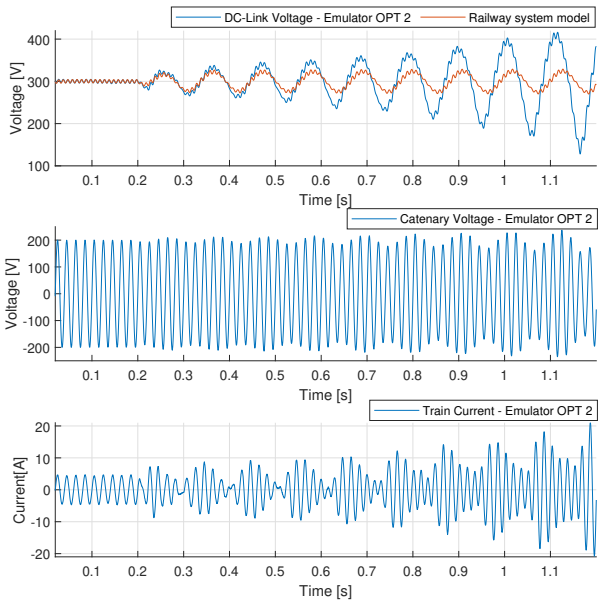

(a) $BWvc_{-e} = 50$ Hz, $BWcc_{-e} = 500$ Hz

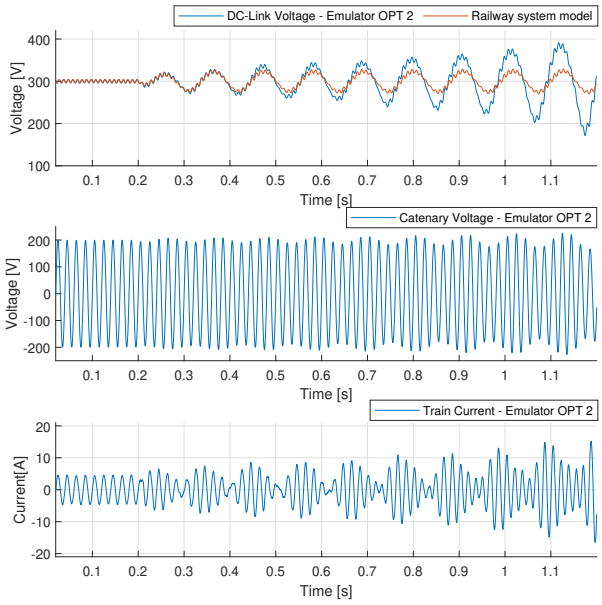

(b) $BWvc_{-e} = 100$ Hz, $BWcc_{-e} = 1000$ Hz

Figure 6.7: Simulation results. Response to line impedance changes using option 2 for the emulator. Line impedance increases from $L_s = 8$ mH, $R_s = 120$ mΩ to $L_s = 10$ mH, $R_s = 150$ mΩ at $t = 0.2$ s. From top to bottom: DC-link Voltage, catenary voltage and train current.

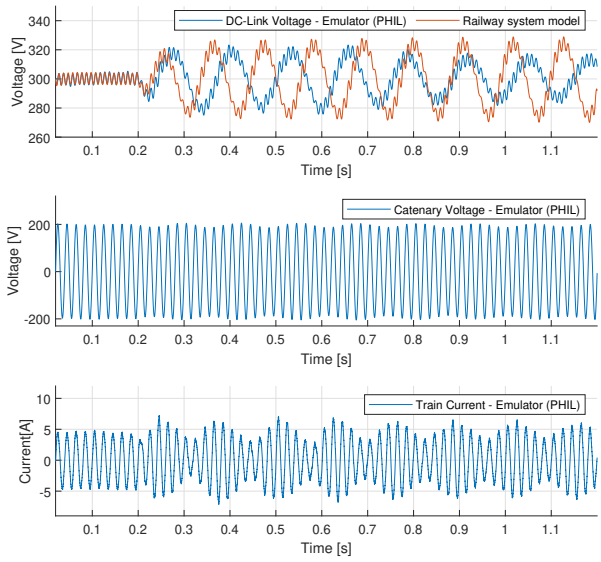

(a) $BWvc_{-e} = 50$ Hz, $BWcc_{-e} = 500$ Hz

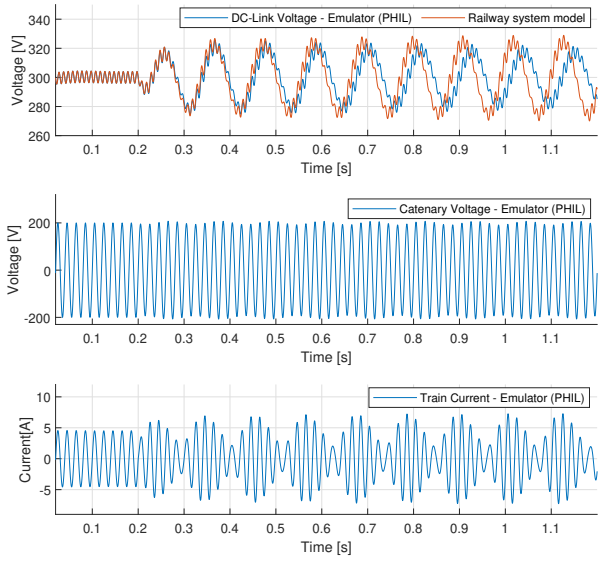

(b) $BWvc_{-e} = 100$ Hz, $BWcc_{-e} = 1000$ Hz

Figure 6.8: Simulation results. Response to line impedance changes using option 3 for the emulator. Line impedance increases from $L_s = 8$ mH, $R_s = 120$ mΩ to $L_s = 10$ mH, $R_s = 150$ mΩ at $t = 0.2$ s. From top to bottom: DC-link Voltage, catenary voltage, and train current.

railway system behave similarly. However, they are seen to show different dynamics. Emulator option 1 fails to reproduce the railway system dynamics. On the contrary, option 3 achieves a remarkable level of similarity.

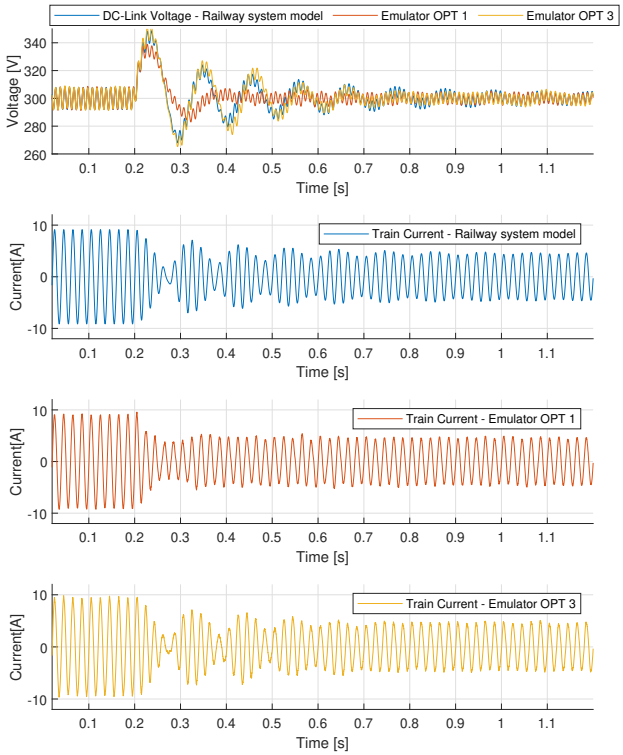

Figure 6.9: Simulation results. Response to load changes using network emulator options 1 and 3. Line impedance $L_s = 8$ mH, $R_s = 120$ mΩ. Load step change from $R_L = 100$ mΩ to $R_L = 200$ mΩ at $t = 0.2$ s. Control bandwidths: $BWcc_{-e} = 1000$ Hz, $BWvc_{-e} = 100$ Hz.

6.3.6 Summary

It is concluded from the simulations presented in this section that high accuracy in reproducing LFO would be obtained using Option 1 for the emulator. However, this option implies that current and voltage control structures and tuning are the same for emulator and actual train, which might be difficult to achieve or even impossible in practice. It is interesting to note although the simulation for this option was performed in real-time, this is not actually required, as there is no feedback from the real train

to the emulator. Therefore, it would be perfectly possible to simulate the train behavior off-line and use the catenary voltage resulting from the simulation to provide the reference signal to emulator v_c^*, see Figure 6.1(b).

In contrast with option 1, option 2 includes a feedback mechanism as it uses the train load current i_L to feed the emulator. However, this method still requires knowledge of train controllers. Furthermore, it is observed from simulation results that this option has the worst accuracy in reproducing the behavior of the actual power system.

Finally, option 3 shows good accuracy in reproducing LFO, and doesn't require knowledge of train control, making it especially appealing.

6.3.7 Discussion

As already explained, low-frequency oscillations are produced by the dynamic interaction between the power supply network and the train (i.e. 4QC) [13]. For option 1 of the emulation; the dynamic interaction which provokes LFO, happens entirely in the simulator between the virtual power supply and the virtual train. In this option, the physical train doesn't contribute to LFO formation due to the open-loop configuration.

For option 2, the dynamic of the physical train is now in the closed loop, and it participates in the LFO formation. This implies repeated elements in the loop. For instance, the dynamics of the 4QC voltage and current controllers affect the system twice (due to the physical train and the virtual train). Although these repeated elements do not affect the steady-state response, they add delays, which impact the transient response and the system dynamics. System delays were already reported to influence LFO instability [1], and would explain the inaccuracy of this option to reproduce the LFO phenomenon.

Using the third option (PHIL-Emulator), LFO are the result of the interaction between the virtual power supply network and the physical train. Although the dynamic of grid-forming VSI is in between, large values of voltage and current control bandwidths, which make this system fast enough, allow accurate replication of the LFO phenomenon.

In conclusion, high control bandwidths would be desirable, as this would reduce control delays which can severely affect emulator performance. The maximum bandwidth that can be achieved would be limited by the Nyquist sampling theorem in the first place. A second concern for the selection of the bandwidths would be the noise mainly coming from sensors, during implementation this was found to be indeed the main limiting factor for the selection of the gains of the controllers, see Section 6.4. Further, it is noted that although all the preceding discussion on the tuning of the controllers has focused on the concept of *bandwidth*, other design aspects, such as natural frequency or settling time, could be used instead for the same purpose since they also contain information about system delays. The detailed impact of additional indices, e.g., damping coefficient, might also need to be considered. A thorough analysis of

the influence of controller design and tuning on emulator performance is a matter of ongoing research.

Finally, in terms of implementation in the micro-controller, option 3 requires less computational effort than the other two options, in which relatively complex electronic power converters have to be simulated in real time.

6.4 Experimental Results

This section presents the experimental results obtained using Option 3 (PHIL-Emulator) discussed in Subsection 6.1.2.3. The other two options were disregarded for experimental verification as they were concluded to be inferior. The test bench is shown in Figures 6.10 and 6.11. Its design was already discussed in Section 6.2. Power supply parameters, train parameters and emulator parameters are the same as for the simulation results in Section 6.3 (see Tables 6.1 and 6.2).

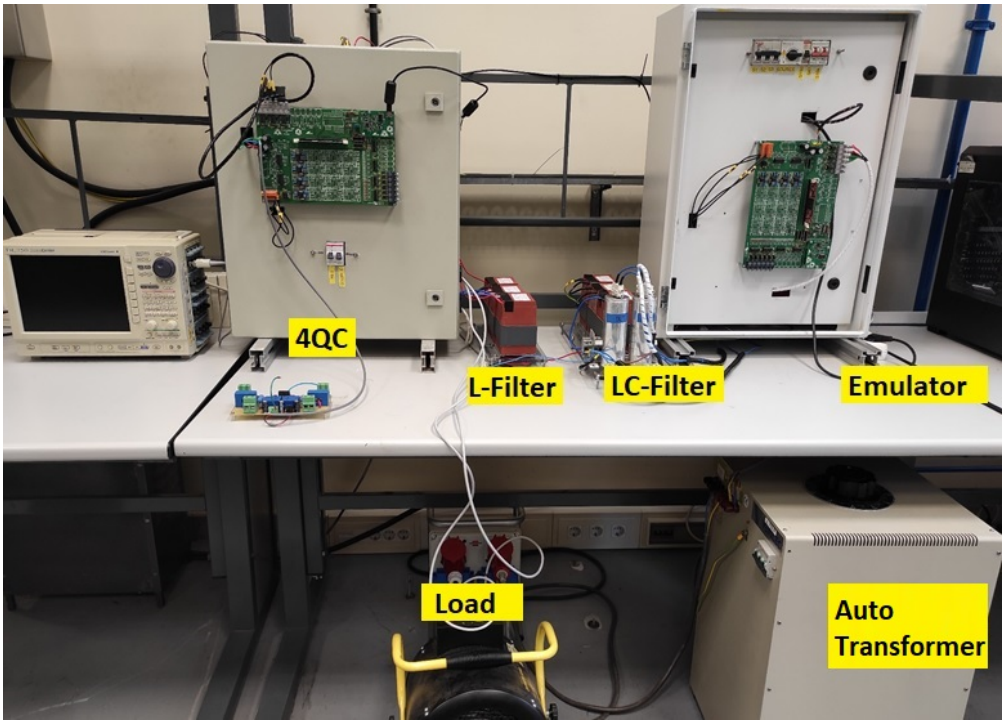

Figure 6.10: Experimental test bench.

Current control and voltage control bandwidths of $BWvc_{-e} = 50$ Hz and $BWcc_{-e} = 500$ Hz, respectively, have been used in the test bench. It was discussed

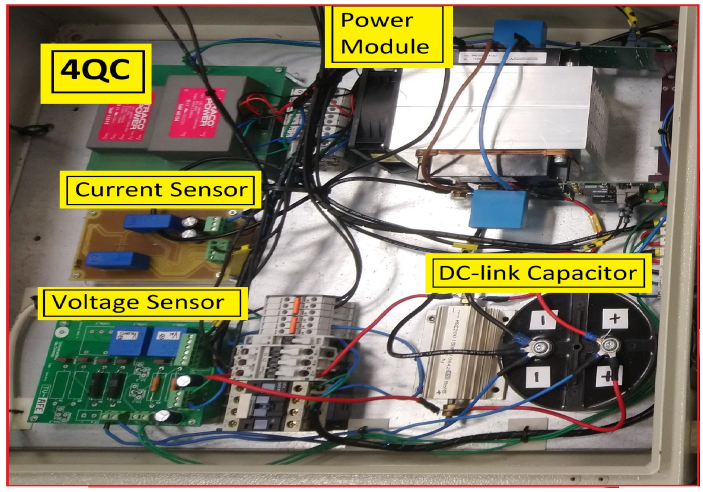

(a) 4QC

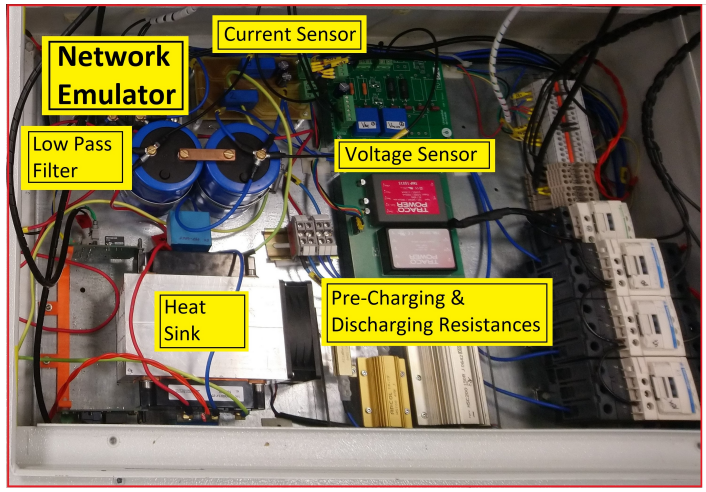

(b) Emulator

Figure 6.11: Experimental test bench. Interior view of 4QC and Emulator

in Section 6.3.4 the relevance of emulator control bandwidths for the accurate reproduction of LFO. Unfortunately, signal noise content in the real system made unfeasible the use of the higher bandwidths.

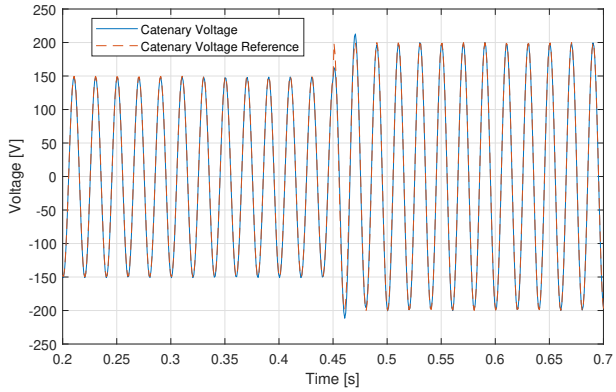

Figure 6.12: Experimental results. Catenary voltage step response. From $V_c = 150$ V to $V_c = 200$ V at t=0.45 s.

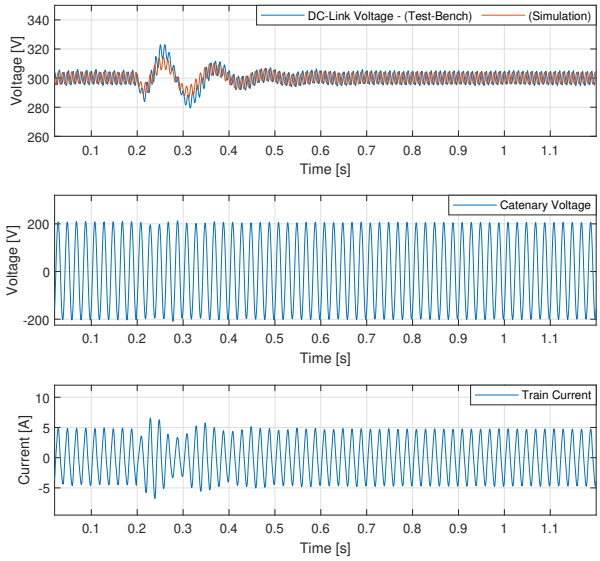

(a) $L_s = 4 \rightarrow 6$ mH, $R_s = 60 \rightarrow 90$ mΩ

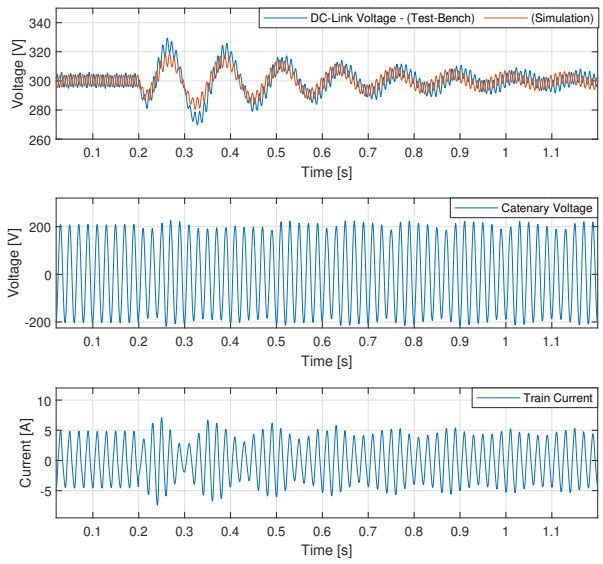

(b) $L_s = 6 \rightarrow 8$ mH, $R_s = 90 \rightarrow 120$ mΩ

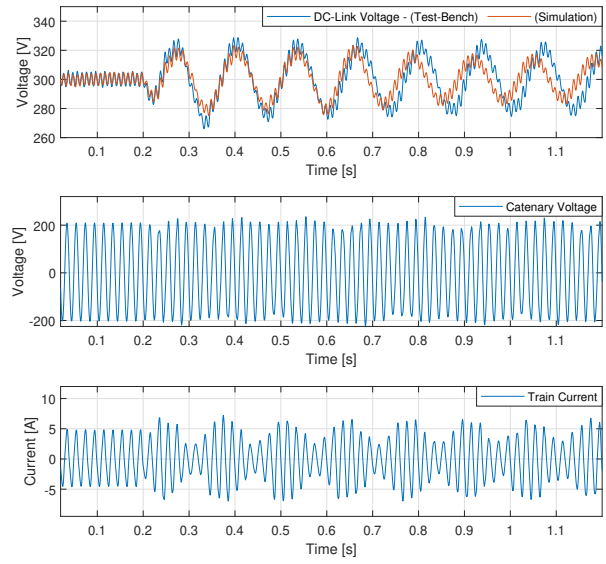

(c) $L_s = 8 \rightarrow 10$ mH, $R_s = 120 \rightarrow 150$ mΩ

Figure 6.13: Experimental results. System response to step-like changes in power network impedance as indicated in the corresponding captions. Changes occur at t=0.2 s. For each case, from top to bottom: DC-link voltage, catenary voltage, and train current. Simulation results are shown for comparison.

Figure 6.12 shows the catenary voltage step response to test the control action of grid-forming VSI.

Figure 6.13 shows the system response to changes in the virtual catenary impedance. LFO are seen to develop as the virtual network impedance increases, eventually reaching the stability limit in Figure 6.13(c). Oscillation frequency at the stability limit occurs at around 8 Hz, which is in good agreement with the simulation results from Figure 6.8(a). The limit values of power network impedance also agree with the values obtained in the simulation. This confirms the correctness of the proposed approach.

6.5 Conclusions

The design of a network emulator able to reproduce the dynamic behavior of a railway traction network, including LFO, has been discussed in this chapter. The emulator allows evaluating the response of the 4QC power converter in the event of LFO in a test bench, avoiding expensive or even non-viable on-track tests.

Three different options for the catenary emulator were considered: open-loop, closed-loop and PHIL. Simulation was used for preliminary verification. It was shown that due to the lack of feedback from the train, the first option can reproduce the LFO only when the virtual and actual traction loads are equal and constant. Additionally, the first two options require precise knowledge of the train controller parameters, which might not be available. PHIL option was shown to overcome these limitations.

The study also showed that the bandwidth of the voltage and current controllers of the grid-forming VSI emulator strongly affect its capability to reproduce LFO. It was concluded that, despite the low-frequency nature of LFO events being targeted, relatively high bandwidths and proper spectral separation between voltage and current control loops bandwidths are required.

The proposed methods were tested in a test bench consisting of a grid-forming inverter and the 4QC connected through an LCL filter. Experimental results were found to be in good agreement with simulation results. Due to noise, the higher control bandwidth values used in the simulation couldn't be achieved in the test bench.

It is noted finally that the work shown in this chapter is a concept validation with a downscale system rated for 10 kW. The design of a full-scale test bench is a future work.

Chapter 7

Conclusions and Future Work

7.1 Conclusions

In this thesis, low-frequency stability in the 25 kV/50 Hz electric traction power system has been studied. The main conclusions made during the development of this dissertation are:

- The LFO phenomenon occurs due to feedback loop effects between the line-side converter controllers and the power supply system. The train controllers force the train input admittance components to be negative at low frequencies (i.e. phase in the range of 90° to 270°). This happens due to the DC-link voltage controller trying to maintain constant input power operation and due to control system delays.

- While the railway system operates on a single-phase basis, it is required to conduct LFO stability analysis within the dq reference frame (MIMO system). Although time-domain simulations are a valuable tool for assessing stability yielding consistent results, their practicality is limited to scenarios with only a few traction chains. Consequently, the dq method is the preferred approach, as it can be applied effectively to much more complex railway systems involving multiple trains at various locations.

- The study of the impact of power consumption shows that the worst case for instability is operation at low power. Therefore, it is required to optimize the 4QC converter control tuning in order to increase the stability limit (i.e. maximum number of trains or distance). This action can be performed according to the results obtained in parameter variations studies from Chapters 2 and 4. Another approach is adding supplementary controllers to the actual 4QC control system.

- Stability of two trains with different controllers was analyzed, showing that in each case, increasing the DC-link voltage-control bandwidth ($BWvc$) decreases the gain margin of the system while increasing the current-control bandwidth ($BWcc$) increases the gain margin. This strongly suggests that the spectral separation between current and voltage controller bandwidths plays a critical role in the occurrence of LFO.

- Increments of transformer leakage inductance with fixed current controlled bandwidth increase lineally the stability limit. This is advantageous for LFO stability and for filtering the AC-side current, however, it limits the power transfer capability. On the other hand, decreasing DC-link capacitance with fixed voltage controller bandwidth increases monotonously the stability limit, which improves faster at lower values of DC-link capacitance. However, decreasing the value of the capacitor will imply losing filter capabilities (i.e. increment of voltage ripple) and system controllability. It was found that variations of inductance and capacitance do not interfere with each other when control bandwidths are maintained constant.

- Delays of the feedforward signal were observed to increase the risks of LFO. If the feedforward signal depends on PLL dynamics, a faster PLL dynamics improves the low-frequency stability.

- The train small-signal admittance model was developed in the synchronous reference frame, and its frequency response matched with the frequency sweep of the simulation of the complete (non-linear) model of the train. The models of the current control, DC-link voltage control, PLL, and QSG-SOGI were included. The analytical input admittance combined with the power network impedance was able to predict the appearance of low-frequency oscillation when several trains in the depot are operating at low power consumption with only auxiliary systems energized.

- The sensitivity analysis of the system stability to train electrical and control parameters was presented. It shows that LFO stability is very sensible to changes in leakage inductance, voltage control bandwidth and current control bandwidths. Due to the non-linear nature of the system, the sensitivity changes according to the operational point.

7.2 Contributions

The main contributions made during the development of this dissertation are:

- The analysis of the influence of the constructive elements and control parameters that contribute to the low-frequency instability using frequency-domain techniques.

- The analysis of the influence of the constructive elements and control parameters that contribute to the low-frequency instability using time-domain simulation along with eigenvalue identification.

- A comparative analysis of two types of synchronization systems and two methods to generate the feedforward signal (direct and indirect). This reveals that delays of the feedforward signal were observed to increase the risks of LFO. This behavior was further validated by testing three contact-line voltage filters with varying dynamics, showing that the fastest filter (i.e. producing the smallest delays) results in a system with the largest gain margin.

- Development of novel train admittance small-signal model. Here, the main contribution is modeling the dynamics due to errors in the coordinate rotations of the single-phase 4QC control system. This system employs the use of asymmetric transfer functions to generate virtual quadrature components. Furthermore, the analytical model of QSG-SOGI transfer function in the synchronous dq-frame was developed. As mentioned in Chapter 3, the QSG-SOGI is an asymmetrical system in charge of filtering the input voltage and creating the quadrature signal; it originally operates in the alpha-beta frame; however, the analytical model of this system was required in the dq-frame to be included in train admittance model. Finally, combining both models allows deriving the small-signal vector transformation between the actual dq-frame and the estimated $\widehat{dq}$-frame.

- Comparative study of two control actions to mitigate LFO. First, power oscillation damping was used as an external loop to the DC-link control system. Second, the virtual impedance-based suppression method in the internal current loop was used.

- The design and implementation of a catenary emulator able to reproduce the dynamic behavior of the railway traction network, including LFO. The emulator allows evaluating the response of the 4QC power converter in the event of LFO in a test bench, avoiding expensive or even non-viable on-track tests.

7.2.1 Journal publications

- Frutos, P.; Ladoux, P.; Roux, N.; Larrazabal, I.; Guerrero, J.M.; Briz, F. "Low Frequency Stability of AC Railway Traction Power Systems: Analysis of the Influence of Traction Unit Parameters". *Electronics 2022*, 11, 1593. https://doi.org/10.3390/electronics11101593

- P. Frutos-Galarza et al., "Power-Hardware-in-the-Loop Emulation of the Low-Frequency Oscillation Phenomenon in AC Railway Networks," in *IEEE Access*, vol. 10, pp. 87374-87386, 2022. https://doi.org/10.1109/ACCESS.2022.3198945.

7.2.2 Conference publications

- P. Frutos, J. M. Guerrero, I. Muniategui, I. Vicente, A. Endemano and F. Briz, "Low-Frequency Oscillations Analysis in AC Railway Networks Using Eigenmode Identification," *2021 IEEE Energy Conversion Congress and Exposition (ECCE)*, Vancouver, BC, Canada, 2021, pp. 1573-1579. https://doi.org/10.1109/ECCE47101.2021.9595947.

7.2.3 Under review publications

- P. Frutos, J. M. Guerrero, I. Muniategui, A. Endemaño, D. Ortega and F. Briz, " Low frequency oscillations in AC railway traction power systems: Train input-admittance calculation and stability analysis," International Journal of Electrical Power & Energy Systems

7.3 Future Work

There are several points that could be addressed in the future in order to continue the research line of this dissertation:

- Designing and modelling the small-signal input admittance model of the 4QC using a current controller in the alpha-beta reference frame. This would allow to compare its performance with the *dq*-frame current controller.
- Modelling different types of synchronization systems and quadrature signal generator systems, such as the adaptive SOGI, in order to study its influence in the railway system stability.
- Designing different control methods to mitigate Low frequency oscillations, and comparing with the methods presented in this document.
- Exploring different methods to measure the input admittance of single phase system in the *dq*-frame. An option could be using the Hilbert transform to calculate orthogonal components. This is a mathematical tool that shifts every input signal component 90° lagging relative to the component's own frequency.

7.4 Dissertation Funding

This work has been supported in part by the Government of the Principality of Asturias under project AYUD/2021/50988.

Chapter 8

Conclusiones y Trabajo Futuro

8.1 Conclusiones

En esta tesis se ha estudiado la estabilidad de baja frecuencia en el sistema ferroviario de tracción eléctrica de 25 kV/50 Hz. Las principales conclusiones extraídas durante el desarrollo de esta tesis son:

- El fenómeno LFO se produce debido a los efectos de la interconexión en lazo cerrado entre el sistema de control del convertidor de línea del vehículo y la red ferroviaria de suministro de eléctrico. Los controladores del tren fuerzan a que los componentes de admitancia de entrada del tren sean negativos a bajas frecuencias (i.e. admitancia en el rango de -90° a 90°). Esto sucede principalmente debido a la acción del controlador de voltaje DC, que provoca que el que tren intente mantener la potencia de entrada constante, y también debido a los retrasos en el sistema de control.

- Si bien el sistema ferroviario es monofásico, para el estudio del fenómeno LFO, es necesario realizar un análisis de estabilidad en el marco de referencia dq (sistema MIMO). Aunque las simulaciones en el dominio del tiempo son una herramienta valiosa para evaluar la estabilidad y producen resultados consistentes, su practicidad se limita a escenarios con solo unas pocas cadenas de tracción. En consecuencia, el método de análisis en dq es el enfoque idóneo para utilizar, ya que se puede aplicar eficazmente a sistemas ferroviarios mucho más complejos que involucran múltiples trenes en varias ubicaciones.

- El estudio del impacto del consumo de energía muestra que el peor caso de estabilidad es el funcionamiento con baja potencia. Por lo tanto, es necesario optimizar la configuración de control del convertidor 4QC para aumentar el límite de estabilidad (es decir, el número máximo de trenes o distancia). Esta acción se

podrá realizar de acuerdo a los resultados obtenidos en los estudios de variación de parámetros de los Capítulos 2 y 4. Otro enfoque para mitigar la inestabilidad es añadir controladores suplementarios al sistema de control del 4QC.

- Se analizó la estabilidad de dos trenes con diferentes controladores, mostrando que ambos casos, aumentar el ancho de banda de control de voltaje del enlace DC ($BWvc$) disminuye el margen de ganancia del sistema, mientras que aumentar el ancho de banda de control de corriente ($BWcc$) aumenta. el margen de ganancia. Esto sugiere fuertemente que la separación espectral entre los anchos de banda del controlador de corriente y voltaje juega un papel crítico en la aparición del LFO.

- Los incrementos de la inductancia de fuga del transformador mientras se mantienen fijo el ancho de banda del controlado de corriente aumenta linealmente el límite de estabilidad. Esto es ventajoso para las LFOs y para filtrar la corriente; sin embargo, limita la capacidad de transferencia de potencia. Por otro lado, la disminución de la capacitancia del enlace DC mientras se mantiene constante el ancho de banda del controlador de voltaje aumenta monótonamente el límite de estabilidad, el cual mejora más rápidamente a valores más bajos del capacitor. Sin embargo, disminuir el valor del capacitor implicará perder la capacidad de filtrado (i.e. incrementa el rizado de voltaje) y también la controlabilidad del sistema. Se encontró que las variaciones de inductancia y capacitancia no interfieren entre sí cuando los anchos de banda de control se mantienen constantes.

- Se observó que los retrasos en la señal de feedforward aumentan los riesgos de LFO. Si la señal feedforward depende de la dinámica del PLL, una dinámica de PLL más rápida mejora la estabilidad de bajas frecuencias.

- Se desarrolló el modelo de pequeña señal de la admitancia de entrada del tren en el marco de referencia síncrono y se comparó con el barrido de frecuencia de la simulación del modelo completo (no lineal) del tren, obteniendo un alto grado de coincidencia. Para esta tarea, se obtuvieron los modelos del control de corriente, control de tensión del enlace DC, PLL y QSG-SOGI. La admitancia de entrada analítica combinada con la impedancia de la red de alimentación de tracción fue capaz de predecir la aparición de oscilaciones de baja frecuencia cuando varios trenes en el depósito operan con bajo consumo de energía, funcionando únicamente los sistemas auxiliares.

- Se presentó el análisis de sensibilidad de la estabilidad del sistema de los parámetros eléctricos y de control. El estudio muestra que la estabilidad LFO es muy sensible a los cambios en la inductancia de fuga, el ancho de banda de control de voltaje y corriente. Debido a la naturaleza no lineal del sistema, la sensibilidad cambia según el punto de operación.

8.2 Contribuciones

Los principales aportes realizados durante el desarrollo de esta tesis son:

- El análisis de la influencia de los elementos constructivos y parámetros de control que contribuyen a la inestabilidad de baja frecuencia utilizando técnicas en el dominio de la frecuencia.

- El análisis de la influencia de los elementos constructivos y parámetros de control que contribuyen a la inestabilidad de baja frecuencia mediante simulación en el dominio del tiempo junto con la identificación de valores propios.

- Un análisis comparativo de dos tipos del sistema de sincronización y dos métodos para generar la señal de feedforward (i.e. método directo e indirecto). Este análisis observó que los retrasos en la señal de feedforward aumenta los riesgos de LFO. Este comportamiento se validó aún más probando tres filtros diferentes del voltaje de catenaria, que demostró que el filtro más rápido (es decir, el que produce los retrasos más pequeños) da como resultado un sistema con mayor margen de ganancia.

- El desarrollo de un nuevo modelo de pequeña señal de la admitancia de entrada del tren. Aquí el principal aporte es modelar la dinámica debido a los errores en la rotación de coordenadas del sistema de control del 4QC, el cual, emplea el uso de funciones de transferencia asimétricas para generar componentes virtuales en cuadratura. Además, se desarrolló el modelo analítico de la función de transferencia QSG-SOGI en el marco sincrónico dq. Como se mencionó en el Capítulo 3, el QSG-SOGI es un sistema asimétrico encargado de filtrar el voltaje de entrada y crear la señal en cuadratura; originalmente opera en el marco alfa-beta; sin embargo, se requería el modelo analítico de este sistema en el marco dq. Finalmente, la combinación de ambos modelos permite derivar la transformación de pequeña señal de vectores el marco dq real y el marco $\widehat{dq}$ estimado.

- El estudio comparativo de dos acciones de control para mitigar el fenómeno LFO. La primera acción consiste se la conoce como POD y se utiliza como un bloque de control externo al sistema de control del voltaje DC. En segundo lugar, se utilizó el método de la impedancia virtual, el cual se consiste en añadir un controlador adicional en lazo interno de control de corriente.

- El diseño e implementación de un emulador de catenaria capaz de reproducir el comportamiento dinámico de la red de tracción ferroviaria, incluido el fenómeno LFO. El emulador permite evaluar la respuesta del convertidor de potencia 4QC en caso de LFO en un banco de pruebas, evitando así las pruebas en la catenaria que podrían llegar a ser muy costosas o incluso inviables.

8.2.1 Publiaciones en Revista

- Frutos, P.; Ladoux, P.; Roux, N.; Larrazabal, I.; Guerrero, J.M.; Briz, F. "Low Frequency Stability of AC Railway Traction Power Systems: Analysis of the Influence of Traction Unit Parameters". *Electronics 2022*, 11, 1593. https://doi.org/10.3390/electronics11101593

- P. Frutos-Galarza et al., "Power-Hardware-in-the-Loop Emulation of the Low-Frequency Oscillation Phenomenon in AC Railway Networks," in *IEEE Access*, vol. 10, pp. 87374-87386, 2022. https://doi.org/10.1109/ACCESS.2022.3198945.

8.2.2 Publicaciones en Conferencia

- P. Frutos, J. M. Guerrero, I. Muniategui, I. Vicente, A. Endemano and F. Briz, "Low-Frequency Oscillations Analysis in AC Railway Networks Using Eigenmode Identification," *2021 IEEE Energy Conversion Congress and Exposition (ECCE)*, Vancouver, BC, Canada, 2021, pp. 1573-1579. https://doi.org/10.1109/ECCE47101.2021.9595947.

8.2.3 Publicaciones en Revisión

- P. Frutos, J. M. Guerrero, I. Muniategui, A. Endemaño, D. Ortega and F. Briz, " Low frequency oscillations in AC railway traction power systems: Train input-admittance calculation and stability analysis," International Journal of Electrical Power & Energy Systems

8.3 Trabajo Futuro

- Obtener el modelo de pequeña señal de la admitancia de entrada del 4QC utilizando un controlador de corriente en el marco de referencia alfa-beta. Esto permitiría comparar su rendimiento con el controlador en el marco de referencia *dq*.

- Modeladar diferentes tipos de sistemas de sincronización y de generación del componente en quadratura con el fin de estudiar su influencia en la estabilidad del sistema ferroviario.

- Diseñar diferentes métodos de control para mitigar las oscilaciones de baja frecuencia y compararlos con los métodos presentados en este documento.

- Explorar diferentes métodos para medir la admitancia de entrada de un sistema monofásico en el marco *dq*. Una opción podría ser utilizar la transformada de Hilbert para calcular componentes ortogonales. Esta es una herramienta

matemática que desplaza cada componente de la señal de entrada 90° con respecto a la propia frecuencia de la componente.

8.4 Financiación

Este trabajo esta financiado en parte por el Gobierno del Principado de Asturias en el marco del proyecto AYUD/2021/50988.

Appendices

Appendix A

Calculation of transfer functions in the synchronous *dq*-frame

The single-phase 4QC control system requires the construction of virtual orthogonal components to operate in the synchronous *dq*-frame. Therefore, it is required to combine single-phase transfer functions (i.e. SISO transfer functions) to treat the control model as a MIMO system that employs both, symmetrical and asymmetrical transfer functions.

In this appendix, the modelling and calculation in the synchronous *dq*-frame of some relevant transfer functions that are part of the 4QC control system is performed.

A.1 QSG-SOGI transfer function

In this section the calculation of the QSG-SOGI transfer function in synchronous *dq*-frame is performed.

A.1.1 Nomenclature

Being the Laplace transform of a variable denoted as $F(s) = \mathcal{L}\{f(t)\}$, the following transformation are defined based on shifting properties of Laplace transform [30]:

- $F^{+} = F(s - j\omega_0) = \mathcal{L}\left\{e^{j\omega_0 t} f(t)\right\}$
- $F^{-} = F(s + j\omega_0) = \mathcal{L}\left\{e^{-j\omega_0 t} f(t)\right\}$
- $F^{++} = F(s - j2\omega_0) = \mathcal{L}\left\{e^{j2\omega_0 t} f(t)\right\}$

- $F^{--} = F(s + j2\omega_0) = \mathcal{L}\left\{e^{-j2\omega_0 t} f(t)\right\}$

Furthermore, using the inverse Euler's formula:

- $\cos\omega_0 t = (e^{j\omega_0 t} + e^{-j\omega_0 t})/2$
- $\sin\omega_0 t = (e^{j\omega_0 t} - e^{-j\omega_0 t})/2j$

A.1.2 Calculation

The QSG-SOGI transfer function can be expressed as (A.1.1) using matrix notation.

$$\begin{bmatrix} \widehat{V}_{n\alpha} \\ \widehat{V}_{n\beta} \end{bmatrix} = \begin{bmatrix} H_{v\alpha}(s) & 0 \\ H_{v\beta}(s) & 0 \end{bmatrix} \begin{bmatrix} V_{n\alpha} \\ V_{n\beta} \end{bmatrix} \tag{A.1.1}$$

$$H_{v\alpha}(s) = \frac{\widehat{V}_{n\alpha}}{V_n} = \frac{k_{vs}\omega_0 s}{s^2 + k_{vs}\omega_0 s + \omega_0^2} \tag{A.1.2}$$

$$H_{v\beta}(s) = \frac{\widehat{V}_{n\beta}}{V_n} = \frac{k_{vs}\omega_0^2}{s^2 + k_{vs}\omega_0 s + \omega_0^2} \tag{A.1.3}$$

The Laplace-domain equation in the $\alpha\beta$ reference frame (A.1.1) becomes a convolution in the time domain as shown in (A.1.4), with $h_{v\alpha}(t)$ and $h_{v\beta}(t)$ being the impulse response of (A.1.2) and (A.1.3) respectively.

$$\begin{bmatrix} \widehat{v}_{n\alpha} \\ \widehat{v}_{n\beta} \end{bmatrix} = \begin{bmatrix} h_{v\alpha}(t) & 0 \\ h_{v\beta}(t) & 0 \end{bmatrix} * \begin{bmatrix} v_{n\alpha} \\ v_{n\beta} \end{bmatrix} \tag{A.1.4}$$

Transformation to the actual dq reference frame is given by (A.1.5).

$$\begin{aligned} \begin{bmatrix} \widehat{v}^e_{nd} \\ \widehat{v}^e_{nq} \end{bmatrix} &= \mathbf{t}_\theta \left(\begin{bmatrix} h_{v\alpha}(t) & 0 \\ h_{v\beta}(t) & 0 \end{bmatrix} * \mathbf{t}_\theta^{-1} \begin{bmatrix} v^e_{nd} \\ v^e_{nq} \end{bmatrix} \right) \\ \mathbf{t}_\theta &= \begin{bmatrix} \cos\omega_0 t & \sin\omega_0 t \\ -\sin\omega_0 t & \cos\omega_0 t \end{bmatrix} \end{aligned} \tag{A.1.5}$$

which yields (A.1.6).

$$\begin{bmatrix} \widehat{v}^e_{nd} \\ \widehat{v}^e_{nq} \end{bmatrix} = \begin{bmatrix} \cos\omega_0 t & \sin\omega_0 t \\ -\sin\omega_0 t & \cos\omega_0 t \end{bmatrix} \begin{bmatrix} h_{v\alpha}(t) * (v^e_{nd}\cos\omega_0 t - v^e_{nq}\sin\omega_0 t) \\ h_{v\beta}(t) * (v^e_{nd}\cos\omega_0 t - v^e_{nq}\sin\omega_0 t) \end{bmatrix} \tag{A.1.6}$$

The expansion of the matrix multiplication is shown in (A.1.7)

$$\begin{bmatrix} \widehat{v}^e_{nd} \\ \widehat{v}^e_{nq} \end{bmatrix} = \begin{bmatrix} \cos\omega_0 t \left(h_{v\alpha}(t) * (v^e_{nd}\cos\omega_0 t - v^e_{nq}\sin\omega_0 t)\right) \\ +\sin\omega_0 t \left(h_{v\beta}(t) * (v^e_{nd}\cos\omega_0 t - v^e_{nq}\sin\omega_0 t)\right) \\ \\ -\sin\omega_0 t \left(h_{v\alpha}(t) * (v^e_{nd}\cos\omega_0 t - v^e_{nq}\sin\omega_0 t)\right) \\ +\cos\omega_0 t \left(h_{v\beta}(t) * (v^e_{nd}\cos\omega_0 t - v^e_{nq}\sin\omega_0 t)\right) \end{bmatrix} \tag{A.1.7}$$

Using the definitions from Appendix A.1.1, it is possible to express the convolutions in (A.1.7) as:

$$\begin{aligned} h_{v\alpha}(t) * (v^e_{nd}\cos\omega_0 t - v^e_{nq}\sin\omega_0 t) &= h_{v\alpha}(t) * \left(v^e_{nd}\frac{e^{j\omega_0 t}+e^{-j\omega_0 t}}{2} - v^e_{nq}\frac{e^{j\omega_0 t}-e^{-j\omega_0 t}}{2j} \right) \\ &= \mathcal{L}^{-1}\left\{ H_{v\alpha}(s)\left(\frac{V^{e+}_{nd}+V^{e-}_{nd}}{2} - \frac{V^{e+}_{nq}-V^{e-}_{nq}}{2j} \right) \right\} \end{aligned} \tag{A.1.8}$$

$$\begin{aligned} h_{v\beta}(t) * (v^e_{nd}\cos\omega_0 t - v^e_{nq}\sin\omega_0 t) &= h_{v\beta}(t) * \left(v^e_{nd}\frac{e^{j\omega_0 t}+e^{-j\omega_0 t}}{2} - v^e_{nq}\frac{e^{j\omega_0 t}-e^{-j\omega_0 t}}{2j} \right) \\ &= \mathcal{L}^{-1}\left\{ H_{v\beta}(s)\left(\frac{V^{e+}_{nd}+V^{e-}_{nd}}{2} - \frac{V^{e+}_{nq}-V^{e-}_{nq}}{2j} \right) \right\} \end{aligned} \tag{A.1.9}$$

Replacing (A.1.8) and (A.1.9) in (A.1.7), the following equation is obtained:

$$\begin{bmatrix} \widehat{v}^e_{nd} \\ \widehat{v}^e_{nq} \end{bmatrix} = \begin{bmatrix} (\cos\omega_0 t)\mathcal{L}^{-1}\left\{ H_{v\alpha}(s)\left(\frac{V^{e+}_{nd}+V^{e-}_{nd}}{2} - \frac{V^{e+}_{nq}-V^{e-}_{nq}}{2j} \right) \right\} \\ +(\sin\omega_0 t)\,\mathcal{L}^{-1}\left\{ H_{v\beta}(s)\left(\frac{V^{e+}_{nd}+V^{e-}_{nd}}{2} - \frac{V^{e+}_{nq}-V^{e-}_{nq}}{2j} \right) \right\} \\ -(\sin\omega_0 t)\,\mathcal{L}^{-1}\left\{ H_{v\alpha}(s)\left(\frac{V^{e+}_{nd}+V^{e-}_{nd}}{2} - \frac{V^{e+}_{nq}-V^{e-}_{nq}}{2j} \right) \right\} \\ +(\cos\omega_0 t)\,\mathcal{L}^{-1}\left\{ H_{v\beta}(s)\left(\frac{V^{e+}_{nd}+V^{e-}_{nd}}{2} - \frac{V^{e+}_{nq}-V^{e-}_{nq}}{2j} \right) \right\} \end{bmatrix} \tag{A.1.10}$$

Applying Laplace transform to (A.1.10) yields:

$$\begin{aligned} \widehat{V}^e_{nd} =& H^+_{v\alpha}\left(\frac{V^{e++}_{nd}+V^e_{nd}}{4} - \frac{V^{e++}_{nq}-V^e_{nq}}{4j} \right) + H^-_{v\alpha}\left(\frac{V^e_{nd}+V^{e--}_{nd}}{4} - \frac{V^e_{nq}-V^{e--}_{nq}}{4j} \right) \\ &+ H^+_{v\beta}\left(\frac{V^{e++}_{nd}+V^e_{nd}}{4j} + \frac{V^{e++}_{nq}-V^e_{nq}}{4} \right) - H^-_{v\beta}\left(\frac{V^e_{nd}+V^{e--}_{nd}}{4j} + \frac{V^e_{nq}-V^{e--}_{nq}}{4} \right) \end{aligned} \tag{A.1.11}$$

$$\begin{aligned} \widehat{V}^e_{nq} =& H^-_{v\alpha}\left(\frac{V^e_{nd}+V^{e--}_{nd}}{4j} + \frac{V^e_{nq}-V^{e--}_{nq}}{4} \right) - H^+_{v\alpha}\left(\frac{V^{e++}_{nd}+V^e_{nd}}{4j} + \frac{V^{e++}_{nq}-V^e_{nq}}{4} \right) \\ &+ H^+_{v\beta}\left(\frac{V^{e++}_{nd}+V^e_{nd}}{4} - \frac{V^{e++}_{nq}-V^e_{nq}}{4j} \right) + H^-_{v\beta}\left(\frac{V^e_{nd}+V^{e--}_{nd}}{4} - \frac{V^e_{nq}-V^{e--}_{nq}}{4j} \right) \end{aligned} \tag{A.1.12}$$

From (A.1.11) and (A.1.12) is seen that in the *dq*-frame, an input voltage of a given frequency ω_0 will produced an output voltage at the same frequency, as well as a component at a frequency $2\omega_0$. For the LFO phenomenon, oscillation frequencies have reported to be no larger than 7 Hz in *dq*-frame [17]. Frequency components at $2\omega_0$ can be therefore safely

disregarded, (A.1.11) - (A.1.12) being simplified to (A.1.13)-(A.1.13).

$$\widehat{V}^e_{nd} \approxeq \frac{V^e_{nd}}{4}\left(H^-_{v\alpha}+H^+_{v\alpha}\right)+j\frac{V^e_{nd}}{4}\left(H^-_{v\beta}-H^+_{v\beta}\right)-\frac{V^e_{nq}}{4}\left(H^-_{v\beta}+H^+_{v\beta}\right)+j\frac{V^e_{nq}}{4}\left(H^-_{v\alpha}-H^+_{v\alpha}\right) \tag{A.1.13}$$

$$\widehat{V}^e_{nq} \approxeq \frac{V^e_{nd}}{4}\left(H^-_{v\beta}+H^+_{v\beta}\right)-j\frac{V^e_{nd}}{4}\left(H^-_{v\alpha}-H^+_{v\alpha}\right)+\frac{V^e_{nq}}{4}\left(H^-_{v\alpha}+H^+_{v\alpha}\right)+j\frac{V^e_{nq}}{4}\left(H^-_{v\beta}-H^+_{v\beta}\right) \tag{A.1.14}$$

Equations (A.1.13) and (A.1.14) can be expressed using matrix notation as (A.1.15)-(A.1.17)

$$\begin{bmatrix} \widehat{V}^e_{nd} \\ \widehat{V}^e_{nq} \end{bmatrix} \approxeq \begin{bmatrix} H^e_{vs-dd}(s) & H^e_{vs-dq}(s) \\ H^e_{vs-qd}(s) & H^e_{vs-qq}(s) \end{bmatrix} \begin{bmatrix} V^e_{nd} \\ V^e_{nq} \end{bmatrix} \tag{A.1.15}$$

$$H^e_{vs-dd}(s) = H^e_{vs-qq}(s) = \frac{1}{4}\left(H^-_{v\alpha}+H^+_{v\alpha}\right)+\frac{j}{4}\left(H^-_{v\beta}-H^+_{v\beta}\right) \tag{A.1.16}$$

$$H^e_{vs-qd}(s) = -H^e_{vs-dq}(s) = \frac{1}{4}\left(H^-_{v\beta}+H^+_{v\beta}\right)-\frac{j}{4}\left(H^-_{v\alpha}-H^+_{v\alpha}\right) \tag{A.1.17}$$

Equations (A.1.16)-(A.1.17) are presented with abbreviate notation defined in Appendix A.1.1. Using the expanded notation yields:

$$\begin{aligned} H^e_{vs-dd}(s) =& \frac{1}{4}\big(H_{v\alpha}(s+j\omega_0)+H_{v\alpha}(s-j\omega_0)\big) \\ &+\frac{j}{4}\big(H_{v\beta}(s+j\omega_0)-H_{v\beta}(s-j\omega_0)\big) \end{aligned} \tag{A.1.18}$$

$$\begin{aligned} H^e_{vs-qd}(s) =& \frac{1}{4}\big(H_{v\beta}(s+j\omega_0)+H_{v\beta}(s-j\omega_0)\big) \\ &-\frac{j}{4}\big(H_{v\alpha}(s+j\omega_0)-H_{v\alpha}(s-j\omega_0)\big) \end{aligned} \tag{A.1.19}$$

A.2 4QC AC-side dynamics coordinate transformation

The 4QC AC-side dynamics corresponds to a RL element and can be defined by (A.2.1).

$$v_n = L_n\frac{di_n}{dt}+R_n i_n + v_t \tag{A.2.1}$$

Assuming that the α voltage and current components coincide with the actual physical single-phase components and that the β signals are perfectly orthogonal, (A.2.1) can be written in $\alpha\beta$ coordinates as:

$$\boldsymbol{v_{n\alpha\beta}} = R_n\boldsymbol{i_{n\alpha\beta}}+L_n\frac{d\boldsymbol{i_{n\alpha\beta}}}{dt}+\boldsymbol{v_{t\alpha\beta}} \tag{A.2.2}$$

Multiplying both sides of (A.2.2) by $e^{-j\omega_0 t}$, then:

$$e^{-j\omega_0 t}\boldsymbol{v_{n\alpha\beta}} = e^{-j\omega_0 t}R_n\boldsymbol{i_{n\alpha\beta}} + e^{-j\omega_0 t}L_n\frac{d\boldsymbol{i_{n\alpha\beta}}}{dt} + e^{-j\omega_0 t}\boldsymbol{v_{t\alpha\beta}} \tag{A.2.3}$$

Transforming (A.2.3) to the synchronous reference frame, (A.2.4) is obtained. [41]:

$$\boldsymbol{v^e_{ndq}} = R_n\boldsymbol{i^e_{ndq}} + e^{-j\omega_0 t}L_n\frac{d}{dt}\left(e^{j\omega_0 t}\boldsymbol{i^e_{ndq}}\right) + \boldsymbol{v^e_{tdq}} \tag{A.2.4}$$

Using product rule for derivatives:

$$\boldsymbol{v^e_{ndq}} = R_n\boldsymbol{i^e_{ndq}} + e^{-j\omega_0 t}L_n e^{j\omega_0 t}\frac{d}{dt}\left(\boldsymbol{i^e_{ndq}}\right) + e^{-j\omega_0 t}L_n\boldsymbol{i^e_{ndq}}\frac{d}{dt}\left(e^{j\omega_0 t}\right) + \boldsymbol{v^e_{tdq}} \tag{A.2.5}$$

which can be simplified as:

$$\boldsymbol{v^e_{ndq}} = R_n\boldsymbol{i^e_{ndq}} + L_n\frac{d\boldsymbol{i^e_{ndq}}}{dt} + j\omega_0 L_n\boldsymbol{i^e_{ndq}} + \boldsymbol{v^e_{tdq}} \tag{A.2.6}$$

and re-writen in the Laplace domain as:

$$\boldsymbol{V^e_{ndq}} = \left(R_n + L_n s + j\omega_0 L_n\right)\boldsymbol{I^e_{ndq}} + \boldsymbol{V^e_{tdq}} \tag{A.2.7}$$

Using matrix notation, the model (A.2.8) is obtained

$$\mathbf{V^e_n} = \begin{bmatrix} R_n + L_n s & -\omega_0 L_n \\ \omega_0 L_n & R_n + L_n s \end{bmatrix}\mathbf{I^e_n} + \mathbf{V^e_t} \tag{A.2.8}$$

where the dq-impedance matrix $\mathbf{Z^e_n}$ is defined by (A.2.9).

$$\mathbf{Z^e_n} = \begin{bmatrix} L_n s + R_n & -\omega_0 L_n \\ \omega_0 L_n & L_n s + R_n \end{bmatrix} \tag{A.2.9}$$

Appendix B

Publications

B.1 Journal publications

B.1.1 Low Frequency Stability of AC Railway Traction Power Systems: Analysis of the Influence of Traction Unit Parameters

Frutos, P.; Ladoux, P.; Roux, N.; Larrazabal, I.; Guerrero, J.M.; Briz, F. "Low Frequency Stability of AC Railway Traction Power Systems: Analysis of the Influence of Traction Unit Parameters". *Electronics 2022*, 11, 1593. https://doi.org/10.3390/electronics11101593

electronics

MDPI

Article

Low Frequency Stability of AC Railway Traction Power Systems: Analysis of the Influence of Traction Unit Parameters

Paul Frutos [1,*], Philippe Ladoux [2], Nicolas Roux [2], Igor Larrazabal [3], Juan M. Guerrero [1] and Fernando Briz [1]

[1] Department of Electrical, Computer & System Engineering, University of Oviedo, 33204 Gijón, Spain; guerrero@uniovi.es (J.M.G.); fbriz@uniovi.es (F.B.)
[2] LAPLACE, Université de Toulouse, CNRS, INPT, UPS, 31000 Toulouse, France; philippe.ladoux@laplace.univ-tlse.fr (P.L.); nicolas.roux@laplace.univ-tlse.fr (N.R.)
[3] Ingeteam Power Technology S.A., Traction R&D, 48170 Zamudio, Spain; igor.larrazabal@ingeteam.com
* Correspondence: frutospaul@uniovi.es

Abstract: Dynamic interactions between AC railway electrification systems and traction unit power converters can result in low frequency oscillation (LFO) of the contact-line voltage amplitude, which can lead to a power outage of the traction substation and the shutdown of train traffic. Several system parameters can influence the low frequency stability of the railway traction power system, including contact-line length and traction unit parameters such as transformer leakage inductance, DC-link capacitance, control bandwidths and synchronization systems. This paper focuses on the influence of these parameters on the LFO. The methodology is based on a frequency-domain analysis. Nyquist and Bode diagrams are used to determine the stability limit. The validation of the method is performed through the use of time-domain simulations.

Keywords: low frequency stability; low frequency oscillations; railway traction system; traction power supply; nyquist stability criteria; input admittance; resonant stability

Citation: Frutos, P.; Ladoux, P.; Roux, N.; Larrazabal, I; Guerrero, J.M.; Briz, F. Low Frequency Stability of AC Railway Traction Power Systems: Analysis of the Influence of Traction Unit Parameters. *Electronics* **2022**, *11*, 1593. https://doi.org/10.3390/electronics11101593

Academic Editors: Rui Castro and Amjad Anvari-Moghaddam

Received: 14 February 2022
Accepted: 6 May 2022
Published: 17 May 2022

1. Introduction

1.1. Review of LFO Events

Modern rail vehicles that operate in the railway system include a large number of power electronic converters aimed to improve performance and efficiency. Despite the benefits, complex dynamic interactions between the railway network and the controlled power converters can produce undesired phenomena, which might result in power system instability, including the LFO phenomenon [1–8], harmonic resonance [8] and electrical resonant instability [9]. The LFO phenomenon has been reported worldwide for different types of railway networks under different operating conditions; see Table 1.

Table 1. LFO reported cases.

Nº	Case	f_0 (Hz)	f_{osc} (Hz)	Time (Year)
1	Zürich, Switzerland [1]	16.7	5	1995
2	Norway [2,3]	16.7	1.6	2007
3	Washington, USA [4]	25	3	2006
4	Thionville, France [5]	50	5	2008
5	Siemens test, Germany [6]	50	7	2006
6	Hudong Depot, China [7]	50	2–4	2008
7	Shanhaiguan Hub, China [8]	50	6–7	2011

Reported events include a 15 kV/16.7 Hz power system supplied from rotary converters [2], a 12 kV/25 Hz system with static frequency converters [4], and 25 kV/50 Hz power systems supplied from the public grid such as the case observed in the sector of Thionville in France [5], shown in Figure 1.

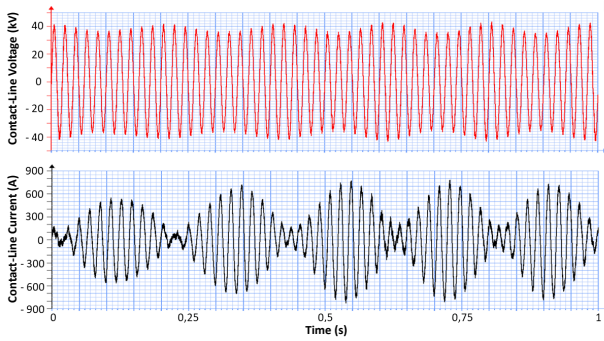

Figure 1. Contact-line voltage and current supplied by the substation. AC 25 kV/50 Hz electric power supply. Measured in Thionville, France. Reprinted with permission from Ref. [5]. Copyright 2014 IEEE.

When LFO occurs, an amplitude modulation of contact-line voltage and current is produced, i.e., the oscillation frequency f_{osc} is presented in the envelope of the signal waveforms, see Figure 1. This is seen in the frequency spectra of voltage and current as a fundamental frequency component at f_0 along with two sideband components at $(f_0 - f_{osc})$ and $(f_0 + f_{osc})$ as explained in [10]. From the events reported in Table 1, the oscillation frequencies reached values up to 7 Hz (i.e., 43–57 Hz in the stationary reference frame). This phenomenon has caused a number of serious issues, such as the malfunction of the protection system, over-voltage and over-current, which could damage the electrical/electronic equipment and cause transportation delays [7].

In the railway system, two specific scenarios in which the LFO phenomenon has been reported are: first, multiple trains in the depot (i.e., all the vehicles located at the same place) [5]; second, a train operating at a very long distance from a substation [3]. From the point of view of the stability analysis, these two scenarios are equivalent, as will be explained in Section 3.1, using the impedance-based small-signal model [6,11,12]. The study presented is applicable to both scenarios. An analysis for multiple trains in different positions of the contact-line is out of the scope of this article, but it should be taken into account for further research. The 25 kV/50 Hz power supply system is considered.

1.2. Content and Contribution

This paper analyzes the influence of some constructive and operational parameters that may contribute to low frequency instability, including contact-line length (i.e., distance from the substation), consumed power on the DC link that supplies the three-phase motor drives, the bandwidth of current and voltage controllers, transformer leakage inductance, DC-link capacitance, synchronization systems and feedforward signals. Since perturbation frequencies are present around f_0, a stability study is performed using an impedance-based analysis in the frequency-domain on the dq synchronous reference frame [11,13]. The train input admittance in the dq frame required for the stability analysis is obtained using a frequency response test as in [5]. Alternatively, the admittance could be obtained from analytical models as in [7,8]; however, these models have been reported to be not accurate enough [14]. Nyquist and Bode diagrams are used to determine the system stability limit, which is defined as the maximum distance from a substation at which a traction unit can

operate safely, or the maximum numbers of traction chains connected in parallel on a specific contact-line sector. This capacity of predicting the stability limit allows to obtain the stability limit curve (SLC) in the complex impedance plane (R, X) [11]. This curve is plotted for a specific traction chain, and it is useful to find the stability limit in any railway traction system. The method for stability analysis used in this article is validated with the use of time-domain simulations. PLECS Blockset software along with MATLAB/Simulink were used for the frequency-domain analysis and for time-domain simulations.

This type of study using frequency-domain stability analysis has not been reported in the literature before; a similar approach of parameter variations study has been performed partially by [4,10] but using eigenvalue migration. Furthermore, in this paper, different types of synchronization systems and some methods to generate the feedforward signal have been considered in a comparison study, which results in a new contribution in the field of low frequency stability.

1.3. Organization

The paper is organized as follows. Section 2 describes the railway traction system model and the control system. Section 3 presents the stability analysis in the frequency-domain for the study of the LFO phenomenon. Section 4 studies the influence of contact-line length; three different cases are studied, and validation of the analysis is performed through simulations. Section 5 deals with the impact of the power consumption on the DC link, stability and limits are calculated for a specific contact-line. Section 6 addresses the combined effect of transformer leakage inductance and current controller parameters. Section 7 deals with the influence of the DC-link capacitor and the voltage controller bandwidth. Section 8 studies the characteristics of the phase-locked loop (PLL) and the impact of the feedforward signal, and four combined cases are considered. Finally, conclusions are drawn in Section 9.

2. Railway Traction System Model for LFO Phenomenon Study

A schematic representation of the railway traction system is shown in Figure 2a. It consists of two main blocks: the power supply network and the traction unit that consists of one or more traction chains [15]. The power supply network is composed of an ideal voltage source at a fixed frequency, the impedance of the substation transformer and the impedance of the contact-line (i.e., transmission line).

An analytical calculation of contact-line impedance performed in [16] using transmission line equations shows that at frequencies around the fundamental frequency $f_0 = 50$ Hz, the contact-line can be approached by an inductive-resistive (RL) element. Capacitive effects would only appear at high frequencies, and could be therefore safely neglected. The simplified RL model is also supported by the experience reported in [1,6,7,12,16], and also is considered in the European standard document for the compatibility of rolling stock and infrastructure EN-50388-2 [17]. Consistently with the previous discussion, Figure 2b shows the main elements of the simplified railway traction system model used for this study, which consists of a single traction chain and an equivalent circuit of the power supply that only considers a resistance (R) and an inductance (L).

The main elements in the traction chain are: an input transformer with its leakage inductance (L_{tr}) and winding resistance (R_{tr}); a single-phase four-quadrant power converter (4QC); a DC-link capacitor (C_d); and traction drives consisting of inverters and motors. In this study, traction drives are modeled as an equivalent current source.

Figure 2c shows the traction chain control system. Two cascaded loops regulate the voltage of the DC link (slow regulation) and the absorbed current at the contact-line (fast regulation) using proportional-integral (PI) regulators [13]. This inner loop is improved with a feedforward estimator that anticipates the voltage drop across the input transformer impedance [13]. To guarantee a power factor close to unity, system synchronization is performed using the estimated contact-line voltage phase angle ($\hat{\theta}$), which is calculated using a PLL. This angle is used for coordinate transformation between the stationary

reference frame and the synchronous reference frame (i.e., dq frame). Independent control of active and reactive power using the currents I_d and I_q can be achieved.

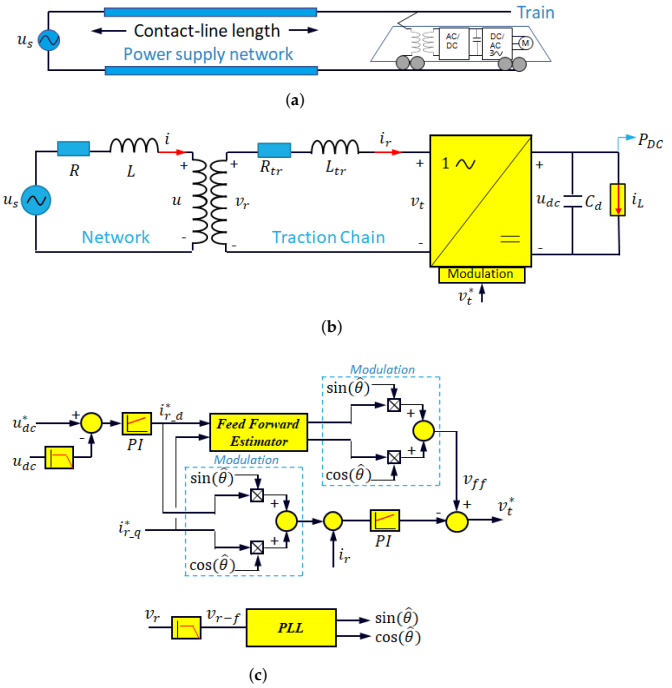

Figure 2. Railway system model and control. (**a**) Railway traction power system, (**b**) Simplified railway system model for the study of LFO. (**c**) Traction chain control system.

In order to obtain the desired current control bandwidth (ω_{bcc}) and voltage control bandwidth (ω_{bvc}), controllers (i.e., kp_{cc}, ki_{cc}, kp_{vc}, ki_{vc}) were tuned using Equations (1) and (2) as described in [13].

$$kp_{cc} = L_{tr} \cdot \omega_{bcc} \ , \ ki_{cc} = \frac{L_{tr} \cdot \omega_{bcc}^2}{\pi}, \tag{1}$$

$$kp_{vc} = C_d \cdot \omega_{bvc} \ , \ ki_{vc} = \frac{C_d \cdot \omega_{bvc}^2}{\pi} \tag{2}$$

3. Impedance-Based Stability Analysis for the Study of the Low Frequency Oscillations Phenomenon

This section describes the use of the frequency-domain stability criteria applied to the impedance-based small-signal model of the railway traction system, aimed to determine the risk of LFO instability. This small-signal model covers the study of the LFO phenomenon reported for multiple trains located at the same place (e.g., trains at depot) and for the case of a train operating at a very long distance from a substation. For both scenarios, the stability study could be performed considering an equivalent case that only takes into account the interaction between a multiple value of the power supply base impedance and a single traction chain.

3.1. Impedance-Based Small-Signal Model

The small-signal model of the traction railway system in the frequency-domain, developed and presented in [2,6,9,12], is shown in Figure 3a, where U_s is the no-load voltage at the substation, U is the contact-line voltage, I is the contact-line current, Z_s is the base network impedance, n is a multiplicative factor of base impedance, Y_t is the admittance of a traction chain, and m is the number of traction chains. Additionally, it is important to define $Z = nZ_s$ as the total network impedance (i.e., power supply impedance) that includes the upstream grid impedance, the substation impedance and the contact-line impedance. The total input admittance is $Y = mY_t$. The delta symbol (Δ) refers to the small variations of the variables around a specific operating point at which the small-signal analysis will be performed. Figure 3 shows that the railway traction small-signal model can be represented as a closed-loop system, whose transfer function $G(j\omega) = \Delta I / \Delta U_s$ is given by Equation (3).

$$G(j\omega) = \frac{mY_t}{1 + nmY_tZ_s} = \frac{Y}{1 + YZ} \tag{3}$$

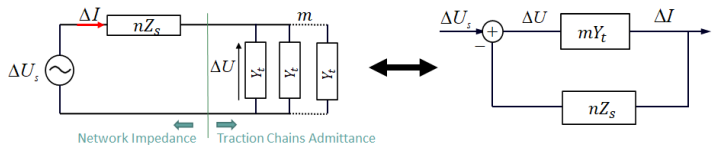

(**a**) (**b**)

Figure 3. Closed loop system equivalence of small-signal model for n network impedance units and m traction chains. (**a**) Railway traction system small-signal model, (**b**) closed loop system.

The denominator of Equation (3) is called the characteristic equation [18], which should not be equal to zero for any frequency in order to guarantee system stability [5]. From the point of view of the stability analysis the multiple number of the base impedance that composes the overhead line (n) and the number of traction chains (m) are interchangeable terms, meaning that $m \cdot n$ will be a critical coefficient of the characteristic equation. Therefore, a system composed of a number of identical traction chains is equivalent to a system with a single traction chain fed through a multiple of the power base impedance; for instance, the case $(n = 1, m = 4)$ has the same characteristic equation as the case $(n = 4, m = 1)$. For the sake of simplicity, in this article $n = m = 1$ will be assumed unless otherwise stated.

3.2. Network Impedance and Traction-Chain Admittance

As explained in Section 2, the control system of the traction chain considers a dq reference frame aligned to the contact-line voltage that allows independent control of active and reactive power using the currents I_d and I_q, respectively. Therefore, the power supply and the traction chain form a multiple-input and multiple-output (MIMO) system in the dq reference frame.

Equation (4) shows the network impedance matrix in the dq reference frame [12,19], which is expressed in terms of the network resistance, R, the network inductance, L, the fundamental angular frequency, $\omega_0 = 2\pi f_0$, and the perturbation (i.e., excitation) angular frequency, $\omega = 2\pi f$.

$$\mathbf{Z_{DQ}}(j\omega) = \begin{bmatrix} Z_{dd}(j\omega) & Z_{dq}(j\omega) \\ Z_{qd}(j\omega) & Z_{qq}(j\omega) \end{bmatrix} = \begin{bmatrix} R + j\omega L & -\omega_0 L \\ \omega_0 L & R + j\omega L \end{bmatrix} \tag{4}$$

Equation (7) shows the input admittance matrix of the traction chain that is obtained using the frequency response scanning method described in [5], where small-signal variations in the $d \rightarrow \sin(\omega_0 t)$ and $q \rightarrow \cos(\omega_0 t)$ components of the contact-line voltage, ΔU_d and ΔU_q, are applied to the traction chain at a certain perturbation angular frequency, ω,

see Equation (5). Then, variations of the current components from Equation (6), $(\Delta I_d, \angle\phi_d)$ and $(\Delta I_q, \angle\phi_q)$, related to each perturbation frequency, are extracted [5,12]. For this study, the perturbation frequencies are in a range up to 20 Hz.

$$u(t) = (U_d + \Delta U_d \sin(\omega t))\sin(\omega_0 t) + \left(\Delta U_q \sin(\omega t)\right)\cos(\omega_0 t) \quad (5)$$

$$i(t) = (I_d + \Delta I_d \sin(\omega t + \phi_d))\sin(\omega_0 t) + \left(I_q + \Delta I_q \sin(\omega t + \phi_q)\right)\cos(\omega_0 t) \quad (6)$$

$$\mathbf{Y_{DQ}}(j\omega) = \begin{bmatrix} Y_{dd}(j\omega) & Y_{dq}(j\omega) \\ Y_{qd}(j\omega) & Y_{qq}(j\omega) \end{bmatrix} = \begin{bmatrix} \frac{\Delta I_d \angle\phi_d}{\Delta U_d}\Big|_{\Delta U_q=0} & \frac{\Delta I_d \angle\phi_d}{\Delta U_q}\Big|_{\Delta U_d=0} \\ \frac{\Delta I_q \angle\phi_q}{\Delta U_d}\Big|_{\Delta U_q=0} & \frac{\Delta I_q \angle\phi_q}{\Delta U_q}\Big|_{\Delta U_d=0} \end{bmatrix} \quad (7)$$

Examples of the dq admittance matrix are presented in Sections 4 and 8.

3.3. Stability Criteria

The rail vehicle connected to an ideal power source is considered a stable system [20]. The impedance of the railway power supply network is a passive element (i.e., RL element), which implies it is also stable. Therefore, these two elements are stable in an open loop. Stability criteria for the interconnection of these two elements in a closed loop system are presented in this section for the study of the LFO phenomenon.

A factorization of the system open loop transfer function, $\mathbf{L}(j\omega)$, is described in Equation (8), where $\mathbf{\Lambda}(j\omega)$ is the eigenvalue matrix and $\mathbf{P}$ is the eigenvector matrix [12,15].

$$\mathbf{L}(j\omega) = \mathbf{Y_{DQ}}(j\omega)\mathbf{Z_{DQ}}(j\omega) = \mathbf{P}\mathbf{\Lambda}(j\omega)\mathbf{P}^{-1} \quad (8)$$

$$\mathbf{\Lambda}(j\omega) = \begin{bmatrix} \lambda_1(j\omega) & 0 \\ 0 & \lambda_2(j\omega) \end{bmatrix} \quad (9)$$

From Equation (9), $\mathbf{\Lambda}(j\omega)$ is presented as a diagonal matrix that allows to study the stability of the eigenvalues $\lambda_1(j\omega)$ and $\lambda_2(j\omega)$ as two decoupled single-input single-output (SISO) systems.

Rever's criterion applied in a Bode diagram [11] and Nyquist criterion [18] are widely used to analyze the stability of SISO systems in the frequency-domain. Both criteria are equivalent, and either one is used at the authors' convenience in this paper. These criteria have been selected since they are trusted and verified, and have been employed in previous studies of low frequency stability. Rever's criterion was selected for the study performed in [12,15], while the Nyquist criterion was used in [6,19,21].

The stability criterion based on Revers specifies that the closed-loop system is stable if, at the crossover frequency f_c, at which $Arg(\lambda_{1,2}(j \cdot 2\pi \cdot f_c)) = -180^o$, the module of the open loop transfer function is less than 1 in absolute units (i.e., less than 0 decibels) [11]. In a similar approach, the Nyquist criterion specifies that the closed loop system is stable if the eigenvalues do not encircle the point $(1, -180^o)$ in the complex plane [18]. Both criteria are equivalent, and either one is used at the authors' convenience in this paper.

The gain margin is defined as $GM = 1/|\lambda_{1,2}(2\pi f_c)|$; therefore, stability is ensured for a gain margin larger than 1 in absolute units (i.e., positive values in db). At point $|\lambda_{1,2}| = 1$, the phase margin is defined as PM = $(Arg(\lambda_{1,2}) - (-180^o))$ [18].

3.4. Stability Limit Curve in the Network Reactance (X) and Resistant (R) Complex Plane

From Section 3.3, the stability limit is reached when any of the eigenvalues is $\lambda_{1,2} = (1, -180^o) = -1$. Thus, for a specific traction chain with an associated input admittance $\mathbf{Y_{DQ}}$, a set of values of network reactance, X, and resistance, R, can be tested to find a curve $X = X(R)$ in the complex impedance plane that takes the system to the stability limit as explained in [12]. This curve can be obtained based on an iterative process using three nested loops. The first loop is used to modify the value of R, the next loop modifies the inductance L, and the third loop checks fulfillment of the critical condition of stability by

the eigenvalues. As explained in [12], since this iterative process is performed using discrete steps, the following thresholds are defined for the eigenvalues that reach the stability limit:

- $-180^{o} < Arg(\lambda_{1,2}) < -178^{o}$
- $0.98 < |\lambda_{1,2}| < 1$

4. Influence of Contact-Line Length on the Railway Traction System Stability

In this section, the stability criteria described in Section 3 are used. A traction unit connected to a contact-line with different lengths (i.e., different network impedance) is considered. Only one traction chain per traction unit is considered (i.e., $m = 1$). The study presents three different cases: a stable system, a system at its stability limit, and an unstable system. Time-domain simulations will be used to verify the stability analysis performed in the frequency-domain.

4.1. Traction Chain Input Admittance

The dq input admittance of the traction chain is presented in Figure 4. The electrical and control parameters of the traction chain are found in Table 2.

Table 2. Traction chain parameters.

Symbol	Description	Value
U	Contact-line voltage	25 kV
f_0	Fundamental frequency	50 Hz
L_{tr}	Leakage inductance	1 mH
C_d	DC-link capacitor	16 mF
BW_{vc}	Voltage control bandwidth	8 Hz
BW_{cc}	Current control bandwidth	100 Hz
P_{DC}	Power at DC-link	100 kW

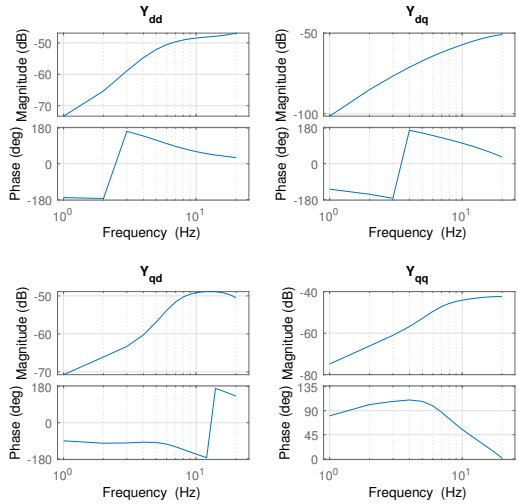

Figure 4. Traction-chain input admittance. Frequency range: 1–20 Hz.

4.2. Network Impedance

The components of the network impedance Z are the upstream grid impedance Z_{ug}, the substation impedance Z_{sst}, and the contact-line impedance $Z_{cl} = d \times Z'_{cl}$, which depends on the distance (d) between the traction unit and the substation (i.e., contact-line length) [12]. See Equation (10).

$$Z = 2 \times Z_{ug} + Z_{sst} + d \times Z'_{cl} \tag{10}$$

The parameters used in this study are the following:

- Z_{ug} = (0.5 Ω; 80º)
- Z_{sst} = (5.5 Ω; 80º)
- Z'_{cl} = (0.5 Ω/km; 80º)

The total network line impedance $Z = nZ_s$ is used for each case of study, where Z_s = (448.1 Ω; 80º) is the base impedance at the stability limit, which occurs at 883.3 km distance. A value $n = 1$ corresponds to the stability limit case; $n = 0.5$ and $n = 1.5$ will be used as examples for the stable and unstable cases. Here, the distance to reach the stability limit is theoretical [12], and it is much higher than the typical length of a sector (around 50 km). In the 25 kV/50 Hz power supply, all the sectors are electrically isolated and there is one transformer per sector. The theoretical distances are used to facilitate the stability study (i.e., to find the stability limit) since only one traction chain is being considered for the analysis [15], so, for a unit equipped with more than one traction chain, the distance limit is reduced according to the equivalence between n and m, explained in Section 3.1. Considering 50 km as the maximum length of a sector in a 25 kV/50 Hz power supply system and vehicles equipped with four traction chains, the stability limit equivalence occurs when 3.55 vehicles are operating at the end of the sector line.

4.3. Stability Analysis

Using the traction chain input admittance matrix and the network impedance matrix, the system eigenvalues of the open-loop transfer function for the three study cases are calculated from Equation (8); they are shown in Figure 5, where the Bode diagram and the Nyquist plot are used for representation. The marked dots in the Bode diagram identify the gain and phase margins. In the Nyquist plot, the gain margin is the reciprocal absolute value of the intersection point between the eigenvalue curve with the negative real axis.

Increasing the contact-line length increases the gain of the total network impedance but keeps constant its phase. Therefore, the variation of contact-line length modifies only the gain of the eigenvalues λ_1 and λ_2 as shown in Figure 5a.

In the same figure, it is seen that the phase of eigenvalue λ_2 never intersects $-180º$ at any frequency, which means that this eigenvalue is not causing instability. This applies to the three study cases. The same conclusion is reached using the Nyquist stability criterion in Figure 5b since λ_2 never encloses -1. For the stable case (red curve), the eigenvalue λ_1 at crossover frequency f_c (i.e., crossing phase at $-180º$) has a magnitude lower than 1, which fulfills the stability criterion explained in Section 3.3. Therefore, for this case, both system eigenvalues guarantee stability.

Increasing the power supply impedance by a factor of two (i.e., $n = 0.5$ to $n = 1$) will move the eigenvalue from $\lambda_1(j2\pi f_c) = (0.5, -180º)$ to $\lambda_1(j2\pi f_c) = (1, -180º)$, causing the system to reach the stability limit operational point. Similarly, when the network impedance is increased by a factor $n = 1.5$, the eigenvalue will go to $\lambda_1(j2\pi f_c) = (1.5, -180º)$, see Figure 5a; thus, the system is not fulfilling the stability criterion anymore and the system becomes unstable.

The same analysis can be done using the Nyquist plot from Figure 5b. For the stable case, the eigenvalue λ_1 does not encloses -1, which fulfills the Nyquist stability criterion; however, the eigenvalue λ_1 intersects the negative real axis; therefore, a risk of instability is present when increasing the gain of the critical eigenvalue (i.e., increasing the power supply

impedance or the number of traction chains, see the equivalence of n and m explained in Section 3.1).

It is important to notice from Figure 5 that the gain margin is less than 1 when systems are unstable, equals 1 at the stability limit, and takes values greater than 1 when the system is stable, so it can be used as the degree of safety from 1 (i.e., minimum value of safety) to infinite (i.e., best case). The gain margin also indicates the number of network impedance units or traction chains where the system reaches the stability limit. On the other hand, the crossover frequency corresponds to the oscillation frequency at the stability limit.

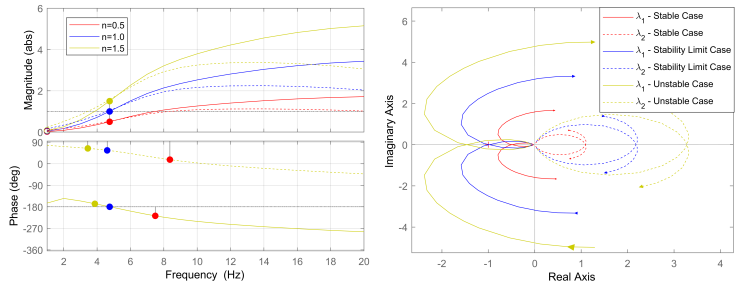

(**a**) (**b**)

Figure 5. System eigenvalues (λ_1, λ_2) of the three study cases. Stable case (red): gain margin = 2 at 4.75 Hz; stability limit case (blue): gain margin = 1 at 4.75 Hz; unstable case (yellow): gain margin = 0.667 at 4.75 Hz. (**a**) Bode Diagram, (**b**) Nyquist Diagram.

Time-domain simulations were performed to verify the stability analysis developed in this section. Figure 6 shows the simulation for the operating point of each study case. DC-link voltage, contact-line voltage, and traction chain current are presented. Initially, the system is operating at a stable state close to the substation; then, the power supply impedance is increased in three steps. The first step change of $0.5 \cdot Z_s$ occurs at $t = 5$ s; here, the system experiences a small oscillation that is damped quickly, and the system is taken again to a stable state. A second step change of $0.5 \cdot Z_s$ in the power supply impedance occurs at $t = 6$ s, where the time response is oscillatory and no damping is present, but the system is still stable; the oscillation frequencies of the DC-link voltage, the envelope of the contact-line voltage and the current correspond to the oscillation frequency predicted by the impedance-based stability analysis; a frequency around 4.75 Hz can be seen in the figure. Finally, following the increase of the power supply impedance at $t = 8$ s, the system becomes unstable.

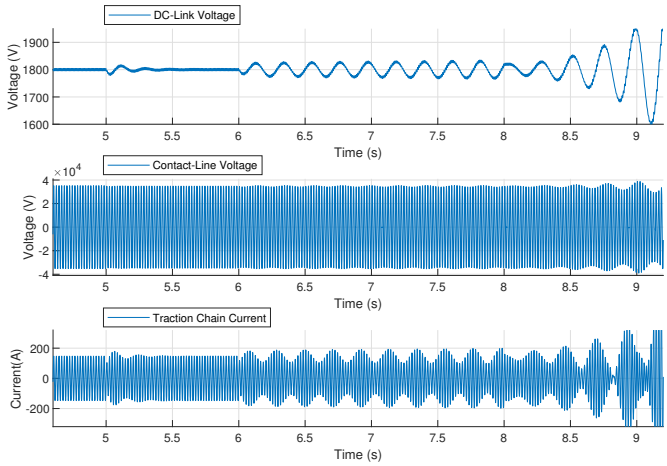

Figure 6. Time-domain simulations. From top to bottom: DC-link voltage, contact-line voltage and train current. Step changes of power supply impedance are consecutively applied along the simulation time. The stable case, stability limit case and unstable case are found at times $t = 5$ s, $t = 6$ s and $t = 8$ s, respectively.

4.4. Stability Limit Curve

Figure 7 shows the stability limit curve of the traction chain in the network reactance (X) and resistance (R) complex plane with an additional dimension to show the oscillation frequency. The stability limit curve separates the stable region and unstable region.

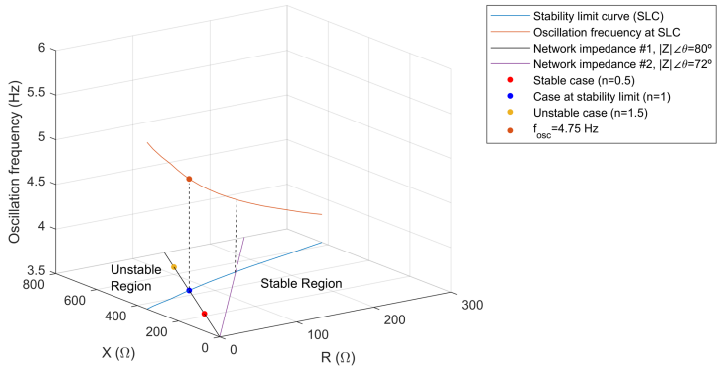

Figure 7. Stability limit curve of the traction chain in the network reactance (X) and resistance (R) complex plane with the corresponding oscillation frequencies. At $P_{DC} = 100$ kW. Power supply system: 25 kV/50 Hz.

From this figure, it can be seen that to go from the unstable region to the stable region, the network resistance must be increased, which suggests that this resistance works as a damping mechanism. On the other hand, for larger values of the reactance, the railway traction power system becomes unstable.

Two different types of contact-lines with a different ratio of reactance and resistance (i.e., different phase) are considered in this example to locate the stability limit. The contact-line impedance grows linearly with the distance (as a parametric variable) until reaching the stability limit, which is the crossing point between the SLC and the impedance linear curve. Figure 7 shows the operating point of the three study cases when the traction chain is located at a different distance from the substation.

5. Influence of Power Absorbed at the DC-Link of the Traction Chain

For this study, the case at stability limit from Section 4 is considered as a reference (i.e., base case). System stability is studied for variations in power consumption at the DC link. For this purpose, the traction chain input admittance matrix is calculated for different power levels and stability is checked using the network base impedance ($Z = Z_s$) from the last section.

Since the eigenvalue λ_2 has no risk of instability, it is neither considered nor plotted. A Bode diagram of the system eigenvalue λ_1 is shown in Figure 8, where the evolution of the gain margin and the phase margin are determined as a function of power consumption from 100 kW to 1.2 MW. Increasing the power from 100 to 500 kW increases the gain and phase margin while it reduces the oscillation frequency; thus, the system stability is improved, and the limit distance increases as well. This is also seen in Figure 9, which shows the stability limit curve plotted for different levels of power. The intersection point of each stability limit curve with the network impedance gives the distance limit and the maximum network impedance that ensures stability for each power level. It is important to note that for power levels greater than 500 kW, the phase of the eigenvalue λ_1 is always below the limit -180^{o} (cf. Figure 8), so the gain margin becomes infinite and there is no risk of instability at any distance for this specific contact-line. This also can be appreciated from Figure 9, where the stability limit curves for power levels of 600 kW and 700 kW never cross the network impedance curve.

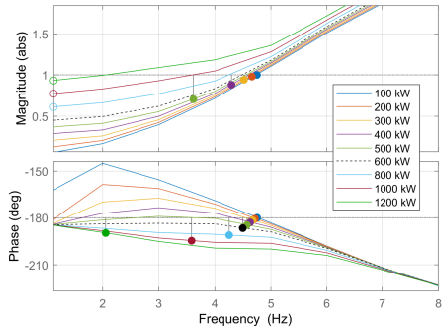

Figure 8. Bode diagram of system eigenvalue λ_1 for different levels of power consumption. Network Impedance: $Z = Z_s$.

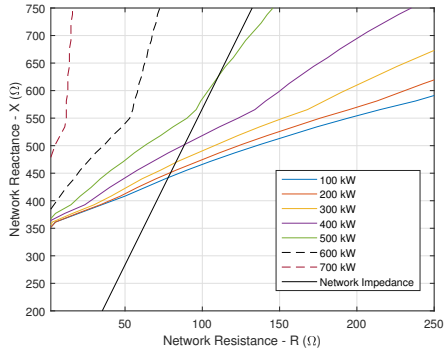

Figure 9. Stability limit curve of traction chain in the network reactance (X) and resistant (R) complex plane. Different levels of power consumption.

Figure 9 shows that the slope of SLC increases with power, which means that at higher power consumption less damping (i.e., network resistance) is needed to maintain system stability. From this figure, the initial point of SLC at $R = 0\,\Omega$ increases with power consumption in a non-linear manner.

Although it is shown that for high power levels the system stability improves and the risk of instability is eliminated, the phase diagram from Figure 8 shows that at very high powers the phase margin starts to decrease going closer to -180^{o} at very low frequencies. Therefore, the risk of instability needs to be checked at very high powers as well as for low power to ensure LFO stability, as was performed in this study.

Similar behavior of low frequency stability has been reported in [4,10] for variations in power consumption. In contrast to this paper where stability analysis is performed in the frequency-domain, eigenmodes identification techniques were used in [4,10] to determine the stability limit.

6. Influence of Current Controller and 4QC Transformer's Leakage Inductance

This section discusses the impact that the inner current controller can have on LFO formation, as well as the influence of leakage inductance of the traction chain transformer. Stability analysis is performed using the network impedance at the stability limit of the reference case ($Z = Z_s$) presented in Section 4. The power consumed at the DC link is $P_{DC} = 100$ kW.

6.1. Influence of Current Controller

The input admittance of a traction chain was calculated for different values of the current controller bandwidth ($\omega_{bcc} = 2\pi \cdot BWcc$), so kp_{cc} and ki_{cc} were modified and tuned using Equation (1), the rest of electrical and control parameter remaining constant.

According to Figures 10 and 11, increasing the current controller bandwidth leads to a raise of the gain margin, which improves system stability and increases the distance limit. Moreover, it is noticed that the oscillation frequency at the stability limit (i.e., crossover frequency) increases as well.

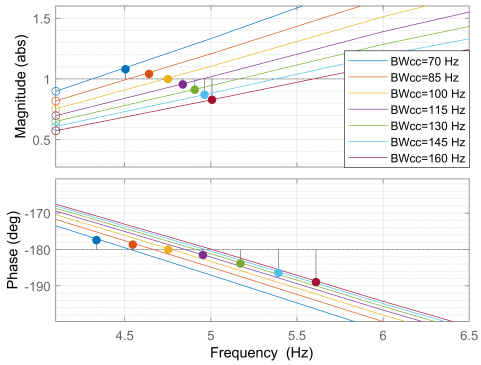

Figure 10. Bode diagram of the system eigenvalue λ_1. Variation of current controller bandwidth.

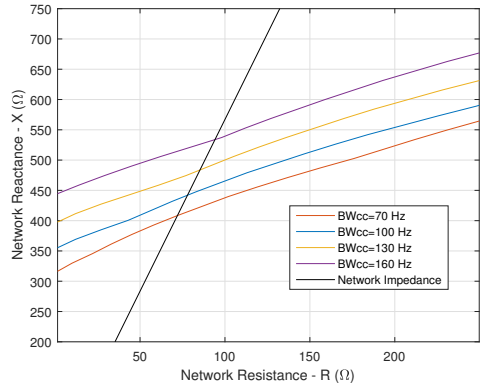

Figure 11. Stability limit curve of a traction chain in the network reactance (X) and resistant (R) complex plane. Variation of current controller bandwidth.

As shown in Figure 11, the stability limit curve shifts parallel to the base case at $BWcc = 100$ Hz and proportionally to the variation of the bandwidth. This characteristic suggests a linear relationship between the current control bandwidth and the maximum distance from the substation that a traction chain can reach (it could also be the maximum number of traction units in the line, see Section 3.1).

6.2. Influence of the Transformer Leakage Inductance

Figure 12 shows the Bode diagram of eigenvalue λ_1 when variations of the transformer leakage inductance L_{tr} are performed from 50% to 150% of the nominal value (1 mH). The rest of the electrical and control parameters are kept constant. From this figure, larger values of the leakage inductance improve LFO stability, while the crossover frequency is reduced. Furthermore, Figure 13 shows that for larger values of leakage inductance, the stability limit curve shifts up parallel to the reference curve. From these figures, a linear relation seems to be present among the transformer leakage inductance, the gain margin, and the distance limit.

It is important to notice that increasing the leakage inductance, while current controller gains remain constant, results in a decrease of the bandwidth of the current control, which should decrease the stability limit according to results found in Section 6.1. Therefore, two effects are happening at the same time in this analysis, and they are opposite. The next section deals with this issue to determine the real effect of leakage inductance variations.

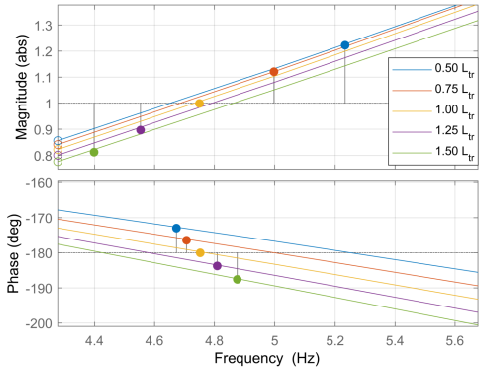

Figure 12. Bode diagram of the system eigenvalue λ_1. Variation of leakage inductance.

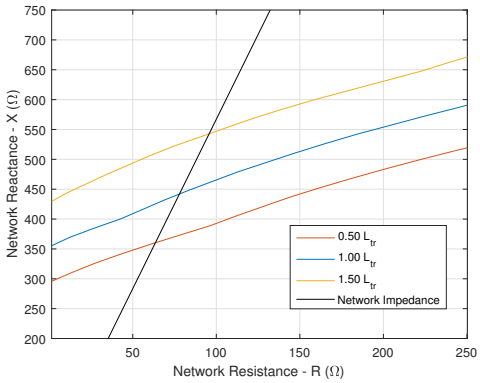

Figure 13. Stability limit curve of a traction chain in the network reactance (X) and resistance (R) complex plane. Variation of leakage inductance.

6.3. Transformer Leakage Inductance Variation with Constant Current Controller Bandwidth

In this section, variations in the leakage inductance are made while the control parameters kp_{cc} and ki_{cc} are re-tuned to maintain the current regulator bandwidth constant at 100 Hz. Figure 14 shows the eigenvalue λ_1 and the gain margin for different values of the inductance, from 50% to 150% of the nominal value (1 mH), as in the previous section. It can be seen that increasing L_{tr} increases the gain margin; thus, the stability is improved. This is also confirmed by the results shown in Figure 15, where stability limit curves resulting from inductance variations are parallel to the reference case. From this figure, a linear relation between the inductance variation and the limit distance is also suggested.

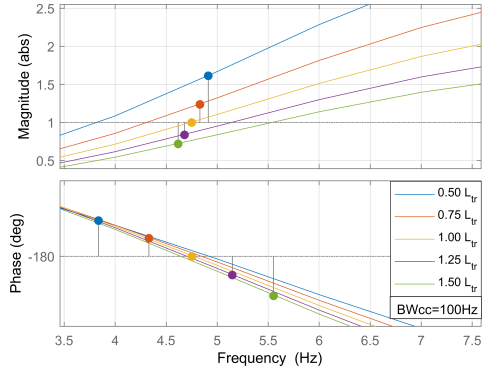

Figure 14. Bode diagram of the system eigenvalue λ_1. Variation of leakage inductance while the keeping current controller bandwidth at 100 Hz.

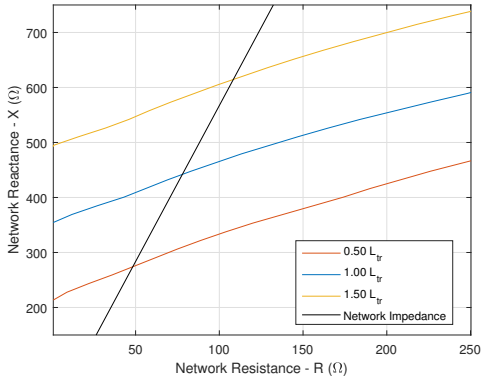

Figure 15. Stability limit curve of a traction chain in the network reactance (X) and resistant (R) complex plane. Variation of leakage inductance while keeping the current controller bandwidth at 100 Hz.

6.4. Summary

Table 3 summarizes the analysis performed in this section. A linear relationship among leakage inductance, current controller bandwidth, and the gain margin was found in this study. The variation of the current controller bandwidth as described in Section 6.1 results in proportional variation of the stability margin. According to Section 6.3, when

Electronics **2022**, *11*, 1593

the controllers are adjusted to keep the bandwidth constant, the independent effect of the leakage inductance variation provokes proportional variations in the gain margin as well. On the other hand, from Section 6.2, it is known that the variation of only the leakage inductance implies the contrary effect on the bandwidth; therefore, a coupled effect that cancels the action of the inductance variation is presented; thus, the gain margin variation results in the superposition of the first two independent effects as shown in the table.

Comparing Figures 13 and 15, it is clear that the effect of leakage inductance variations while keeping constant the current control bandwidth has a larger impact compared to the case where only leakage inductance is modified.

Table 3. Impact of current controller and transformer leakage inductance in LFO stability. Arrows ↑ stands for increments and ↓ stands for decrements.

L_{tr}	kp_{cc} & ki_{cc} Adjusted	BW_{cc}	Stability Margins
-	YES	↑	↑↑
↑	YES	-	↑↑↑
↑	NO	↓	↑↑↑ + ↓↓ = ↑

7. Influence of Voltage Controller Bandwidth and DC-Link Capacitance

This section discusses the impact that the voltage controller can have on LFO stability, as well as the influence of the DC-link capacitance. Stability analysis is performed using the network impedance at the stability limit of the reference case ($Z = Z_s$) presented in Section 4. The power consumed at the DC link is $P_{DC} = 100$ kW.

7.1. Influence of Voltage Controller Bandwidth

The input admittance of the traction chain was calculated for different values of the voltage controller bandwidth ($\omega_{bvc} = 2\pi \cdot BWvc$), with kp_{vc} and ki_{vc} being tuned using Equation (2). The remaining electrical and control parameters have been kept constant.

According to Figures 16 and 17, decreasing the voltage controller bandwidth increases the gain margin, which improves system stability and increases the distance limit. Furthermore, it is observed that this action provokes the oscillation frequency decreases. From Figure 17, smaller values of voltage controller bandwidth have stability limit curves with larger slopes, which means that less damping (i.e., network resistance) is needed to maintain system stability when the network inductance increases.

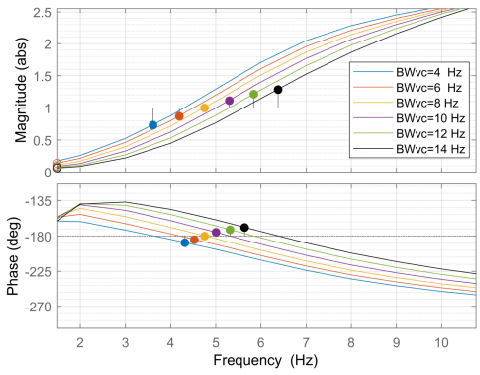

Figure 16. Bode diagram of the system eigenvalue λ_1 for different values of voltage controller bandwidth.

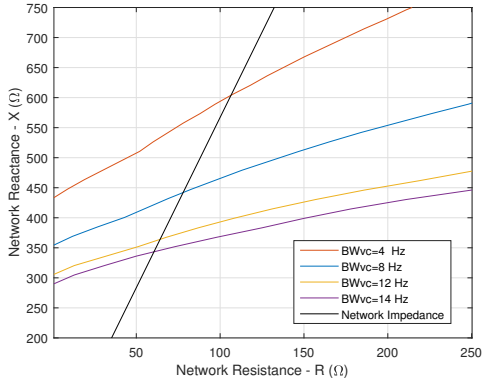

Figure 17. Stability limit curve of a traction chain in the network reactance (X) and resistant (R) complex plane. Variation of voltage controller bandwidth.

7.2. Influence of DC-Link Capacitance

Figure 18 shows the Bode diagram of the critical eigenvalue λ_1 for different values of the DC-link capacitance, from 50% to 200% of its nominal value (16 mF). Other electrical and control parameters are kept constant.

Variation of DC-link capacitance has a non-linear impact on LFO stability: decreasing C_d increments the gain margin; thus, stability is improved and the crossover frequency increases. On the other hand, increasing C_d leads to an unstable system, but at some point, this action is reversed, so at double the nominal value, the system becomes stable again. This behavior is also appreciated in Figure 19, which shows that decreasing capacitance by half has a considerable improvement in the stability limit curve. Increasing capacitance slightly decreases the stability limit, but when the capacitance reaches 200% of its nominal value, the limit is the same as the reference case.

It is important to note that the variation in DC-link capacitance implies that the voltage controller bandwidth is modified as well, so the next section analyzes this issue.

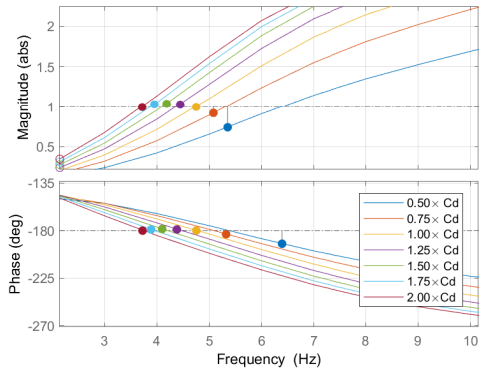

Figure 18. Bode diagram of the system eigenvalue λ_1. Variation of DC-link capacitance.

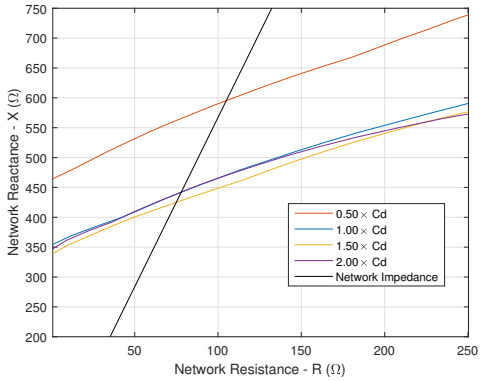

Figure 19. Stability limit curve of a traction chain in the network reactance (X) and resistant (R) complex plane. Variation of DC-link capacitance.

7.3. DC-Link Capacitance Variation with Constant Voltage Controller Bandwidth

In this section, variations in the DC-link capacitance are made while the control parameters kp_{vc} and ki_{vc} are tuned in order to maintain a constant bandwidth of 8 Hz according to Equation (2).

Figure 20 shows the eigenvalue λ_1 and the gain margin evolution for different values of the capacitance, from 50% to 200% of its nominal value (16 mF). Decreasing C_d from the nominal value raises the gain margin; thus, stability is improved. On the other hand, increasing C_d leads to an unstable system.

Figure 21 shows that decreasing capacitance moves the stability limit curve up, and increasing the capacitor takes the curve down. From these two figures, the non-linear relationship between the variations of DC-link capacitance, gain margin and stability limit is appreciated, since the sensitivity of the variation is not the same. Gain margin and stability limit variations seem to be more sensitive at lower values of C_d.

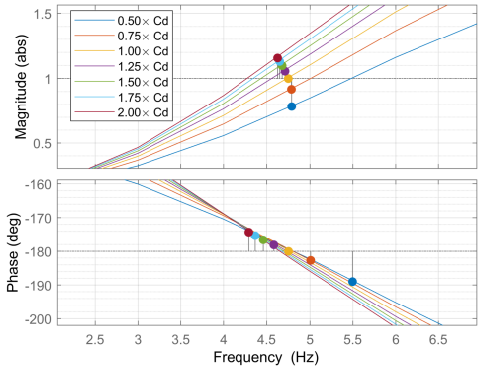

Figure 20. Bode diagram of the system eigenvalue λ_1. Variation of DC-link capacitance while keeping the voltage controller bandwidth at 8 Hz.

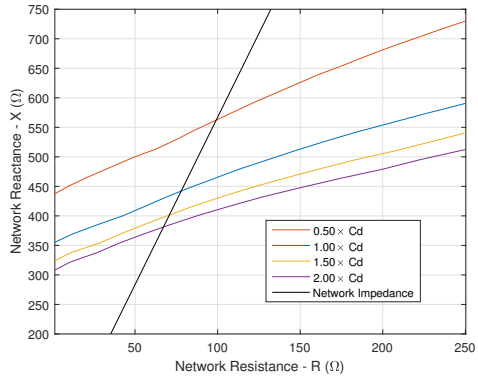

Figure 21. Stability limit curve of a traction chain in the network reactance (X) and resistant (R) complex plane. Variation of DC-link capacitance while keeping the voltage controller bandwidth at 8 Hz.

7.4. Discussion

Although the study for the variation of voltage controller bandwidth and DC-link capacitance shows a non-linear relationship among these parameters and the stability margins, lower voltage control loop bandwidths and lower values of DC-link capacitance always improve the LFO stability in the range of variations performed in this study.

A linear behavior was found only in a very small variation range (around 10% of nominal values). Table 4 summarizes the relationships between the variation of the parameters and the stability margins for very small variations.

From Table 4, three linear events are identified. First, decreasing the voltage controller bandwidth increases stability margins. Second, variation of DC-link capacitance, while the voltage controller bandwidth is kept constant, is inversely proportional to the variation of the stability margin. Finally, decreasing only the DC-link capacitance implies the superposition of the first two events. These trends can be seen in Figure 22, which shows that decreasing capacitance by 10% while BW_{vc} is kept constant (i.e., re-tuning controllers) goes further to the right of the critical point (i.e., more stable) than the case when only the capacitance is decreased.

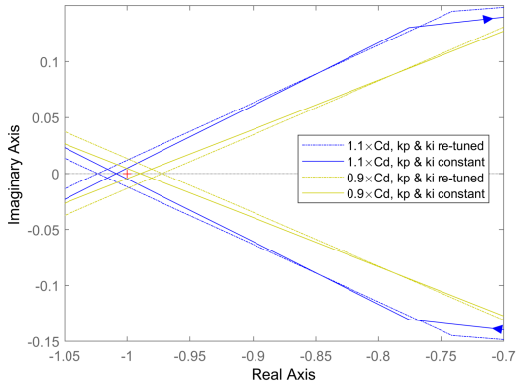

Figure 22. Nyquist plot for the eigenvalue λ_1. Small variation of DC-link capacitance.

Table 4. Impact of very small variations of voltage controller and DC-link capacitance on LFO stability. Arrows ↑ stands for increments and ↓ stands for decrements.

C_d	kp_{vc} & ki_{vc} Adjusted	BW_{vc}	Stability Margins
-	YES	↓	↑↑
↓	YES	-	↑↑↑
↓	NO	↑	↑↑↑ + ↓↓ = ↑

8. Impact of Phase-Locked Loop and Feedforward Signal

In this section, the influence of the PLL and the feedforward signal are studied. Two PLL options are considered: PLL #1 is the synchronization method described in [13], which achieves the synchronization by determining the zero-crossing of contact-line voltage. PLL #2 is described in [22] and it consists of a phase detector in a feedback loop; this option uses an adaptive second-order generalized integrator (SOGI) to generate the quadrature signal.

Figure 23 shows the estimated frequency time response for both cases when a step occurs in the frequency of the contact-line voltage. Both systems are able to track the frequency changes, with the only difference being that PLL #2 is faster than the original synchronization system.

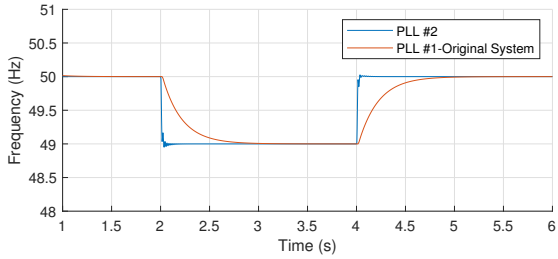

Figure 23. Estimated frequency step response of two different phase-locked loops. The frequency of contact-line voltage is changing to $f = 49$ Hz at $t = 2$ s, and going back to $f = 50$ Hz at $t = 4$ s.

With both PLL systems, two different configurations are considered for the generation of the feedforward signal V_{ff} shown in the control diagram in Figure 2c. In addition to the use of the feedforward estimator block, the signal V_{ff} can also be generated directly from the output of the contact-line voltage filter as shown in [4]; thus, $V_{ff} = V_{r-f}$. Therefore, four different cases are studied and compared, which is summarized in Table 5. Figure 24 shows the traction chain input admittance, and Figure 25 shows the critical system eigenvalue λ_1 using Bode and Nyquist plots for the four study cases.

Table 5. Study cases: influence of the PLL and the feedforward (FF).

	PLL #1	PLL #2	Estimated FF	Direct FF	Stability Ranking
Case 1	X		X		BAD
Case 2		X	X		GOOD
Case 3	X			X	GOOD
Case 4		X		X	GOOD

Case 1 is the reference case, using the original synchronization system PLL #1 and the feedforward estimator. According to Figure 25, the original case is at the stability limit

($GM = 1$). The replacement of only the PLL (i.e., case 2) improves the stability margin by a factor larger than 2. With case 3, only the generation of the feedforward signal is modified, and the stability is improved by at least a factor of 2. In summary, replacing only the PLL or only the feedforward estimator improves stability. In case 4, both the PLL and feedforward are modified; as expected, system stability improves, but the improvement is not the addition of each individual effect of cases 2 and 3.

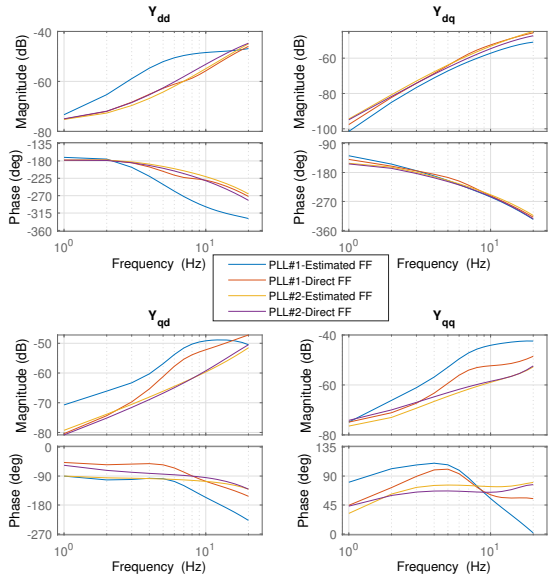

Figure 24. Traction chain input admittance. Frequency range: 1–20 Hz. Influence of the PLL and the feedforward.

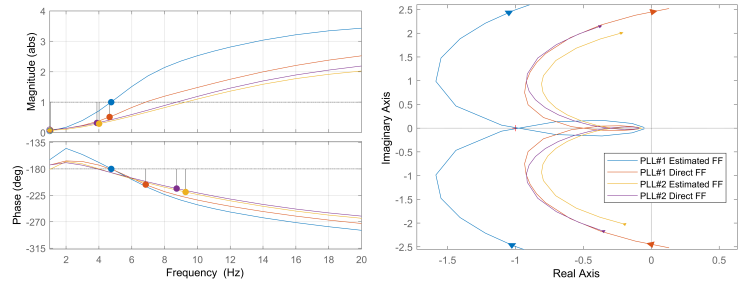

(**a**) (**b**)

Figure 25. System eigenvalue λ_1. Influence of the PLL and the feedforward. (**a**) Bode diagram, (**b**) Nyquist diagram.

The stability analysis of cases 1 and 2 might suggest that PLL #1 is the main source of instabilities. However, the large stability margin of case 3 would not support this assumption. For cases 3 and 4, the feedforward signal is taken directly from the voltage filter, which means that no dynamic influence of the synchronization system exists in the

generation of the feedforward signal. Thus, the impact of the PLL can only be noticed when the estimator block is used to generate the feedforward signal such as in cases 1 and 2. Since the main difference between PLL #1 and PLL #2 is the system delay in the transient state as shown in Figure 23, this suggests that the delay in the feedforward signal has an important influence on LFO stability.

In summary, large stability margins are presented in cases 3 and 4 since only the small delay of the contact-line voltage filter influences the feedforward signal dynamics. A fast synchronization system, such as PLL #2 in case 2, results in a small delay of the feedforward signal as well. On the other hand, in case 1, the low dynamics by the synchronization system results in a large feedforward delay.

To check this hypothesis (i.e., the influence of the feedforward signal delay), the original (Filter #1) contact-line voltage filter, from Figure 2c, in charge of filtering the third and fifth voltage harmonics, was first replaced by a band-pass filter (Filter #2) with a slower dynamic and later by a first-order high bandwidth low pass filter (Filter #3) that has a very fast dynamic. It is important to mention that the goal of this study was not the rejection of harmonics, but rather a sinusoidal contact-line voltage waveform with no harmonics is considered; therefore, the criterion for choosing the voltage filter was based on the speed of the dynamic response that minimizes delays. Filter #3 is closer to the case of having no filter since almost no delays are present.

Figure 26 shows the traction chain input admittance, and Figure 27 shows the critical system eigenvalue λ_1 using Bode and Nyquist plots for the three different filters; PLL #2 and the estimated feedforward signal are used for this analysis, and the original reference case is also plotted. As the hypothesis suggested, the stability margin is proportional to the filter delay, and from the figure is clear that the system with the fastest filter (i.e., Filter #3) has the largest gain margin.

Figure 26 shows that for the cases with better stability margins, the phase of the input admittance Y_{qq} gets closer to 0° at very low frequencies (i.e., the gain margin is proportional to the phase of the input admittance Y_{qq} at very low frequencies).

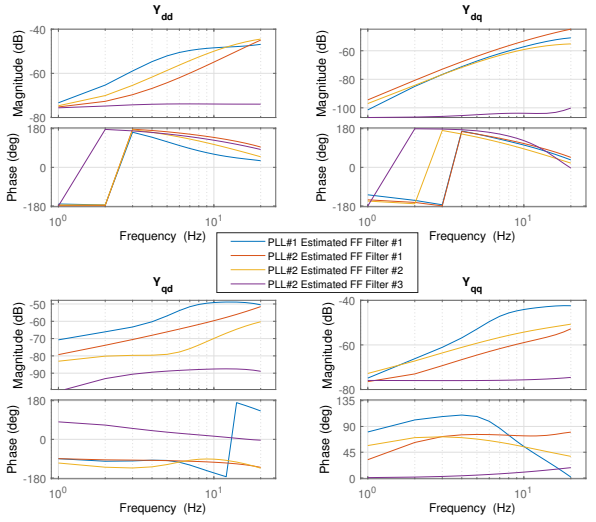

Figure 26. Traction chain input admittance. Frequency range: 1–20 Hz. Contact-line voltage filter influence.

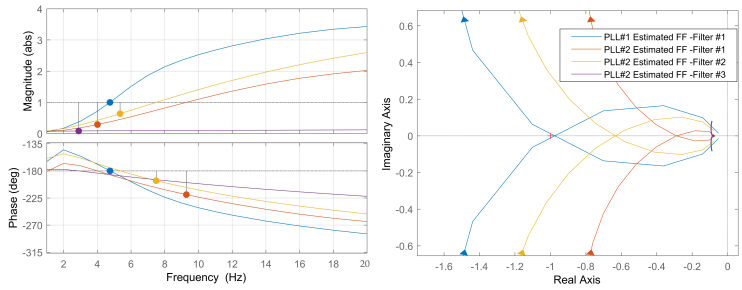

(**a**) (**b**)

Figure 27. System eigenvalue λ_1. Influence of contact-line voltage filter. (**a**) Bode diagram, (**b**) Nyquist diagram.

9. Conclusions

In this paper, impedance-based stability analysis techniques in the frequency-domain have been used to study the impact of electrical and control parameters in the appearance of low frequency oscillations, including contact-line length (i.e., distance from substation), consumed power, bandwidth of current and voltage controllers, leakage inductance of transformer, DC-link capacitor, synchronization system and feedforward signal. Time-domain simulations were further used to validate the results of the analysis.

The influence of the contact-line length and number of traction chains on LFO has been widely reported. The study of the impact of power consumption shows that the worst case for instability is at low power. The stability limit curve for different power consumption levels was presented with a specific pattern of its evolution.

It has been concluded that current control bandwidth and stability margins have a linear relationship. Variations of transformer leakage inductance are inversely proportional to the current control bandwidth, this effect can be canceled by tuning controllers to keep the bandwidth constant; then, the leakage inductance and stability margins will also show a linear relationship.

Decreasing voltage controller bandwidth increases gain margin. On the other hand, the variation of DC-link capacitance showed a non-linear relationship with the stability margins, where increasing capacitance decreases stability margins and voltage controller bandwidth, but at some point, stability margins will be reversed. Finally, decreasing DC-link capacitance while keeping constant the voltage controller bandwidth causes a monotonous improvement of the system stability for the range of variations considered in this study.

Faster dynamics for the PLL improves the low-frequency stability. Delays of the feedforward signal were observed to increase the risks of LFO, but this topic requires further research.

For future research on low-frequency stability, the influence of using different types of compensators for the control of the onboard transformer current should be studied. Proportional resonant compensators and PI compensators in the dq reference frame should be considered; therefore, a comparative analysis can be performed. As already mentioned, the low-frequency stability for multiple trains located at different positions of the contact-line was out of the scope of this paper but it should be considered for future research since it has not been reported yet.

Author Contributions: Methodology, P.L. and N.R.; traction chain model, P.L. and N.R.; implementation of scanning algorithms P.F.; software and simulations, P.F.; analysis P.F.; validation, P.L., N.R. and F.B.; writing—original draft preparation, P.F.; writing—review and editing, P.F., P.L., N.R., F.B., J.M.G. and I.L. All authors have read and agreed to the published version of the manuscript.

Funding: This research was partially funded by the Government of Asturias under grant AYUD/2021/50988 and FEDER funds.

Institutional Review Board Statement: Not applicable.

Informed Consent Statement: Not applicable.

Data Availability Statement: The data presented in this study are available upon request from the corresponding author.

Conflicts of Interest: The authors declare no conflict of interest.

References

1. Danielsen, S.; Molinas, M.; Toftevaag, T.; Fosso, O. Constant power load characteristic's influence on the low-frequency interaction between advanced electrical rail vehicle and railway traction power supply with rotary converters. In Proceedings of the MET' 2009, Gdanjsk, Poland, 24–26 September 2009.
2. Buhrkall, L.; Danielsen, S.; Eisele, A.; Bergman, M.; Galic, J. Low-frequency oscillations in Scandinavian railway power supply—Part I: Basic considerations. *eb-Elektr. Bahnen* **2010**, *108*, 56–64.
3. Buhrkall, L.; Danielsen, S.; Eisele, A.; Bergman, M.; Galic, J. Low-frequency oscillations in Scandinavian railway power supply—Part 2: Test of traction units. *eb-Elektr. Bahnen* **2010**, *108*, 103–111.
4. Danielsen, S. Electric Traction Power System Stability: Low-Frequency Interaction between Advanced Rail Vehicles and a Rotary Frequency Converter. Ph.D. Thesis, Norwegian University of Science and Technology, Trondheim, Norway, April 2010.
5. Suarez, J.; Ladoux, P.; Roux, N.; Caron, H.; Guillame, E. Measurement of locomotive input admittance to analyse low frequency instability on AC rail networks. In Proceedings of the 2014 International Symposium on Power Electronics, Electrical Drives, Automation and Motion, Ischia, Italy, 18–20 June 2014; pp. 790–795. [CrossRef]
6. Menth, S.; Meyer, M. Low frequency power oscillations in electric railway systems. *eb-Elektr. Bahnen* **2006**, *104*, 216–221.
7. Wang, H.; Mingli, W.; Sun, J. Analysis of Low-Frequency Oscillation in Electric Railways Based on Small-Signal Modeling of Vehicle-Grid System in dq Frame. *IEEE Trans. Power Electron.* **2015**, *30*, 5318–5330. [CrossRef]
8. Hu, H.; Tao, H.; Blaabjerg, F.; Wang, X.; He, Z.; Gao, S. Train–Network Interactions and Stability Evaluation in High-Speed Railways–Part I: Phenomena and Modeling. *IEEE Trans. Power Electron.* **2018**, *33*, 4627–4642. [CrossRef]
9. Hu, H.; Tao, H.; Wang, X.; Blaabjerg, F.; He, Z.; Gao, S. Train–Network Interactions and Stability Evaluation in High-Speed Railways—Part II: Influential Factors and Verifications. *IEEE Trans. Power Electron.* **2018**, *33*, 4643–4659. [CrossRef]
10. Frutos, P.; Guerrero, J.M.; Muniategui, I.; Vicente, I.; Endemano, A.; Briz, F. Low-Frequency Oscillations Analysis in AC Railway Networks Using Eigenmode Identification. In Proceedings of the 2021 IEEE Energy Conversion Congress and Exposition (ECCE), Vancouver, BC, Canada, 10–14 October 2021; pp. 1573–1579. [CrossRef]
11. Hachicha, Y.; Cypers, D.; Takuefou, M.; Belin, S.; Ladoux, P.; Roux, N. Use of a HIL railway traction simulator for low frequency network stability studies. In Proceedings of the 2018 IEEE International Conference on Electrical Systems for Aircraft, Railway, Ship Propulsion and Road Vehicles International Transportation Electrification Conference (ESARS-ITEC), Nottingham, UK, 7–9 November 2018; pp. 1–5. [CrossRef]
12. Ladoux, P.; Hachicha, Y.; Cypers, D.; Meli, M.; Roux, N. New method for determining the low-frequency Stability Limit of a 50 Hz electric traction power system. *Elektr. Bahnen* **2020**, *18*, hal-03286350.
13. Suarez, J. Étude et Modélisation des Interactions éLectriques entre les Engins et les Installations Fixes de Traction éLectrique 25 kV/50 Hz. Ph.D. Thesis, University of Toulouse, Toulouse, France, 2014.
14. Liao, Y.; Liu, Z.; Zhang, H.; Wen, B. Low-Frequency Stability Analysis of Single-Phase System with dq-Frame Impedance Approach—Part I: Impedance Modeling and Verification. *IEEE Trans. Ind. Appl.* **2018**, *54*, 4999–5011. [CrossRef]
15. Hachicha, Y.; Cypers, D.; Belin, S.; Meli, M.; Ladoux, P.; Roux, N. Towards a unified low frequency Stability criterion for 15 kV/16.7 Hz and 25 kV/50 Hz railway power system. In Proceedings of the PCIM Europe Digital Days 2020; International Exhibition and Conference for Power Electronics, Intelligent Motion, Renewable Energy and Energy Management, Virtual, 7–8 July 2020; pp. 1–8.
16. Buhrkall, L. Traction system case study. In Proceedings of the 2008 IET Professional Development course on Electric Traction Systems, Manchester, UK, 3–7 November 2008; pp. 45–63. [CrossRef]
17. EN 50388-2:2017. Railway Applications—Fixed Installations and Rolling Stock—Technical Criteria for the Coordination between Power Supply and Rolling Stock to Achieve Interoperability—Part 2: Stability and Harmonics. Available online: https://standards.iteh.ai/catalog/standards/clc/f5fb00d6-1f29-4dd4-a8fd-e3e478907499/pren-50388-2-2017 (accessed on 7 July 2017).
18. Ogata, K. *Modern Control Engineering (Instrumentation and Controls Series)*; Prentice-Hall, Inc.: Upper Saddle River, NJ, USA, 2010.

19. Liao, Y.; Liu, Z.; Zhang, H.; Wen, B. Low-Frequency Stability Analysis of Single-Phase System With dq-Frame Impedance Approach—Part II: Stability and Frequency Analysis. *IEEE Trans. Ind. Appl.* **2018**, *54*, 5012–5024. [CrossRef]
20. Pendharkar, I. A generalized Input Admittance Criterion for resonance stability in electrical railway networks. In Proceedings of the 2014 European Control Conference (ECC), Strasbourg, France, 24–27 June 2014; pp. 690–695. [CrossRef]
21. Wang, X.; Blaabjerg, F. Harmonic Stability in Power Electronic-Based Power Systems: Concept, Modeling, and Analysis. *IEEE Trans. Smart Grid* **2019**, *10*, 2858–2870. [CrossRef]
22. Teodorescu, R.; Liserre, M.; Rodriguez, P. Grid Synchronization in Single Phase Power Converters. In *Grid Converters for Photovoltaic and Wind Power Systems*; John Wiley & Sons: West Sussex, UK, 2011; pp. 43–91. [CrossRef]

B.1.2 Power-Hardware-in-the-Loop Emulation of the Low-Frequency Oscillation Phenomenon in AC Railway Networks

P. Frutos-Galarza et al., "Power-Hardware-in-the-Loop Emulation of the Low-Frequency Oscillation Phenomenon in AC Railway Networks," in *IEEE Access*, vol. 10, pp. 87374-87386, 2022. https://doi.org/10.1109/ACCESS.2022.3198945.

IEEE Access
Multidisciplinary ⋮ Rapid Review ⋮ Open Access Journal

Received 24 July 2022, accepted 7 August 2022, date of publication 16 August 2022, date of current version 25 August 2022.

Digital Object Identifier 10.1109/ACCESS.2022.3198945

RESEARCH ARTICLE

Power-Hardware-in-the-Loop Emulation of the Low-Frequency Oscillation Phenomenon in AC Railway Networks

PAUL FRUTOS-GALARZA[1], (Student Member, IEEE), JUAN M. GUERRERO[1], (Senior Member, IEEE), IKER MUNIATEGUI-ASPIAZU[2], IBAN VICENTE-MAKAZAGA[2], AITOR ENDEMAÑO-ISASI[2], DAVID ORTEGA-RODRIGUEZ[2], AND FERNANDO BRIZ[1], (Senior Member, IEEE)

[1]Department of Electrical, Computer and System Engineering, University of Oviedo, 33204 Gijón, Spain
[2]Traction Research and Development Department, Ingeteam Power Technology S.A., 48170 Zamudio, Spain

Corresponding author: Paul Frutos-Galarza (frutospaul@uniovi.es)

This work was supported in part by the European Commission H2020 under Grant UE-18-POWER2POWER-826417; in part by the Spanish Ministry of Science, Innovation and Universities under Grant MCIU-19-PCI2019-103490; and in part by the Government of Asturias under Project AYUD/2021/50988.

ABSTRACT Dynamic interactions among the AC railway traction network and power electronics converters feeding the trains have been reported to cause low-frequency oscillations (LFO) of the catenary voltage and current. This can result in railway system instability, eventually leading to a power outage and the shutdown of the train traffic. To avoid LFO, control of train power electronic converters must be properly designed and tuned. Experimental verification of control performance regarding the LFO phenomenon in the railway traction network is not easy. Alternatively, the railway traction network can be emulated using a power electronic converter, which would feed the train power converter under test. This paper addresses the design of a network emulator able to reproduce the dynamic behavior of the actual network at low frequencies, including LFO. Three different options will be considered for the network emulator. Their performance will be studied first by means of simulations. Finally, the selected solution will be verified on a downscale test bench.

INDEX TERMS Low-frequency oscillations, resonant stability, railway system, traction unit, railway traction power supply, catenary emulator, power-hardware-in-the-loop, real-time simulation, grid-forming voltage source inverter.

I. INTRODUCTION

Modern onboard railway systems include a large number of power electronic converters aimed to improve the controllability and efficiency of the train. While the benefits brought by power electronic converters are undoubtful, dynamic interactions among these and the railway traction network can produce undesired phenomena which might result in power system instability, including low-frequency oscillations (LFO) [1], [2], [3], [4], [5], [6], [7].

LFO have been reported worldwide for different types of railway traction networks under different operating conditions, see Table 1. This phenomenon leads to a large variation of the catenary voltage and current at relatively low frequencies, typically in the range of 10%-30% the fundamental frequency (f_0) [4]. Harmful consequences of

TABLE 1. Reported LFO cases.

N°	Case	f_0 (Hz)	f_{osc} (Hz)	Year
1	Zürich, Switzerland [1]	16.7	5	1995
2	Norway [2], [3]	16.7	1.6	2007
3	Washington, USA [4]	25	3	2006
4	Siemens test, Germany [5]	50	7	2006
5	Thionville, France [6]	50	5	2008
6	Hudong Depot, China [7]	50	2-4	2008
7	Shanhaiguan Hub, China [7]	50	6-7	2011

The associate editor coordinating the review of this manuscript and approving it for publication was Sze Sing Lee.

such events include malfunction of protection systems, overvoltages/overcurrents that could damage the electrical/electronic equipment, transportation delays, among others [5], [7].

Different methods such as pole migration analysis [4], [8], [9] and impedance-based analysis [6], [10], [11], [12] have been used to study the LFO phenomenon. In these methods, the network impedance and the train input admittance are required to determine the railway system stability. The network impedance should be provided by the grid infrastructure administrator. On the other hand, the train input admittance can be measured using a frequency response test [6]. Alternatively, the train admittance can be obtained from analytical models [7], [13]. However, these models have been reported not to be accurate enough [14].

In [2], [5], it was concluded that LFO are influenced by the negative train input admittance, which appears due to the train behaving as a constant power load. On the contrary, regenerative breaking will inject power into the grid, improving stability [2]. So, LFO will only appear in motoring operation mode.

The LFO phenomenon has been mainly reported both for multiple trains in depot [6], [7] and for a train operating at a very long distance from the substation [2], [5]. This paper focuses on this last scenario. Therefore, the stability limit of the railway system for LFO will be defined as the maximum distance that a traction unit (i.e., a train) consuming a certain amount of power can reach from the substation. The maximum distance is associated with a maximum value of the network impedance. This limit is influenced by the train parameters such as transformer leakage inductance, DC-link capacitance, voltage and current control design and bandwidths, and the synchronization method used by the onboard catenary-side converter [11].

Testing the LFO phenomenon in a railway traction network is not easy, as the results would only be valid for that specific network, also it could affect other users operating in the catenary line [1]. Alternatively, train-network interactions can be studied by means of simulations. Available approaches for this purpose would include off-line simulations; real-time simulation platforms such as software-in-the-loop (SIL); hardware-in-the-loop (HIL); and power-hardware-in-the-loop (PHIL), each having advantages and disadvantages. Off-line simulations are commonly used during the initial analysis. However, real-time simulations are required at further development stages to properly evaluate the performance of the control. Only real-time options are considered in this paper.

SIL simulation integrates the compiled source control code into a time simulation. In HIL solutions, the source code is implemented on the actual control platform; different options exist in this case, mainly related to time resolution, e.g., depending on whether switching events are reproduced or only the average behavior over a switching period is considered. Independently of the implementation being used, no physical power flow occurs.

Finally, PHIL usually is made up of two parts: the emulator, and the unit under test (UUT). The emulator consists of an electronic power converter and associated real-time control, which interacts with the UUT, involving power exchange [15], [16]. This allows testing of UUT parts such as power semiconductor devices, transformers, capacitors, and inductors under close-to-real-world operating conditions before their integration in the real system.

The aim of this paper is to design, model, and build an emulator prototype of the railway traction network, able to reproduce the low-frequency oscillation phenomenon. In this study, the UUT consists of a four-quadrant power converter (4QC), which is responsible for generating the DC-link feeding all onboard systems. The interactions between the emulator and the 4QC should reliably reproduce the LFO phenomenon occurring in the real railway traction system. The emulator will be used to validate the response of the 4QC in adverse scenarios regarding LFO, and redesign train voltage and current controllers if needed. Furthermore, control mitigation techniques implemented in the controllers of traction units such as in [3] could be tested in this platform.

The paper is organized as follows: section II describes the railway system model further used for the LFO study; section III deals with LFO description and modelling; section IV discusses different design options for the emulator; section V presents the filter design for the train-emulator connection; simulation results are presented in section VI; section VII deals with the test bench construction and experimental results; finally, conclusions are drawn in section VIII.

It is finally noted that the prototype shown in this paper is intended as a proof of concept and was designed for downscale power and voltage values (10 kW AC 200 V/50 Hz), which are significantly smaller than the actual (full-rated) system values (n-hundred kW AC 25 kV/50 Hz). Based on this experience, the design of a full-rated emulator with the concepts proposed here is ongoing.

II. RAILWAY SYSTEM MODEL

A simplified representation of the railway system is shown in Fig. 1. It consists of two main elements: the traction network (i.e., power supply network) and the train [10], [12], [17], [18]. The power supply network is composed of an ideal voltage source which can be DC or AC, and the transmission line (i.e., catenary line). AC 25 kV/50 Hz electric power supply is considered here. For the study of LFO, an equivalent circuit of the transmission line based only on resistance and inductance is widely used [1], [5], [7], [9], as line capacitive effects can be safely neglected at low frequency. Fig. 2 shows the equivalent railway system model that will be used in this study, where v_c is the catenary voltage at PCC between the network and the train, and i_s is the catenary current. Network inductance (L_s) and resistance (R_s) vary almost linearly with the catenary line length (i.e., the distance between the substation and the train).

The main elements in the train are: power transformer, L-filter, single-phase four-quadrant power converter (4QC),

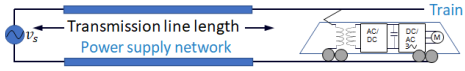

FIGURE 1. Simplified representation of the railway system. AC 25 kV/50 Hz electric power supply is considered in this work.

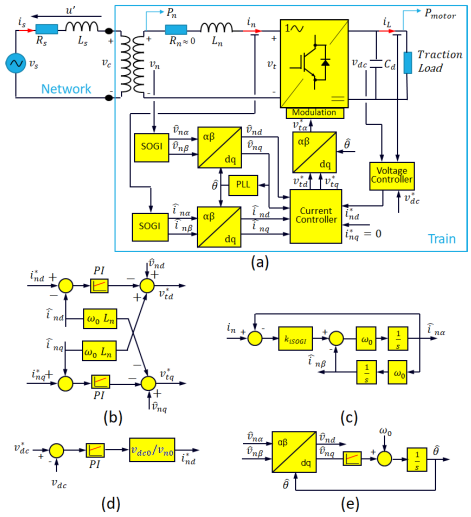

FIGURE 2. Railway control system model. (a) Train-Network model, (b) Current controller, (c) SOGI, (d) DC Voltage controller, (e) PLL.

DC-link capacitor, and traction drives consisting of inverters and motors. The 4QC behavior will determine the interaction between the train and the network [1], [5], [8], [9]. On the other hand, switching harmonics will not affect the low-frequency dynamics involved in the LFO phenomenon [8], [17]. It is safe therefore to replace the traction drives by an equivalent linear load as shown in Fig. 2, enormously simplifying analysis and simulations.

A cascaded control structure consisting of an outer voltage control loop and an inner current control loop is used. Therefore, the DC-link voltage v_{dc} is regulated through the controlled train current i_n. The 4QC control shown in Fig. 2 operates in dq coordinates, aligning the d-axis with the catenary voltage complex vector. Current and voltage controllers were tuned using zero-pole cancellation as described in [19], with BW_{CC-t} and BW_{VC-t} being the corresponding bandwidths (subscript $_{-t}$ stands for train control parameters, to distinguish from emulator parameters, $_{-e}$, discussed later). A phase-lock loop (PLL) is used to obtain the estimated grid voltage phase angle $\hat{\theta}$, which is required for the coordinate transformations into the synchronous reference frame [13]. The PLL was designed and tuned as described in [20], where the selection of the proportional gain k_{i-PLL} involves a trade-off between PLL filtering capability and dynamic response, and the integral gain is chosen as $k_{i-PLL} = k_{p-PLL}^2/2$. A second-order generalized integrator (SOGI) is used to obtain the quadrature signals. The gain k_{i-SOGI} of the second order generalized integrator (SOGI) was chosen as described in [5].

III. LFO MODELING

An example of the catenary line voltage and train current waveforms when the LFO phenomenon occurs, and the corresponding harmonic spectra, are shown in Fig. 3 [9]. The fundamental frequency of the AC signals is f_0, with their magnitude (envelope) varying at a frequency f_{osc}. The frequency spectra show the fundamental component f_0 with two sideband components at $f_L = f_0 - f_{osc}$ and $f_H = f_0 + f_{osc}$ respectively. The fundamental angular frequency is defined as $\omega_0 = 2\pi f_0$.

The waveforms in Fig. 3 can be approached as (1).

$$u(t) = U(t)\sin(2\pi f_0 t) = [U_0 + \Delta U \cos(2\pi f_{osc} t)]\sin(2\pi f_0 t)$$

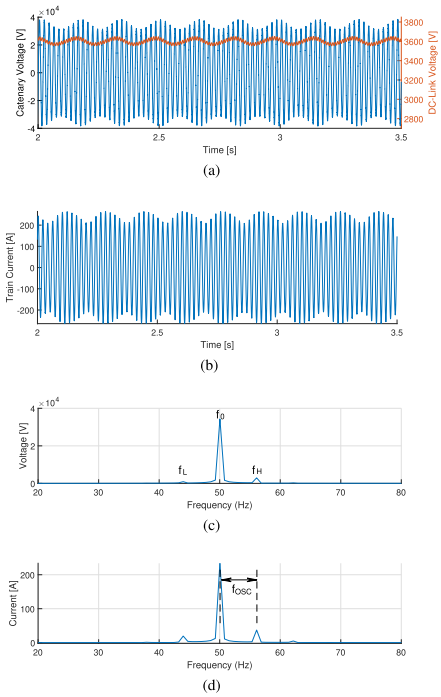

FIGURE 3. Simulation results. AC 25 kV/50 Hz railway power supply. (a) Catenary line voltage and train DC-Link voltage. (b) Train current. Frequency spectrum of (c) catenary line voltage and (d) train current FFT.

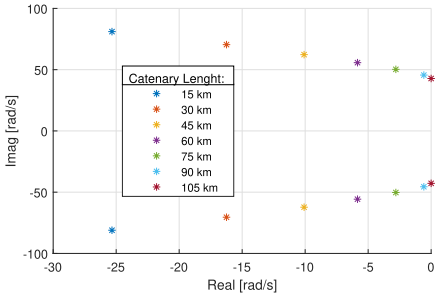

FIGURE 4. Eigenvalue migration for different catenary line length.

$$= U_0 \sin(2\pi f_0 t) + \frac{\Delta U}{2} \sin(2\pi f_L t) + \frac{\Delta U}{2} \sin(2\pi f_H t) \quad (1)$$

A widely used approach for LFO analysis is to develop a small signal model of the power network and train input admittance [8]. Fig. 4 shows an example of the dominant eigenvalue migration of the resulting system as the catenary line length increases [9]. The stability limit occurs when the eigenvalues cross the imaginary axis of the complex plane [8]. It is observed that the risk of instability increases with the distance from the substation. The frequency at which the eigenvalues cross the imaginary axis corresponds to f_{osc} in (1).

IV. TRACTION NETWORK EMULATOR DESIGN

This section discusses different approaches for the design of the railway traction network emulator aimed to reproduce the LFO phenomenon. In order to perform this task, the emulator should be able to simulate the railway system dynamics for changing values of the network resistance (R_s) and the network inductance (L_s) with the variable distance from the train to the substation.

A. SYSTEM DESCRIPTION

As discussed in Section II, the two main elements of the railway system model are the power supply network (i.e., ideal voltage source and varying impedance) and the train (see Fig. 5a). The power supply emulator replaces the power supply network feeding the train as shown in Fig. 5b and Fig. 5c. The emulator consists of two main structures:

- Real-time simulator. It reproduces the dynamic behavior of the power supply network in real-time, its output being the catenary voltage reference, v_c^*. Its design is discussed in Subsection IV-B.
- Single-phase voltage source inverter (VSI) operating in a grid-forming mode. It supplies the desired catenary voltage v_c to the train, it is described in Subsection IV-C.

It is noted that in the railway system model from Fig. 2, the power supply network current i_s and the train current i_n

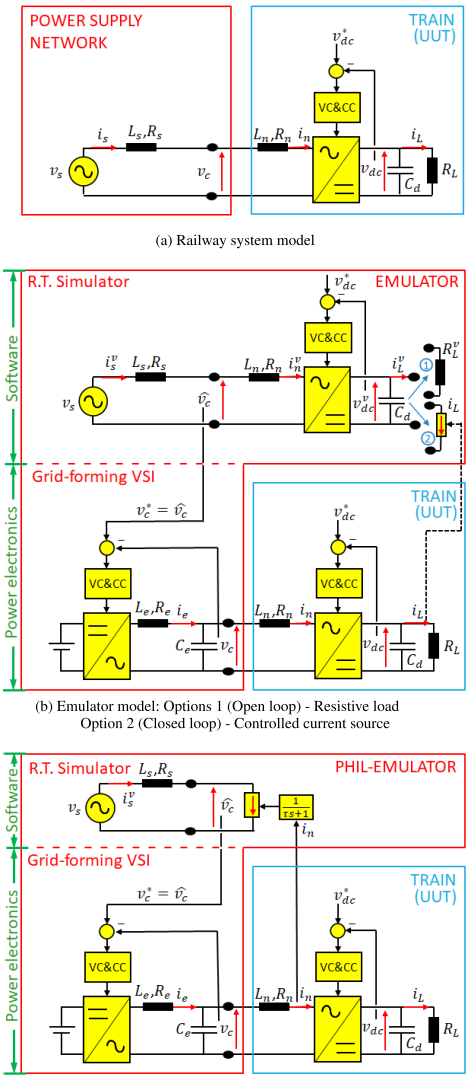

(a) Railway system model

(b) Emulator model: Options 1 (Open loop) - Resistive load
Option 2 (Closed loop) - Controlled current source

(c) PHIL-Emulator model (Option 3)

FIGURE 5. Railway system model and emulator models. Superscript "v" indicates virtual variables.

are different due to the step-down transformer present in the traction unit. For the analysis in this section, the transformer will not be considered, therefore $i_s = i_n$ as shown in Fig. 5a. However, it was preferred to keep both current definitions in the schematics to visualize the actual physics of the system.

B. REAL-TIME SIMULATOR

The design of the real-time simulator is not trivial. Three different options will be discussed, which correspond to different stages of this research, i.e., later options improve the limitations found in the preceding ones. The reason to include earlier designs is to highlight those aspects which will play a relevant role in accurate emulation of the LFO phenomenon occurring in the railway system.

For the discussion following, variables that exist only in the simulator, i.e., virtual variables, will be indicated by a superscript "^{v}". There are variables that coincide both in the virtual domain and in the physical domain. Such variables are labeled without "^{v}" superscript.

1) OPTION 1: OPEN-LOOP

In this option, the simulator generates the catenary voltage reference, v_c^*, simulating the complete railway system. The configuration is shown in Fig. 5b. The simulator includes a virtual power supply network and a virtual train. The load connected to the virtual DC-link is a constant resistance R_L^v. This option requires previous knowledge of train parameters as it runs in parallel with the physical train (i.e., real train). Furthermore, there is no feedback from the physical train to the emulator. Consequently, this option works only properly for constant values of train load R_L, since in this case, $R_L^v = R_L$. However, if a change in load R_L is desired, it should simultaneously occur along with a change in R_L^v in the virtual domain, which can be problematic due to the lack of information that the emulator receives from the physical train. Option 2 overcomes this drawback, as will be discussed following.

2) OPTION 2: CLOSED-LOOP

This option is also shown in Fig. 5b. R_L^v is now replaced by a controlled current source as a virtual load. By doing this, the load current in the simulator will track the measured load current i_L which circulates through the real load R_L. Therefore, this option allows emulation with varying loads.

Regardless of this improvement, a drawback of both options 1 and 2 is they require in advance precise knowledge of control design and tuning of the UUT to emulate catenary voltage dynamics, which is not often available. The approach discussed next is aimed at overcoming this drawback.

3) OPTION 3: PHIL

This option is shown in Fig. 5c. A virtual *RL* circuit is used to obtain the estimated catenary voltage $\widehat{V}_c(s)$. From the railway system model in Fig. 5a, the equation defining the catenary voltage $V_c(s)$ is given by (2).

$$V_c(s) = V_s(s) - (L_s s + R_s)\, I_s(s) \tag{2}$$

Since this equation is a non-causal system, it cannot be used for estimation purposes. A low-pass filter is then added for real-time implementation, see (3) and Fig. 6. A time constant of $\tau = 31.8\ \mu$s was selected, corresponding to a cut-off frequency of 5 kHz. This is the maximum frequency complying with the Nyquist-Shannon criteria considering 10 kHz as the sampling frequency of the grid-forming VSI [21].

$$\widehat{V}_c(s) = V_s(s) - \frac{(L_s s + R_s)}{\tau s + 1} I_n(s) \tag{3}$$

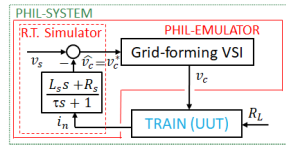

FIGURE 6. Real-time simulator block diagram in the PHIL system.

A simplified representation of a PHIL system is shown in Fig. 6. Here, the closed-loop configuration that the real-time simulator creates between the grid-forming VSI and the train is easily seen. An appealing characteristic of this option is that it does not require previous knowledge of train characteristics. The train can be considered a black box, the emulator behaving as a power supply network whose properties are independent of the load (i.e., train). This option also allows the implementation and testing of controls strategies aimed to mitigate LFO such as Power-Oscillation-Damping [3] and Virtual-Impedance-Based Suppression Method [22].

C. GRID-FORMING VSI

The block diagram of the single-phase VSI is shown in Fig. 7. It consists of a two-level single-phase converter (H-bridge), which is fed from a voltage source on the DC-side, and has an LC filter connected to its AC side. Unipolar modulation is used in this study.

A cascaded control is used as shown in Fig. 7. The inner loop controls the inductor current i_e, while the outer loop controls the capacitor voltage v_c (i.e., catenary voltage), to which the traction unit is connected.

Current control is performed in a stationary reference frame using a proportional-resonant (PR) controller as shown in Fig. 7(b). The corresponding transfer function is given by (4), where k_{p-cc} and k_{r-cc} are the gains to be tuned to obtain the desired closed loop current control bandwidth BW_{CC-e} [23], see (5) and (6). The basic concept of the PR controller is to obtain an infinite gain at a selected resonant frequency, as this will guarantee zero steady-state error at that frequency. The resonant controller can be seen therefore as a generalization of the PI controller, in which the infinite gain occurs not at DC, but at the desired frequency. The resonance frequency is the fundamental frequency f_0. The coefficient K_f adjusts the bandpass in (4), it takes values from 0.25 to 1 [23]. Furthermore, in Fig. 7(b) the measured train

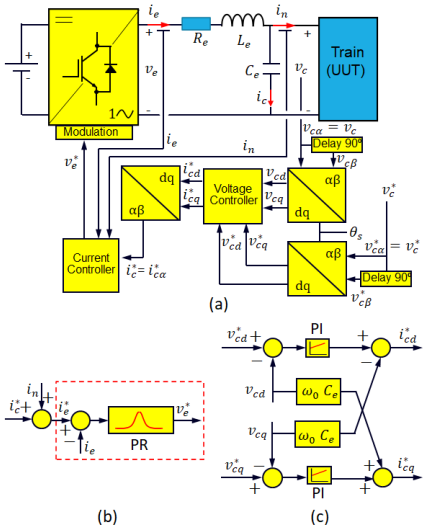

FIGURE 7. Grid-forming single-phase VSI. (a) Overall block diagram, (b) Current controller, (c) Voltage controller.

current i_n is added to the current command as a feed-forward term to improve the dynamic response of the voltage control loop [19].

$$PR(s) = 2k_{p-cc}\frac{s^2 + s\left(k_{r-cc}/k_{p-cc}\right) + (2\pi f_0)^2}{s^2 + (2\pi f_0)^2} \quad (4)$$

$$k_{p-cc} = \sqrt{2}\,(2\pi BW_{CC-e})\,L_e \quad (5)$$

$$k_{r-cc} = K_f\,(2\pi BW_{CC-e})^2\,L_e \quad (6)$$

The catenary voltage control is performed in a synchronous reference frame using a PI controller as shown in Fig. 7c, where the proportional gain and the integral gain are given by (7) and (8) as function of the desired voltage control bandwidth BW_{VC-e}.

$$k_{p-vc} = \sqrt{2}\,(2\pi BW_{VC-e})\,C_e \quad (7)$$

$$k_{i-vc} = (2\pi BW_{VC-e})^2\,C_e \quad (8)$$

A virtual quadrature component of the catenary voltage is obtained by delaying 90 degrees the alpha component. For that purpose, the filter in (9) is used. Feedforward terms are used in the voltage controller to eliminate cross-coupling between $d-$ and $q-$axes, see Fig. 7c.

$$G_{Delay-90}(s) = \frac{2\pi f_0 - s}{s + 2\pi f_0} \quad (9)$$

D. MULTIPLE TRAINS

From Subsections IV-C to IV-A, it is noted that the emulator is aimed to replace the traction network. For the case when multiple trains are in the depot (i.e., located at the same place), it does not modify the network topology since all the trains are connected in parallel. Therefore, only one train with an equivalent input admittance can be used.

On the other hand, for the case of multiple trains operating in the same power supply section at different locations, the network topology must be modified to include additional connection nodes, therefore, the virtual network in the real-time simulator must be modified, but the proposed methodology would still apply. Also, additional virtual trains can be added.

These analyses are not included in this article due to space constraints, but it is worth it to mention them.

V. INVERTERS AND FILTER DESIGN

Design of inverters and passive elements of the downscale prototype is addressed in this section. A similar methodology would be followed for the full-rated emulator.

As observed from Fig. 5b, grid-forming VSI and 4QC are connected through $LC + L$ filters. L_n corresponds to the inductance seen by the 4QC (see Fig. 2). It should be large enough to filter the current harmonics, but realizing that excessively large values will limit power transfer capability. Therefore, a trade-off is required. For simulations and test bench, a DC-link voltage $V_{dc} = 300$ V has been selected for the inverters, with a catenary peak voltage of $V_c = 200$ V. These voltages were chosen to provide a large safety margin with respect to power devices and DC-link capacitor voltage limits, as some of the experiments reproducing LFO might produce large excursions of the voltages. Nominal power of 10 kW, with a current ripple $< 4\%$ of the train nominal current have been defined as design targets.

The maximum transfer power with a unity power factor between train and network is given by (10) [24]. From this equation, a value of $L_n = 7.1$ mH is obtained to transfer the targeted power $P_n = 10$ kW. Due to availability issues, a value of $L_n = 6$ mH was selected.

$$P_n = \frac{\sqrt{V_c^2 V_{dc}^2 - V_c^4}}{2X_n} \quad (10)$$

Current ripple can be approached using (11), where load angle ψ is the phase difference between catenary voltage v_c and the 4QC terminal voltage v_t [24].

$$\Delta i(\%) = \frac{\pi\sqrt{(2)}V_c\,(1 - (V_t/V_{dc})\cos(\psi))}{(f_{sw}/f_0)X_n I_n}100 \quad (11)$$

For the targeted current ripple limit of 4 % and the selected value of L_n, the switching frequency provided by (11) is $f_{sw} = 7.5$ kHz. A slightly larger value, $f_{sw} = 10$ kHz, was finally chosen.

Once L_n is selected, there would be two degrees of freedom for the design of catenary emulator LC filter [25]. An option in this case is to analyze the $LC + L$ filters as an equivalent LCL filter. It is advantageous for the design of LCL filters to have the same values for both inductances, as this minimizes the size of the filter components [26].

Assumed that the inductances have been selected such that $L_e = L_n = L$, and neglecting the resistive terms of

inductances and capacitors, the transfer function between the capacitor voltage at the point of coupling (i.e., v_c) and the voltage being applied by any of the two inverters (i.e., v_t,v_e) is given by (12). The filter behaves as a second order system, an undamped resonance occurring at the cut-off frequency ω_c which is given by (13).

$$\frac{V_c(s)}{V(s)} = \frac{1}{s^2 LC_e + 2} \tag{12}$$

$$\omega_c = \sqrt{\frac{2}{LC_e}} \tag{13}$$

Capacitor C_e was chosen to get a cut-off frequency around 600 Hz, which is much higher than the fundamental frequency but far enough from the switching frequency. The parameters of 4QC and VSI filters are presented in Tables 2 and 3 respectively. Fig. 8 shows the resulting Bode diagram from (12). It is observed that the attenuation at the switching frequency is larger than −50 dB.

TABLE 2. Train-network parameters.

Symbol	Description	Value
Power supply network		
L_s	Line Inductance (Limit)	10 mH
R_s	Line Resistance (Limit)	150 mΩ
V_s	Supply Voltage Amplitude	200 V
f_0	Fundamental Frequency	50 Hz
Train (4QC)		
L_n	4QC Inductance	6 mH
R_n	4QC Resistance	10 mΩ
f_{sw}	Switching Frequency	10 kHz
BW_{VC-t}	Voltage Control Bandwidth	10 Hz
BW_{CC-t}	Current Control Bandwidth	100 Hz
R_L	Resistive Load	200 Ω
V_{dc}	DC-link Voltage	300 V

Any topology able to produce a single-phase AC voltage with a fundamental frequency of 50 Hz would be suitable for grid-forming VSI. Two issues should be considered. First, since the LFO will occur when the active power is flowing from emulator to 4QC, the grid-forming converter will not

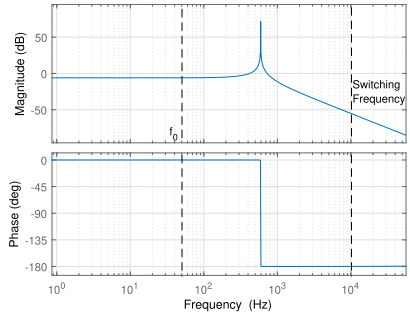

FIGURE 8. Bode diagram of capacitor vs. inverter voltage. $V_c(j\omega)/V(j\omega)$.

TABLE 3. Network emulator parameters.

Symbol	Description	Value
L_e	Emulator Inductance	6 mH
R_e	Emulator Resistance	10 mΩ
C_e	Emulator Capacitance	24 mF
f_{sw}	Switching Frequency	10 kHz
BW_{VC-e}	Voltage Control Bandwidth	50 Hz / 100 Hz
BW_{CC-e}	Current Control Bandwidth	500 Hz / 1000 Hz

be required to absorb power. Second, to reduce the effects of switching harmonics produced by the grid-forming inverter and ease the design of the LC filter at the output of the emulator, high switching frequencies and/or multilevel topologies (e.g., NPC) are preferable, however, cost and control complexity must be also considered. A two-level full bridge has been used for the downscale prototype developed in this paper. The same topology has been considered for the 4QC.

VI. SIMULATION RESULTS

In this section, time domain simulations of the emulation methods proposed in Section IV (see Fig. 5) are carried out to test their performance.

The behavior of the railway system model in Fig. 5a will be first simulated in Subsection VI-A to be later used as a reference to assess the performance of the different methods. Power supply network parameters and train control parameters are shown in Table 2.

Regarding the catenary emulator, it has been observed during this work that the bandwidths of the voltage and current controllers of the grid-forming VSI will strongly affect to the emulator capability to accurately reproduce LFO. To illustrate this, the behavior of the different emulator designs was tested for two different sets of control bandwidths; set #1 is ($BW_{VC-e} = 50$ Hz, $BW_{CC-e} = 500$ Hz), and set #2 is ($BW_{VC-e} = 100$ Hz, $BW_{CC-e} = 1000$ Hz). Emulator parameters are shown in Table 3. On the other hand, train voltage and current control bandwidths, BW_{VC-t} and BW_{CC-t}, were kept constants for all the cases.

A. LFO USING RAILWAY SYSTEM MODEL

Fig. 9 shows the DC-link voltage, catenary voltage, and train current using the railway system model shown in Fig. 5a, when step-like changes in network impedance occur. Such changes would reproduce the effect of increasing the transmission line length from the substation transformer to the traction unit. It is noted that while step-like changes will not occur in the real system, still they are a useful excitation to obtain the damping ratio, settling time, oscillation frequency, and eigenvalues for the system time response. Indeed, step-like changes they have been frequently used for LFO and stability studies [1], [5], [8]. It is observed from Fig. 9 that LFO progressively develop when the impedance increases keeping constant the L/R ratio, the stability limit occurring at $L_s = 10$ mH and $R_s = 150$ mΩ.

Since increasing the network impedance decreases system damping and increases the settling time, it is inferred that

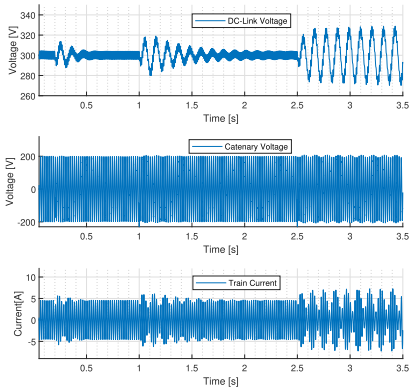

FIGURE 9. Simulation results. LFO when line inductance and resistance increase from ($L_S = 4$ mH, $R_S = 60$ mΩ) to ($L_S = 10$ mH and $R_S = 150$ mΩ) in steps of $\Delta L_S = 2$ mH and $\Delta R_S = 30$ mΩ) at t = 0.2 s, t = 1 s, and t = 2.5 s.

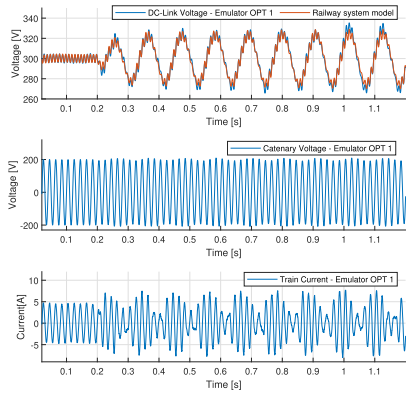

FIGURE 10. Simulation results using option 1 for emulator. Line impedance increases from $L_S = 8$ mH, $R_S = 120$ mΩ to $L_S = 10$ mH, $R_S = 150$ mΩ at $t = 0.2$ s. From top to bottom: DC-link Voltage, catenary voltage and train current. $BW_{CC-e} = 500$ Hz, $BW_{VC-e} = 50$ Hz.

critical system eigenvalues move from the negative real side of the complex plane (i.e., stable region) to the right (i.e., unstable region). At the stability limit, the real component of critical eigenvalues is zero, and the imaginary component can be identified from the oscillation frequency, which is $f_{osc} \approx 9$ Hz.

B. LFO USING OPEN-LOOP EMULATOR (OPTION 1)

Fig. 10 shows LFO when network inductance and resistance increase using option 1 of the emulator in Fig. 5b. Only the results for set #1 of voltage and current control bandwidths are presented, as no significant differences were found for this particular case when using set #2.

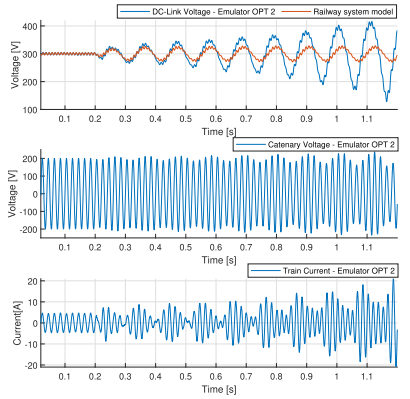

(a) $BW_{VC-e} = 50$ Hz, $BW_{CC-e} = 500$ Hz

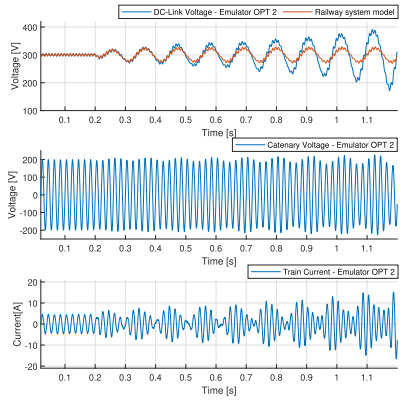

(b) $BW_{VC-e} = 100$ Hz, $BW_{CC-e} = 1000$ Hz

FIGURE 11. Simulation results using option 2 for the emulator. Line impedance increases from $L_S = 8$ mH, $R_S = 120$ mΩ to $L_S = 10$ mH, $R_S = 150$ mΩ at $t = 0.2$ s. From top to bottom: DC-link Voltage, catenary voltage and train current.

The DC-link voltage response of the real railway system model is also shown in Fig. 10 for comparison purposes. A good agreement is observed between real and emulated systems. However, simulations using this option are only possible if the load R_L is constant, and the precise knowledge of train control design is available as discussed in Subsection VI-F, which might not be always possible.

C. LFO USING CLOSED-LOOP EMULATOR (OPTION 2)

Time-domain simulation results using the emulator model option 2 are shown in Fig. 11 for the two different sets of controllers bandwidths. As shown in Fig. 11a, the system

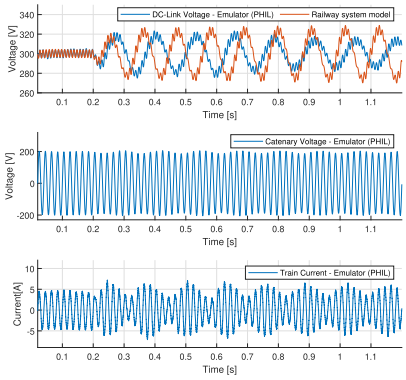

(a) $BW_{VC-e} = 50$ Hz, $BW_{CC-e} = 500$ Hz

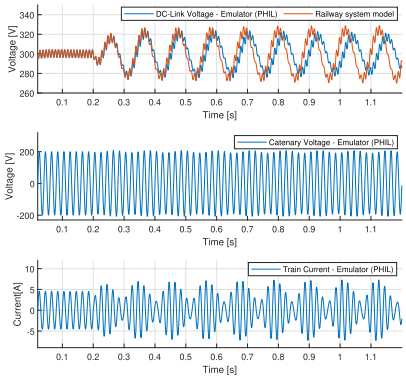

(b) $BW_{VC-e} = 100$ Hz, $BW_{CC-e} = 1000$ Hz

FIGURE 12. Simulation results using option 3 for the emulator. Line impedance increases from $L_S = 8$ mH, $R_S = 120$ mΩ to $L_S = 10$ mH, $R_S = 150$ mΩ at $t = 0.2$ s. From top to bottom: DC-link Voltage, catenary voltage and train current.

becomes unstable when the change in line impedance is applied. Increasing VSI control bandwidth slightly reduces the rate of increase of the oscillations, but still, the system is unstable as shown in Fig. 11b. These results suggest that the use of this option is not advisable as it fails to reproduce the LFO phenomenon.

D. LFO USING PHIL EMULATOR (OPTION 3)

Time domain simulations using the PHIL-Emulator are shown in Fig. 12. The case for bandwidths set #1 is shown in Fig. 12a. The response is seen to be more damped compared to the actual power system response, LFO also occurring at

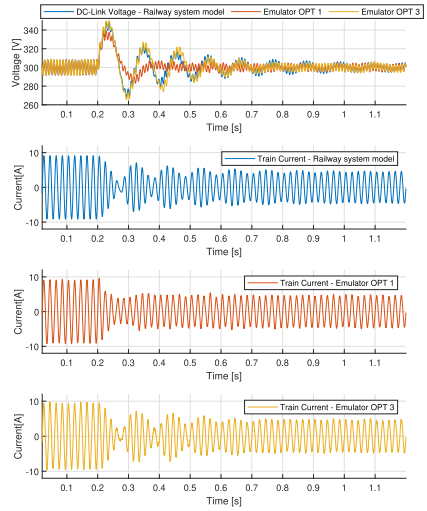

FIGURE 13. Simulation results using network emulator options 1 and 3. Line impedance $L_S = 8$ mH, $R_S = 120$ mΩ. Load step change from $R_L = 100$ mΩ to $R_L = 200$ mΩ at $t = 0.2$ s. Control bandwidths: $BW_{CC-e} = 1000$ Hz, $BW_{VC-e} = 100$ Hz.

lower frequencies (8 Hz for emulator vs. 9 Hz for the actual railway system model). The improvement when VSI controllers bandwidths are increased can be observed in Fig. 12b, but oscillations are seen still to be slightly damped and occur at a slightly lower frequency compared to the actual railway system case.

E. RESPONSE TO LOAD CHANGES (VARIABLE R_L)

Time domain simulations showing the response to step change in the load using the emulator model options 1 and 3 are shown in Fig. 13. Option 2 was not considered for this test since its performance has already been found to be inferior in Subsection VI-C.

From Fig. 13 the emulated systems and the railway system reach the same steady-state, however, they present different dynamics, this can be appreciated in the transient state. The emulator option 1 is not capable to emulate the railway system dynamic for this type of test, on the other hand, option 3 is able to reproduce the phenomenon accurately.

F. SUMMARY

It is concluded from the simulations presented in this section that the highest accuracy in reproducing LFO would be obtained using Option 1 for the emulator. However, this option implies that current and voltage control structures and tuning are the same for emulator and actual train, which might be difficult to achieve or even impossible in practice. It is interesting to note although the simulation for this option was performed in real-time, this is not actually required,

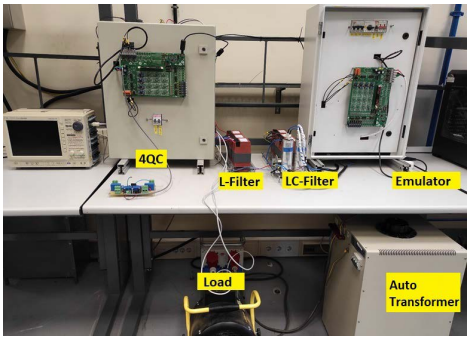

FIGURE 14. Experimental test bench.

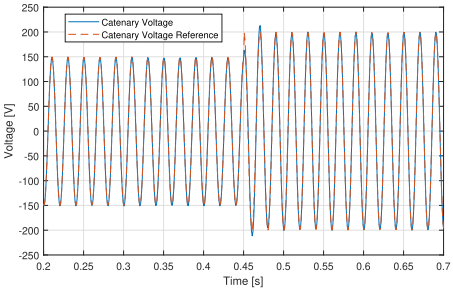

FIGURE 15. Experimental results. Catenary voltage step response. From $V_C = 150$ V to $V_C = 200$ V at t = 0.45 s.

as there is no feedback from the real train to the emulator. Therefore, it would be perfectly possible to simulate the train behavior off-line and use the catenary voltage resulting from the simulation to provide the reference signal to emulator v_c^* (see Fig. 5b).

In contrast with option 1, option 2 includes a feedback mechanism as it uses the train load current i_L to feed the emulator. However, this method still requires knowledge of train controllers. Furthermore, it is observed from simulation results that this option has the worst accuracy in reproducing the behavior of the actual power system.

Finally, option 3 shows good accuracy in reproducing LFO, and doesn't require knowledge of train control, making it especially appealing.

G. DISCUSSION

As already explained, the low-frequency oscillations are produced by the dynamic interaction between the power supply network and the train (i.e., 4QC) [13]. For option 1 of the emulation; the dynamic interaction which provokes LFO, happens entirely in the simulator between the virtual power

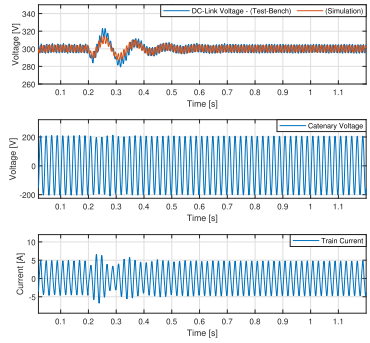

(a) $L_s = 4 \rightarrow 6$ mH, $R_s = 60 \rightarrow 90$ mΩ

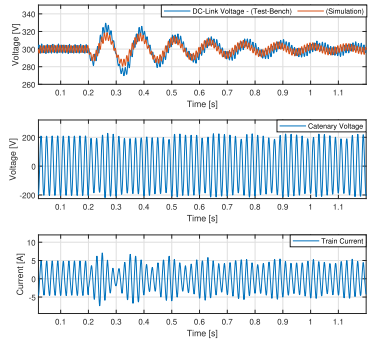

(b) $L_s = 6 \rightarrow 8$ mH, $R_s = 90 \rightarrow 120$ mΩ

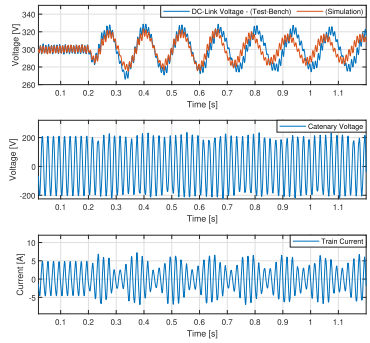

(c) $L_s = 8 \rightarrow 10$ mH, $R_s = 120 \rightarrow 150$ mΩ

FIGURE 16. Experimental results. System response to step-like changes in power network impedance as indicated in the captions. Changes occur at t = 0.2 s. For each case, from top to bottom: DC-link voltage, catenary voltage, and train current. Simulation results are shown for comparison.

supply and the virtual train. In this option, the physical train doesn't contribute to LFO formation due to the open-loop configuration.

For option 2, the dynamic of the physical train is now in the closed-loop, and it participates in the LFO formation. This implies repeated elements in the loop. For instance, the dynamics of the 4QC voltage and current controllers affect the system twice (due to the physical train and the virtual train). Although these repeated elements do not affect the steady-state response, they add delays, which impact the transient response and the system dynamics. System delays were already reported to influence LFO instability [11], and would explain the inaccuracy of this option to reproduce the LFO phenomenon.

Using the third option (PHIL-Emulator), LFO are the result of the interaction between the virtual power supply network and the physical train. Although the dynamic of grid-forming VSI is in between, large values of voltage and current control bandwidths, which make this system fast enough, allow accurately replicating of the LFO phenomenon.

In conclusion, high control bandwidths would be desirable, as this would reduce control delays which can severely affect emulator performance. The maximum bandwidth that can be achieved would be limited by Nyquist sampling theorem in the first place. A second concern for the selection of the bandwidths would be the noise mainly coming from sensors, during implementation this was found to be indeed the main limiting factor for the selection of the gains of the controllers, see Section VII. Further, it is noted that although all the preceding discussion on the tuning of the controllers has focused on the concept of *bandwidth*, other design aspects, such as natural frequency or settling time, could be used instead for the same purpose since they also contain information about system delays. The detailed impact of additional indices, e.g., damping coefficient, might also need to be considered. A thorough analysis of the influence of controller design and tuning on emulator performance is a matter of ongoing research.

Finally, in terms of implementation in the micro-controller, option 3 requires less computational effort than the other two options, in which relatively complex electronic power converters have to be simulated in real-time.

VII. EXPERIMENTAL RESULTS

This section presents experimental results obtained using the Option 3 (PHIL-Emulator) discussed in Subsection IV-B3. The other two options were disregarded for experimental verification as they were concluded to be inferior. The test bench is shown in Fig. 14. Its design was already discussed in Section V. Power supply parameters, train parameters and emulator parameters are the same as for the simulation results in Section VI (see Tables 2 and 3).

Current control and voltage control bandwidths of $BW_{VC-e} = 50$ Hz and $BW_{CC-e} = 500$ Hz, respectively, have been used in the test bench. It was discussed in Section VI-D the relevance of emulator control bandwidths for the accurate reproduction of LFO. Unfortunately, signal noise content in the real system avoided the use of the higher bandwidths. Fig. 15 shows the catenary voltage step response to test the control action of grid-forming VSI.

Fig. 16 shows the system response to changes in the virtual catenary impedance. LFO are seen to develop as the virtual network impedance increases, eventually reaching the stability limit in Fig. 16c. Oscillation frequency at the stability limit occurs at around 8 Hz, which is in good agreement with the simulation results from Fig. 12a. The limit values of power network impedance also agree with the values obtained in the simulation. This confirms the correctness of the proposed approach.

VIII. CONCLUSION

The design of a network emulator able to reproduce the dynamic behavior of a railway traction network, including LFO, has been discussed in this paper. The emulator will allow evaluating the response of the 4QC power converter in the event of LFO in a test bench, avoiding expensive or even non-viable on-track tests.

Three different options for the catenary emulator were considered: open-loop, closed-loop, and PHIL. Simulation was used for preliminary verification. It was shown that due to the lack of feedback from the train, the first option can reproduce the LFO only when the virtual and actual traction loads are equal and constant; additionally, the first two options require precise knowledge of the train controller parameters, which might not be available. PHIL option was shown to overcome these limitations.

The study also showed that the bandwidth of the voltage and current controllers of the grid-forming VSI emulator strongly affect its capability to reproduce LFO. It was concluded that, despite the low-frequency nature of LFO events being targeted, relatively high bandwidths and proper spectral separation between voltage and current control loops bandwidths are required.

The proposed methods were tested in a test bench consisting of a grid-forming inverter and the 4QC connected through an LCL filter. Experimental results were found to be in good agreement with simulation results. Due to noise, the higher control bandwidths values used in the simulation couldn't be achieved on the test bench.

It is noted finally that the work shown in this paper is a concept validation with a downscale system rated for 10 kW. The design of a full-scale test bench is ongoing.

REFERENCES

[1] S. Menth and M. Meyer, "Low frequency power oscillations in electric railway systems," *Elektrische Bahnen.*, vol. 104, no. 4, pp. 216–221, 2006.

[2] L. Buhrkall, S. Danielsen, A. Eisele, M. Bergman, and J. Galic, "Low-frequency oscillations in Scandinavian railway power supply—Part I: Basic considerations," *Elektrische Bahnen*, vol. 108, pp. 56–64, Jan. 2010.

[3] L. Buhrkall, S. Danielsen, A. Eisele, M. Bergman, and J. Galic, "Low-frequency oscillations in Scandinavian railway power supply—Part 2: Test of traction units," *Elektrische Bahnen*, vol. 108, pp. 103–111, Mar. 2010.

[4] S. Danielsen, T. Toftevaag, and O. Fosso, "Application of linear analysis in traction power system stability studies," in *Proc. 11th Int. Conf. Comput. Syst. Design Operation Railway Transit Syst.*, vol. 103, Aug. 2008, pp. 401–410.

[5] S. Danielsen, M. Molinas, T. Toftevaag, and O. Fosso, "Constant power load characteristic's influence on the low-frequency interaction between advanced electrical rail vehicle and railway traction power supply with rotary converters," *Modern Electr. Traction*, pp. 1–6, Sep. 2009.

[6] J. Suarez, P. Ladoux, N. Roux, H. Caron, and E. Guillame, "Measurement of locomotive input admittance to analyse low frequency instability on AC rail networks," in *Proc. Int. Symp. Power Electron., Electr. Drives, Autom. Motion*, Jun. 2014, pp. 790–795.

[7] H. Wang, W. Mingli, and J. Sun, "Analysis of low-frequency oscillation in electric railways based on small-signal modeling of vehicle-grid system in *dq* frame," *IEEE Trans. Power Electron.*, vol. 30, no. 9, pp. 5318–5330, Sep. 2015.

[8] S. Danielsen, "Electric traction power system stability: Low-frequency interaction between advanced rail vehicles and a rotary frequency converter," Ph.D. dissertation, NTNU Trykk, Trondheim, Norway, 2010.

[9] P. Frutos, J. M. Guerrero, I. Muniategui, I. Vicente, A. Endemano, and F. Briz, "Low-frequency oscillations analysis in AC railway networks using eigenmode identification," in *Proc. IEEE Energy Convers. Congr. Expo. (ECCE)*, Oct. 2021, pp. 1573–1579.

[10] Y. Hachicha, D. Cypers, S. Belin, M. Meli, P. Ladoux, and N. Roux, "Towards a unified low frequency Stability criterion for 15 kV / 16.7 Hz and 25 kV / 50 Hz railway power system," in *Proc. PCIM Eur. Digit., Int. Exhib. Conf. Power Electron., Intell. Motion, Renew. Energy Energy Manag.*, 2020, pp. 1–8.

[11] P. Frutos, P. Ladoux, N. Roux, I. Larrazabal, J. M. Guerrero, and F. Briz, "Low frequency stability of AC railway traction power systems: Analysis of the influence of traction unit parameters," *Electronics*, vol. 11, no. 10, p. 1593, May 2022. [Online]. Available: https://www.mdpi.com/2079-9292/11/10/1593

[12] *Railway Applications—Fixed Installations and Rolling Stock—Technical Criteria for the Coordination Between Power Supply and Rolling Stock to Achieve Interoperability—Part 2: Stability and Harmonics*, document EN 50388-2:2017, 2017.

[13] H. Hu, H. Tao, F. Blaabjerg, X. Wang, Z. He, and S. Gao, "Train–network interactions and stability evaluation in high-speed railways—Part I: Phenomena and modeling," *IEEE Trans. Power Electron.*, vol. 33, no. 6, pp. 4627–4642, Jun. 2018.

[14] Y. Liao, Z. Liu, H. Zhang, and B. Wen, "Low-frequency stability analysis of single-phase system with *dq*-frame impedance approach—Part I: Impedance modeling and verification," *IEEE Trans. Ind. Appl.*, vol. 54, no. 5, pp. 4999–5011, Sep. 2018.

[15] Y. Huo, G. Gruosso, and L. Piegari, "Power hardware in the loop simulator of photovoltaic plant for smart grid interation analysis," in *Proc. IEEE Int. Conf. Environ. Electr. Eng. IEEE Ind. Commercial Power Syst. Eur. (EEEIC/I CPS Eur.)*, Jun. 2017, pp. 1–5.

[16] A. Castaings, A. Bouscayrol, W. Lhomme, and R. Trigui, "Power hardware-in-the-loop simulation for testing multi-sources vehicles," in *Proc. 20th IFAC World Congr.*, Toulouse, France, Jul. 2017, vol. 50, no. 1, pp. 10971–10976. [Online]. Available: https://hal.archives-ouvertes.fr/hal-01745537

[17] Y. Hachicha, D. Cypers, M. Takuefou, S. Belin, P. Ladoux, and N. Roux, "Use of a HIL railway traction simulator for low frequency network stability studies," in *Proc. IEEE Int. Conf. Electr. Syst. Aircr., Railway, Ship Propuls. Road Vehicles Int. Transp. Electrific. Conf. (ESARS-ITEC)*, Nov. 2018, pp. 1–5.

[18] P. Ladoux, Y. Hachicha, D. Cypers, M. Meli, and N. Roux, "New method for determining the low-frequency stability limit of a 50 Hz electric traction power system," *Elektrische Bahnen*, vol. 10, no. 10, p. 18, Oct. 2020. [Online]. Available: https://hal-univ-tlse3.archives-ouvertes.fr/hal-03286350

[19] A. Yazdani and R. Iravani, *Voltage-Sourced Converters in Power Systems*. Hoboken, NJ, USA: Wiley, 2010.

[20] S. Golestan and J. M. Guerrero, "Conventional synchronous reference frame phase-locked loop is an adaptive complex filter," *IEEE Trans. Ind. Electron.*, vol. 62, no. 3, pp. 1679–1682, Mar. 2015.

[21] K. Ogata, *Modern Control Engineering* (Instrumentation and Controls Series). Upper Saddle River, NJ, USA: Prentice-Hall, 2010. [Online]. Available: https://books.google.es/books?id=Wu5GpNAelzkC

[22] Y. Zhou, H. Hu, X. Yang, J. Yang, Z. He, and S. Gao, "Low frequency oscillation traceability and suppression in railway electrification systems," *IEEE Trans. Ind. Appl.*, vol. 55, no. 6, pp. 7699–7711, Nov. 2019.

[23] X. Yuan, W. Merk, H. Stemmler, and J. Allmeling, "Stationary-frame generalized integrators for current control of active power filters with zero steady-state error for current harmonics of concern under unbalanced and distorted operating conditions," *IEEE Trans. Ind. Appl.*, vol. 38, no. 2, pp. 523–532, Mar. 2002.

[24] L. Buhrkall, "Traction system case study," in *Proc. IET Prof. Develop. Course Electric Traction Syst.*, 2008, pp. 53–71.

[25] G. Calzo, A. Lidozzi, L. Solero, and F. Crescimbini, "LC filter design for on-grid and off-grid distributed generating units," *IEEE Trans. Ind. Appl.*, vol. 51, pp. 1560–1639, Mar. 2015.

[26] S. Jayalath and M. Hanif, "Generalized LCL-filter design algorithm for grid-connected voltage-source inverter," *IEEE Trans. Ind. Electron.*, vol. 64, no. 3, pp. 1905–1915, Mar. 2017.

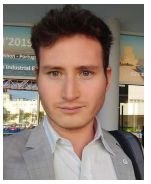

PAUL FRUTOS-GALARZA (Student Member, IEEE) received the B.S. degree in electrical engineering from the San Francisco de Quito University, Quito, Ecuador, in 2013, and the M.Sc. degree from the University of Nottingham, Nottingham, U.K., in 2017. He is currently pursuing the Ph.D. degree in electrical engineering with the University of Oviedo, Asturias, Spain. His research interests include control strategies for multilevel inverters, solid-state transformers, stability studies of high-speed railway systems, and the development of control strategies of power converters for traction applications.

JUAN M. GUERRERO (Senior Member, IEEE) received the M.E. degree in industrial engineering and the Ph.D. degree in electrical and electronic engineering from the University of Oviedo, Gijón, Spain, in 1998 and 2003, respectively. Since 1999, he has occupied different teaching and research positions with the Department of Electrical, Computer and Systems Engineering, University of Oviedo, where he is currently a Full Professor. From February 2002 to October 2002, he was a Visiting Scholar at the University of Wisconsin, Madison. From June 2007 to December 2007, he was a Visiting Professor at the Tennessee Technological University, Cookeville. His research interests include control of electric drives and power converters, electric traction, and renewable energy generation. He is an Associate Editor of the IEEE TRANSACTIONS ON INDUSTRY APPLICATIONS.

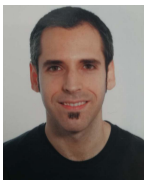

IKER MUNIATEGUI-ASPIAZU received the Industrial Technical Engineering degree (electronic design specialization) and the Industrial Automatics and Electronics Engineering degree from the University of Mondragon, Mondragon, Spain, in 2004 and 2007, respectively. In September 2006, he joined Ingeteam Power Technology (formerly TEAM), Zamudio, Spain, where he worked as a Control and Regulation Engineer, and he is currently a Control and Regulation Manager of the Traction Department. His current research interests include power converter and advanced control drives, modulation techniques, and railway research issues such as ac catenary stability and mechanical vibrations in drive trains.

IBAN VICENTE-MAKAZAGA graduated in electrical engineering from the University of Mondragon, Mondragon, Spain, in 2003, and the M.S. and Ph.D. degrees from the University of Manchester, U.K., in 2004 and 2009, respectively. He joined Ingeteam Power Technology (formerly TEAM), Zamudio, Spain, where he works as a Control and Regulation Engineer involved in railway traction control for trams, locomotives, and EMUs. His current research interests include power converters and advanced control drives, modulation techniques, machine parameters, and speed estimation techniques as well as railway research issues such as ac catenary stability and mechanical vibrations in drive trains.

AITOR ENDEMAÑO-ISASI received the Industrial Technical Engineering degree (electronic design specialization) and the Industrial Automatics and Electronics Engineering degree, from the University of Mondragon, Mondragon, Spain, in 1997 and 2000, respectively, and the Ph.D. degree from Heriot-Watt University, Edinburgh, Scotland, U.K., in 2003. In 2003, he joined Traction Department, Ingeteam Power Technology (formerly TEAM), Zamudio, Spain, where he has been a Control and Regulation Engineer, involved in several traction control design projects for trams, locomotives, and EMUs. His current research interests include power converter and advanced control drives, modulation techniques, and railway research issues such as ac catenary stability and mechanical vibrations in drive trains.

DAVID ORTEGA-RODRIGUEZ received the Licentiate degree in electric and electronic engineering from Universidad Pais Vasco of Bilbao (UPV), Spain, in 2004. He worked as a Development Engineer at the Traction Department, Ingeteam, from 2004 to April 2010. He joined Euskotren as a Rolling Stock Maintenance Engineer. Later in December 2010, he again joined the Traction Department, Ingeteam, where he is currently a Technology Coordination Manager. His research interests include rolling stock architectures, EMC, noise, efficiency, and high-power converters for traction and energy recovery systems.

FERNANDO BRIZ (Senior Member, IEEE) received the M.S. and Ph.D. degrees from the University of Oviedo, Gijón, Spain, in 1990 and 1996, respectively. He is currently a Full Professor with the Department of Electrical, Computer and Systems Engineering, University of Oviedo. His current research interests include electronic power converters and ac drives, power systems, machine monitoring and diagnostics, and digital signal processing. He received an IEEE Transactions on Industry Applications Award and nine IEEE Industry Applications Society Conference and IEEE Energy Conversion Congress and Exposition prize paper awards. He is the Past Chair of the Industrial Drives Committee of the Industrial Power Conversion System Department (IPCSD), IAS. He is currently the Vice Chair of IPCSD. He has served on scientific committees and as the Vice Chair or a Technical Program Chair for several conferences, including ECCE, IEMDC, ICEM, ICEMS, and SLED. He is a Member of the Steering Committee of IEEE Journal of Emerging and Selected Topics in Power Electronics. He is an Editor of IEEE Journal of Emerging and Selected Topics in Power Electronics and an Associate Editor of *IAS Transactions*.

B.2 Conference publications

B.2.1 Low-Frequency Oscillations Analysis in AC Railway Networks Using Eigenmode Identification

P. Frutos, J. M. Guerrero, I. Muniategui, I. Vicente, A. Endemano and F. Briz, "Low-Frequency Oscillations Analysis in AC Railway Networks Using Eigenmode Identification," *2021 IEEE Energy Conversion Congress and Exposition (ECCE)*, Vancouver, BC, Canada, 2021, pp. 1573-1579. https://doi.org/10.1109/ECCE47101.2021.9595947.

Low-Frequency Oscillations Analysis in AC Railway Networks Using Eigenmode Identification

Paul Frutos*, Juan Manuel Guerrero*, Iker Muniategui†, Iban Vicente†, Aitor Endemano†, and Fernando Briz*
*University of Oviedo, Department of Electrical, Computer & System Engineering, Gijón, Spain
Email: frutospaul@uniovi.es, guerrero@uniovi.es, fbriz@uniovi.es
† Ingeteam Power Technology S.A., Traction R&D, Zamudio, Spain
Email: iker.muniategui@ingeteam.com, iban.vicente@ingeteam.com, aitor.endemano@ingeteam.com

2021 IEEE Energy Conversion Congress and Exposition (ECCE) | 978-1-7281-5135-9/21/$31.00 ©2021 IEEE | DOI: 10.1109/ECCE47101.2021.9595947

***Abstract*—Dynamic interactions among AC railway networks and train power converters have been reported to cause low-frequency oscillations (LFO) and eventually instability phenomena, which can collapse the railway power system. Several system parameters can influence the appearance of LFO, including catenary line length, power consumption, control bandwidths, etc. This paper proposes a methodology for the analysis and understanding of the impact of all these parameters on the LFO. The proposed method combines time-domain simulations with eigenvalue analysis. Eigenvalue migration will be shown to be a powerful tool to understand the risk of instability and to analyse potential remedial actions.**

I. Introduction

Modern train railway systems include a large number of power electronic converters, aimed to improve performance and efficiency. Despite the benefits, complex dynamic interactions among the railway network and the controlled power converters can produce undesired phenomena, which might result in power system instability, including LFO phenomena [1]–[7] and harmonic instability [8]

LFO phenomena have been reported worldwide for different types of railway networks under different operating conditions (see Table I).

TABLE I: LFO reported cases

N º	Case	$f_0[Hz]$	$f_{osc}[Hz]$	Time
1	Zürich, Switzerland [5]	16.67	5	1995
2	Norway [3]	16.67	1.6	2007
3	Washington, USA [9]	25	3	2006
4	Thionville, France [4]	50	5	2008
5	Siemens test, Germany [1]	50	7	2006
6	Hudong Depot, China [6]	50	2-4	2008
7	Shanhaiguan Hub, China [7]	50	6-7	2011

Reported events include 16,6 Hz catenaries fed from rotary converters [3], and static frequency converters [9], as well as 50 Hz catenaries fed from the grid [4]. Therefore, this paper considers the phenomena occurred when the low-frequency dynamics are mainly determined by the train vehicle.

There is a number of constructive and operational aspects that will affect LFO formation, including catenary line length, consumed power, design, and tuning of train catenary-side converter controllers (bandwidth of current and voltage controllers, PLLs, SOGI, etc), interference from other trains, etc [5]. It is not trivial therefore to determine the circumstances in which LFO will occur.

In this paper, modes of operation (i.e. eigenmodes) that can produce LFO are first obtained by means of time-domain simulations, system dynamics being characterized using eigenvalues estimation techniques. Sensitivity is then studied by means of eigenvalue migration analysis. System parameters considered for the analysis presented in this paper include: catenary length; power consumption; characteristics of on-board catenary side converter: current and dc voltage control bandwidths, second-order generalized integrator (SOGI), phase-locked loop (PLL); leakage inductance of the transformer; and dc-link capacitor.

The paper is organized as follows. Section II describes rail-network model used for the study. Section III deals with LFO description and modelling; section IV addresses eigenvalue migration and sensitivity analysis. Finally, conclusions are drawn in section V.

II. Train-network control system model

A simplified representation of the railway system is shown in Fig. 1, it is seen to consist of three main elements: power source, transmission line (i.e. catenary line), and power load (i.e. train). For the study of LFO, an equivalent circuit of the transmission line with only resistance and inductance is widely used [1], [5], [6], as capacitive effects can be safely neglected. Fig. 2 shows the rail-network model, including control loops, that will be used in this study. The main elements interfacing the network and the traction inverters are the transformer, single-phase four-quadrant power converter (4QC), and DC-link capacitor. The traction inverter is represented as an equivalent linear load in Fig. 2.

A cascaded control structure consisting of an outer voltage control loop and an inner current control loop is used to regulate the DC link voltage v_{dc} [9]. The control in Fig. 2 operates in dq coordinates, the d-axis voltage corresponding to the catenary voltage. A second-order generalized integrator is being used to obtain the quadrature signals. A PLL is used to obtain the grid voltage phase angle required for the coordinate transformations to the synchronous reference frame [7].

In order to get the desired current control bandwidth (BW_{cc}) and the voltage control bandwidth (BW_{vc}), controllers (i.e Kp_{cc},Ki_{cc},Kp_{vc},Ki_{vc}) were tuned using the zero-pole cancellation as described in [10]. The design of the PLL was performed according to [11] where the PLL proportional and

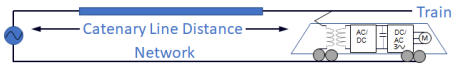

Fig. 1: Simplified representation of the train-network system

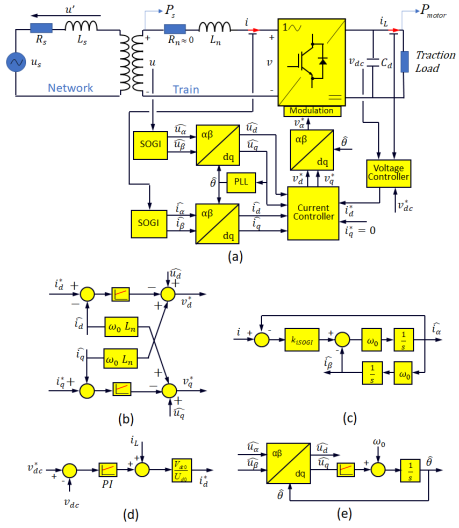

Fig. 2: Rail-network control system model (a) Complete Model (b) Current Controller (c) SOGI (d) DC Voltage Controller (e) PLL

integral gain are chosen as Kp_{pll}=K_{pll}, Ki_{pll}=$K^2_{pll}/2$. Finally, the value of gain K_{sogi} for SOGI was chosen as described in [5]

III. LFO MODELING

The typical catenary line voltage and train current waveforms when LFO occur, and its harmonic spectra, are shown in Fig. 3. AC signals in the time domain oscillate at a frequency f_0, their magnitude (envelope) varying at a frequency f_{osc}. The corresponding spectrums show the fundamental component an f_0 escorted by two sidebands at $f_L = f_0 - f_{osc}$ and $f_H = f_0 + f_{osc}$ respectively. This behavior can be modelled mathematically as shown by (1).

$$\begin{aligned} u(t) &= U(t)\sin(2\pi f_0 t) \\ &= (U_0 + \Delta U\cos(2\pi f_{osc} t))\sin(2\pi f_0 t) \\ &= U_0\sin(2\pi f_0 t) + \frac{\Delta U}{2}\sin(2\pi f_L t) + \frac{\Delta U}{2}\sin(2\pi f_H t) \end{aligned} \quad (1)$$

It is important to notice that, in general, the magnitude of the harmonic spectra components f_L and f_H are not equal, contrary to equation (1) illustrate. The accurate simulation in Fig. 3 shows the actual asymmetry of spectra components. Due to this distortion in the catenary line voltage and vehicle current, the low-frequency oscillations have caused a number of serious issues, such as the malfunction of the protection system, high-voltage, and current that could damage the electrical/electronic equipment, transportation delays, and so on.

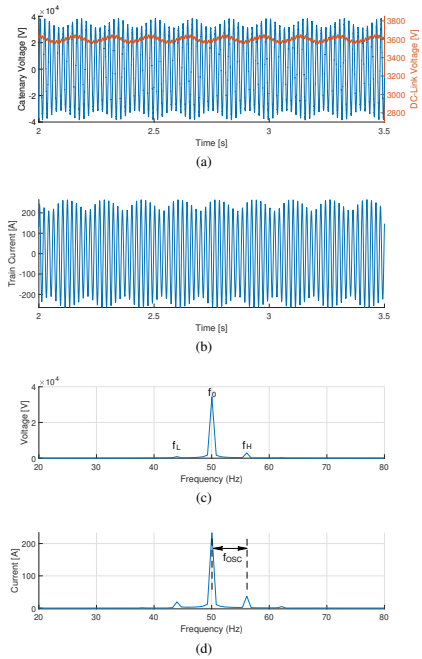

Fig. 3: Simulated LFO phenomena: (a) Catenary Line Voltage and Train DC-Link Voltage (b) Train Current (c) Catenary Line Voltage FFT (d) Train Current FFT

IV. LFO ANALYSIS USING EIGENMODE IDENTIFICATION

In this section, eigenmodes are used to characterize the system dynamic behavior when LFO occurs. Associated eigenvalues to each eigenmode are obtained by means of numerical estimation techniques.

The impact on LFO of catenary length and consumed power are first considered. The sensitivity to 4QC control parameters, transformer leakage inductance, and dc-link capacitor is then discussed using this approach.

A. Eigenvalue migration due to catenary length

Fig. 4 shows the time domain transient response to a disturbance of the dc-link voltage, for different lengths of

catenary line. For this analysis, it is considered that 4QC control parameters are constant. The power consumed by the vehicle was only 300 kW. This corresponds to the low power condition reported in [4].

Degradation of dc-link voltage control as the distance increases is readily observed in Fig. 4, eventually leading to instability. Transient responses shown in Fig. 4 in response to changes in catenary length can modeled as a set of complex conjugates eigenvalues as shown in Fig. 5. The following terms are defined from Fig. 5: ω_n is the natural frequency and σ is the attenuation constant and θ the eigenvalue angle. Using these last two terms, damping ratio ζ and settling time T_s are defined (2). Notice that the damping ratio is zero when $\theta = \pi/2$, which is the stability limit.

$$\zeta = \frac{\sigma}{\omega_n} = \cos(\theta) \ , \ T_s = \frac{\ln(0.02)}{\sigma} \tag{2}$$

The trajectory followed by the eigenvalues as the catenary length increases show a smaller damping coefficient and slower dynamics, which results in a degradation of the system behavior, eventually becoming unstable.

B. Eigenvalue migration with catenary length and consumed power

Eigenvalue migration with load power is shown in Fig. 6 for three different catenary lengths, short-line (20 km), medium-line (60 km), and long-line (120 km). It is interesting to note that the overall shape of the eigenvalue trajectory is similar for all three cases. Lower power consumption results in lower damping, i.e. higher instability risks. A closer analysis also reveals that long catenaries combined with low power consumption lead to the highest risk of instability, which is consistent with the behavior reported in the literature [3], [12].

C. Eigenvalue migration with dc-link voltage and current control bandwidths

The influence of the 4QC voltage and current control closed-loop bandwidths is discussed following. For the sake of simplicity, four scenarios are considered for catenary length and power consumption: 1) low distance - low power; 2) low distance - high power; 3) high distance - low power; 4) high distance - high power.

Fig. 7 shows the eigenvalues for different current-control and voltage-control bandwidths for the long-distance catenary - low power consumption case. The general trend is that, for a given current control bandwidth, higher voltage-control bandwidths result in eigenvalue angle θ (as defined in Fig. 5) closer to $\pi/2$ which means shorter damping ratio and larger settling times (σ decreases) and larger natural frequency. On the other hand, it is observed that for a given voltage control bandwidth, larger current-control bandwidths result in larger damping ratio shorter settling times (σ increases), and larger natural frequencies. From Fig. 7 it can be noticed that eigenvalue migration due to simultaneous variation in voltage-control bandwidths and voltage-control bandwidth in

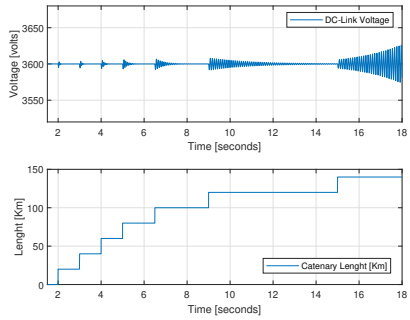

Fig. 4: dc-link time response for variations in catenary-line lenght

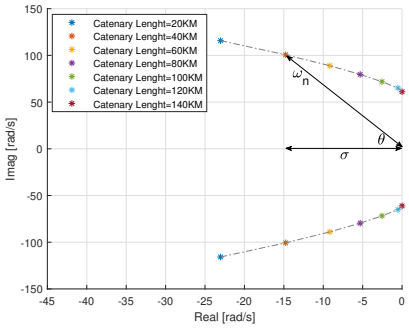

Fig. 5: Eigenvalue migration for variations in catenary-line lenght

this region are close to being orthogonal. It is concluded from Fig. 7 that rather than the bandwidth of the current and voltage control loops, the ratio BWcc/BWv will be critical for system stability.

Fig. 8 shows the damping ratio, settling time and natural frequency, as a function of BWcc and BWvc, for two different values of the current control bandwidth and the four scenarios discussed at the beginning of this section are considered: 1) low distance - low power; 2) low distance - high power; 3) high distance - low power; 4) high distance - high power. The following conclusions are reached:

- It is observed from Fig. 8(a) that the damping ratio (i.e. system stability) always increases as the BWcc/BWvc ratio increases. Low values of the BWcc/BWvc ratio will jeopardize system stability for any operation mode. This trend is independent of the catenary distance and load power.
- From Fig. 8(a), is observed that high distance - low power scenario shows the highest risk of instability (lower

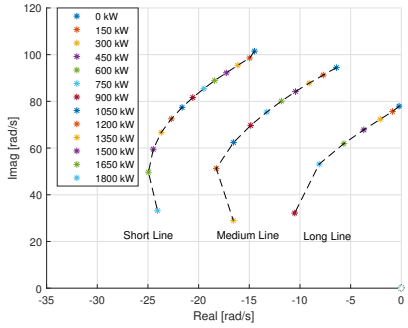

Fig. 6: Eigenvalue migration for variations in load power. Cases: short line (20 km), medium line (60 km) and long line (120) km

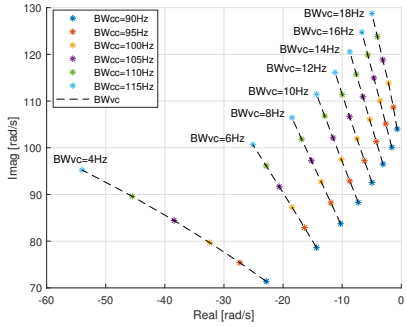

Fig. 7: Eigenvalue migration as a function of dc-link voltage and current control bandwidths, for the case of a long catenary and low power consumption. BWcc and BWvc stand for current and voltage control bandwidths

damping ratio). The damping ratio is seen to change linearly with BWcc/BWvc, independent of BWcc.

- The damping ratio increases when the load power level increases and decreases when the catenary line increases. This behavior is consistent with previous studies [7].
- It is observed from Fig. 8(b) that the settling time of the oscillations decreases as BWcc/BWvc increases. Low BWcc/BWvc ratios in the high distance - low power scenario values result in significant settling times, i.e. dc-link voltage oscillation can persist for seconds.
- The natural frequency shown in Fig. 8(c) tend to decrease as the BWcc/BWvc ratio increases, but differences by a factor of 2 can be observed depending on the scenario. The frequency of the LFO might need to be considered if control strategies aimed to cancel LFO are to be implemented [12].

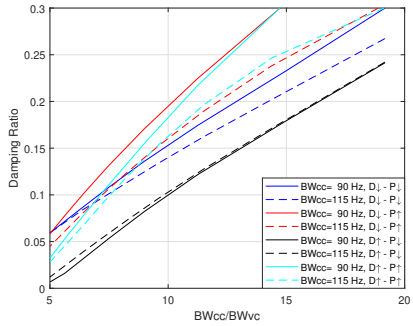

(a) Damping ratio vs. BWcc/BWvc

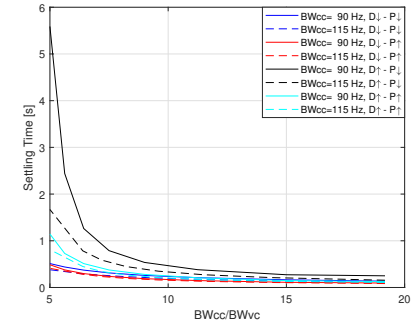

(b) Settling Time vs. BWcc/BWvc

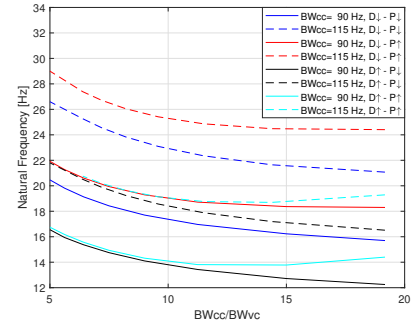

(c) Natural Frequency vs. BWcc/BWvc

Fig. 8: Damping ratio, Settling Time and Natural Frequency as a function of BWcc/BWvc ratio for different current control bandwidths (90 Hz and 115 Hz). D↓ and D↑ stands for low (20 km) and high (120 km) distance, P↓ and P↑ stands for low and high power respectively

D. Eigenvalue migration with PLL and SOGI tuning

In addition to the control bandwidths and catenary distance discussed previously, other elements involved in the control of the 4QC might influence the LFO. These can include the PLL used to synchronize the 4QC with the catenary ac voltage, and the SOGI (depending on the control strategy being used).

Fig. 9 shows the eigenvalue migration for variations in gains Kv_{sogi} and Ki_{sogi} of voltage and current SOGI. The gains are varied within a range of 0.7 to 1.3 or their nominal values, $Kv_{sogi-nominal} = 0.8$ and $Ki_{sogi-nominal} = 1$ respectively. Increasing Kv_{sogi} migrates system eigenvalues towards instability limit (i.e. shorter damping ratio) while increasing Ki_{sogi}, migrate the eigenvalues away from stability limit (i.e. larger damping ratio). However, increasing Ki_{sogi} implies an increase of its bandwidth, which could compromise SOGI low-pass filter characteristic. It is concluded that a trade-off is required, sensitivity analysis of SOGI is performed in section IV-F.

Fig. 10 shows eigenvalue migration for variations in gain K_{pll}. As mentioned in section II, the design of the PLL was performed according to [11] where the PLL proportional and integral gain are chosen as Kp_{pll}=K_{pll}, Ki_{pll}=$K_{pll}^2/2$. Generally speaking, PLL was found to have a marginal impact. Increasing K_{pll} by a factor as large as ten is seen to have a marginal effect on the eigenvalues. A sensitivity analysis of PLL is performed in section IV-F.

E. Eigenvalue migration due to the leakage inductance (L_n) of transformer and dc-link capacitor (C_d)

Fig. 11 shows the eigenvalue migration as a function of leakage inductance of transformer and dc-link capacitor. From this figure, it is possible to see that larger values of capacitance and inductance of the transformer improve stability against LFO. However, bigger capacitors are bulky and expensive, what places obvious constraints on the values that could be used. Also, designing a transformer to get a larger value of leakage inductance could limit the power transfer capability. Finally, from Fig. 11, close to the stability limit, low values of the leakage inductance might provoke oscillations at lower frequencies than low values of the DC-Link capacitance. The trajectory of the eigenvalue migration of Cd tends to go to stability limit meanwhile increasing the oscillation frequency.

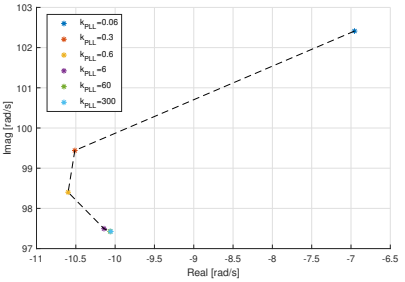

Fig. 10: Eigenvalue migration for variations in gain K_{pll}

F. Combined sensitivity analysis

A different approach to analyze the sensitivity to system parameters discussed in the previous subsections is to obtain the variation of the eigenvalues to an incremental variation of a given parameter, with the rest of system parameters remaining constant.

Fig. 12 shows the variation of damping ratio, settling time and natural frequency, which results from this analysis. The analysis is performed for the case of of a catenary length of 120 km and a power consumption of 300 kW. The system is in this case close to the stability limit. System parameters being considered are changed within a range of 0.8 to 1.2 of their nominal value.

From Fig. 12 the magnitude of the slope of each curve at the operational point (O.P) gives the sensitivity of the damping ratio, settling time and natural frequency to variation

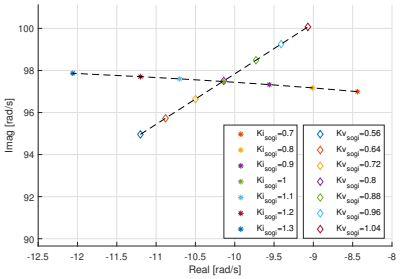

Fig. 9: Eigenvalue migration for variations in gains Kv_{sogi} and Ki_{sogi} correspond to voltage and current quadrature signal generator SOGI.

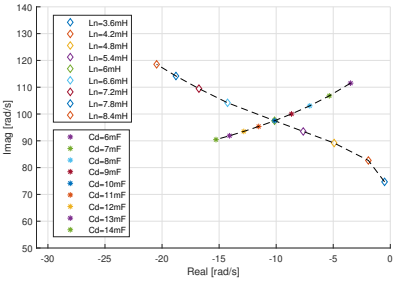

Fig. 11: Eigenvalue migration as a function of leakage inductance of transformer and dc-link capacitor

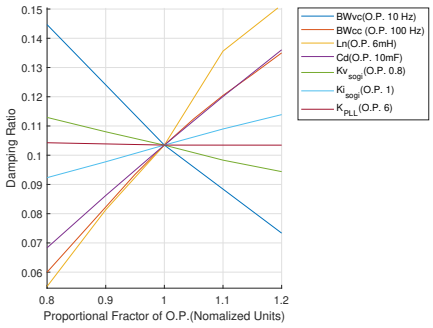

(a) Damping ratio vs. Proportional Factor (Normalized Units)

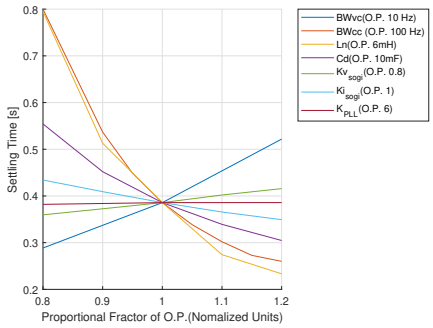

(b) Settling Time vs. Proportional Factor (Normalized Units)

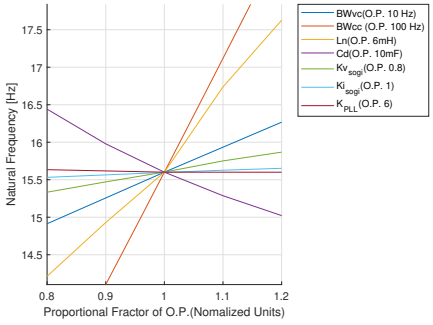

(c) Natural Frequency vs. Proportional Factor (Normalized Units)

Fig. 12: Damping ratio, Settling Time and Natural Frequency as a function of proportional factor of O.P.

in the proportional factor. For the damping ratio, positive slopes indicate that the system becomes more stable as the parameter being consider increases, the contrary occurs for negative slopes. Same reasoning applies for the setting time and natural frequency.

TABLE II: Sensitivity of dynamic system characteristics at O.P. Arrows ↑ and ↓ stands for positive sensitivity and negative sensitivity. Number of arrows show the degree of sensitivity.

	Damping R.(ζ)	Settling T.(T_s)	Natural Freq. (ω_n)
BWvc	↓↓	↑↑	↑↑
BWcc	↑↑	↓↓	↑↑↑
L_n	↑↑↑	↓↓↓	↑↑↑
C_d	↑↑	↓↓	↓↓
Kv_{sogi}	↓	↑	↑
Ki_{sogi}	↑	↓	↑
K_{pll}	-	-	-

Table II summarizes the results shown in Fig. 12. It is observed that for the operating point being considered, LFO shows high sensitivity to L_n and control bandwidths, while sensitivity to SOGI parameters is low, practically no sensitivity to PLL tuning is observed.

It is interesting to note that increasing the voltage-control bandwidth decreases the damping of the system while increasing the current-control bandwidth increases the damping of the system, they are opposites. From Fig. 12(a), BWvc and BWcc curves can be considered as symmetric with respect to the x-axis. Rather than the absolute values of the current and voltage control bandwidths, the system response is primarily given by the ratio BWcc/BWvc. Therefore increasing both bandwidths doesn't even vary the system damping since the BWcc/BWvc could still be the same. This goes in accordance with the analysis presented in section IV-C. It is concluded that low values of BWcc/BWvc significantly increase the risk of LFO.

Finally, it is noted that the trajectories shown in Fig. 12 and not necessarily straight lines. This is due to the non-linear nature of the system. This suggests that parameter sensitivity will depend on the operating point, this is a subject of ongoing research.

V. Conclusions

Time-domain simulation combined with eigenvalue migration analysis is proposed in this paper for the analysis of LFO phenomena in AC railway systems. The proposed method allows an insightful visualization of the sensitivity of LFO to catenary and train parameters and consequently identifying critical modes of operation, as well as proposing remedial actions. It is concluded from the analysis performed in this paper that the worst scenario for LFO stability occurs for the case of trains operating far from substations and with low-power consumption. In such a case, the ratio BWcc/BWv is critical for system stability. Finally, a comparison of each parameter sensitivity was performed.

REFERENCES

[1] S. Menth and Meyer.M., "Low frequency power oscillations in electric railway systems," *eb - Elektrische Bahnen*, vol. 104, pp. 216–221, 2006.

[2] Y. Liao, Z. Liu, H. Zhang, and B. Wen, "Low-frequency stability analysis of single-phase system with dq-frame impedance approach—part i: Impedance modeling and verification," *IEEE Transactions on Industry Applications*, vol. 54, no. 5, pp. 4999–5011, 2018.

[3] L. Buhrkall, S. Danielsen, A. Eisele, M. Bergman, and J. Galic, "Low-frequency oscillations in scandinavian railway power supply - part i: Basic considerations," *eb - Elektrische Bahnen*, vol. 108, pp. 56–64, 01 2010.

[4] J. Suarez, P. Ladoux, N. Roux, H. Caron, and E. Guillame, "Measurement of locomotive input admittance to analyse low frequency instability on ac rail networks," in *2014 International Symposium on Power Electronics, Electrical Drives, Automation and Motion*, 2014, pp. 790–795.

[5] S. Danielsen, M. Molinas, T. Toftevaag, and O. Fosso, "Constant power load characteristic's influence on the low-frequency interaction between advanced electrical rail vehicle and railway traction power supply with rotary converters," 01 2009.

[6] H. Wang, W. Mingli, and J. Sun, "Analysis of low-frequency oscillation in electric railways based on small-signal modeling of vehicle-grid system in dq frame," *IEEE Transactions on Power Electronics*, vol. 30, no. 9, pp. 5318–5330, 2015.

[7] H. Hu, H. Tao, F. Blaabjerg, X. Wang, Z. He, and S. Gao, "Train–network interactions and stability evaluation in high-speed railways–part i: Phenomena and modeling," *IEEE Transactions on Power Electronics*, vol. 33, no. 6, pp. 4627–4642, 2018.

[8] H. Hu, H. Tao, X. Wang, F. Blaabjerg, Z. He, and S. Gao, "Train–network interactions and stability evaluation in high-speed railways—part ii: Influential factors and verifications," *IEEE Transactions on Power Electronics*, vol. 33, no. 6, pp. 4643–4659, 2018.

[9] S. Danielsen, "Ph.d. thesis: Electric traction power system stability: Low-frequency interaction between advanced rail vehicles and a rotary frequency converter," 2010.

[10] A. Yazdani and R. Iravani, *Voltage-Sourced Converters in Power Systems*. John Wiley & Sons, Ltd, 2010.

[11] S. Golestan and J. M. Guerrero, "Conventional synchronous reference frame phase-locked loop is an adaptive complex filter," *IEEE Transactions on Industrial Electronics*, vol. 62, no. 3, pp. 1679–1682, 2015.

[12] L. Buhrkall, S. Danielsen, A. Eisele, M. Bergman, and J. Galic, "Low-frequency oscillations in scandinavian railway power supply -part 2: Test of traction units," vol. 108, pp. 103–111, 03 2010.

B.3 Under review publications

B.3.1 Low frequency oscillations in AC railway traction power systems: Train input-admittance calculation and stability analysis

P. Frutos, J. M. Guerrero, I. Muniategui, A. Endemaño, D. Ortega and F. Briz, " Low frequency oscillations in AC railway traction power systems: Train input-admittance calculation and stability analysis," International Journal of Electrical Power & Energy Systems

Low-frequency oscillations in AC railway traction power systems: Train input-admittance calculation and stability analysis⋆

Paul Frutos[a,*], Juan Manuel Guerrero[a], Iker Muniategui[b], Aitor Endemaño[b], David Ortega[b] and Fernando Briz[a]

[a]University of Oviedo, Department of Electrical, Computer & Systems Engineering, Gijón, 33204, Spain
[b]Ingeteam Power Technology S.A., Traction R&D, Zamudio, Spain

ABSTRACT

Dynamic interactions among the AC railway power supply network and power electronic converters feeding the trains can result in low-frequency oscillation (LFO) of the catenary voltage, leading to a power outage of the substation and the shutdown of train traffic. In order to determine the low-frequency stability of the railway traction power systems, the impedance of the power supply network and the total differential admittance of the trains are required. This paper addresses the development of an analytical small-signal model of the train input admittance. For this purpose, small-signal models of each dynamic element in the control loops are obtained, including the calculation of the second-order generalized integrator (SOGI) model in the synchronous frame. Numerical methods are used for the validation of the models. The concept of the small-signal vector transformation from the actual dq-frame to the estimated dq-frame is presented to model the dynamics due to errors in the coordinate rotation, the mathematical tool was developed for this task. Furthermore, a stability analysis of the railway system is performed, different operational points in power consumption at the DC-link were tested showing the model can predict instabilities at low-power operation (depot case). Finally, sensitivity analysis is performed and presented.

Nomenclature

f	Variable in the time domain
$f(t)$	Impulse response in the time domain
F	Variable in the Laplace domain
$F(s)$	Transfer function in the Laplace domain
$F(j\omega)$	Transfer function in the frequency domain
f^s	Superscript indicating matrices and vectors in the stationary reference frame
f^e	Superscript indicating matrices, transfer functions, vectors, and vector components in the synchronous true reference frame
$f^{\hat{e}}$	Superscript indicating matrices, transfer functions, vectors and vector components in the estimated synchronous reference frame
f_0	Subscrit indicating the steady state value of a variable, for linearization purposes

$\mathbf{f^x} = [f_d^x, f_q^x]^T$	Real space vector in the time domain in a generic reference frame $x \epsilon \{e, \hat{e}\}$
$\boldsymbol{f_{dq}^x} = f_d^x + j f_q^x$	Complex space vector in the time domain in a generic reference frame $x \epsilon \{e, \hat{e}\}$
$\mathbf{F^x} = [F_d^x, F_q^x]^T$	Real space vector in the Laplace domain in a generic reference frame $x \epsilon \{e, \hat{e}\}$
$\boldsymbol{F_{dq}^x} = F_d^x + j F_q^x$	Complex space vector in the Laplace domain in a generic reference frame $x \epsilon \{e, \hat{e}\}$
$\mathbf{f^s} = [f_\alpha, f_\beta]^T$	Real space vector in the time domain in the stationary reference frame
$\boldsymbol{f_{\alpha\beta}^s} = f_\alpha + j f_\beta$	Complex space vector in the time in the stationary reference frame
$\mathbf{F^s} = [F_\alpha, F_\beta]^T$	Real space vector in the Laplace in the stationary reference frame
$\boldsymbol{F_{\alpha\beta}^s} = F_\alpha + j F_\beta$	Complex space vector in the Laplace in the stationary reference frame

⋆ This work was supported in part by the European Commission HORIZON and KDTJU under the project POWERIZED GA No 101096387; in part by the Spanish Ministry of Science and Innovation under grant MCINN-23-PCI2022-135021-2; and in part by the Government of the Principality of Asturias under project AYUD/2021/50988.

*Corresponding author
frutospaul@uniovi.es (P. Frutos); guerrero@uniovi.es (J.M. Guerrero); iker.muniategui@ingeteam.com (I. Muniategui); aitor.ndemano@ingeteam.com (A. Endemaño); david.ortega@ingeteam.com (D. Ortega); fbriz@uniovi.es (F. Briz)
ORCID(s): 0000-0002-2937-8125 (P. Frutos); 0000-0001-5529-9837 (J.M. Guerrero); 0000-0002-6658-8746 (F. Briz)

1. Introduction

Modern onboard railway systems include a large number of power electronic converters aimed to improve the controllability and efficiency of the train. While the benefits brought by power electronic converters are indubitable, dynamic interactions among these and the railway traction network can produce undesired phenomena which might result in power system instability, including resonant instability [1, 2] and low-frequency oscillation (LFO) phenomenon [3–9].

LFO phenomenon has been reported worldwide for different types of railway traction networks and under different operating conditions, see Table 1. LFO phenomenon produces large variation of the catenary voltage at relatively low

Table 1
Reported LFO cases.

N º	Case	f_0 (Hz)	f_{osc} (Hz)	Year
1	Zürich, Switzerland [3]	16.7	5	1995
2	Norway [4, 5]	16.7	1.6	2007
3	Washington, USA[6]	25	3	2006
4	Siemens test, Germany[7]	50	7	2006
5	Thionville, France[8]	50	5	2008
6	Hudong Depot, China[9]	50	2-4	2008
7	Shanhaiguan Hub, China[9]	50	6-7	2011

frequencies, typically in the range of 10%-30% the fundamental frequency (f_0) [6]. Harmful consequences of such events include malfunction of protection systems, overvoltages/overcurrents that could damage the electrical/electronic equipment, and transportation delays, among others [7, 9].

Two particular situations where the LFO phenomenon has been documented are: 1) multiple trains in the depot (i.e., all the vehicles located at the same spot) operating with low power consumption (typically only train's auxiliary system are active) [8]; 2) a train operating far from the substation [4]. The stability analysis performed in this paper focuses in the case of multiples trains operating at depot. However, from the point of view of the stability analysis, these two scenarios are equivalent as explained in [10].

The system resulting from the connection of two or more dynamic systems (e.g. grid and power converters) will be stable if all the elements are passive [11]. The passivity of a system is ensured when the differential input admittance, also referred as input admittance in [12], has a non-negative real part (i.e., non-negative conductance). Usually, the grid (i.e., power supply network) is considered a passive system, since it consists of R, L, and C elements; however, controlled power converters are not passive systems. The differential input admittance of power converters can be studied using small-signal models.

Different small-signal models to calculate the input admittance in both single-phase and three-phase voltage source converters (VSCs) have been presented in several papers [11, 13, 14]. However, most of these works focus on specific elements (e.g. current control) but don't include all the dynamic elements affecting to LFO. A relevant aspect to consider is that AC catenaries are single-phase systems. Extrapolation of analysis and results for three-phase systems might not be therefore straightforward. A relevant difference between the control of three-phase VSCs and single-phase ones, also called four quadrature-converters (4QCs), is that the latter often include one or more quadrature signal generator (QSG) systems.

In [1] and [2] a small-signal model of train input admittance was developed to study railway system instability phenomena, including resonant instability and LFOs; however, the model fails to accurately calculate the train admittance in the low-frequency range.

In [12], the input admittance of a three-phase VSC was calculated including all the dynamic elements (i.e., synchronization system, feedforward filter, etc). This work focuses on a three-phase balanced system (i.e., symmetric dynamic transfer function), and do not include elements which can be relevant for 4QC dynamics as the QSG. In addition, all the dynamic elements in the controller in this work are referred to the same reference frame. However, it often happens that there are elements which are insensitive to errors in the coordinate rotations, while other elements will be affected. Modelling this phenomena will be require the use of multiple reference frames.

Three different reference frames are used for this study: stationary reference frame; synchronous reference aligned with the fundamental component of the catenary voltage; and estimated synchronous reference frame. Small-signal vector transformation from the actual synchronous frame to the estimated synchronous frame will be shown to be key for the development of accurate analytical models of the train.

This paper presents the calculation of the analytical small-signal model of the train input admittance, that can be used for low-frequency stability analysis of the railway systems. Elements considered for the analysis include: DC-link voltage controller; inner current controller; phase-locked loop (PLL) used for synchronization; second order generalized integrator (SOGI) used for filtering action and for quadrature signal generation; finally, delays due to discrete implementation of the control and PWM are also modeled. Verification of the analytical model is performed using a full system simulation model of the catenary and train 4QC converter.

Main contributions of this paper are the inclusion QSG-SOGI model and the use as well as modelling the dynamics due to errors in the coordinate rotation. These will be shown to be critical for accurate modeling of LFO due to its impact in the synchronization system dynamics and in the current control loop.

The paper is organized as follows: Notation and reference frames used in this paper are first defined in Section Nomenclature at the beginning of this article. Section 2 describes the railway system model whose main elements are the power supply network and trains; Section 3 deals with modeling the small-signal train input admittance; Section 4 discusses stability theory needed for the study of the low-frequency stability in the railway system; Section 5 presents stability analysis of the railway for several trains operating at the depot under different operating points; sensitivity analysis of train electrical and control parameter is developed in Section 6; finally, conclusions are drawn in Section 7.

2. Railway System Model

The railway system consists of two main elements: the power supply network and the train [15–18]. The power supply network is composed of an stiff voltage source v_s, the substation impedance and the catenary line. An AC 25 kV/50 Hz electric power supply is considered in this paper. For the study of LFO, an equivalent circuit based only on resistance and inductance is widely used [3, 7, 9, 19], as line capacitive effects can be safely neglected at low

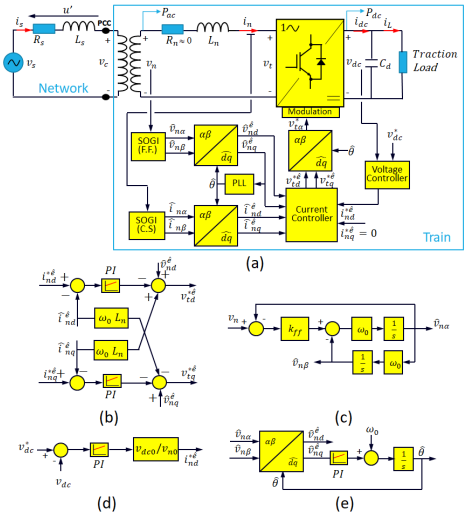

Figure 1: Railway control system model. (a) Train-Network complete model, (b) Current controller, (c) SOGI, (d) DC Voltage controller, (e) PLL.

frequency. Fig. 1 shows the equivalent railway system model that will be used in this study, where v_c is the catenary voltage at point of common coupling (PCC) between the network and the train, and i_s is the catenary current. The network inductance L_s and resistance R_s are modeled as lumped parameters.

The main elements in the train are: power transformer, L-filter, single-phase four-quadrant power converter, DC-link capacitor, and traction drives consisting of inverters and motors. The 4QC behavior will determine the interaction between the train and the network [3, 7, 14, 19]. On the other hand, switching harmonics will not affect the low-frequency dynamics involved in the LFO phenomenon [14, 15]. It is safe therefore to replace the traction drives with an equivalent linear load as shown in Fig. 1, to simplify the analysis and simulations. Here the voltage at secondary of the transformer is defined as the input voltage v_n to the 4QC; i_n is the 4QC inductor current and the terminal voltage is v_t

The 4QC control shown in Fig. 1 operates in dq coordinates, aligning the d-axis with the catenary voltage complex vector. A cascaded control structure consisting of an outer voltage control loop and an inner current control loop is used. In order to get the desired current control bandwidth ($BWcc$) and the voltage control bandwidth ($BWvc$), controllers were tuned using the zero-pole cancellation as described in [20]. A phase-lock loop is used to obtain the estimated grid voltage phase angle $\hat{\theta}$, which is required for the coordinate transformations into the synchronous reference frame [1]. The PLL was designed and tuned as described in [21], where the selection of the gains involves a trade-off between its filtering capability and dynamic response. PLL proportional and integral gains were chosen as $k_{ppll}=k_{pll}$, $k_{ipll}=k_{pll}^2/2$. A second order generalized integrator (SOGI) is used to obtain the quadrature signals, also acting as a voltage feed-forward filter. The gain k_{ff} of the SOGI was chosen as described in [7].

3. Train Input Admittance: Small-Signal Model in dq-frame

The calculation of a small-signal model of the train input admittance is described in this section. Small-signal models of the elements relevant for LFO analysis are presented following. These include the QSG-SOGI, PLL, current controller, and DC-link voltage controller.

3.1. Notation and reference frames

Proper modeling of effects due to errors in the reference estimation will show to be relevant for the accurate modelling of LFO. Furthermore, both complex vector and matrix notation will be used. This subsection is aimed to clarify the notation that will be used throughout the paper. Details on the notation are provided in the Nomenclature section at the beginning of this paper.

3.1.1. Equivalence between matrix and complex vector notation

The use of complex vector notation is convenient for dynamic analysis of symmetric three-phase systems (e.g., balanced impedance) [22, 23]. However, for asymmetrical systems, it is necessary to use matrix notation with the corresponding real space vectors. An example of the equivalence between matrix notation and complex numbers for symmetric systems (i.e., $g^e_{dd} = g^e_{qq}$ and $g^e_{dq} = -g^e_{qd}$.) is shown in (1), where g^e and $\mathbf{g^e}$ are time transfer functions.

$$\mathbf{v^e} = \underbrace{\begin{bmatrix} g^e_{dd} & g^e_{dq} \\ g^e_{qd} & g^e_{qq} \end{bmatrix}}_{\mathbf{g^e}} \mathbf{i^e} \longleftrightarrow \boldsymbol{v}^e_{\boldsymbol{dq}} = (g^e_{dd} - jg^e_{dq})\boldsymbol{i}^e_{\boldsymbol{dq}} \quad (1)$$

3.1.2. Reference Frames

From Fig. 1, the AC voltages and currents in the railway system are single-phase quantities. By using a virtual quadrature component, they can be treated as vectors in the stationary reference frame [24]. By doing this, these quantities can be transformed to a synchronous reference frame aligned with the fundamental component of the catenary voltage v_c. The angle of rotation θ is obtained as (2), where ω_0 is the fundamental power supply frequency imposed by the substation voltage. This reference frame will be termed the *actual grid dq-frame*.

$$d\theta/dt = \omega_0 \quad (2)$$

In order to perform control action, the PLL estimates the catenary voltage phase angle $\hat{\theta}$. This angle defines the

estimated dq-frame, which ideally coincides with the actual dq-frame.

Vector transformations from the actual and estimated dq-frames to the stationary reference frame are given by (3) and (4), respectively. Therefore, the relation between vectors in the actual and estimated dq-frames is given by (5), where $\tilde{\theta}$ is defined as the angle estimation error. See Fig. 2.

$$\boldsymbol{v}^{\boldsymbol{s}}_{\boldsymbol{\alpha\beta}} = e^{j\theta}\boldsymbol{v}^{\boldsymbol{e}}_{\boldsymbol{dq}} \tag{3}$$

$$\boldsymbol{v}^{\boldsymbol{s}}_{\boldsymbol{\alpha\beta}} = e^{j\hat{\theta}}\boldsymbol{v}^{\hat{\boldsymbol{e}}}_{\boldsymbol{dq}} \tag{4}$$

$$\boldsymbol{v}^{\hat{\boldsymbol{e}}}_{\boldsymbol{dq}} = e^{-j\tilde{\theta}}\boldsymbol{v}^{\boldsymbol{e}}_{\boldsymbol{dq}}\ ,\ \tilde{\theta} = \hat{\theta} - \theta \tag{5}$$

Due to the integral action of the PLL, the error angle $\tilde{\theta}$ is zero in the steady state. However, PLL dynamics would result in transient errors which must be included in the model as they can contribute to LFO phenomenon.

In the Laplace domain, and using matrix notation, the vector transformation in (5) can be expressed by (6) using the $dq/\widehat{dq}$ transformation matrix $\mathbf{T}_{\tilde{\theta}}$.

$$\mathbf{V}^{\hat{\mathbf{e}}} = \mathbf{T}_{\tilde{\theta}}\mathbf{V}^{\mathbf{e}} \tag{6}$$

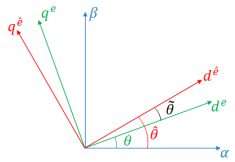

Figure 2: Stationary reference frame and dq-frames

In the steady state transformation matrix $\mathbf{T}_{\tilde{\theta}}$ is equivalent to the identity matrix.

3.1.3. *Small-signal $dq/\widehat{dq}$ vector transformation in the Laplace domain: Influence of error angle $\tilde{\theta}$*

Since $\tilde{\theta}$ only appears in the transient and its variations can be assumed to be small, linear approximation of (5) is performed by taking partial derivatives as shown in (7), where $\tilde{\theta}_0$ and $\boldsymbol{v}^{\boldsymbol{e}}_{\boldsymbol{dq0}}$ are steady state quantities. Moreover, it can be assumed that $\tilde{\theta}_0 = 0$ and $\boldsymbol{v}_{\boldsymbol{dq0}} \equiv \boldsymbol{v}^{\boldsymbol{e}}_{\boldsymbol{dq0}} = \boldsymbol{v}^{\hat{\boldsymbol{e}}}_{\boldsymbol{dq0}} = v_{d0} + jv_{q0}$ since in steady state both dq-frames are aligned.

$$\begin{aligned}\delta\boldsymbol{v}^{\hat{\boldsymbol{e}}}_{\boldsymbol{dq}} &= \left.\frac{e^{-j\tilde{\theta}}\partial\left(\boldsymbol{v}^{\boldsymbol{e}}_{\boldsymbol{dq}}\right)}{\partial\boldsymbol{v}^{\boldsymbol{e}}_{\boldsymbol{dq}}}\right|_0 \delta\boldsymbol{v}^{\boldsymbol{e}}_{\boldsymbol{dq}} + \left.\frac{\boldsymbol{v}^{\boldsymbol{e}}_{\boldsymbol{dq}}\partial\left(e^{-j\tilde{\theta}}\right)}{\partial\tilde{\theta}}\right|_0 \delta\tilde{\theta} \\ &= e^{-j\tilde{\theta}_0}\delta\boldsymbol{v}^{\boldsymbol{e}}_{\boldsymbol{dq}} - je^{-j\tilde{\theta}_0}\boldsymbol{v}^{\boldsymbol{e}}_{\boldsymbol{dq0}}\delta\tilde{\theta} \\ &= \delta\boldsymbol{v}^{\boldsymbol{e}}_{\boldsymbol{dq}} - j\boldsymbol{v}_{\boldsymbol{dq0}}\delta\tilde{\theta}\end{aligned} \tag{7}$$

Applying the Laplace transformation to (7), the small-signal $dq/\widehat{dq}$ vector transformation is obtained (8), which corresponds to (9) using matrix notation.

$$\delta\boldsymbol{V}^{\hat{\boldsymbol{e}}}_{\boldsymbol{dq}} = \delta\boldsymbol{V}^{\boldsymbol{e}}_{\boldsymbol{dq}} - j\boldsymbol{v}_{\boldsymbol{dq0}}\delta\tilde{\Theta} \tag{8}$$

$$\underbrace{\begin{bmatrix}\delta V^{\hat{e}}_d \\ \delta V^{\hat{e}}_q\end{bmatrix}}_{\delta\mathbf{V}^{\hat{\mathbf{e}}}} = \underbrace{\begin{bmatrix}\delta V^{e}_d \\ \delta V^{e}_q\end{bmatrix}}_{\delta\mathbf{V}^{\mathbf{e}}} - \underbrace{\begin{bmatrix}0 & -1 \\ 1 & 0\end{bmatrix}\begin{bmatrix}v_{d0} \\ v_{q0}\end{bmatrix}}_{\mathbf{V_0}}\delta\tilde{\Theta} \tag{9}$$

It is concluded from the previous discussion that the small-signal behavior of any vector in the estimated dq reference frame is a function of the small-signal behavior of the vector in the actual dq reference frame as well as of the small-signal behavior of the angle estimation error $\tilde{\theta}$.

3.2. Phase-locked Loop and Second order generalized integrator

3.2.1. *QSG-SOGI*

The QSG-SOGI structure is commonly used in single-phase systems, such as AC catenaries, due to its simple implementation, filtering properties, and capability to provide the quadrature signal. The structure of the QSG-SOGI is presented in Fig. 1(c). The input voltage V_n is applied to QSG-SOGI system, generating the estimated input voltage signal $\hat{V}_{n\alpha}$ and creating the estimated virtual quadrature component $\hat{V}_{n\beta}$. These filtered signals are used for synchronization and as feed-forward to the current control loop.

Defining $V_{n\alpha} = V_n$, and considering $V_{n\beta}$ is an ideal virtual quadrature component of the input voltage, the QSG-SOGI transfer function can be expressed as (10) using matrix notation. The transfer functions of the second-order band-pass filter and QSG are given by (11) and (12) respectively.

$$\underbrace{\begin{bmatrix}\hat{V}_{n\alpha} \\ \hat{V}_{n\beta}\end{bmatrix}}_{\hat{\mathbf{V}}^{\mathbf{s}}_{\mathbf{n}}} = \underbrace{\begin{bmatrix}H_{f\alpha}(s) & 0 \\ H_{f\beta}(s) & 0\end{bmatrix}}_{\mathbf{H}^{\mathbf{s}}_{\mathbf{ff}}}\underbrace{\begin{bmatrix}V_{n\alpha} \\ V_{n\beta}\end{bmatrix}}_{\mathbf{V}^{\mathbf{s}}_{\mathbf{n}}} \tag{10}$$

$$H_{f\alpha}(s) = \frac{\hat{V}_{n\alpha}}{V_n} = \frac{k_{ff}\omega_0 s}{s^2 + k_{ff}\omega_0 s + \omega_0^2} \tag{11}$$

$$H_{f\beta}(s) = \frac{\hat{V}_{n\beta}}{V_n} = \frac{k_{ff}\omega_0^2}{s^2 + k_{ff}\omega_0 s + \omega_0^2} \tag{12}$$

The Laplace-domain equation in the $\alpha\beta$ reference frame (10) becomes a convolution in the time domain as shown in (13), with $h_{f\alpha}(t)$ and $h_{f\beta}(t)$ being the impulse response of (11) and (12) respectively.

$$\begin{bmatrix}\hat{v}_{n\alpha} \\ \hat{v}_{n\beta}\end{bmatrix} = \begin{bmatrix}h_{f\alpha}(t) & 0 \\ h_{f\beta}(t) & 0\end{bmatrix} * \begin{bmatrix}v_{n\alpha} \\ v_{n\beta}\end{bmatrix} \tag{13}$$

Transformation to the actual dq reference frame is given by (14).

$$\begin{bmatrix} \hat{v}^e_{nd} \\ \hat{v}^e_{nq} \end{bmatrix} = \mathbf{t}_\theta \left(\begin{bmatrix} h_{f\alpha}(t) & 0 \\ h_{f\beta}(t) & 0 \end{bmatrix} * \mathbf{t}_\theta^{-1} \begin{bmatrix} v^e_{nd} \\ v^e_{nq} \end{bmatrix} \right) \qquad \mathbf{t}_\theta = \begin{bmatrix} \cos\omega_0 t & \sin\omega_0 t \\ -\sin\omega_0 t & \cos\omega_0 t \end{bmatrix} \tag{14}$$

Solving the convolution and taking the Laplace transform of (14) (see Appendix A), (15)-(19) are obtained.

$$\underbrace{\begin{bmatrix} \hat{V}^e_{nd} \\ \hat{V}^e_{nq} \end{bmatrix}}_{\hat{\mathbf{V}}^e_{\mathbf{n}}} \cong \underbrace{\begin{bmatrix} H^e_{ff-dd}(s) & H^e_{ff-dq}(s) \\ H^e_{ff-qd}(s) & H^e_{ff-qq}(s) \end{bmatrix}}_{\mathbf{H}^e_{\mathbf{ff}}} \underbrace{\begin{bmatrix} V^e_{nd} \\ V^e_{nq} \end{bmatrix}}_{\mathbf{V}^e_{\mathbf{n}}} \tag{15}$$

$$H^e_{ff-dd}(s) = H^e_{ff-qq}(s) \tag{16}$$

$$H^e_{ff-dd}(s) = H^e_{ff-qq}(s) \tag{17}$$

$$H^e_{ff-dd}(s) = \frac{1}{4}\left(H_{f\alpha}(s+j\omega_0) + H_{f\alpha}(s-j\omega_0)\right) + \frac{j}{4}\left(H_{f\beta}(s+j\omega_0) - H_{f\beta}(s-j\omega_0)\right) \tag{18}$$

$$H^e_{ff-qd}(s) = \frac{1}{4}\left(H_{f\beta}(s+j\omega_0) + H_{f\beta}(s-j\omega_0)\right) - \frac{j}{4}\left(H_{f\alpha}(s+j\omega_0) - H_{f\alpha}(s-j\omega_0)\right) \tag{19}$$

It is noted that since (10) is not a symmetric system, frequency components around $2\omega_0$ can appear in the synchronous reference frame [25]. This is explained in Appendix A. Since this study is focused in LFO, frequency components around $2\omega_0$ are not expected to affect, and will be disregarded. So, $\mathbf{H^e_{ff}}$ is the approximated QSG-SOGI transfer function that relates the input voltage and the estimated input voltage, both in the actual dq-frame.

Fig. 3(a) shows the voltage QSG-SOGI action and the park transformation to the estimated dq-frame. Fig. 3(b) shows; first, $\alpha\beta - dq - \widehat{dq}$ decomposition, that is when the rotation action performed by the estimated angle $\hat{\theta}$ is decomposed in cascade rotations by θ and $\tilde{\theta}$, in to order to obtain the estimated input voltage in the actual dq-frame; second, the QSG-SOGI transformation from stationary frame to the actual dq-frame.

Fig. 4 shows the frequency response obtained both using the analytical model of the SOGI (15), and from simulation using the model in Fig. 3(b), the agreement being remarkable.

The current QSG-SOGI has the same structure as the voltage QSG-SOGI shown in Fig. 1c, but the gain now being k_{cs}. Consequently, the preceding methodology and discussion applies in this case too. Therefore, the current QSG-SOGI transfer function in the actual dq-frame $\mathbf{H^e_{cs}}$ is obtained following the same steps for $\mathbf{H^e_{ff}}$.

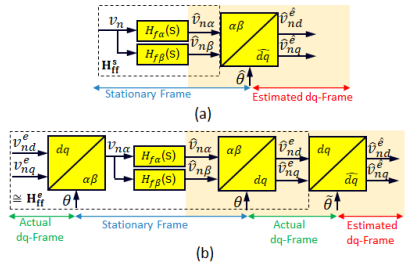

Figure 3: (a) QSG-SOGI in $\alpha\beta$-frame and the park transformation to estimated dq-frame. (b) $\alpha\beta - dq - \widehat{dq}$ decomposition & QSG-SOGI in actual dq-frame

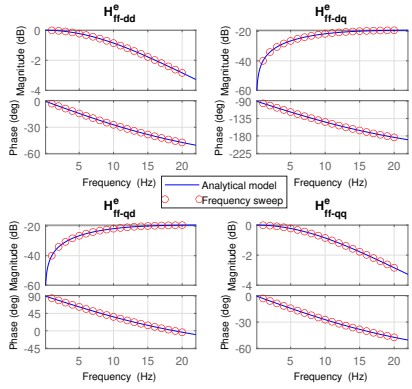

Figure 4: Frequency response: SOGI transfer function ($\mathbf{H^e_{ff}}$) in the actual dq-frame. Analytical low-frequency model vs. frequency sweep of simulation model.

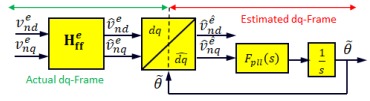

Figure 5: Phase locked loop in dq-frame

3.2.2. *Phase-locked Loop*

PLL structure in dq-frame' is shown in Fig. 5, the controller transfer function being:

$$F_{pll}(s) = k_{ppll} + \frac{k_{ipll}}{s} \tag{20}$$

The linear relationship between the error angle $\tilde{\theta}$ and the estimated input q-axis voltage in the estimated frame $\hat{v}^{\hat{e}}_{nq}$ is

readily observed from the figure. It is therefore straightforward to obtain the small-signal (21).

$$\delta\tilde{\Theta} = \frac{F_{pll}(s)}{s}\delta\hat{V}^{\hat{e}}_{nq} \tag{21}$$

By applying the small-signal transformation (8) to the estimated input voltage complex vector $\hat{\boldsymbol{V}}^{\hat{e}}_{\boldsymbol{ndq}}$, (22) is derived.

$$\delta\hat{\boldsymbol{V}}^{\hat{e}}_{\boldsymbol{ndq}} = \delta\hat{\boldsymbol{V}}^{\boldsymbol{e}}_{\boldsymbol{ndq}} - j\left(v_{nd0} + jv_{nq0}\right)\delta\tilde{\Theta} \tag{22}$$

It is noted that in the steady state, estimated and real values of input voltage are equal; consequently $\boldsymbol{v_{ndq0}} \equiv \hat{\boldsymbol{v}}^{\hat{e}}_{\boldsymbol{ndq0}} = \hat{\boldsymbol{v}}^{\boldsymbol{e}}_{\boldsymbol{ndq0}} = \boldsymbol{v}^{\boldsymbol{e}}_{\boldsymbol{ndq0}} = v_{nd0}+jv_{nq0}$. Since in steady state $v_{nq0} = 0$, (23) is obtained.

$$\delta\hat{V}^{\hat{e}}_{nq} = \delta\hat{V}^{e}_{nq} - v_{nd0}\delta\tilde{\Theta} \tag{23}$$

Now, replacing (23) in (21), the small-signal model of the error angle is given by (24)

$$\delta\tilde{\Theta} = \underbrace{\frac{F_{pll}(s)}{s + v_{nd0}F_{pll}(s)}}_{G_{pll}(s)}\delta\hat{V}^{e}_{nq} \tag{24}$$

Eq. (24) shows that small variations of the error angle $\tilde{\theta}$ depends on the small variations of the q-axis component of the estimated input voltage $\hat{v}^{e}_{nq}$, which means it depends implicitly on the SOGI dynamics. This is further analyzed in Section 3.2.3.

3.2.3. Small-signal $dq/\widehat{dq}$ vector transformation: Influence of SOGI and PLL

So far PLL and SOGI have been analyzed independently. However, the differential error angle depends on both PLL and SOGI dynamics as shown in Section 3.2.2. Therefore, the small-signal $dq/\widehat{dq}$ vector transformation can be obtained first combining (9) and (24), and then using (15) to add explicitly the SOGI dynamics dependency in (25). This transformation is a function of the input voltage.

$$\delta\mathbf{V}^{\hat{\mathbf{e}}} = \delta\mathbf{V}^{\mathbf{e}} - \underbrace{\begin{bmatrix} 0 & -1 \\ 1 & 0 \end{bmatrix}\mathbf{V_0}\begin{bmatrix} 0 & G_{pll}(s) \end{bmatrix}}_{\mathbf{G_{PLL}(V_0)}}\mathbf{H}^{\mathbf{e}}_{\mathbf{ff}}\delta\mathbf{V}^{\mathbf{e}}_{\mathbf{n}} \tag{25}$$

A similar expression of (25) without including the SOGI dynamics dependency was presented in [12], but obtained with a different derivation method and only for specific vectors; however, using the approach based on partial derivatives as shown in this paper; the derivation of $dq/\widehat{dq}$ vector transformation is straightforward and valid for any vector (e.g., input voltage vector).

Equation (25) will be used to build the small-signal current control model in Section 3.3 and to integrate in the model the DC-link control system in Section 3.4

3.3. Current Control

From Fig. 1a, the AC-side 4QC dynamics is seen to correspond to an LR filter and can be defined by (26).

$$v_n = L_n\frac{di_n}{dt} + R_n i_n + v_t \tag{26}$$

Assuming that ideal orthogonal components for voltage and current signals in (26), are available, and transforming the equivalent $\alpha\beta$ system to the actual dq-frame, the model (27)-(28) in Laplace domain is obtained.

$$\mathbf{V}^{\mathbf{e}}_{\mathbf{n}} = \mathbf{Z}^{\mathbf{e}}_{\mathbf{n}}\mathbf{I}^{\mathbf{e}}_{\mathbf{n}} + \mathbf{V}^{\mathbf{e}}_{\mathbf{t}} \tag{27}$$

$$\mathbf{Z}^{\mathbf{e}}_{\mathbf{n}} = \begin{bmatrix} L_n s + R_n & -\omega_0 L \\ \omega_0 L & L_n s + R_n \end{bmatrix} \tag{28}$$

Fig. 6 shows the current control system in the actual and estimated dq-frames. The voltage command $\mathbf{V}^{*\hat{\mathbf{e}}}_{\mathbf{t}}$ generated by the controller is obtained using (29), where $\hat{\mathbf{V}}^{\hat{\mathbf{e}}}_{\mathbf{n}}$ is the estimated input voltage in the estimated dq-frame (30), $\hat{\mathbf{I}}^{\hat{\mathbf{e}}}_{\mathbf{n}}$ is estimated inductance current in the estimated dq-frame (31), and $\mathbf{I}^{*\hat{\mathbf{e}}}_{\mathbf{n}}$ is the current reference in the estimated dq-frame.

$$\mathbf{V}^{*\hat{\mathbf{e}}}_{\mathbf{t}} = \hat{\mathbf{V}}^{\hat{\mathbf{e}}}_{\mathbf{n}} - \mathbf{G}^{\hat{\mathbf{e}}}_{\mathbf{cc}}\left(\mathbf{I}^{*\hat{\mathbf{e}}}_{\mathbf{n}} - \hat{\mathbf{I}}^{\hat{\mathbf{e}}}_{\mathbf{n}}\right) - \mathbf{G}^{\hat{\mathbf{e}}}_{\omega_0\mathbf{L_n}}\hat{\mathbf{I}}^{\hat{\mathbf{e}}}_{\mathbf{n}} \tag{29}$$

$$\hat{\mathbf{V}}^{\hat{\mathbf{e}}}_{\mathbf{n}} = \mathbf{T}_{\tilde{\theta}}\mathbf{H}^{\mathbf{e}}_{\mathbf{ff}}\mathbf{V}^{\mathbf{e}}_{\mathbf{n}} \tag{30}$$

$$\hat{\mathbf{I}}^{\hat{\mathbf{e}}}_{\mathbf{n}} = \mathbf{T}_{\tilde{\theta}}\mathbf{H}^{\mathbf{e}}_{\mathbf{cs}}\mathbf{I}^{\mathbf{e}}_{\mathbf{n}} \tag{31}$$

The current controller transfer function matrix $\mathbf{G}^{\hat{\mathbf{e}}}_{\mathbf{cc}}$ in the estimated dq-frame is shown in (32), PI current controller transfer function being (33).

$$\mathbf{G}^{\hat{\mathbf{e}}}_{\mathbf{cc}} = \begin{bmatrix} G^{\hat{e}}_{\mathrm{cc}}(s) & 0 \\ 0 & G^{\hat{e}}_{\mathrm{cc}}(s) \end{bmatrix} \tag{32}$$

$$G^{\hat{e}}_{\mathrm{cc}}(s) = k_{pcc} + \frac{k_{icc}}{s} \tag{33}$$

Cross-coupling decoupling in (29) is achieved using (34).

$$\mathbf{G}^{\hat{\mathbf{e}}}_{\omega_0\mathbf{L_n}} = \begin{bmatrix} 0 & -\omega_0 L_n \\ \omega_0 L_n & 0 \end{bmatrix} \tag{34}$$

Control delays can affect significantly to the current regulator performance. A total time delay $T_d = 1.5T_s$ due to computation time (i.e., T_s) and zero-order hold (i.e., $0.5T_s$), where $T_s = 1/f_s$ is the sampling time, which is the inverse of the sampling frequency f_s. The delay is modeled as (35)

$$G^{e}_{d}(s) = e^{-T_d s} \tag{35}$$

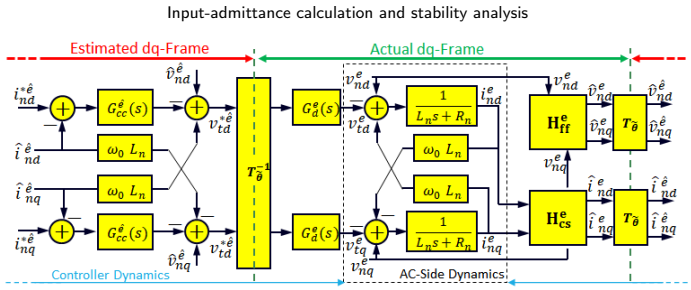

Figure 6: Current control system dq-Frame. AC-side dynamics and controller dynamics

Finally, the terminal voltage $\mathbf{V_t^e}$ in the actual dq-frame is defined by equation (36), where $\mathbf{G_d^e} = G_d^e(s)\mathbf{I}$ is the product of the delay transfer function and the identity matrix $\mathbf{I}$.

$$\mathbf{V_t^e} = \mathbf{G_d^e}\mathbf{T}_{\tilde{\theta}}^{-1}\mathbf{V_t^{*\hat{e}}} \tag{36}$$

Using equations (27)-(36) the closed loop current control system that corresponds to the block diagram in Fig. 6 is defined by (37)-(38).

$$\mathbf{I_n^e} = \mathbf{Z_f^{-1}}(\mathbf{I} - \mathbf{G_d^e}\mathbf{H_{ff}^e})\mathbf{V_n^e} + \mathbf{Z_f^{-1}}\mathbf{G_d^e}\mathbf{T}_{\tilde{\theta}}^{-1}\mathbf{G_{cc}^{\hat{e}}}\mathbf{I_n^{*\hat{e}}} \tag{37}$$

$$\mathbf{Z_f} = \mathbf{Z_n^e} + \mathbf{G_d^e}\mathbf{G_{cc}^e}\mathbf{H_{cs}^e} - \mathbf{G_d^e}\mathbf{G_{\omega_0 L_n}^e}\mathbf{H_{cs}^e} \tag{38}$$

with $\mathbf{G_{cc}^e} = \mathbf{T}_{\tilde{\theta}}^{-1}\mathbf{G_{cc}^{\hat{e}}}\mathbf{T}_{\tilde{\theta}}$ and $\mathbf{G_{\omega_0 L_n}^e} = \mathbf{T}_{\tilde{\theta}}^{-1}\mathbf{G_{\omega_0 L_n}^{\hat{e}}}\mathbf{T}_{\tilde{\theta}}$

One inconvenient of (37) is that it includes vectors and transfer functions in two different reference frames as well as the inverse of matrix rotation. By transforming all terms to the actual synchronous reference frame, (39) is obtained.

$$\mathbf{I_n^e} = \mathbf{Z_f^{-1}}(\mathbf{I} - \mathbf{G_d^e}\mathbf{H_{ff}^e})\mathbf{V_n^e} + \mathbf{Z_f^{-1}}\mathbf{G_d^e}\mathbf{G_{cc}^e}\mathbf{I_n^{*e}} \tag{39}$$

Reference frame transformations of a system produces a frequency displacements in the corresponding transfer function. The effect of an error between estimated and actual frequencies therefore implies a change in the Laplace operator $s \longrightarrow s + j\tilde{\omega}$, where $\tilde{\omega} = d\tilde{\theta}/dt$ is the frequency error. In the steady state actual and estimated dq frames are aligned, i.e., $\tilde{\omega} = 0$. On the other hand, during transients the error frequency $\tilde{\omega}$ is very small compared to ω_0 [12], and can be safely neglected. Therefore, it is considered that both dq-frames are rotating at the same frequency and (40) can be assumed.

$$\mathbf{G^e} = \mathbf{T}_{\tilde{\theta}}^{-1}\mathbf{G^{\hat{e}}}\mathbf{T}_{\tilde{\theta}} \cong \mathbf{G^{\hat{e}}} \tag{40}$$

Equal rotation frequency does not imply the phase of vectors in both dq-frames is the same. PLL is in charge of maintaining vectors aligned in the steady state, but this does not happen in transients and the error angle can not be neglected in the LFO study; therefore, $dq/\hat{dq}$ small-signal vector transformation (25) is required to be applied in the reference current vector $\mathbf{I_n^{*e}}$ in (39) to obtain the small-signal closed-loop current control system model, which is expressed by (41). For the vector transformation, it is necessary taking into account that in the steady state, the reference current and the 4QC current are the same in both dq-frames $\mathbf{I_{n0}} \equiv \mathbf{I_{n0}^{*\hat{e}}} = \mathbf{I_{n0}^{*e}} = \mathbf{I_{n0}^e}$.

$$\begin{aligned}\delta\mathbf{I_n^e} =& \mathbf{Z_f^{-1}}(\mathbf{I} - \mathbf{G_d^e}\mathbf{H_{ff}^e})\delta\mathbf{V_n^e} \\ &+ \mathbf{Z_f^{-1}}\mathbf{G_d^e}\mathbf{G_{cc}^e}(\delta\mathbf{I_n^{*\hat{e}}} + \mathbf{G_{pll}}(\mathbf{I_{n0}})\mathbf{H_{ff}^e}\delta\mathbf{V_n^e})\end{aligned} \tag{41}$$

where $\mathbf{G_{pll}}(\mathbf{I_{n0}}) = \begin{bmatrix} 0 & -i_{nq0}G_{pll}(s) \\ 0 & -i_{nd0}G_{pll}(s) \end{bmatrix}$

Rearranging (41) the small-signal model of the current control system transfer function (42) is obtained, which is represented in Fig. 7 as an inner loop of the 4QC input admittance.

$$\delta\mathbf{I_n^e} = \mathbf{G_{ci}}\delta\mathbf{I_n^{*e}} + \mathbf{Y_{ci}}\delta\mathbf{V_n^e} \tag{42}$$

where $\mathbf{G_{ci}} = \mathbf{Z_f^{-1}}\mathbf{G_d^e}\mathbf{G_{cc}^e}$
and $\mathbf{Y_{ci}} = \mathbf{Z_f^{-1}}\left(\mathbf{I} - \mathbf{G_d^e}\mathbf{H_{ff}^e} + \mathbf{G_d^e}\mathbf{G_{cc}^e}\mathbf{G_{pll}}(\mathbf{I_{n0}})\mathbf{H_{ff}^e}\right)$

3.4. DC-Link Voltage Control

3.4.1. DC-Link Voltage Dynamics

Since the impedance of the 4QC is mainly inductive ($R_n \approx 0$), associated Joule losses can be safely neglected. Commutation loses in the converter are neglected as well due to LFO occurs at low power consumption [15]. Under this assumptions, power conservation between the converter AC-side and DC-side can be assumed (43).

$$\underbrace{v_{dc}i_{dc}}_{P_{dc}} \cong \underbrace{v_{nd}^e i_{nd}^e + v_{nq}^e i_{nq}^e}_{P_{ac}} \tag{43}$$

Taking partial derivatives in (43), the small-signal variation in the DC-side current is obtained (44), with subscript "$_0$" indicating steady-state values.

$$\begin{aligned}\delta i_{dc} =& \frac{v_{nd0}}{v_{dc0}}\delta i_{nd}^e + \frac{i_{nd0}}{v_{dc0}}\delta v_{nd}^e + \frac{v_{nq0}}{v_{dc0}}\delta i_{nq}^e \\ &+ \frac{i_{nq0}}{v_{dc0}}\delta v_{nq}^e - \frac{v_{nd0}i_{nd0} + v_{nq0}i_{nq0}}{v_{dc0}^2}\delta v_{dc}\end{aligned} \tag{44}$$

Taking Laplace transform and considering that in the steady state the train operates with unity power factor (i.e., $i_{nq0} = 0$), the input voltage vector is aligned with the synchronous frame (i.e., $v_{nq0} = 0$), and $P_{dc0} \cong P_{ac0} = v_{nd0} i_{nd0}$, (45) is obtained.

$$\delta I_{dc} = \frac{v_{nd0}}{v_{dc0}} \delta I^e_{nd} + \frac{i_{nd0}}{v_{dc0}} \delta V^e_{nd} - \frac{v_{nd0} i_{nd0}}{v^2_{dc0}} \delta V_{dc} \quad (45)$$

Loads connected to the DC-link include traction converters and auxiliary loads. For LFO analysis they can be modeled as an equivalent resistor [3, 14]. The small-signal model of the 4QC DC-side coincides in this case with the transfer function of the RC circuit (46), as seen in Fig. 1(a).

$$\delta V_{dc} = \left(\frac{R_L}{R_L C_d s + 1} \right) \delta I_{dc} \quad (46)$$

Finally (47) is obtained combining (46) and (45), where $G_{vv}(s)$ and $G_{iv}(s)$ are the transfer functions that relates small variation of DC-link voltage with the d-axis component of input voltage and 4QC inductance current.

$$\delta V_{dc} = \underbrace{\frac{v_{nd0}}{v_{dc0}} \left(\frac{1}{C_d s + 2/R_L} \right)}_{G_{iv}(s)} \delta I^e_{nd} + \underbrace{\frac{i_{nd0}}{v_{dc0}} \left(\frac{1}{C_d s + 2/R_L} \right)}_{G_{vv}(s)} \delta V^e_{nd} \quad (47)$$

3.4.2. *Voltage Controller*

Voltage controller is shown in Fig. 1(d). Voltage controller is modelled as (48), the PI controller transfer function being (49).

$$I^{*\hat{e}}_{nd} = \left(V^*_{dc} - V_{dc} \right) G_{vc}(s) k_d \quad (48)$$

$$G_{vc}(s) = k_{pvc} + \frac{k_{ivc}}{s} \quad (49)$$

Considering that the DC-link voltage command is not changing, the small-signal model in (50) is obtained, where $k_d = i_{nd0}/i_{dc0} = v_{dc0}/v_{nd0}$ is the gain relating AC and DC quantities.

$$\delta I^{*\hat{e}}_{nd} = -G_{vc}(s) k_d \delta V_{dc} \quad (50)$$

Transforming (47)-(48) to use matrix notation, the relationship between the input voltage to the train current and the command to the current regulator is obtained (51), where $\mathbf{G^e_{vc}} = G^e_{vc}(s)\mathbf{I}$.

$$\delta \mathbf{I}^{*\hat{\mathbf{e}}}_{\mathbf{n}} = -k_d \left(\mathbf{G_{vc} G_{iv}} \delta \mathbf{I^e_n} + \mathbf{G_{vc} G_{vv}} \delta \mathbf{V^e_n} \right) \quad (51)$$

$$\text{with } \mathbf{G_{iv}} = \begin{bmatrix} G_{iv}(s) & 0 \\ 0 & 0 \end{bmatrix} \text{ and } \mathbf{G_{vv}} = \begin{bmatrix} G_{vv}(s) & 0 \\ 0 & 0 \end{bmatrix}$$

3.5. Train input admittance

Combining DC-link voltage small-signal dynamics given by (51) and closed loop current control dynamics given by (42), the small-signal input admittance of the train that relates small variations of the input voltage and 4QC current in the actual dq-frame is obtained as (52)-(53). The corresponding block diagram is shown in Fig. 7.

$$\frac{\delta \mathbf{I^e_n}}{\delta \mathbf{V^e_n}} = \mathbf{Y_{tn}} \quad (52)$$

$$\mathbf{Y_{tn}} = \frac{\mathbf{I} - \mathbf{G^e_d H^e_{ff}} - k_d \mathbf{G^e_d G^e_{cc} G_{vc} G_{vv}} + \mathbf{G^e_d G^e_{cc} G_{pll}(I_{n0}) H^e_{ff}}}{\mathbf{Z^e_n} + \mathbf{G^e_d G^e_{cc} H^e_{cs}} - \mathbf{G^e_d G^e_{\omega_0 L_n} H^e_{cs}} + k_d \mathbf{G^e_d G^e_{cc} G_{vc} G_{iv}}} \quad (53)$$

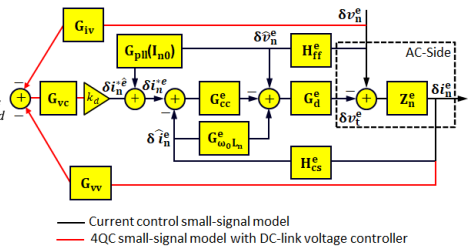

Figure 7: Block diagram of the 4QC (train) input admittance in the actual dq-frame $\mathbf{Y_{tn}}$

Finally train admittance seen from the catenary line is given by (54), where k is the transformer turns ratio.

$$\mathbf{Y_t} = \frac{1}{k^2} \mathbf{Y_{tn}} \quad (54)$$

Correctness of (54) was confirmed by means of simulation using the *frequency scanning* method described in [8]. System model is shown in Fig. 8.

Train and control parameters are shown in Table 2.

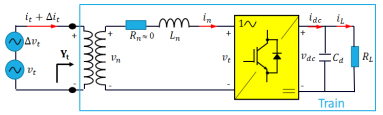

Figure 8: Frequency scanning method to obtain the input admittance in the dq-frame.

The voltage being applied is (55), where the terms with sub-index "$_0$" stand for the steady state voltage, while the voltages with Δ are the small-signal excitation, ω being the frequency of the small-signal excitation.

Symbol	Description	Value
V_c	RMS Catenary Voltage	25 kV
V_{dc}	Nominal DC-link Voltage	3600 V
k	Transformer Ratio	14.12
L_n	4QC Inductance	3 mH
R_n	4QC Resistance	10 mΩ
$BWvc$	Voltage Control Bandwidth	5 Hz
$BWcc$	Current Control Bandwidth	50 Hz
k_{ff}	Voltage SOGI Gain	0.80
k_{cs}	Current SOGI Gain	1
k_{pll}	Phase-Locked Loop Gain	6
P_{dc}	Power Load	50 kW
f_{sw}	Switching Frequency	700 Hz
f_s	Sampling Frequency	1400 Hz

Table 2
Train electrical and control parameters.

$$v_t + \Delta v_t = \big(V_{td0} + \Delta V_{td}\sin(\omega t)\big)\cos(\omega_0 t) + \big(\Delta V_{tq}\sin(\omega t)\big)\sin(\omega_0 t) \tag{55}$$

The resulting current will be of the form shown by (56).

$$i_t + \Delta i_t = \big(I_{td0} + \Delta I_{td}\sin(\omega t + \phi_d)\big)\cos(\omega_0 t) + \big(I_{tq0} + \Delta I_{tq}\sin(\omega t + \phi_q)\big)\sin(\omega_0 t) \tag{56}$$

The train admittance is obtained from the injected voltage and the measured current as (57)

$$\mathbf{Y_t}(j\omega) = \begin{bmatrix} \frac{\Delta I_{td}\angle\phi_d}{\Delta V_{td}}\Big|_{\Delta V_{tq}=0} & \frac{\Delta I_{td}\angle\phi_d}{\Delta V_{tq}}\Big|_{\Delta V_{td}=0} \\ \frac{\Delta I_{tq}\angle\phi_q}{\Delta V_{td}}\Big|_{\Delta V_{tq}=0} & \frac{\Delta I_{tq}\angle\phi_q}{\Delta V_{tq}}\Big|_{\Delta V_{td}=0} \end{bmatrix} \tag{57}$$

Fig.9 shows the train admittance obtained obtained from (53), the level of agreement being remarkable.

4. LFO Stability Theory

This section covers the frequency-domain stability criteria used to determine the risk of LFO instability. The stability criteria are applied over the impedance-based small-signal model of the railway traction system [2–4, 16], which is used for the study of the LFO phenomenon reported for multiple trains located at a specific place in the power supply network (e.g. trains at the depot).

4.1. Impedance-based small-signal model

Fig. 10 shows the impedance-based small-signal model of the railway traction system, which can be viewed as as a closed-loop system defined by (58), where $\mathbf{Z_s}$ is the total network impedance in the actual dq-frame, $\mathbf{Y_T} = n\mathbf{Y_t}$ is the total input admittance in the actual dq-frame and n, is the total number of trains connected to the catenary line at the same spot.

$$\mathbf{G} = \frac{\delta \mathbf{I_s^e}}{\delta \mathbf{V_s^e}} = \frac{\mathbf{Y_T}}{\mathbf{I} + \mathbf{Y_T Z_s}} \tag{58}$$

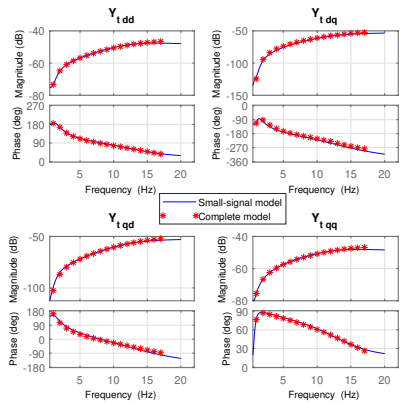

Figure 9: Train input admittance in the actual dq-frame obtained from the analytical small-signal model vs frequency sweep of complete simulation model

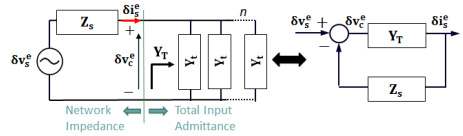

Figure 10: Impedance based small-signal model

The input admittance of a single train $\mathbf{Y_t}$ (52) was already obtained in Section 3. The network impedance matrix $\mathbf{Z_s}$ is given by (59), being function of the network resistance and inductance, R_s and L_s, and the fundamental frequency ω_0.

$$\mathbf{Z_s} = \begin{bmatrix} L_s s + R_s & -\omega_0 L_s \\ \omega_0 L_s & L_s s + R_s \end{bmatrix} \tag{59}$$

4.2. Stability Criteria

To guarantee system stability, the denominator of (58), which is the characteristic equation, should not be equal to zero when $s = j\omega$ for any value of ω [26].

The impedance of the power supply network is an RL circuit, which is a stable system. A train connected to an ideal power source is also considered a stable system [27]. Therefore, these elements are stable in open loop. However, these conditions do not guarantee stability when they are interconnected in a closed-loop system [7]; so, additional stability criteria must be considered in this case. Specific criteria for the study of low-frequency oscillations are defined in the following text.

Since the control system allows independent control of active and reactive power using the currents i_{nd} and i_{nq} respectively, the railway model is considered a multiple-input and multiple-output (MIMO) system. A factorization of the MIMO open-loop transfer function, $\mathbf{Y_T}(j\omega)\mathbf{Z_s}(j\omega)$, is described in (60), where $\mathbf{\Lambda}(j\omega)$ is the eigenvalue matrix and $\mathbf{P}$ is the eigenvector matrix [16, 17].

$$\mathbf{Y_T}(j\omega)\mathbf{Z_s}(j\omega) = \mathbf{P}\mathbf{\Lambda}(j\omega)\mathbf{P}^{-1} \tag{60}$$

$$\mathbf{\Lambda}(j\omega) = \begin{bmatrix} \lambda_1(j\omega) & 0 \\ 0 & \lambda_2(j\omega) \end{bmatrix} \tag{61}$$

As observed in (61), $\mathbf{\Lambda}(j\omega)$ is a diagonal matrix. This allows to analyze the stability from eigenvalues $\lambda_1(j\omega)$ and $\lambda_2(j\omega)$ as two decoupled single-input single-output (SISO) systems [10].

In the frequency domain, the Nyquist criterion [26] and Rever's criterion [17] are extensively used for examining the stability of SISO systems. Both criteria are equivalent, indeed both have been used for LFO analysis in [3, 10] and [16, 17] respectively

The stability criterion, as defined by Rever, is equivalent to the traditional stability criteria applied in Bode diagram that indicates that the closed-loop system is stable if, at the crossover frequency f_c (i.e., where the phase of eigenvalues $\lambda_{1,2}$ reaches $-180º$), the magnitude of the open loop transfer function is less than 1 in absolute units (i.e., less than 0 decibels) [16]. Using a comparable method, Nyquist criterion specifies that the closed loop system is stable if the eigenvalues $\lambda_{1,2}$ do not encircle the point $(1, -180º)$ in the complex plane [26].

The gain margin is defined as $GM = 1/|\lambda_{1,2}(2\pi f_c)|$; therefore, stability is ensured for a gain margin larger than 1 in absolute units (i.e., positive values in dB); the phase margin is defined as $PM = arg(\lambda_{1,2}) + 180º$ [10], where $|\lambda_{1,2}| = 1$.

5. Stability Analysis

In this section, the stability criteria from Section 4 are applied to test a railway system model with a different number of trains in the depot. The effect of increasing the power consumption at DC-link is studied too.

5.1. Stability Analysis of trains on depot

For the sake of simplicity, in this analysis it is considered that all the trains in the depot are identical (i.e., they have the same electrical and control parameters) and operating at the same base power of 50 kW; therefore, they have the same input admittance. The analysis for the case of different input admittances would follow the same methodology used in this section. The only difference is that in such case, the total admittance is not a multiple of the single train admittance but the sum of admittances [10].

The stability analysis in three different cases is presented: a stable system ($n = 17$), a system at its stability limit ($n = 27$), and an unstable system ($n = 37$). Time-domain simulations are used to verify the analysis.

The specific train admittance used for the analysis is shown in Figure 9, which corresponds to the train parameters in Table 2. The components of the network impedance Z_s are the upstream grid impedance Z_{ug}, and the substation impedance Z_{sst} as seen in (62) [10].

$$Z_s = 2 \times Z_{ug} + Z_{sst} \tag{62}$$

The following impedance parameters at fundamental frequency ω_0 are used in this study [16]:

$$|Z_{ug}| = 0.5\Omega, \angle Z_{ug} = 80º\ ;\ |Z_{sst}| = 6.5\Omega, \angle Z_{sst} = 80º$$

Once train admittance matrix, network impedance matrix and number of trains are defined, the eigenvalues of the system are calculated using (60) in the range of frequencies of interest. Nyquist plots and the Bode diagrams for the three cases are shown in Fig. 11(a) and Fig. 11(b) respectively. The gain margin is shown for Bode plots as marked filled circles. The frequency response obtained using the simulation model is also shown to assess the accuracy of the analytical small-signal model. From Fig. 11(b) it is seen that increasing the number of trains at the depot, n, only increases the magnitude of eigenvalues λ_1 and λ_2, the phase remaining constant. As noticed in Fig. 11(b), the phase of the eigenvalue λ_2 never intersects 180º, therefore it is not causing any instability. This applies to the three examined cases. Nyquist stability criterion confirms the same result since λ_2 never encloses -1.

It is observed from the Nyquist plot in Fig. 11(a) that for $n = 17$, the eigenvalue λ_1 (green curve) does not enclose -1, which fulfills the Nyquist stability criterion. For $n = 27$, the eigenvalue λ_1 (blue curve) almost crosses -1 and the system is at the stability limit. For $n = 37$ trains, which is larger than the limit number, it is very clear that the red curve encloses -1; thus, the system is not fulfilling the stability criterion anymore and the system becomes unstable.

It is observed from Fig. 11(b) that for $n = 17$ (stable case), $|\lambda_1|$ at phase crossover frequency f_c is less than 0 dB (i.e., positive gain margin), which fulfills the stability criterion. At the system stability limit for $n = 27$, $|\lambda_1|$ at the crossover frequency is 0 dB, in this case, the crossover frequency f_c will define the oscillation frequency, that is 4.5 Hz. If there are more than 27 trains connected to the power supply network, $|\lambda_1|$ at the crossover frequency will take positive values (i.e., negative gain margin) and the system will become unstable.

Time domain simulations of the three cases are shown in Fig. 12. Catenary voltage, DC-link voltage, and inductor current per train are shown. Initially, the system is operating with $n = 7$ trains at the depot; here the system is in steady state; then, at $t = 5$ s, ten more trains are connected to the network as a step change (i.e., $n = 17$); here, the system experiences small oscillations that are damped quickly, and the system remains stable. A second step change in the

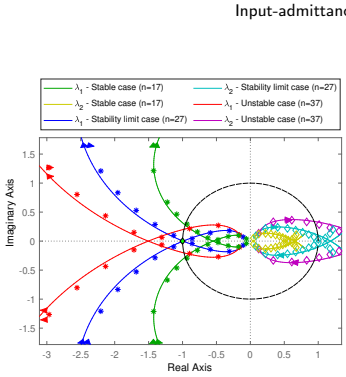

(a) Nyquist plot

(b) Bode Diagram

Figure 11: System eigenvalues for different number of trains n in the depot (DC-link power consumption 50 kW). $n = 17$ (stable), $n = 27$ (limit of stability) and $n = 37$ (unstable). Small signal analytical model (continuous line). Frequency swept using complete simulation model ($\lambda_1 \rightarrow *$, $\lambda_2 \rightarrow \Diamond$).

number of trains (i.e., $n = 27$) occurs at $t = 6$ s, time response is pure oscillatory, damping is almost negligible and the system is at the stability limit. The frequency of the oscillations observed in all the signals ≈ 4.5 Hz is seen to be in good agreement with the frequency predicted from the small-signal based analysis. Finally, following a step change in the number of trains (i.e., $n = 37$) at $t = 8$ s, the system becomes unstable.

5.2. Influence of power consumption at the DC-link

The reference point for this study is the limit of stability (i.e., GM=0 dB) reached with $n = 27$ identical trains on depot are operating at 50 kW each. System stability is studied in this section for variations in power consumption at the

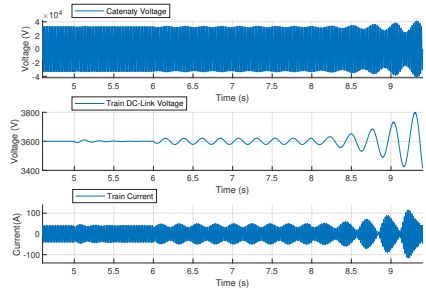

Figure 12: Time-domain simulations when the number of trains in depot change (DC-link power consumption 50 kW). $n = 7$ for $t < 5$ s (initial steady state); $n = 17$ at $t = 5$ s (stable case), $n = 27$ at $t = 6$ s (limit case), $n = 37$ at $t = 8$ s (unstable case).

DC-link of the trains, the number of trains and the rest of the electrical and control parameters are kept the same.

As discussed in Section 5.1, the eigenvalue λ_2 doesn't pose any risk of instability; therefore, it is not shown. Nyquist plot and Bode diagram of system eigenvalue λ_1 are shown in Fig. 13 for four different levels of power consumption at the DC-link.

Since the trains are operating at the depot (i.e., only auxiliary systems are drawing power), the increments of power are relatively small. Fig. 13(a) shows that increasing the dc-link power consumption improves the system stability. Similarly, Fig. 13(b) shows that going from 50 kW to 100 kW increases the gain margin, which means the system moves away from the stability limit becoming more stable while it reduces the oscillation frequency. At 150 kW and 200 kW the phase of the eigenvalue λ_1 is below 180º, which means that it never intersects the 180º line at any of low frequencies, having no risk of LFO instability. The fact that increasing the power increases system stability is in agreement with the results reported in [1, 3, 14, 16].

6. Sensitivity Analysis

In this section, the sensitivity analysis of the system stability to train electrical and control parameters using the small-signal model is performed. As in the previous sections, identical trains connected at the depot are considered.

The reference operating point for this analysis is the stability limit case presented in Section 5.1 with $n = 27$ trains connected at the depot, operating at a power of 50 kW each. The sensitivity analysis, variation of the critical eigenvalue λ_1 with incremental variation of a given parameter is obtained, with the rest of the system parameters remaining constant. The range of variation of the parameters being considered is 0.8 to 1.2 from its base value.

Fig. 14(a) and (b) show the gain margin and oscillation frequency (i.e., phase crossover frequency) as a function of

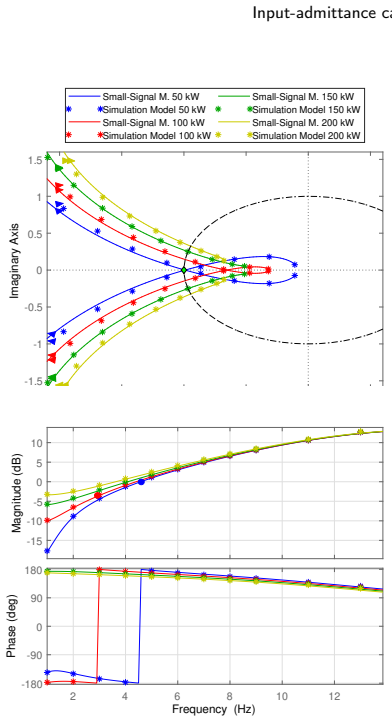

(b) Bode Diagram

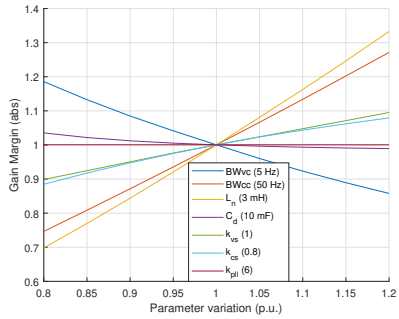

(a) Gain Margin

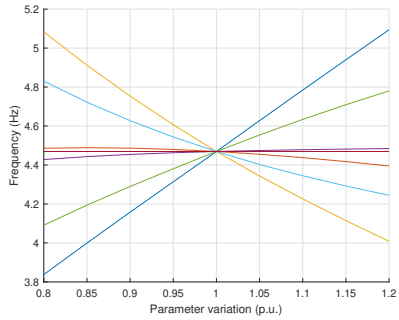

(b) Oscillation Frequency

Figure 13: Critical system eigenvalue λ_1 for different levels of DC-link power consumption. $n = 27$ trains at depot. Analytical small-signal model and frequency swept of complete simulation model.

Figure 14: a) Gain Margin of critical system eigenvalue λ_1 and b) oscillation frequency, as a function of p.u. parameter variation

the per unit value of different electrical or control parameter of the train, respectively. At the stability limit operating with nominal values, the gain margin is GM = 1 (i.e., 0 dB), and the oscillation frequency is 4.5 Hz. The slope of each curve gives the sensitivity of the gain margin and oscillation frequency. Positive slopes in Fig. 14(a) indicate that the system becomes more stable as the parameter being considered increases, the contrary occurs for negative slopes. According to the magnitude of slopes in Fig. 14(a) LFO shows high sensitivity to L_n and current control bandwidth, medium sensitivity to voltage control bandwidth and current-SOGI, while sensitivity to C_d and voltage-SOGI is low, practically no sensitivity to PLL tuning is observed. Table. 3 summarizes the results shown in Fig. 14.

It is noted that increasing the voltage-control bandwidth ($BWvc$) decreases the gain margin of the system while increasing the current-control bandwidth ($BWcc$) increases the gain margin. This strongly suggest that the spectral separation between current and voltage controller bandwidths will play a critical role in the occurrence of LFO. This is in agreement with the results reported in [19].

Finally, it is noted that the trajectories shown in Fig. 14 are not necessarily straight lines. This is due to the non-linear nature of the system. This suggests that parameter sensitivity when more than one parameter changes might not be agree with the results obtained from simple superposition of the effects of changing parameters individually. This is a subject of ongoing research.

	Gain Margin (GM)	Oscillation Frequency
BW_{vc}	↓↓↓	↑↑↑
BW_{cc}	↑↑↑↑	↓
L_n	↑↑↑↑↑	↓↓↓
C_d	↓	↑
k_{vs}	↑↑	↑↑
k_{cs}	↑↑	↓↓
k_{pll}	-	-

Table 3
Sensitivity of low-frequency stability to train parameters. ↑ and ↓ stands for positive sensitivity and negative sensitivity. Number of arrows show the degree of sensitivity.

7. Conclusions

An accurate train small-signal input admittance model that is useful for the analysis of low-frequency stability was developed and presented in this paper. The small-signal model was developed in the synchronous frame, and its frequency response matched with the frequency swept of the simulation of the complete (non-linear) model of the train. An approximated small-signal model of the QSG-SOGI in the synchronous frame valid in the low-frequency range was calculated and included in the system along with the PLL to model the dynamics due to errors in the coordinate rotation.

A stability analysis of the railway system was performed and checked with numerical methods. The different cases were analyzed for different numbers of trains operating at the depot, showing that increasing the number of trains increases the risk of instability.

The train small-signal input admittance model combined with power network admittance was able to predict the appearance of low-frequency oscillation when trains are operating at low power consumption with only auxiliary systems energized. Finally, using the small-signal model, the sensitivity analysis of the system stability to train electrical and control parameters was presented.

8. Acknowledgment

This work was supported in part by the European Commission HORIZON and KDTJU under the project POWERIZED GA No 101096387; in part by the Spanish Ministry of Science and Innovation under grant MCINN-23-PCI2022-135021-2; and in part by the Government of the Principality of Asturias under project AYUD/2021/50988.

A. QSG-SOGI IN SYNCHRONOUS DQ-FRAME

The expansion of (14) is shown in (A.1)

$$\begin{bmatrix} \hat{v}^e_{nd} \\ \hat{v}^e_{nq} \end{bmatrix} = \begin{bmatrix} \cos\omega_0 t \left(h_{f\alpha}(t) * (v^e_{nd}\cos\omega_0 t - v^e_{nq}\sin\omega_0 t) \right) + \sin\omega_0 t \left(h_{f\beta}(t) * (v^e_{nd}\cos\omega_0 t - v^e_{nq}\sin\omega_0 t) \right) \\ -\sin\omega_0 t \left(h_{f\alpha}(t) * (v^e_{nd}\cos\omega_0 t - v^e_{nq}\sin\omega_0 t) \right) + \cos\omega_0 t \left(h_{f\beta}(t) * (v^e_{nd}\cos\omega_0 t - v^e_{nq}\sin\omega_0 t) \right) \end{bmatrix} \tag{A.1}$$

Using the Laplace transform $F(s) = \mathcal{L}\{f(t)\}$, then $\mathcal{L}\left\{e^{j\omega_0 t}f(t)\right\} = F(s - j\omega_0) = F^{+}$, $\mathcal{L}\left\{e^{-j\omega_0 t}f(t)\right\} = F(s + j\omega_0) = F^{-}$, $\mathcal{L}\left\{e^{j2\omega_0 t}f(t)\right\} = F(s - j2\omega_0) = F^{++}$, $\mathcal{L}\left\{e^{-j2\omega_0 t}f(t)\right\} = F(s + j2\omega_0) = F^{--}$. Furthermore, using the inverse Euler's formula: $\cos\omega_0 t = (e^{j\omega_0 t} + e^{-j\omega_0 t})/2$ and $\sin\omega_0 t = (e^{j\omega_0 t} - e^{-j\omega_0 t})/2j$. It is then possible to express the convolutions as:

$$\begin{aligned} h_{f\alpha}(t) * (v^e_{nd}\cos\omega_0 t - v^e_{nq}\sin\omega_0 t) &= h_{f\alpha}(t) * \left(v^e_{nd}\frac{e^{j\omega_0 t} + e^{-j\omega_0 t}}{2} - v^e_{nq}\frac{e^{j\omega_0 t} - e^{-j\omega_0 t}}{2j} \right) \\ &= \mathcal{L}^{-1}\left\{ H_{f\alpha}(s)\left(\frac{V^{e+}_{nd} + V^{e-}_{nd}}{2} - \frac{V^{e+}_{nq} - V^{e-}_{nq}}{2j} \right) \right\} \end{aligned} \tag{A.2}$$

$$\begin{aligned} h_{f\beta}(t) * (v^e_{nd}\cos\omega_0 t - v^e_{nq}\sin\omega_0 t) &= h_{f\beta}(t) * \left(v^e_{nd}\frac{e^{j\omega_0 t} + e^{-j\omega_0 t}}{2} - v^e_{nq}\frac{e^{j\omega_0 t} - e^{-j\omega_0 t}}{2j} \right) \\ &= \mathcal{L}^{-1}\left\{ H_{f\beta}(s)\left(\frac{V^{e+}_{nd} + V^{e-}_{nd}}{2} - \frac{V^{e+}_{nq} - V^{e-}_{nq}}{2j} \right) \right\} \end{aligned} \tag{A.3}$$

Combining equations (A.1) and (A.2) and (A.3)

$$\begin{bmatrix} \hat{v}^e_{nd} \\ \hat{v}^e_{nq} \end{bmatrix} = \begin{bmatrix} \frac{e^{j\omega_0 t}+e^{-j\omega_0 t}}{2}\mathcal{L}^{-1}\left\{ H_{f\alpha}(s)\left(\frac{V^{e+}_{nd}+V^{e-}_{nd}}{2} - \frac{V^{e+}_{nq}-V^{e-}_{nq}}{2j} \right) \right\} + \frac{e^{j\omega_0 t}-e^{-j\omega_0 t}}{2j}\mathcal{L}^{-1}\left\{ H_{f\beta}(s)\left(\frac{V^{e+}_{nd}+V^{e-}_{nd}}{2} - \frac{V^{e+}_{nq}-V^{e-}_{nq}}{2j} \right) \right\} \\ -\frac{e^{j\omega_0 t}-e^{-j\omega_0 t}}{2j}\mathcal{L}^{-1}\left\{ H_{f\alpha}(s)\left(\frac{V^{e+}_{nd}+V^{e-}_{nd}}{2} - \frac{V^{e+}_{nq}-V^{e-}_{nq}}{2j} \right) \right\} + \frac{e^{j\omega_0 t}+e^{-j\omega_0 t}}{2}\mathcal{L}^{-1}\left\{ H_{f\beta}(s)\left(\frac{V^{e+}_{nd}+V^{e-}_{nd}}{2} - \frac{V^{e+}_{nq}-V^{e-}_{nq}}{2j} \right) \right\} \end{bmatrix} \tag{A.4}$$

Taking the Laplace transform of each element of the vector voltage in (A.4) yields:

$$\begin{aligned} \hat{V}^e_{nd} =& H^{+}_{f\alpha}\left(\frac{V^{e++}_{nd} + V^{e}_{nd}}{4} - \frac{V^{e++}_{nq} - V^{e}_{nq}}{4j} \right) + H^{-}_{f\alpha}\left(\frac{V^{e}_{nd} + V^{e--}_{nd}}{4} - \frac{V^{e}_{nq} - V^{e--}_{nq}}{4j} \right) \\ &+ H^{+}_{f\beta}\left(\frac{V^{e++}_{nd} + V^{e}_{nd}}{4j} + \frac{V^{e++}_{nq} - V^{e}_{nq}}{4} \right) - H^{-}_{f\beta}\left(\frac{V^{e}_{nd} + V^{e--}_{nd}}{4j} + \frac{V^{e}_{nq} - V^{e--}_{nq}}{4} \right) \end{aligned} \tag{A.5}$$

$$\begin{aligned} \hat{V}^e_{nq} =& H^{-}_{f\alpha}\left(\frac{V^{e}_{nd} + V^{e--}_{nd}}{4j} + \frac{V^{e}_{nq} - V^{e--}_{nq}}{4} \right) - H^{+}_{f\alpha}\left(\frac{V^{e++}_{nd} + V^{e}_{nd}}{4j} + \frac{V^{e++}_{nq} - V^{e}_{nq}}{4} \right) \\ &+ H^{+}_{f\beta}\left(\frac{V^{e++}_{nd} + V^{e}_{nd}}{4} - \frac{V^{e++}_{nq} - V^{e}_{nq}}{4j} \right) + H^{-}_{f\beta}\left(\frac{V^{e}_{nd} + V^{e--}_{nd}}{4} - \frac{V^{e}_{nq} - V^{e--}_{nq}}{4j} \right) \end{aligned} \tag{A.6}$$

From equations (A.5) and (A.6) is clear that in the dq-frame for any excitation frequency at the input voltage, the output voltage will present a component at the same excitation frequency but also another component at a shifted excitation frequency by $2\omega_0$, for the LFO analysis oscillations frequencies have reported to frequencies no larger than 7 Hz in dq-frame (add reference), therefore the output response due to the shifted excitation frequencies are neglected. Finally having:

$$\begin{bmatrix} \hat{V}^e_{nd} \\ \hat{V}^e_{nq} \end{bmatrix} \approx \frac{1}{4}\begin{bmatrix} \left(H^{-}_{f\alpha} + H^{+}_{f\alpha}\right) + j\left(H^{-}_{f\beta} - H^{+}_{f\beta}\right) & -\left(\left(H^{-}_{f\beta} + H^{+}_{f\beta}\right) - j\left(H^{-}_{f\alpha} - H^{+}_{f\alpha}\right)\right) \\ \left(H^{-}_{f\beta} + H^{+}_{f\beta}\right) - j\left(H^{-}_{f\alpha} - H^{+}_{f\alpha}\right) & \left(H^{-}_{f\alpha} + H^{+}_{f\alpha}\right) + j\left(H^{-}_{f\beta} - H^{+}_{f\beta}\right) \end{bmatrix}\begin{bmatrix} V^e_{nd} \\ V^e_{nq} \end{bmatrix} \tag{A.7}$$

Note that equation (A.7) is presented with abbreviate notation in this section but is presented with the expand notation in section 3 by (15), (18) and (19).

References

[1] H. Hu and H. Tao and F. Blaabjerg and X. Wang and Z. He and S. Gao, Train–network Interactions and Stability Evaluation in High-Speed Railways Part I: Phenomena and Modeling, IEEE Transactions on Power Electronics 33 (2018) 4627–4642. doi:10.1109/TPEL.2017.2781880.

[2] H. Hu, H. Tao, X. Wang, F. Blaabjerg, Z. He, S. Gao, Train–network interactions and stability evaluation in high-speed railways—part ii: Influential factors and verifications, IEEE Transactions on Power Electronics 33 (2018) 4643–4659. doi:10.1109/TPEL.2017.2781879.

[3] S. Menth, Meyer.M., Low frequency power oscillations in electric railway systems, eb - Elektrische Bahnen 104 (2006) 216–221.

[4] L. Buhrkall, S. Danielsen, A. Eisele, M. Bergman, J. Galic, Low-frequency oscillations in scandinavian railway power supply - part i: Basic considerations, eb - Elektrische Bahnen 108 (2010) 56–64.

[5] L. Buhrkall, S. Danielsen, A. Eisele, M. Bergman, J. Galic, Low-frequency oscillations in scandinavian railway power supply -part 2: Test of traction units 108 (2010) 103–111.

[6] S. Danielsen, T. Toftevaag, O. Fosso, Application of linear analysis in traction power system stability studies, volume 103, 2008, pp. 401–410. doi:10.2495/CR080401.

[7] S. Danielsen, M. Molinas, T. Toftevaag, O. Fosso, Constant power load characteristic's influence on the low-frequency interaction between advanced electrical rail vehicle and railway traction power supply with rotary converters, Modern electric traction, 2009 (2009).

[8] J. Suarez, P. Ladoux, N. Roux, H. Caron, E. Guillame, Measurement of locomotive input admittance to analyse low frequency instability on ac rail networks, in: 2014 International Symposium on Power Electronics, Electrical Drives, Automation and Motion, 2014, pp. 790–795. doi:10.1109/SPEEDAM.2014.6872025.

[9] H. Wang, W. Mingli, J. Sun, Analysis of low-frequency oscillation in electric railways based on small-signal modeling of vehicle-grid system in dq frame, IEEE Transactions on Power Electronics 30 (2015) 5318–5330. doi:10.1109/TPEL.2015.2388796.

[10] Frutos, Paul and Ladoux, Philippe and Roux, Nicolas and Larrazabal, Igor and Guerrero, Juan M. and Briz, Fernando, Low Frequency Stability of AC Railway Traction Power Systems: Analysis of the Influence of Traction Unit Parameters, Electronics 11 (2022). URL: https://www.mdpi.com/2079-9292/11/10/1593. doi:10.3390/electronics11101593.

[11] M. Meyer, Rail network modelling and stability: The input admittance criterion.

[12] L. Harnefors, M. Bongiorno, S. Lundberg, Input-admittance calculation and shaping for controlled voltage-source converters, IEEE Transactions on Industrial Electronics 54 (2007) 3323–3334. doi:10.1109/TIE.2007.904022.

[13] L. Harnefors, Analysis of subsynchronous torsional interaction with power electronic converters, IEEE Transactions on Power Systems 22 (2007) 305–313. doi:10.1109/TPWRS.2006.889038.

[14] S. Danielsen, Ph.d. thesis: Electric traction power system stability: Low-frequency interaction between advanced rail vehicles and a rotary frequency converter, NTNU Trykk (2010). doi:10.1109/TPEL.2015.2388796.

[15] Hachicha, Y. and Cypers, D. and Takuefou, M. and Belin, S. and Ladoux, P. and Roux, N, Use of a HIL railway traction simulator for low frequency network stability studies, in: 2018 IEEE International Conference on Electrical Systems for Aircraft, Railway, Ship Propulsion and Road Vehicles International Transportation Electrification Conference (ESARS-ITEC), 2018, pp. 1–5. doi:10.1109/ESARS-ITEC.2018.8607620.

[16] Ladoux, Philippe and Hachicha, Yosr and Cypers, David and Meli, Maxime and Roux, Nicolas, New method for determining the low-frequency Stability Limit of a 50 Hz electric traction power system, Elektrische Bahnen (2020) 18 p. URL: https://hal-univ-tlse3.archives-ouvertes.fr/hal-03286350.

[17] Hachicha, Yosr and Cypers, David and Belin, Sebastien and Meli, Maxime and Ladoux, Philippe and Roux, Nicolas, Towards a unified low frequency Stability criterion for 15 kV / 16.7 Hz and 25 kV / 50 Hz railway power system, in: PCIM Europe digital days 2020; International Exhibition and Conference for Power Electronics, Intelligent Motion, Renewable Energy and Energy Management, 2020, pp. 1–8.

[18] EN 50388-2:2017 - railway applications - fixed installations and rolling stock - technical criteria for the coordination between power supply and rolling stock to achieve interoperability - part 2: stability and harmonics (????).

[19] Frutos, Paul and Guerrero, Juan Manuel and Muniategui, Iker and Vicente, Iban and Endemano, Aitor and Briz, Fernando, Low-Frequency Oscillations Analysis in AC Railway Networks Using Eigenmode Identification, in: 2021 IEEE Energy Conversion Congress and Exposition (ECCE), 2021, pp. 1573–1579. doi:10.1109/ECCE47101.2021.9595947.

[20] A. Yazdani, R. Iravani, Voltage-Sourced Converters in Power Systems, John Wiley & Sons, Ltd, 2010. doi:https://doi.org/10.1002/9780470551578.ch1.

[21] S. Golestan, J. M. Guerrero, Conventional synchronous reference frame phase-locked loop is an adaptive complex filter, IEEE Transactions on Industrial Electronics 62 (2015) 1679–1682. doi:10.1109/TIE.2014.2341594.

[22] F. Briz, M. Degner, R. Lorenz, Analysis and design of current regulators using complex vectors, IEEE Transactions on Industry Applications 36 (2000) 817–825. doi:10.1109/28.845057.

[23] L. Harnefors, Modeling of three-phase dynamic systems using complex transfer functions and transfer matrices, IEEE Transactions on Industrial Electronics 54 (2007) 2239–2248. doi:10.1109/TIE.2007.894769.

[24] B. Crowhurst, E. F. El-Saadany, L. E. Chaar, L. A. Lamont, Single-phase grid-tie inverter control using dq transform for active and reactive load power compensation, in: 2010 IEEE International Conference on Power and Energy, 2010, pp. 489–494. doi:10.1109/PECON.2010.5697632.

[25] M. W. Degner, C. M. Wolf, Transient analysis of asymmetric ac systems using complex vectors, in: 2017 IEEE International Electric Machines and Drives Conference (IEMDC), 2017, pp. 1–8. doi:10.1109/IEMDC.2017.8002378.

[26] K. Ogata, Modern Control Engineering, Instrumentation and controls series, Prentice Hall, 2010. URL: https://books.google.es/books?id=Wu5GpNAelzkC.

[27] I. Pendharkar, A generalized input admittance criterion for resonance stability in electrical railway networks, 2014, pp. 690–695. doi:10.1109/ECC.2014.6862219.

PAUL FRUTOS received the B.S. degree in Electrical Engineering from the San Francisco de Quito University, Quito, Ecuador, in 2013, and the M.Sc. degree from the University of Nottingham, Nottingham, United Kingdom, in 2017. He is currently working towards a Ph.D. degree in Electrical Engineering at the University of Oviedo, Asturias, Spain. His research interests include control strategies for multilevel inverters, solid-state transformers, stability studies of high-speed railway systems, and the development of control strategies of power converters for traction applications.

JUAN MANUEL GUERRERO (Senior Member, IEEE) received the M.E. degree in industrial engineering and the Ph.D. Degree in Electrical and Electronic Engineering from the University of Oviedo, Gijón, Spain, in 1998 and 2003, respectively. Since 1999, he has occupied different teaching and research positions with the Department of Electrical, Computer and Systems Engineering, University of Oviedo, where he is currently a Full Professor. From February 2002 to October 2002, he was a Visiting Scholar at the University of Wisconsin, Madison. From June to December 2007, he was a Visiting Professor at the Tennessee Technological University, Cookeville. His research interests include control of electric drives and power converters, electric traction, and renewable energy generation. He is an Associate Editor of the IEEE TRANSACTIONS ON INDUSTRY APPLICATIONS.

IKER MUNIATEGUI received the Industrial Technical Engineering Degree (Electronic Design specialization) and the Industrial Automatics and Electronics Engineering Degree, from the University of Mondragon, Mondragon, Spain, in 2004 and 2007 respectively. In September 2006, he joined Ingeteam Power Technology (formerly TEAM), Zamudio, Spain, where he worked as a Control and Regulation Engineer, and he is currently Control and Regulation manager of Traction department. His current research interests include power converter and advanced control drives, modulation techniques, railway research issues such as AC catenary stability and mechanical vibrations in the drive-train.

AITOR ENDEMAÑO received the Industrial Technical Engineering Degree (Electronic Design specialization) and the Industrial Automatics and Electronics Engineering Degree, from the University of Mondragon, Mondragon, Spain, in 1997 and 2000 respectively, and the PhD from Heriot-Watt University, Edinburgh, Scotland, UK, in 2003. In 2003 he joined Traction department at Ingeteam Power Technology (formerly TEAM), Zamudio, Spain, where since then he has been a Control and Regulation Engineer, involved in several traction control design projects for trams, locomotives and EMU-s. His current research interests include power converter and advanced control drives, modulation techniques, railway research issues such as AC catenary stability and mechanical vibrations in the drive-train.

DAVID ORTEGA received Licentiate degree in Electric and Electronic Engineering from Universidad Pais Vasco of Bilbao (UPV), Spain in 2004. He worked in Traction Department of Ingeteam from 2004 until April 2010 as Development Engineer, when he joined Euskotren as Rolling Stock Maintenance Engineer. Later in December 2010 he joined again Traction Department of Ingeteam where he is Technology Coordination Manager. His research interests are in the field of Rolling Stock architectures, EMC, noise, efficiency, high power converters for Traction and Energy Recovery Systems.

FERNANDO BRIZ (Senior Member, IEEE) received the M.S. and Ph.D. degrees from the University of Oviedo, Gijón, Spain, in 1990 and 1996, respectively. He is currently a Full Professor with the Department of Electrical, Computer and Systems Engineering, University of Oviedo.

His research interests include electronic power converters and ac drives, power systems, machine monitoring and diagnostics, and digital signal processing. He is a member of the Executive Board of ECCE. He was a recipient of the IEEE TRANSACTIONS ON INDUSTRY APPLICATIONS Award and the nine IEEE Industry Applications Society Conference and IEEE Energy Conversion Congress and Exposition Prize Paper Awards. He is the Chair of the Industrial Power Conversion System Department (IPCSD) of the IAS. He is the Past Chair of the Industrial Drives Committee of IPCSD. He has served for scientific committees and as the Vice Chair or the Technical Program Chair for several conferences, including ECCE, IEMDC, ICEM, ICEMS, and SLED. He is the Deputy Editor-in-Chief and a member of the Steering Committee of IEEE JOURNAL OF EMERGING AND SELECTED TOPICS IN POWER ELECTRONICS. He is an Associate Editor of IEEE TRANSACTIONS ON INDUSTRY APPLICATIONS.

Bibliography

[1] Frutos, Paul and Ladoux, Philippe and Roux, Nicolas and Larrazabal, Igor and Guerrero, Juan M. and Briz, Fernando, "Low Frequency Stability of AC Railway Traction Power Systems: Analysis of the Influence of Traction Unit Parameters," *Electronics*, vol. 11, no. 10, 2022. [Online]. Available: https://www.mdpi.com/2079-9292/11/10/1593

[2] L. Buhrkall, S. Danielsen, A. Eisele, M. Bergman, and J. Galic, "Low-frequency oscillations in scandinavian railway power supply - part i: Basic considerations," *eb - Elektrische Bahnen*, vol. 108, pp. 56–64, 01 2010.

[3] S. Schmidt, D. Wuergler, P. Terwiesch, and U. Henning, "Electrical system compatibility for advanced rail vehicles: a survey," in *8th International Conference on Harmonics and Quality of Power. Proceedings (Cat. No.98EX227)*, vol. 2, 1998, pp. 623–629 vol.2.

[4] H. Lee, C. Lee, G. Jang, and S. hyuk Kwon, "Harmonic analysis of the korean high-speed railway using the eight-port representation model," *IEEE Transactions on Power Delivery*, vol. 21, no. 2, pp. 979–986, 2006.

[5] E. Mollerstedt and B. Bernhardsson, "Out of control because of harmonics-an analysis of the harmonic response of an inverter locomotive," *IEEE Control Systems Magazine*, vol. 20, no. 4, pp. 70–81, 2000.

[6] H. Hu, H. Tao, X. Wang, F. Blaabjerg, Z. He, and S. Gao, "Train–network interactions and stability evaluation in high-speed railways—part ii: Influential factors and verifications," *IEEE Transactions on Power Electronics*, vol. 33, no. 6, pp. 4643–4659, 2018.

[7] S. Danielsen, M. Molinas, T. Toftevaag, and O. Fosso, "Constant power load characteristic's influence on the low-frequency interaction between advanced electrical rail vehicle and railway traction power supply with rotary converters," 01 2009.

[8] L. Buhrkall, S. Danielsen, A. Eisele, M. Bergman, and J. Galic, "Low-frequency oscillations in scandinavian railway power supply -part 2: Test of traction units," *eb - Elektrische Bahnen*, vol. 108, pp. 103–111, 03 2010.

[9] S. Danielsen, "Ph.d. thesis: Electric traction power system stability: Low-frequency interaction between advanced rail vehicles and a rotary frequency converter," 2010.

[10] J. Suarez, P. Ladoux, N. Roux, H. Caron, and E. Guillame, "Measurement of locomotive input admittance to analyse low frequency instability on ac rail networks," in *2014 International Symposium on Power Electronics, Electrical Drives, Automation and Motion*, 2014, pp. 790–795.

[11] S. Menth and Meyer.M., "Low frequency power oscillations in electric railway systems," *eb - Elektrische Bahnen*, vol. 104, pp. 216–221, 2006.

[12] H. Wang, W. Mingli, and J. Sun, "Analysis of low-frequency oscillation in electric railways based on small-signal modeling of vehicle-grid system in dq frame," *IEEE Transactions on Power Electronics*, vol. 30, no. 9, pp. 5318–5330, 2015.

[13] H. Hu, H. Tao, F. Blaabjerg, X. Wang, Z. He, and S. Gao, "Train–network interactions and stability evaluation in high-speed railways–part i: Phenomena and modeling," *IEEE Transactions on Power Electronics*, vol. 33, no. 6, pp. 4627–4642, 2018.

[14] D. Frugier and P. Ladoux, "Voltage disturbances on 25kv-50 hz railway lines – modelling method and analysis," in *SPEEDAM 2010*, 2010, pp. 1080–1085.

[15] "EN 50388-2:2017 - railway applications - fixed installations and rolling stock - technical criteria for the coordination between power supply and rolling stock to achieve interoperability - part 2: stability and harmonics."

[16] X. Wang, F. Blaabjerg, and W. Wu, "Modeling and analysis of harmonic stability in an ac power-electronics-based power system," *IEEE Transactions on Power Electronics*, vol. 29, no. 12, pp. 6421–6432, 2014.

[17] S. Danielsen, "Ph.d. thesis: Electric traction power system stability: Low-frequency interaction between advanced rail vehicles and a rotary frequency converter," *NTNU Trykk*, 2010.

[18] Y. Hachicha, D. Cypers, M. Takuefou, S. Belin, P. Ladoux, and N. Roux, "Use of a hil railway traction simulator for low frequency network stability studies," in *2018 IEEE International Conference on Electrical Systems for Aircraft, Railway, Ship Propulsion and Road Vehicles International Transportation Electrification Conference (ESARS-ITEC)*, 2018, pp. 1–5.

[19] M. Debruyne, "Low frequency instability in the amtrak's 12kv-25hz network," in *Interaction Workshop 2006*, Thun, Switzerland, 2006.

[20] S. Danielsen, T. Toftevaag, and O. Fosso, "Application of linear analysis in traction power system stability studies," vol. 103, 08 2008, pp. 401–410.

[21] P. Frutos, J. M. Guerrero, I. Muniategui, I. Vicente, A. Endemano, and F. Briz, "Low-frequency oscillations analysis in ac railway networks using eigenmode identification," in *2021 IEEE Energy Conversion Congress and Exposition (ECCE)*, 2021, pp. 1573–1579.

[22] A. Steimel, "Power-electronics issues of modern electric railway systems," in *Proceedings of the 9th International Conference on Development and Application Systems*, Suceava, Romania, 1–6 2010.

[23] ——, *Electric Traction - Motive Power and Energy Supply.* München: Oldenbourg Industrieverlag, 2008.

[24] Hachicha, Y. and Cypers, D. and Takuefou, M. and Belin, S. and Ladoux, P. and Roux, N, "Use of a HIL railway traction simulator for low frequency network stability studies," in *2018 IEEE International Conference on Electrical Systems for Aircraft, Railway, Ship Propulsion and Road Vehicles International Transportation Electrification Conference (ESARS-ITEC)*, 2018, pp. 1–5.

[25] A. Yazdani and R. Iravani, *Voltage-Sourced Converters in Power Systems.* John Wiley & Sons, Ltd, 2010.

[26] S. Golestan and J. M. Guerrero, "Conventional synchronous reference frame phase-locked loop is an adaptive complex filter," *IEEE Transactions on Industrial Electronics*, vol. 62, no. 3, pp. 1679–1682, 2015.

[27] J. Suarez, "Ph.d. thesis: Étude et modélisation des interactions électriques entre les engins et les installations fixes de traction électrique 25kv/50hz," University of Toulouse, December 2014.

[28] P. Ladoux, Y. Hachicha, D. Cypers, M. Meli, and N. Roux, "New method for determining the low-frequency Stability Limit of a 50 Hz electric traction power system," *Elektrische Bahnen*, no. 10, p. 18 p., Oct 2020. [Online]. Available: https://hal-univ-tlse3.archives-ouvertes.fr/hal-03286350

[29] K. Ogata, *Modern Control Engineering*, ser. Instrumentation and controls series. Prentice Hall, 2010. [Online]. Available: https://books.google.es/books?id=Wu5GpNAelzkC

[30] G. F. Franklin, J. D. Powell, and A. Emami-Naeini, *Feedback Control of Dynamic Systems*, 7th ed. Upper Saddle River, NJ: Pearson, 2014.

[31] Y. Liao, Z. Liu, H. Zhang, and B. Wen, "Low-frequency stability analysis of single-phase system with dq-frame impedance approach—part ii: Stability and frequency analysis," *IEEE Transactions on Industry Applications*, vol. 54, no. 5, pp. 5012–5024, 2018.

[32] R. H. Myers, D. C. Montgomery, and G. G. Vining, *Data Analysis Using the Method of Least Squares*. Boca Raton, FL: CRC Press, 2006.

[33] I. Pendharkar, "A generalized input admittance criterion for resonance stability in electrical railway networks," 06 2014, pp. 690–695.

[34] Y. Hachicha, D. Cypers, S. Belin, M. Meli, P. Ladoux, and N. Roux, "Towards a unified low frequency stability criterion for 15 kv / 16.7 hz and 25 kv / 50 hz railway power system," in *PCIM Europe digital days 2020; International Exhibition and Conference for Power Electronics, Intelligent Motion, Renewable Energy and Energy Management*, 2020, pp. 1–8.

[35] X. Wang and F. Blaabjerg, "Harmonic stability in power electronic-based power systems: Concept, modeling, and analysis," *IEEE Transactions on Smart Grid*, vol. 10, no. 3, pp. 2858–2870, 2019.

[36] R. Teodorescu, M. Liserre, and P. Rodriguez, *Grid Synchronization in SinglePhase Power Converters*, 2007, pp. 43–91.

[37] M. Meyer, "Rail network modelling and stability: The input admittance criterion."

[38] L. Harnefors, M. Bongiorno, and S. Lundberg, "Input-admittance calculation and shaping for controlled voltage-source converters," *IEEE Transactions on Industrial Electronics*, vol. 54, no. 6, pp. 3323–3334, 2007.

[39] L. Harnefors, "Analysis of subsynchronous torsional interaction with power electronic converters," *IEEE Transactions on Power Systems*, vol. 22, no. 1, pp. 305–313, 2007.

[40] V. Blahnik, T. Kosan, and J. Talla, "Control of single-phase ac/dc converter based on sogi-pll voltage synchronization," in *Proceedings of the 16th International Conference on Mechatronics - Mechatronika 2014*, 2014, pp. 652–655.

[41] P. C. Krause, O. Wasynczuk, and S. D. Sudhoff, *Reference-Frame Theory*, 2002, pp. 109–140.

[42] M. W. Degner and C. M. Wolf, "Transient analysis of asymmetric ac systems using complex vectors," in *2017 IEEE International Electric Machines and Drives Conference (IEMDC)*, 2017, pp. 1–8.

[43] F. Briz, M. Degner, and R. Lorenz, "Analysis and design of current regulators using complex vectors," *IEEE Transactions on Industry Applications*, vol. 36, no. 3, pp. 817–825, 2000.

[44] L. Harnefors, "Modeling of three-phase dynamic systems using complex transfer functions and transfer matrices," *IEEE Transactions on Industrial Electronics*, vol. 54, no. 4, pp. 2239–2248, 2007.

[45] B. Crowhurst, E. F. El-Saadany, L. E. Chaar, and L. A. Lamont, "Single-phase grid-tie inverter control using dq transform for active and reactive load power compensation," in *2010 IEEE International Conference on Power and Energy*, 2010, pp. 489–494.

[46] D. Janík, J. Talla, T. Komrska, and Z. Peroutka, "Optimalization of sogi pll for single-phase converter control systems: Second order generalized integrator (sogi)," in *2013 International Conference on Applied Electronics*, 2013, pp. 1–4.

[47] L. Harnefors, A. G. Yepes, A. Vidal, and J. Doval-Gandoy, "Passivity-based controller design of grid-connected vscs for prevention of electrical resonance instability," *IEEE Transactions on Industrial Electronics*, vol. 62, no. 2, pp. 702–710, 2015.

[48] T.-T. Tay, I. Mareels, and J. B. Moore, *High Performance Control*. Birkhäuser, 1998.

[49] Z. Qionglin, "A probe on causes and solutions of the hxd1 ac locomotive's resonance," *World Inverters*, vol. 5, no. 5, pp. 40–44, May 2009.

[50] X. Jiang, H. Hu, J. Yang, Y. Zhou, Z. He, Q. Qian, P. Tricoli, S. Hillmansen, and C. Roberts, "The mitigation technology of typical low-frequency voltage fluctuation in china electrified railway," in *2018 International Symposium on Power Electronics, Electrical Drives, Automation and Motion (SPEEDAM)*, 2018, pp. 632–637.

[51] L. Buhrkall, "Traction system case study," in *The 9th Institution of Engineering and Technology Professional Development Course on Electric Traction Systems*, 2006, pp. 53–71.

[52] Z. Rafique, H. M. Khalid, S. Muyeen, and I. Kamwa, "Bibliographic review on power system oscillations damping: An era of conventional grids and renewable energy integration," *International Journal of Electrical Power & Energy Systems*, vol. 136, p. 107556, 2022. [Online]. Available: https://www.sciencedirect.com/science/article/pii/S0142061521007912

[53] A. S. P. Babu and S. P R, "Power oscillation damping by utilizing pv-statcom," in *2022 IEEE Delhi Section Conference (DELCON)*, 2022, pp. 1–6.

[54] N. Mithulananthan, C. Canizares, J. Reeve, and G. Rogers, "Comparison of pss, svc, and statcom controllers for damping power system oscillations," *IEEE Transactions on Power Systems*, vol. 18, no. 2, pp. 786–792, 2003.

[55] Y. Zhao, K. M. Alshuaibi, X. Jia, C. Zhang, Y. Liu, D. Ramasubramanian, L. Zhu, and E. Farantatos, "Comparison of wide-area and local power oscillation damping control through inverter-based resources," in *2023 IEEE Power & Energy Society Innovative Smart Grid Technologies Conference (ISGT)*, 2023, pp. 1–5.

[56] M. Aboul-Ela, A. Sallam, J. McCalley, and A. Fouad, "Damping controller design for power system oscillations using global signals," *IEEE Transactions on Power Systems*, vol. 11, no. 2, pp. 767–773, 1996.

[57] J. M. Alcala, M. Castilla, L. G. de Vicuña, J. Miret, and J. C. Vasquez, "Virtual impedance loop for droop-controlled single-phase parallel inverters using a second-order general-integrator scheme," *IEEE Transactions on Power Electronics*, vol. 25, no. 12, pp. 2993–3002, 2010.

[58] J. Guerrero, L. G. de Vicuna, J. Matas, M. Castilla, and J. Miret, "Output impedance design of parallel-connected ups inverters with wireless load-sharing control," *IEEE Transactions on Industrial Electronics*, vol. 52, no. 4, pp. 1126–1135, 2005.

[59] P. Dahono, Y. Bahar, Y. Sato, and T. Kataoka, "Damping of transient oscillations on the output lc filter of pwm inverters by using a virtual resistor," in *4th IEEE International Conference on Power Electronics and Drive Systems. IEEE PEDS 2001 - Indonesia. Proceedings (Cat. No.01TH8594)*, vol. 1, 2001, pp. 403–407 vol.1.

[60] L. Zhang, L. Harnefors, and H.-P. Nee, "Power-synchronization control of grid-connected voltage-source converters," *IEEE Transactions on Power Systems*, vol. 25, no. 2, pp. 809–820, 2010.

[61] Y. Tao, Q. Liu, Y. Deng, X. Liu, and X. He, "Analysis and mitigation of inverter output impedance impacts for distributed energy resource interface," *IEEE Transactions on Power Electronics*, vol. 30, no. 7, pp. 3563–3576, 2015.

[62] X. Wang, Y. W. Li, F. Blaabjerg, and P. C. Loh, "Virtual-impedance-based control for voltage-source and current-source converters," *IEEE Transactions on Power Electronics*, vol. 30, no. 12, pp. 7019–7037, 2015.

[63] P. Rodriguez, I. Candela, C. Citro, J. Rocabert, and A. Luna, "Control of grid-connected power converters based on a virtual admittance control loop," in *2013 15th European Conference on Power Electronics and Applications (EPE)*, 2013, pp. 1–10.

[64] J. A. Suul, M. Molinas, and P. Rodríguez, "Exploring the range of impedance conditioning by virtual inductance for grid connected voltage source converters," in *2012 3rd IEEE PES Innovative Smart Grid Technologies Europe (ISGT Europe)*, 2012, pp. 1–9.

[65] J. S. Lee and G. Choi, "Modeling and hardware-in-the-loop system realization of electric machine drives — a review," *CES Transactions on Electrical Machines and Systems*, vol. 5, no. 3, pp. 194–201, 2021.

[66] Z. Liu, T. Li, M. Shu, Y. Sun, and L. Ma, "Using hardware-in-the-loop simulation platform for empirical testing of photovoltaic system," in *2020 IEEE 3rd International Conference on Electronics Technology (ICET)*, 2020, pp. 452–456.

[67] A. Cebi, L. Guvenc, M. Demirci, C. Karadeniz, K. Kanar, and E. Guraslan, "A low cost, portable engine electronic control unit hardware-in-the-loop test system," in *Proceedings of the IEEE International Symposium on Industrial Electronics, 2005. ISIE 2005.*, vol. 1, 2005, pp. 293–298.

[68] F.-G. Paul, J. M. Guerrero, I. Muniategui-Aspiazu, I. Vicente-Makazaga, A. Endemaño-Isasi, D. Ortega-Rodriguez, and F. Briz, "Power-hardware-in-the-loop emulation of the low-frequency oscillation phenomenon in ac railway networks," *IEEE Access*, vol. 10, pp. 87 374–87 386, 2022.

[69] Y. Huo, G. Gruosso, and L. Piegari, "Power hardware in the loop simulator of photovoltaic plant for smart grid interation analysis," in *2017 IEEE International Conference on Environment and Electrical Engineering and 2017 IEEE Industrial and Commercial Power Systems Europe (EEEIC / I CPS Europe)*, 2017, pp. 1–5.

[70] A. CASTAINGS, A. BOUSCAYROL, W. LHOMME, and R. Trigui, "Power Hardware-In-the-Loop simulation for testing multi-sources vehicles," in *20th IFAC World Congress*, vol. 50, no. 1, TOULOUSE, France, Jul. 2017, pp. pp. 10 971–10 976, 20th IFAC World Congress, TOULOUSE, FRANCE, 09-/07/2017 - 14/07/2017. [Online]. Available: https://hal.archives-ouvertes.fr/hal-01745537

[71] Zhou, Yi and Hu, Haitao and Yang, Xiaowei and Yang, Jie and He, Zhengyou and Gao, Shibin, "Low Frequency Oscillation Traceability and Suppression in Railway Electrification Systems," *IEEE Transactions on Industry Applications*, vol. 55, no. 6, pp. 7699–7711, 2019.

[72] X. Yuan, W. Merk, H. Stemmler, and J. Allmeling, "Stationary-frame generalized integrators for current control of active power filters with zero steady-state error for current harmonics of concern under unbalanced and distorted operating conditions," *IEEE Transactions on Industry Applications*, vol. 38, no. 2, pp. 523–532, 2002.

[73] P. Frutos, E. Christopher, A. Sanchez, and O. Aguirre, "A performance comparison of stationary frame control of three-leg and four-leg voltage source inverters in power system applications," in *IECON 2018 - 44th Annual Conference of the IEEE Industrial Electronics Society*, 2018, pp. 925–931.

[74] G. Calzo, A. Lidozzi, L. Solero, and F. Crescimbini, "Lc filter design for on-grid and off-grid distributed generating units," *IEEE Transactions on Industry Applications*, vol. 51, pp. 1639–1560, 03 2015.

[75] S. Jayalath and M. Hanif, "Generalized lcl-filter design algorithm for grid-connected voltage-source inverter," *IEEE Transactions on Industrial Electronics*, vol. 64, no. 3, pp. 1905–1915, 2017.